MEASUREMENTS OF INJECTED IMPURITY TRANSPORT IN TEXT USING MULTIPLY FILTERED SOFT X-RAY DETECTORS

by

KEVIN WAYNE WENZEL

B.S . Nuclear Engineering, University of Illinois, Urbana
1983

Submitted to the Department of
Nuclear Engineering
in Partial Fulfillment of the
Requirements for the Degree of

DOCTOR OF PHILOSOPHY

at the

MASSACHUSETTS INSTITUTE OF TECHNOLOGY
FEBRUARY 1990

Signature of Author _____
Department of Nuclear Engineering
December 1989

Certified by _____
Richard D. Petrasso
Thesis Supervisor

Certified by _____
Dieter J. Sigmar
Thesis Reader

Accepted by _____
Allan F. Henry
Chairman, Departmental Graduate Committee

Measurements of Injected Impurity Transport in TEXT Using Multiply Filtered Soft X-Ray Detectors

by

KEVIN WAYNE WENZEL

Submitted to the Department of Nuclear Engineering
on *December 11, 1989* in partial fulfillment of the
Requirements for the Degree of Doctor of Philosophy in
Nuclear Engineering

Abstract

Aluminum was injected into TEXT to study trace, non-recycling impurity transport. A 92-channel, three array x-ray imaging system was constructed and installed to measure temporally-resolved density profiles of the three highest charge states. A novel krypton filter in one array discriminated between the He-like and H-like resonance lines, and a hard filter responded mostly to the fully stripped charge state.

The impurity confinement time scaled approximately as $\tau_c \sim \bar{n}_e Z_{eff} \sqrt{m_i/Z_i}/I_P$ (i denotes the background gas). Aluminum density profiles averaged over a sawtooth period were measured in several different discharges. Profile changes during sawtooth crashes were also measured for a few discharges. Sawteeth strongly enhanced the inward impurity flow immediately following injection, when the density was still peaked near the plasma edge. Those discharges with the longest sawtooth period obtained the most peaked aluminum density profiles; thus sawteeth were also important in ameliorating impurity accumulation on the tokamak axis. The charge state balance of the aluminum ions obtained from the measured profiles was compared to predictions of coronal equilibrium. Somewhat surprisingly the aluminum ions were close to coronal, except in those discharges with very short sawtooth periods or very large inversion radii. Preliminary evidence of up-down asymmetric density profiles was also found.

Numerical simulations of aluminum transport were performed. The effect of sawtooth oscillations was taken into account with a simple flattening model. The data disagreed with a constant D anomalous model except in the plasma center; enhanced outward transport was required. The experiments did not agree with neoclassical simulations, because the theory had outward convection that was too large.

Thesis Supervisor: Dr. Richard D. Petrasso

Title: Principal Research Scientist, Plasma Fusion Center

Acknowledgments

Any project whose goal is as difficult as controlled thermonuclear fusion is necessarily a cooperative effort Throughout my work in this field I have benefitted from such cooperation with many people. I take this opportunity to thank them.

First, I extend thanks to my advisor, Dr. Richard Petrasso. He provided strong motivation throughout this work, both technical and emotional. Rich is unrelenting in his efforts to be do only the highest quality research (and sometimes in his efforts to ensure others are not guilty of fooling people into believing low quality results). I hope that I have learned well the lessons he has taught me over the last five years.

Second, I thank the faculty members who have taught me so much, especially how to continue learning. At MIT: Professors Dieter Sigmar, Jeff Freidberg, Ian Hutchinson, Larry Lidsky, Kim Molvig, Abe Bers, Miklos Porkolab, Neal Todreas, and Sidney Yip. Professor Sigmar deserves extra appreciation for spending many hours patiently explaining numerous details of neoclassical transport theory to me and for serving as my thesis reader. At the University of Texas: Professors Ken Gentle, Wendell Horton, and Marshall Rosenbluth. At the University of Illinois: Professor Chan Choi (now at Purdue). Special thanks are due to Professors Freidberg, Hutchinson, and Lidsky for serving on my thesis committee.

Third, I would like to acknowledge the invaluable assistance of both the TEXT and Alcator technical staffs. One of the unique advantages of this project was the chance to work with both of these excellent groups of people. In particular, Tom Herman of TEXT was instrumental in the design and construction of the vacuum systems. Joe Bryan, Steve Hilsberg and Paul Landers of TEXT were helpful regarding the design of the electronics. Joe Bosco and Bill Parkin of Alcator kindly provided filter modules modified to allow higher cutoff frequencies than previously available. Dr. Robert Granetz generously loaned us the Traq I digitizer system, previously used on Alcator-C. Martha Baker and Dr. Ken Gentle assisted in the design of the vertical x-ray array vacuum box. The TEXT engineering staff, Jim Jagger, David Terry, David Pavlovsky, and Deb Foster did an excellent job of keeping TEXT up and running.

Fourth, I want to thank all those scientists who contributed to this work by running TEXT or operating diagnostics in support of this work. Dr. Ron Bravenec, Dr. Steve McCool, Dr. William Rowan, Dr. Alan Wootton, Dr. David Sing, Dr. Perry Phillips, Dr. Jiayu Chen, Dr. David Brower, Dr. Roger Bengtson, Dr. Burton Richards, and Dr. Gary Hallock were all helpful at the University of Texas.

Fifth, I would like to thank my fellow students, both at MIT and the University of Texas, for their academic help and also for many interesting conversations on physics and life in general At MIT Mark Melvin, Scott Peng, Bob Witt, Mark Sands, John Massidda, Russ Benjamin (from JHU) Ken Pendergast, John Machuzak, Manos Chaniotakis, and Jim Hopf. At UT: Max Austin, Mark Foster, Dale Crockett, Ed Synakowski, Andy Meigs, Roger Durst, Brackin Smith, and Abdelhamid Ouroua.

Sixth, I want to thank my family. My parents Joseph and Patricia Wenzel, and my sister Eileen, were a continuing source of support. Of course without my folks' emphasis on the importance of education early in my life, I never would have made it this far. Thank you Wenzels.

Finally, I want to thank my fiance, Laura Kasper, for her endless love and support over the last few years. She has made it all worthwhile. She is also responsible for typing the majority of this thesis.

Contents

Acknowledgments **3**

List of Figures **7**

List of Tables **11**

1 Introduction **13**

1.1 The Concepts of Fusion and Tokamaks 13

1.2 The Importance of Impurities in Tokamak Plasmas 16

1.3 Review of Impurity Transport Measurements 17

1.4 Review of Neoclassical Impurity Transport Theory 23

1.5 Motivation for and Summary of Method on TEXT 30

1.6 TEXT 30

1.7 Organization of the Thesis 31

2 Modeling the Plasma X-Ray Emissivity **34**

2.1 Introduction 34

2.2 Continuum X-Radiation 35

2.2.1 Bremsstrahlung Radiation 36

2.2.2 Radiative Recombination 37

2.3 Discrete Line Radiation 40

2.3.1 Line Radiation after Electron Impact Excitation 41

2.3.2 Line Radiation after Dielectronic Recombination 42

2.3.3 Line Radiation after Inner Shell Excitation 44

2.3.4 Line Radiation after Recombination into Upper Levels 44

2.4 Conclusion 45

3 X-Ray Measurement Systems on TEXT **47**

3.1 Introduction 47

3.2 Broadband X Ray Detectors 47

3.2.1 Calibration and Response Measurements 49

3.3 Array Systems Installed on TEXT 66

3.3.1 X-Ray Imaging System Components 68

3.3.2 Krypton Filtering and Preliminary Results 79

4 Measurements of the Transport of Injected Aluminum in TEXT **84**

4.1 Introduction 84

4.2 Experimental Method 84

4.2.1 Injection Techniques 84

4.2.2 Diagnostics 85

4.2.3 X-Ray Data Analysis 89

4.3 Experimental Results 102

4.3.1 Aluminum Ion Confinement Time Scalings 102

4.3.2 Aluminum Density Profiles 116

4.3.3 Charge State Distribution Profiles 132

4.3.4 Preliminary Observations of Up-Down Asymmetric Impurity Densities 143

4.4 Conclusions 151

5 Simulation of the Transport of Injected Impurities **152**

5.1 Introduction 152

5.2 Explicit Numerical Charge State Transport Code 154

5.3 Implicit Numerical Charge State Transport Code 156

5.4 Benchmarking the Transport Codes 159

5.5 Sawtooth Model Incorporated in the Transport Codes 162

5.6 Simulations of TEXT Discharges with Aluminum Injection 163

5.6.1 Transport Simulations with Anomalous Coefficients 163

5.6.2 Transport Simulation with Neoclassical Coefficients 168

6 Comparison of Measured Particle Transport Coefficients on TEXT from Different Techniques **176**

7 Summary and Conclusions; Suggestions for Future Work **178**

7.1 Summary 178

7.2 Future Work 180

A Neoclassical Calculations of K_{ij}^a in the Pfirsch-Schlüter Regime **182**

B Neoclassical Calculation of the Trace Impurity Flux in the Pfirsch-Schlüter Regime **184**

C Atomic Parameters for X-Ray Emissivity Calculations **187**

D Some Comments on Abel Inversion **203**

D.1 Introduction 203

D.2 Broad X-Ray Brightness Profiles 204

D.3 Peaked X-Ray Brightness Profiles 204

E Comparison of Recombination Rates for Aluminum **207**

F Uncertainties in Aluminum Density Profiles **209**

Bibliography **213**

List of Figures

1.1 Tokamak geometry 15
1.2 Schematic view of TEXT 33

2.1 Bremsstrahlung 36
2.2 Radiative recombination. 38
2.3 $\chi_n/T_e e^{\chi_n/T_e}$ vs. χ_n/T_e 39
2.4 Carbon x-ray spectrum 40
2.5 Line radiation 42
2.6 Dielectronic recombination 43
2.7 Aluminum x-ray spectrum 46

3.1 X-ray detector equivalent circuit 48
3.2 SBD signal 54
3.3 Calibration spectra 55
3.4 Calibration source linearity 56
3.5 Calibration circuits 58
3.6 Absolute detector response 59
3.7 SBD response linearity 60
3.8 SBD response vs. bias voltage 61
3.9 Absolute SBD responses 64
3.10 TEXT x-ray imaging system 69
3.11 Vertical x-ray array 70
3.12 Horizontal x-ray array 71
3.13 45° x-ray array 72
3.14 Detector surface transmissivities 75
3.15 Data acquisition system 76
3.16 Circuit frequency responses 78

3.17 X-ray filter responses 80
3.18 X-ray data 82
3.19 X-ray brightness profiles 83

4.1 Aluminum pellet injection 86
4.2 Aluminum pellet injection 86
4.3 Laser ablation and pellet injection 87
4.4 Injection data 88
4.5 X-ray spectrometer response 89
4.6 Net x-ray emissivity profiles 91
4.7 Sawtooth discrimination 93
4.8 Gross and net x-ray signals 94
4.9 Filter A emissivity profile 95
4.10 Filter G emissivity profile 95
4.11 Filter D emissivity profile 96
4.12 Initial aluminum profile estimate 97
4.13 Neutral density profile 98
4.14 Abel inversion sensitivity 100
4.15 Effective chord radius shift 101
4.16 Aluminum confinement time τ_c 107
4.17 τ_c vs. $Z_{eff}\bar{n}_e$ 108
4.18 $\tau_c/(Z_{eff}\bar{n}_e)$ vs. m_i/Z_i 110
4.19 Plasma current scaling of τ_c 112
4.20 τ_c regression analysis 115
4.21 Al profiles; shot 143989 117
4.22 Al profiles; shot 143995 118
4.23 Al profiles; shot 144004 119
4.24 Al profiles; shot 144027 120
4.25 Al profiles; shot 148034 121
4.26 Al profiles; shot 148039 122
4.27 Al profiles; shot 148135 123
4.28 Al profiles; shot 148152 124
4.29 Al profiles; shot 148237 125
4.30 Impurity influx change attributed to sawteeth 127
4.31 Central soft x-ray and temperature signals 129

4.32 Pre- and post-sawtooth aluminum density profiles 130
4.33 Pre and post sawtooth x-ray brightness profiles 131
4.34 Sawtooth-induced profile change; high $\bar{n}_e$, low q_a 133
4.35 Sawtooth-induced profile change; low $\bar{n}_e$, low q_a 134
4.36 Sawtooth-induced profiles change; low $\bar{n}_e$, high q_a 135
4.37 Charge state distribution; 143989 136
4.38 Charge state distribution; 143995 137
4.39 Charge state distribution; 144004 137
4.40 Charge state distribution; 144027 138
4.41 Charge state distribution; 148034 138
4.42 Charge state distribution; 148039 139
4.43 Charge state distribution; 148135 139
4.44 Charge state distribution; 148152 140
4.45 Charge state distribution; 148237 140
4.46 Coronal equilibrium comparison 142
4.47 Temporal behavior of up-down asymmetry 146
4.48 Experimental asymmetry parameter; low q_a 147
4.49 Experimental asymmetry parameter; high q_a 148

5.1 Explicit transport code results 160
5.2 Implicit transport code results 161
5.3 Simulation results without sawteeth 165
5.4 Simulation results with sawteeth 166
5.5 Simulation results of a high q_a discharge 167
5.6 Simulation results with reduced combination 169
5.7 Neoclassical transport coefficients 172
5.8 Ion collisionalities 173
5.9 Neoclassical simulation result 174

C.1 Carbon x-ray power functions 195
C.2 Oxygen x-ray power functions 196
C.3 Titanium x-ray power functions 197
C.4 Iron x-ray power functions 198
C.5 Filter A aluminum x-ray power functions 199
C.6 Filter D aluminum x-ray power functions 200

C.7 Filter F aluminum x-ray power functions 201
C.8 Filter G aluminum x-ray power functions 202

D.1 Broad x-ray profiles 205
D.2 Broad x-ray profiles 205
D.3 Peaked x-ray profiles 206
D.4 Peaked x-ray profiles 206

F.1 Uncertainty due to emissivity uncertainty 211
F.2 Uncertainty due to temperature uncertainty 212

List of Tables

1.1 Text Diagnostics 32

2.1 T_e/χ_n ratios for equal bremsstrahlung and recombination 39

3.1 Experiments using SBDs 50
3.2 Calibrated SBDs 53

4.1 TEXT discharges used for τ_c scaling 103
4.2 TEXT discharges for Al density profiles 116
4.3 Central charge state distributions 141

6.1 Measured transport coefficients in TEXT 177

C.1 Atomic parameters for aluminum 189
C.2 Atomic parameters for silicon 190
C.3 Atomic parameters for titanium 191
C.4 Atomic parameters for iron 192
C.5 X-ray filters 194

E.1 Comparison of aluminum recombination rates 208

Chapter 1

Introduction

1.1 The Concepts of Fusion and Tokamaks

Severe problems are directly caused by burning fossil fuels to generate useful energy. Limited fuel supplies and degradation of the environment as a consequence of transporting and burning such fuels are only two examples. The problem of limited resources and their rapid depletion has motivated attempts to harness renewable resources for energy production (e.g., solar, wind, hydro-electric), because such resources offer essentially eternal energy supplies. Fusion energy, while not strictly renewable, may be thought of as offering a nearly infinite supply of energy because the primary fuel element is deuterium ($_1D^2$), which constitutes approximately one in every 6500 hydrogen atoms on earth [1]. There has therefore understandably been great interest in developing practical economic fusion energy on earth since the late 1930s, when it was realized that fusion reactions between light elements provide the power source of the sun and stars [2,3].

However progress toward controlled fusion power has been gradual. This is due to the difficulty in bringing two positively charged nuclei close enough together for the strong, short range attractive nuclear force to overcome the longer range Coulombic repulsion. When the nuclei approach each other closely enough, they can undergo the most favorable nuclear reactions between deuterium and tritium ($_1T^3$) or between deuterium and deuterium:

$$
\begin{aligned}
{}_1D^2 + {}_1T^3 &\longrightarrow {}_2He^4(3.6\text{ MeV}) + {}_0n^1(14.7\text{ MeV}) \\
{}_1D^2 + {}_1D^2 &\longrightarrow {}_2He^3(0.82\text{ MeV}) + {}_0n^1(2.45\text{ MeV}) \\
{}_1D^2 + {}_1D^2 &\longrightarrow {}_1T^3(1.01\text{ MeV}) + {}_1H^1(3.02\text{ MeV}).
\end{aligned}
$$

The most extensively pursued means to achieve these reactions in the laboratory has

been to raise the temperature of a hydrogen gas to the point where the individual particles have sufficient kinetic energy to overcome the Coulomb potential between the nuclei. At such extreme temperatures, collisions between electrons and the initially neutral atoms cause ionization, and the gas becomes an ionized gas called a *plasma* [4], sometimes referred to as the fourth state of matter [5].

Confinement of laboratory plasmas using magnetic fields has been compelling historically for two main reasons: first, charged particles exhibit cyclotron (helical orbit) motion in the presence of a magnetic field, hence the particles are "glued" to the field lines; and second, confinement of high-temperature plasmas using material boundaries is impossible because a plasma with a low energy density will rapidly lose all its energy to the container walls upon contact. For these reasons, magnetic confinement approaches to controlled fusion have dominated the international effort.[1,2]

Currently the leading candidate for a fusion reactor scheme utilizing magnetic confinement is the *tokamak*, a Russian acronym for toroidal magnetic geometry [15,16]. The tokamak confines the plasma in a strong toroidal field ($B_T \sim 1 - 13$ T) generated by magnetic field coils encircling the plasma in the short (poloidal) direction, as represented schematically in Fig. 1.1. A smaller poloidal field, required for plasma stability, is generated by driving a large current ($I_p \sim 50\ kA - 10\ MA$) through the plasma by making the plasma column act as the secondary winding of a transformer. The plasma current also serves to heat the plasma through the action of ohmic (resistive) heating. The major parameters of a tokamak, determined largely by magnet technology and engineering constraints, are the toroidal field B_T, the plasma current I_P, and the aspect ratio $A = R_0/a$.

[1] U. S. Department of Energy funding for magnetic fusion in fiscal year 1989 was $350.7 million; that for inertial, or laser, fusion was $163.8 million [6].

[2] Two other approaches to fusion are inertial confinement and so-called "cold fusion." In inertial confinement, strong lasers are focussed symmetrically on a small pellet containing fuel atoms. The subsequent compression and heating is anticipated to give rise to density and temperature regimes sufficient to cause fusion reactions to occur in a micro-explosion. "Cold fusion," on the other hand, occurs between hydrogen nuclei in TD or DD molecules. Normally the nuclei in these molecules are too far apart for any significant fusion to occur. However, the internuclear spacing in the hydrogen molecule may be reduced by either replacing an electron with a heavier particle (*e.g.*, a muon) [7], or by electrochemically doping metals with large amounts of hydrogen isotopes [8,9]. Only small fusion rates were reported by Jones using the latter method [8], and large amounts of heat reported by Fleischmann, Pons and Hawkins, also using the latter method [9], remain unsubstantiated (*e.g.*, see reference [10]). Furthermore, evidence of nuclear fusion products presented by Fleischmann, *et. al.* is severely flawed [11,12,13], and independent measurements using the same cells indicate no evidence of fusion activity [14]. Thus cold fusion appears least likely to evolve into a useful source of energy.

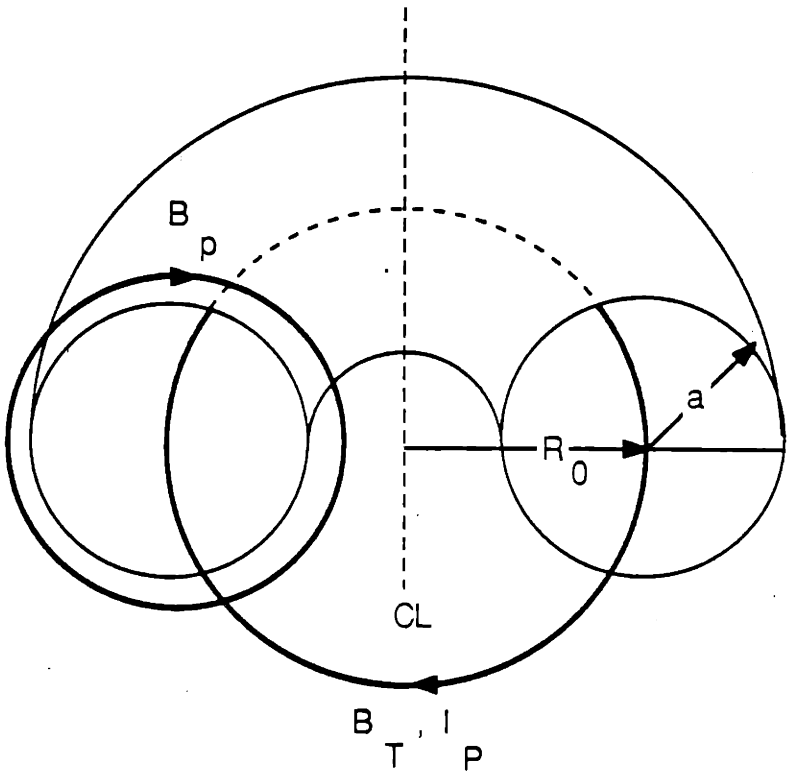

Figure 1.1: This schematic of tokamak geometry illustrates the predominant fields and currents used for plasma confinement in toroidal geometry. The largest field, the toroidal field B_T, is generated by coils external to the plasma and encircling it in the short (poloidal) direction. The toroidal plasma current I_P, driven by using the plasma as the secondary winding in a transformer circuit, itself generates a poloidal magnetic field B_P. The main geometric parameters in a tokamak with circular cross section are the major radius R_0 and the minor radius a.

1.2 The Importance of Impurities in Tokamak Plasmas

Understanding the behavior of impurity dynamics is important in thermonuclear fusion research because of the multifaceted effects impurities can have on fusion plasmas. In fact the JET group considers plasma impurities unequivocally the most important problem facing fusion research today [17]. Impurity species in high temperature fusion plasmas can play an important role in determining the quality of plasma behavior. Several effects impurities have on the plasma are discussed in more detail below.

The engineering parameters of tokamaks introduced in section 1.1 and illustrated in Fig. 1.1 often determine the plasma parameters achievable in a given tokamak. In the context of fusion research, one of the most important of these parameters is specified by the Lawson criterion [18] which dictates the product of the plasma density n and the energy confinement time τ_E necessary to achieve energetic breakeven at a given temperature. For example, the minimum ion temperature for breakeven with DT reactions is 2.5 keV. At this temperature, $n\tau_E$ must be infinite, and at 10 keV, $n\tau_E$ must be $\sim 10^{20}$ m^{-3}s [18]. Such criteria are generally derived by balancing the energy lost from the plasma by bremsstrahlung radiation against the energy produced in the plasma by fusion reactions. As will be shown in the next chapter, the power radiated through bremsstrahlung depends strongly on the charge of the radiating ion ($P_b \propto Z^2$; see Eq. 2.3). In fact, energy loss from radiative processes other than bremsstrahlung (e.g., radiative recombination and line radiation) scale even more strongly with the ionic charge [19]. This consideration provides the primary motivation for maintaining as clean a plasma as possible as well as the need to understand the behavior of impurity species in the plasma.

Another detrimental effect that impurities have on fusion plasmas is the dilution of fuel (H isotope) ions. This occurs because the total electron density is limited by I_P, a, B_T and R_0 [20,21], and impurity ions contribute more electrons per atom than hydrogen. Hence as the impurity density increases, the fuel density must decrease substantially.

Another significant effect impurities have on plasma behavior is on the magnetic stability. The profile of the current density plays a strong role in magnetohydrodynamic modes in high temperature plasmas. The distribution of the plasma current depends on the induced toroidal electric field and the local plasma conductivity. The conductivity parallel to the magnetic field in turn scales approximately as $T_e^{3/2}/Z_{eff}$ [22], so again the effective charge of the plasma, as determined by the impurity population, can directly

affect plasma stability properties ($Z_{eff} = \Sigma_i n_i Z_i^2/n_e$). Furthermore, impurity-induced changes in the plasma resistivity profile can enhance turbulent transport in the plasma edge [23].

Impurities can also strongly affect plasma transport processes. An impure plasma will have a much greater energy transport through the ion channel than a pure hydrogen/electron plasma [24]. This is largely due to the increased collisionality in a dirty plasma, because the collision frequency scales as Z^2. Another way impurities may enhance plasma thermal transport is that impurity density gradients can act as a free energy source for microturbulence-driven transport [25].

These few examples of impurity behavior illuminate the need to fully understand impurity transport characteristics of high temperature plasmas. The question of impurity transport is therefore being attacked extensively on both experimental and theoretical grounds. These two efforts are briefly reviewed in the next two sections.

1.3 Review of Impurity Transport Measurements

A brief review of past impurity transport measurements in tokamaks is offered in this section. The primary emphasis here is the comparison of experimental findings with the most well-established theoretical model of impurity particle transport, neoclassical theory, introduced in the next section. A comparison with neoclassical transport is important not only as a test of the validity of the theory itself, but also because collisional transport determines an absolute minimum level of energy and particle losses [26]. A general review of experimental transport results was given in 1983 by Hugill [27]. Many other important physics issues related to impurities were given a comprehensive treatment in the review of Isler [28]: atomic physics calculations, impurity production, impurity transport and control. The discussion herein concentrates on four facets of experimental impurity studies: comparisons between experimental findings and neoclassical predictions, measured changes in impurity transport due to MHD instabilities, measurements of the charge state distribution of impurities in tokamaks, and scaling studies of the global impurity confinement times.

Whether impurities behave neoclassically is a crucial issue, because the theory predicts, in many situations, that impurities should accumulate in the center of a tokamak plasma. The prediction of impurity peaking can be easily understood by examining the

general form of the particle flux,

$$\Gamma = -D\nabla n - nV, \tag{1.1}$$

where V is the inward "convection" velocity, driven by ion temperature gradients and background particle gradients. (Both conventions for choosing the sign of V are present in the literature. In this thesis, *inward* convection is represented by positive V, and all experimental results reported in this section have been written to conform to this choice.) As a simple illustrative example, D is assumed constant with radius, $D(r) = D_0$, and V is assumed to be linear, $V(r) = V_0(r/a)$. Then in steady state the flux is zero, and the solution to Eq. 1.1 is simply

$$n(r) = n_0 e^{-V_0 r^2/2D_0 a} \tag{1.2}$$

Thus as the ratio $V_0/2D_0a$ increases the equilibrium profile becomes more peaked.

A consequence of the above argument is that experiments with flat impurity density profiles or values of D_0 much larger than the neoclassical prediction (small $V/2D_0a$) are described as not behaving neoclassically. These experiments are often described in terms of an anomalous diffusion D_{an} much greater than the diffusion coefficient obtained from neoclassical calculations (D_{neo}). Many experiments have been interpreted in this manner. For instance in Alcator-A, profiles of OV, OVI, and NV measured spectroscopically could only be adequately described with a model including diffusion four times that predicted by neoclassical theory [29]. Oxygen and carbon profiles in TFR were simulated accurately only with a large diffusion coefficient $D = 250\nu_e\rho_e^2(1+1.6q^2)$, where ν_e is the electron collision frequency, ρ_e is the electron gyroradius, and q is the local magnetic safety factor, $q = rB_T/R_0B_P$. The same TFR results were also modeled with a constant diffusion coefficient $D = 0.3$ m^2/s; both forms of D were much larger than D_{neo} [30]. The transport of injected heavy impurities (V, Cr, Ni) in TFR was also simulated numerically with large anomalous transport coefficients $D_{an} \simeq 2 \sim 4$ m^2/s and $V_0 \simeq 4$–8 m/s [31]. Similarly, in JT60 injections of Ti were consistent with small convection and constant $D_{an} \simeq 1$ m^2/s in both ohmic [32] and neutral beam heated discharges [33]. (The JT60 experiments were interesting at least for the method of injection; some Ti injections were "accidental", and others were achieved by briefly turning off the divertor coils so that the plasma contacted the TiC-coated limiter and increased the Ti content of the plasma.) Injection experiments in other tokamaks have also required transport parameters larger than neoclassical. In Alcator-C injections of

many impurities were consistent with D_{an} on the order of 0.1 to 0.5 m^2/s, and small convection [34]. In TEXT, injections of Sc were modeled with $D_{an} \sim 1$ m^2/s and $V_0 \sim$ 5–10 m/s [35]. Results from spectroscopic measurements of intrinsic impurities (mostly C) in TFTR gave flat density profiles, inconsistent with neoclassical predictions [36]. Important caveats are necessary before concluding that all these results serve to negate the validity of neoclassical theory: first MHD oscillations, especially sawteeth, were not explicitly taken into account in many of these experiments; and second most reports did not explain the method of calculating the neoclassical transport coefficients, in particular whether impurity-impurity collisions were taken into account or whether the terms from all collisionality regimes were properly included in the calculations. The difficulty of accurately calculating neoclassical transport coefficients will be borne out in the next section.

In contrast with those experiments described above, several experiments have shown impurity peaking and behavior at least qualitatively consistent with neoclassical theory. For example in the ATC tokamak, aluminum injection experiments were well described using a numerical simulation with neoclassical fluxes [37]. Similarly, iron injected into the low-field tokamak TJ-1 [38] was reported to follow the neoclassical impurity confinement scaling of Rozhanskii [39]. Central accumulation of intrinsic impurities occurred in Pulsator when the machine was run near the high density limit [40]. In this case the high central impurity concentration led to disruptions. Impurity accumulation is also often seen in tokamaks following some perturbation to the plasma. For instance after injecting frozen hydrogen pellets for fueling Alcator-C, neoclassical-like peaked carbon and molybdenum density profiles were observed [41,42]. Furthermore, there was some evidence for a change in the sign of the convective velocity with increasing plasma radius, also in qualitative agreement with neoclassical theory [43]. A model with $D = 0.03 + 1.875(r/a)^2$ m^2/s and $V = 10(r/a) - 30(r/a)^3$ was shown to reproduce the correct equilibrium carbon profile shape [43]. After multiple pellet injection in ASDEX, sawtooth oscillations were suppressed and accumulation of high Z impurities occurred [44]. However, in contrast to predictions of the neoclassical model used by the ASDEX group, light impurities were reported not to peak. Light impurity peaking was found more recently in ASDEX during high density improved ohmic confinement discharges [45]. During neutral beam heating experiments in PBX, a Z-dependent impurity accumulation was seen during both H-mode [46] and L-mode [47] discharges. Z-dependent peaking is predicted by neoclassical theory because the convective velocity terms and

the diffusion terms vary differently with increasing Z depending on the collisionality. In the banana-plateau collisionality regime the diffusion coefficient scales as $1/Z^2$, and the convective velocity scales approximately as $1/Z$. In the collisional regimes (Pfirsch-Schlüter and classical) the diffusion coefficient is independent of Z, and the convective velocity terms scale as Z. In both cases the ratio $V/2aD$ increases with Z, which implies that heavier impurities should have more peaked profiles in cases where V is inward. In PBX, the ratio of convection to diffusion, $C_Z \equiv V_0 a/2D_0$ was approximately 4 for light impurities and 20 for heavy impurities. H-mode discharges in ASDEX also produced high Z (Fe) accumulation [48]. With increasing electron density in TEXTOR the plasma became detached and the confinement time of injected iron increased from 75 to 300 ms [49]. This change in confinement was consistent with the change in the neoclassically predicted convection due to the change in edge gradients [50]; however the diffusion necessary to describe the iron transport was anomalous for both normal and detached discharges, $D_{an} \simeq 0.9$ m^2/s. The transport of Ni in DIIID, measured between edge localized mode oscillations (ELMs), was also consistent with anomalous diffusion, $D_{an} \simeq 1$ m^2/s, but neoclassical-like convection [51]. In contrast, peaking of light impurities (C and O) following hydrogen pellet injection in TEXT was consistent with nearly neoclassical diffusion, $D_0 \simeq 0.15$ m^2/s, but anomalous convection $V_0 = 6.5$ m/s [52].

The examples above show that impurity dynamics in agreement with neoclassical theory and impurity transport much larger than the theory have both been observed experimentally, sometimes under similar plasma conditions. Thus the question of what determines the dominant transport process for impurity particles remains open. Perhaps a more fundamental issue is if neoclassical transport is not dominant, what is driving transport of impurities? Theories for turbulent transport of impurity species are lacking, so for now comparisons of experimental data with neoclassical theory and phenomenological descriptions of transport larger than predicted by that theory must suffice.

Another important issue for plasma impurities is the degree to which high Z elements are ionized. This is particularly important for determining the power radiated from the plasma, since the power radiated by atomic species I can be expressed as

$$P_{RAD} = n_e \sum_Z n_I f_Z P_Z(T_e) \tag{1.3}$$

where f_Z is the fraction of species I ionized to the charge state $+Z$, and $P_Z(T_e)$ is the

power radiated per ion. In plasmas where transport effects are negligible, the charge state distribution should be determined by coronal equilibrium, so called because it occurs in the solar corona where the density is low, and the dominant atomic processes are collisional ionization, radiative recombination and dielectronic recombination. In steady state the ratio of adjacent charge states is then simply given by (see also section 4.3.3)

$$\frac{n_{j+1}}{n_j} = \frac{I_j}{R_{j+1}} \tag{1.4}$$

where I_j is the ionization rate coefficient ($j \longrightarrow j+1$), and R_{j+1} is the total recombination rate coefficient ($j+1 \longrightarrow j$). Measurements of the charge state distribution of various impurities have therefore been made on several tokamaks. In TFR heavy impurities (Ni and Cr) were found to be in ionization equilibrium within a factor of two uncertainty in the atomic ionization and recombination rates [53]. In Alcator-C injected silicon was shown to be in coronal equilibrium; this was attributed to the high electron density, where typical atomic transition times were much less than transport times [54]. Later work in TFR showed that metal impurities (Ni, Cr and Fe) were not in ionization equilibrium, but their data could be adequately simulated if transport effects were properly accounted for and the quantity I_j/R_{j+1} was used as an adjustable parameter. The experimental results could be simulated with $D_0 \simeq 0.2$ m^2/s, $V_0 = 8$ m/s and I_j/R_{j+1} multiplied by 0.75 for the Li-like, Be-like and B-like states [55]. From these observations, one might conclude that coronal equilibrium is only achieved when the longest ionization time is shorter than the shortest transport time. Otherwise the effect of transport must be explicitly accounted for when determining the charge state distribution.

Another question regarding impurity transport is the effect of MHD oscillations, including sawteeth. Sawteeth are manifested in tokamak plasmas by periodic peaking and flattening of temperature and particle density profiles [56,57,58]. These oscillations have also been shown to be responsible for flattening impurity density profiles experimentally [54,59,60,61,48,62] and theoretically, especially when the inward convection velocity is large [63]. In ohmic TFR discharges, however, no modification of impurities with sawteeth was reported, but with neutral beam injection the central nickel density was strongly modulated by sawteeth [31]. Another form of MHD oscillation seen during H-mode discharges in diverted tokamaks is the edge localized mode (ELM). These edge oscillations also ameliorate impurity accumulation [64,51]. In fact during "burst-free" H-mode discharges in ASDEX strong impurity accumulation causing radiative disrup-

tions was found. Thus MHD oscillations are clearly important in determining overall impurity transport behavior. Indeed these oscillations may be a mechanism contributing to the deviation of measured impurity transport from neoclassical predictions.

The last issue in this section involves scaling studies of impurity confinement times. Scaling studies are important because it is often difficult to directly compare the absolute magnitude of measured particle fluxes to those predicted by theory. Comparisons of scalings provide a simpler means to negate or validate a particular theory and for discovering differences between machines. The most extensive measurement of impurity confinement times was performed on Alcator-C [34]. This work resulted in the empirical formula

$$\tau_Z(ms) = 0.075 a m_i R_0^{0.75} Z_{eff}/q_a Z_i, \tag{1.5}$$

where a and R_0 are the minor and major radii in cm, m_i is the mass of the background gas in amu, q_a is the magnetic safety factor at the limiter radius and Z_i is the charge of the background gas. (The dependences on R_0 and Z_{eff} are not as concrete as the other scalings.) In TEXT the scandium confinement time was found to decrease with increasing magnetic field and increasing plasma current [65]; the B_T scaling is in qualitative agreement with Marmar [34], but the I_P scaling is just opposite. The scandium confinement time in TEXT was also found to scale as $\sim Z_{eff}\sqrt{m_i}$ [66], which is also qualitatively similar to the Alcator-C results. In the TJ-1 tokamak the confinement time of injected iron was found to increase with B_T [38] in direct contrast with Marmar [34]. Thus, there is some disagreement as to how impurity confinement times scale with global plasma parameters in different machines, but this may be indicative of different plasma regimes where different transport mechanisms dominate. These differences dictate caution in concluding that a result from a given machine allows identification of a particular theoretical transport model, whether it be neoclassical or turbulent.

This section has reviewed experimental results in four broad areas of impurity behavior: comparisons with neoclassical theory, measurements of ion charge state distributions, effects of MHD oscillations on impurity transport, and impurity confinement time scalings. An extensive review of all observations of impurities in tokamaks was not intended. However a representative set of experiments illustrative of the various impurity dynamics observed was presented.

1.4 Review of Neoclassical Impurity Transport Theory

As discussed in the previous section, impurity transport is often found to be anomalous, or much greater than predicted by neoclassical transport theory. This anomalous transport is now thought to be driven by microturbulent fluctuations in the plasma [67]. Nonetheless, neoclassical impurity transport theory is important for at least three reasons. First, collisional transport represents an irreducible minimum because of the ubiquity of Coulomb interactions and drift orbits [26]. Second, recent tokamak experiments with improved confinement have shown central impurity accumulation consistent with neoclassical predictions [41,47,68]. Third, no adequate theory yet exists to relate turbulent fluctuations to impurity transport, and even if there were such a theory, there is currently insufficient diagnosis of turbulent fluctuations in the plasma center from which to calculate impurity fluxes [67]. In this section the neoclassical impurity fluxes are derived, in outline, for different regimes of collisionality. (For this derivation cgs units are used.)

The classical theory of plasma transport was worked out in detail by Braginskii [69]. Neoclassical transport theory is the extension of the classical collisional transport theory into toroidal geometry. The fundamentals of particle and heat transport in neoclassical theory were reviewed in 1976 by Hinton and Hazeltine [26]. The details of neoclassical transport including impurity species was fundamentally developed and then reviewed in 1981 by Hirshman and Sigmar [24]. The treatment of this reference is closely followed here.

The starting point for deriving impurity fluxes is the Vlasov Fokker-Planck equation for the distribution function, f_a, of species a,

$$\frac{\partial f_a}{\partial t} + \vec{v}_a \cdot \frac{\partial f_a}{\partial \vec{r}} + \vec{a}_a \cdot \frac{\partial f_a}{\partial \vec{v}} = C_a + S_a. \tag{1.6}$$

The acceleration due to the Lorentz force is given by $\vec{a}_a = (e_a/m_a)(\vec{E} + \vec{v}_a \times \vec{B}/c)$, C_a is the Coulomb collision operator, and S_a represents any external source or sink of species a. The first three velocity moments of this equation give the fluid expressions for conservation of particles, momentum, and energy, respectively:

$$\frac{\partial n_a}{\partial t} + \nabla \cdot (n_a \vec{u}_a) = S_{na} \tag{1.7}$$

$$m_a n_a \frac{d\vec{u}_a}{dt} = n_a e_a \left(\vec{E} + \frac{\vec{u}_a \times \vec{B}}{c} \right) - \nabla p_a - \nabla \cdot \overleftrightarrow{\pi}_a + F_{a1} \tag{1.8}$$

$$\frac{d}{dt}\left(\frac{1}{2}n_a m_a u_a^2 + \frac{3}{2}p_a\right) + \nabla\cdot\left[\left(\frac{1}{2}n_a m_a u_a^2 + \frac{5}{2}p_a\right)\vec{u}_a + \overleftrightarrow{\pi}_a\cdot\vec{u}_a + \vec{q}_a\right]$$
$$= \left(e_a n_a \vec{E} + \vec{F}_{a1}\right)\cdot\vec{u}_a + Q_a + S_{Ea}. \qquad (1.9)$$

In these equations, the fluid variables have been defined as follows: the particle density $n_a \equiv \int f_a\, d\vec{v}$, the fluid velocity $\vec{u}_a \equiv \int \vec{v} f_a\, d\vec{v}/n_a$, the particle source $S_{na} \equiv \int S_a\, d\vec{v}$, $p_a \equiv \int m_a(|\vec{v}-\vec{u}_a|^2/3) f_a\, d\vec{v}$, the viscosity tensor $\overleftrightarrow{\pi}_a \equiv \int m_a[(\vec{v}-\vec{u}_a)(\vec{v}-\vec{u}_a) - |\vec{v}-\vec{u}_a|^2 \overleftrightarrow{I}/3] f_a\, d\vec{v}$, the friction force $F_{a1} \equiv \int m_a \vec{v} C_a(f_a)\, d\vec{v}$, the heat flux $q_a \equiv \int(\vec{v}-\vec{u}_a)(m_a|\vec{v}-\vec{u}_a|^2/2) f_a\, d\vec{v}$, the collisional heat transfer $Q_a \equiv \int \frac{1}{2} m_a |\vec{v}-\vec{u}_a|^2 C_a(f_a)\, d\vec{v}$, and the energy source $S_{Ea} \equiv \int (m_a v^2/2) S_a\, d\vec{v}$. Note that the viscosity tensor $\overleftrightarrow{\pi}$ is defined as the difference between the pressure tensor $\overleftrightarrow{P}_a \equiv \int m_a[(\vec{v}-\vec{u}_a)(\vec{v}-\vec{u}_a)] f_a\, d\vec{v}$ and the scalar pressure $p_a \equiv \int m_a(|\vec{v}-\vec{u}_a|^2/3) f_a\, d\vec{v}$ times the unit matrix $\overleftrightarrow{I}$.

The cross-field particle flux is the primary quantity of interest here. This can be obtained by taking the cross product between $\vec{B}$ and Eq. 1.8, the momentum conservation equation, and defining the flux $\vec{\Gamma}_a \equiv n_a \vec{u}_{a1}$. Then in steady state

$$\vec{\Gamma}_{a1} = n_a c \frac{\vec{E}\times\vec{B}}{B^2} + \hat{n}\times\frac{\nabla\cdot\overleftrightarrow{P}_a}{m_a\Omega_a} + \frac{\vec{F}_{a1}\times\hat{n}}{m_a\Omega_a}, \qquad (1.10)$$

where $\hat{n}$ is the unit vector in the direction of $\vec{B}$, and recall $\overleftrightarrow{P}_a \equiv \overleftrightarrow{\pi}_a + p_a \overleftrightarrow{I}$.

In Eq. 1.10, the neoclassical contribution to transport can already be seen. The first term is due to the $E \times B$ drift. The second term represents the neoclassical part, driven by anisotropies in the pressure and collisional friction parallel to the magnetic field. The last term is just the classical flux, driven by collisional friction perpendicular to the magnetic field ($\vec{F}_{a1}^{\perp}$).

An alternate derivation of the neoclassical fluxes more readily demonstrates the origin of the different collisionality regimes [70,42]. This derivation is performed in flux surface coordinates (ψ, θ, ϕ), defined such that $|\nabla\psi| = RB_\theta\hat{e}_\psi$, $|\nabla\phi| = \hat{e}_\phi/R$, and $\vec{B} = B_P + B_T = \nabla\phi\times\nabla\psi + I\nabla\phi$ where $I = RB_\phi$ is a flux quantity, $I = I(\psi)$. Then, taking the dot product of $R\hat{e}_\phi$ with Eq. 1.8 gives, in steady state

$$0 = Rn_a e_a \hat{e}_\phi\cdot\vec{E} + Rn_a e_a \hat{e}_\phi\cdot(\vec{u}_a\times\vec{B}) - R\hat{e}_\phi\cdot\nabla p_a - R\hat{e}_\phi\cdot\nabla\cdot\overleftrightarrow{\pi} + R\hat{e}_\phi\cdot\vec{F}_{a1}. \qquad (1.11)$$

The second term gives the radial flux, since $\hat{e}_\phi\cdot(\vec{u}_a\times\vec{B}) = \vec{u}_a\cdot(\vec{B}\times\hat{e}_\phi) = \vec{u}_a\cdot((\nabla\phi\times\nabla\psi)\times\hat{e}_\phi + I\nabla\phi\times\hat{e}_\phi) = B_\theta\vec{u}_a\cdot\hat{e}_\psi$, using the relations defined above. Then Eq. 1.11 becomes

$$e_a n_a \vec{u}_a\cdot\nabla\psi = -Rn_a e_a\hat{e}_\phi\cdot\vec{E} - R\hat{e}_\phi\cdot\nabla p_a - R\hat{e}_\phi\cdot\nabla\cdot\overleftrightarrow{\pi}_a - R\hat{e}_\phi\cdot\vec{F}_{a1}. \qquad (1.12)$$

The friction term can be decomposed into a parallel and perpendicular part, $\vec{F}_{a1} = F_{a1}^{\parallel}\vec{B}/B + \vec{F}_{a1}^{\perp}$. The *contravariant* flux, $\vec{\Gamma}_a$, is then defined to be the flux surface average of Eq. 1 12,

$$e_a\vec{\Gamma}_a \quad \langle e_a n_a u_a \quad \nabla\psi\rangle = \quad \left\langle \frac{RF_{a1}^{\parallel}B_\phi}{B} \right\rangle - \left\langle R\hat{e}_\phi \quad \vec{F}_{a1}^{\perp} \right\rangle, \tag{1.13}$$

where the $< >$ represent the flux surface average, $< G >\equiv \oint G(1+\epsilon\cos\theta)d\theta/2\pi$. Thus the contravariant flux contains in it a factor RB_θ (from $\nabla\psi$), and it is the conjugate to the thermodynamic forces of the form p'/p. In this case $'$ denotes the derivative with respect to ψ (*i.e.*, $p' = \partial p/\partial\psi = (1/RB_\theta)\partial p/\partial r$). The first and second terms in Eq 1.12 vanish upon flux surface averaging in an axisymmetric tokamak, because axisymmetry implies that $< \hat{e}_\phi \cdot \nabla G >\equiv 0$ for any scalar quantity G. The third term becomes $< R^2\nabla\phi\cdot\nabla\cdot\overleftrightarrow{\pi} >= \frac{1}{V'}\frac{\partial}{\partial\psi}V' < R^2\nabla\phi\cdot\overleftrightarrow{\pi}\cdot\nabla\psi >$, where $V' \equiv \frac{dV}{d\psi}$ is the differential volume. The operator $\frac{1}{V'}\frac{\partial}{\partial\psi}V'$ reduces to $\left(\frac{1}{RB_P}\right)\left(\frac{1}{r}\frac{\partial}{\partial r}r\right)$ in circular flux geometry, and $< R^2\nabla\phi\cdot\overleftrightarrow{\pi}\cdot\nabla\psi >\equiv \pi_{\phi\psi}$ is the flux of toroidal momentum in the radial direction. This is the plasma viscosity which can be neglected here. Now the first term on the right may also be written, using $I = RB_\phi$,

$$\begin{aligned}\left\langle \frac{F_{a1}^{\parallel}RB_\phi}{B} \right\rangle &= \left\langle F_{a1}^{\parallel}RB_\phi\frac{B}{B^2}\left((1-\frac{B^2}{\langle B^2\rangle}+\frac{B^2}{\langle B^2\rangle}\right)\right\rangle \\ &= I\left\langle \frac{F_{a1}^{\parallel}B}{B^2}\left(1-\frac{B^2}{\langle B^2\rangle}\right)\right\rangle + I\frac{\langle F_{a1}^{\parallel}B\rangle}{\langle B^2\rangle},\end{aligned} \tag{1.14}$$

and the flux becomes

$$e_a\vec{\Gamma}_a = -I\left\langle \frac{F_{a1}^{\parallel}B}{B^2}\left(1-\frac{B^2}{\langle B^2\rangle}\right)\right\rangle - I\frac{\langle F_{a1}^{\parallel}B\rangle}{\langle B^2\rangle} - \langle R\hat{e}_\phi\cdot\vec{F}_{a1}^{\perp}\rangle. \tag{1.15}$$

The first term represents the neoclassical flux dominant in the regime of high collisionality (the Pfirsch-Schlüter regime). In this regime the collision frequency is much greater than the transit frequency (the frequency with which an ion completes an excursion around the entire minor radius), $\omega_T = v_{th}/Rq$, and $v_{th} \equiv \sqrt{2T/m}$, so $F_{a1}^{\parallel}$ will be able to retain θ-dependencies. In this case the effective step size squared that appears in the diffusion coefficient (from the familiar random walk argument) is $2q^2\rho_i^2$, where q is the safety factor and ρ_i is the ion gyroradius. The diffusion coefficient is then $D_i \sim 2q^2\rho_i^2\nu_{iz}$. The factor $2q^2$ comes from the term $\langle\frac{1}{B^2} - \frac{1}{\langle B^2\rangle}\rangle$ in a circular plasma with large aspect ratio ($\epsilon = A^{-1} < 1$). This is called the Pfirsch-Schlüter factor, and it represents the neoclassical enhancement over classical diffusion in the collisional regime. In the long mean free path regime (the banana-plateau regime) $F_{a1}^{\parallel}B$ loses its

θ dependence, so the first term in Eq. 1.15 vanishes. The second term on the right side of Eq. 1.15 survives only in the banana-plateau regime, and is dominant when the collision frequency is much less than the transit frequency. This is clear noting that this term is driven by pressure anisotropies in the flux surface which can be seen by examining the flux-surface-averaged parallel momentum balance (obtained from the dot product of $\vec{B}$ with Eq. 1.8) in steady state

$$0 = -\langle \vec{B} \cdot \nabla \cdot \vec{\pi}_a \rangle + B\langle \vec{F}_{a1}^{\parallel} \rangle. \tag{1.16}$$

Thus, this flux vanishes when the collisionality is high, because collisions tend to remove pressure anisotropies in a flux surface, $< \vec{B} \cdot \nabla \cdot \overleftrightarrow{\pi}_a > \sim 1/\nu_{ii}$. The last term in Eq. 1.15 is again the classical part of the flux, driven by the perpendicular friction. It scales as $D_{cl}\partial n/\partial\psi$, with $D_{cl} \sim \rho_i^2 \nu_{iz}$, without the $2q^2$ factor found in the Pfirsch-Schlüter flux. Thus the classical and Pfirsch-Schlüter fluxes can be comparable in the tokamak center where $2q^2 \simeq 1.5$.

The rigorous derivation of $\overleftrightarrow{\pi}_a$, and thus $\vec{B} \cdot \nabla \cdot \overleftrightarrow{\pi}_a$, can only be done on the kinetic level. Using the kinetic results from Ref. [24],

$$\langle \vec{B} \cdot \nabla \cdot \overleftrightarrow{\pi}_a \rangle = \mu_{a1} u_{pa} + \mu_{a2} q_{pa}, \tag{1.17}$$

the parallel viscious force is expressed in terms of the poloidal particle and heat flows u_{pa} and q_{pa}. Then the fluid level (Eqs. 1.13 and 1.16) can be used to obtain the particle fluxes below. Invoking ambipolarity $\Sigma_j e_j \Gamma_j = 0$ and neglecting the small electron flux Γ_e, the classical fluxes are given by

$$Z_i \Gamma_i^{Cl} = -Z_I \Gamma_I^{Cl} = -\langle \rho_i^2 |\nabla\psi|^2 \rangle \nu_{iI} n_i \left[\frac{p_i'}{p_i} - \frac{e_i T_I}{e_I T_i} \frac{p_I'}{p_I} - \frac{3T_i'}{2T_i} \right]. \tag{1.18}$$

In this expression subscript i denotes the working ion species; subscript I denotes the impurity species. The ion gyroradius is $\rho_i = v_{thi} m_i c/e_e B$, and the collision frequency is obtained from Braginskii's expression [69] (see Eq. B.30 in Appendix B). The banana-plateau fluxes are given by

$$e_i \Gamma_i^{BP} = -e_I \Gamma_I^{BP} = -\frac{3\langle (\vec{n} \cdot \nabla B)^2 \rangle}{\langle B^2 \rangle^2} \left(\frac{2\pi \langle I \rangle}{\chi'} \right)^2 \frac{c^2 T}{e_i e_I} \left[\frac{1}{(K_{11}^i)^{-1} + (K_{11}^I)^{-1}} \right]$$
$$\times \left[e_I \left(\frac{p_i'}{p_i} - \frac{5T_i'}{2T_i} \right) - e_i \left(\frac{p_I'}{p_I} - \frac{5T_I'}{2T_I} \right) + \left(\frac{e_I K_{12}^i}{K_{11}^i} - \frac{e_i K_{12}^I}{K_{11}^I} \right) \frac{T'}{T} \right] \tag{1.19}$$

where the quantities K_{ij} are related to the viscosity coefficients in Eq. 1.17, and are given in the plateau regime by

$$K_{ij}^{a,P} = \frac{p_a \sqrt{\pi}}{3\omega_{Ta}} \Gamma(i + j + 1), \tag{1.20}$$

and ω_{Ta} is the transit frequency for species a, ω_{Ta} v_{tha}/Rq, $v_{tha} \equiv \sqrt{2T_a/m_a}$, and Γ is the gamma function. The metric factor $(2\pi/\chi')$ 1 for the flux coordinates (ψ, θ, ϕ).

The K_{ij}s have also been calculated in other collisionality regimes [24]. In the Pfirsch-Schlüter regime

$$K_{ij}^{a,PS} = p_a \tau_{aa} \iota_{ij}^a \tag{1.21}$$

where the ι_{ij}s are given in Appendix A. In the banana regime

$$K_{ij}^{a,B} = \frac{f_t}{f_c} \frac{n_a m_a}{\tau_{aa}} \left\{ x_a^{2(i+j-2)} \nu_D^a \tau_{aa} \right\} \frac{\langle B^2 \rangle}{3\langle (\vec{n} \cdot \nabla B)^2 \rangle} \tag{1.22}$$

The flux surface averages are $\langle B^2 \rangle \simeq B_0^2/\sqrt{1-\epsilon^2} \simeq B_0^2$, and $\langle (\vec{n} \cdot \nabla B)^2 \rangle \simeq B_0^2/2R^2$, so that

$$K_{ij}^{a,B} = \frac{f_t}{f_c} \frac{n_a m_a}{\tau_{aa}} \frac{2R^2 B_0^2}{3B_\theta^2} \left\{ x_a^{2(i+j-2)} \nu_D^a \tau_{aa} \right\}. \tag{1.23}$$

In this expression f_t is the fraction of trapped particles ($f_t \simeq \sqrt{2\epsilon}$), $f_c = 1 - f_t$ is the fraction of circulating particles, and $\nu_D^a \equiv \sum_b \nu_D^{ab}$ is the deflection frequency for pitch angle scattering [24], where the ν^{ab} are given such that the quantities in brackets in Eq. 1.23 satisfies

$$\begin{aligned}
\{\nu_D^{ab}\}\tau_{ab} &= (1 + x_{ab}^2)^{1/2} + x_{ab}^2 \ln \left[\frac{x_{ab}}{1 + (1 + x_{ab}^2)^{1/2}} \right] \\
\{x_a^2 \nu_D^{ab}\}\tau_{ab} &= (1 + x_{ab}^2)^{-1/2} \\
\{x_a^4 \nu_D^{ab}\}\tau_{ab} &= \frac{2(1 + \frac{5}{4} x_{ab}^2)}{(1 + x_{ab}^2)^{3/2}}, \\
\text{and} \quad x_{ab} &\equiv v_{thb}/v_{tha}.
\end{aligned}$$

The above forms for K_{ij}^a are strictly valid only when the collisionality is deep into the applicable regime. It is convenient to have a formula to calculate K_{ij}^a over all values of collisionality. For this Hirshman and Sigmar gave a simple rational approximation,

$$K_{ij}^a = \frac{K_{ij}^{a,B}}{(1 + K_{ij}^{a,B}/K_{ij}^{a,P})(1 + K_{ij}^{a,P}/K_{ij}^{a,PS})}. \tag{1.24}$$

The Pfirsch-Schlüter fluxes are given by

$$Z_i \Gamma_i = -Z_I \Gamma_I = -n_i \langle (I\rho_i)^2 \rangle \nu_{iI} \left(\frac{2\pi}{\chi'} \right)^2 \times \left[1 - \frac{\langle I^2 \rangle / \langle B^2 \rangle}{\langle I^2/B^2 \rangle} \right] \times \left[K \left(\frac{n_i'}{n_i} - \frac{e_i n_I'}{e_I n_I} \right) + H \frac{T_i'}{T_i} \right], \tag{1.25}$$

where K and H depend on the impurity strength and the collisionality:

$$K(g, \alpha) = 1 - \frac{0.52\alpha}{0.59 + \alpha + 1.34 g^{-2}} \tag{1.26}$$

$$H(g,\alpha) \simeq -0.5 + \frac{0.29 + 0.68\alpha}{0.59 + \alpha + 1.34g^{-2}}. \tag{1.27}$$

In these last two equations, α is the impurity strength parameter $\alpha_I \equiv n_I e_I^2/n_i e_i^2$, and g is the ratio of the ion self-collision frequency to its transit frequency, $g \equiv \nu_{ii}/\omega_{ti}$.

All of the above fluxes are for the special case of a single impurity species (subscript I) diffusing on a working ion species (subscript i). The case of several impurities, which may be in different collisionality regimes, is much more difficult. It was worked out in Ref. [24] only for a trace impurity (subscript T) in the Pfirsch-Schlüter regime diffusing against a main impurity (I) and a working ion (i). In this case the working ion and main impurity may be in different collisionality regimes than the trace impurity. The resultant flux is

$$\Gamma_T = -\left(\frac{2\pi c}{\chi'}\right)^2 \frac{T}{e_T}\left[\left\langle\frac{I^2}{B^2}\right\rangle - \frac{\langle I\rangle^2}{\langle B^2\rangle}\right] \left[\frac{L_1}{e_I}\frac{p_I'}{p_I} + \frac{L_2}{e_I}\frac{p_I'}{p_I} + \frac{L_3}{e_I}\frac{T_I'}{T_I} + L_{11}^{Ti}\frac{T_i}{T_I e_i}\frac{p_i'}{p_i} + \frac{L_{11}^{TT}}{e_T}\frac{p_T'}{p_T} + L_{12}^{Ti}\frac{T_i'}{e_i T_I}\right]. \tag{1.28}$$

The L coefficients for this equation are given in terms of the plasma parameters in Appendix B. See also Ref. [42].

The neoclassical fluxes given above are written in the contravariant form in flux surface coordinates (recall $\Gamma_{con} \equiv n_a \vec{u}_a \cdot \nabla\psi = n_a \vec{u}_a \cdot RB_\theta \hat{e}_\psi$; $\nabla\phi = \hat{e}_\phi/R$). It is more useful for comparison with experimental results to have the fluxes in their covariant forms (without the extra RB_θ factors). In this form the transport coefficients linearly relate the particle fluxes $\vec{\Gamma}_{co} \equiv n_a \vec{u}_a \cdot \hat{e}_\psi$ to the thermodynamic forces in the form $\partial \ln p/\partial r$, where the derivative is now with respect to r, and not ψ. The covariant fluxes are obtained below for the case of a circular, large-aspect ratio tokamak from their contravariant counterparts in Eqs. 1.18–1.28. Flux surface average notation is dropped; quantities are assumed to be constant on the approximately circular flux surfaces.

The classical flux is easily converted to

$$Z_i\Gamma_i^{Cl} = -Z_I\Gamma_I^{Cl} = -\rho_i^2 \nu_{iI} n_i \left(\frac{\partial \ln p_i}{\partial r} - \frac{e_i T_I}{e_I T_i}\frac{\partial \ln p_I}{\partial r} - \frac{3}{2}\frac{\partial \ln T_i}{\partial r}\right). \tag{1.29}$$

The banana-plateau covariant fluxes are obtained by calculating $\langle(\vec{n}\cdot\nabla B)^2\rangle \simeq B_\theta^2/2R^2$, $\langle B^2\rangle \simeq B_0^2/\sqrt{1-\epsilon^2}$, $\langle I^2\rangle \simeq R^2 B_0^2$, and noting that $(2\pi/\chi') = 1$ [24]. Then the banana plateau flux is

$$e_i\Gamma_i^{BP} = -e_I\Gamma_I^{BP} = \frac{-3c^2 T}{B_\phi^2 R^2 e_i e_I}\left(\frac{1}{1/K_{11}^i + 1/K_{11}^I}\right)\left[e_I\left(\frac{\partial \ln p_i}{\partial r} - \frac{5}{2}\frac{\partial \ln T_i}{\partial r}\right)\right.$$

$$- e_i \left(\frac{\partial \ln p_I}{\partial r} - \frac{5}{2} \frac{\partial \ln T_I}{\partial r} \right) + \left(\frac{e_I K_{12}^i}{K_{11}^i} - \frac{e_i K_{12}^I}{K_{11}^I} \right) \frac{\partial \ln T}{\partial r} \Bigg]. \tag{1.30}$$

Similarly the Pfirsch-Schlüter flux becomes

$$Z_i \Gamma_i^{PS} = Z_I \Gamma_I^{PS} = n_i \rho_i^2 \nu_{iI} 2q^2 \left[K \left(\frac{\partial \ln n_i}{\partial r} - \frac{e_i}{e_I} \frac{\partial \ln n_I}{\partial r} \right) + H \frac{\partial \ln T_i}{\partial r} \right]. \tag{1.31}$$

For the special case of a trace impurity diffusing against a working ion species and a main impurity, the Pfirsch-Schlüter flux becomes

$$\begin{aligned} \Gamma_T^{PS} = & -\frac{2c^2 T q^2}{e_T B_0^2} \left[\left(\frac{L_1 + L_2}{e_I} \right) \frac{\partial \ln p_I}{\partial r} + \frac{L_3}{e_I} \frac{\partial \ln T_I}{\partial r} + \frac{L_{11}^{Ti} T_i}{T_I e_i} \frac{\partial \ln p_i}{\partial r} \right. \\ & \left. + \frac{L_{11}^{TT}}{e_T} \frac{\partial \ln p_T}{\partial r} + \frac{L_{12}^{Ti} T_i}{e_i T_i} \frac{\partial \ln T_i}{\partial r} \right]. \end{aligned} \tag{1.32}$$

These forms may now be used for modeling neoclassical impurity transport in circular flux surface plasmas. Chapter 5 shows a result of neoclassical impurity transport modeling for a characteristic TEXT discharge.

Somewhat simpler forms for these fluxes, strictly valid only when the collisionality is deep in the particular regime, have been published [30,28]. They are given (after the correct temperature gradient terms are included) by

$$\Gamma_I^{CL} = \frac{\nu_{iI} \rho_i^2}{2 Z_I T} \left[\frac{\partial P_i}{\partial r} - \frac{n_i}{Z_I n_I} \frac{\partial P_I}{\partial r} - 1.5 n_i \frac{\partial T}{\partial r} \right] \tag{1.33}$$

$$\Gamma_I^{P} = 1.25 \frac{q}{R} \sqrt{m_I} \frac{T^{3/2} c^2 n_I}{B_T^2 Z_I e^2 n_i} \left[\frac{\partial n_i}{\partial r} - \frac{n_i}{Z_I n_I} \frac{\partial n_I}{\partial r} + \frac{1.5 n_i}{T} \frac{\partial T}{\partial r} \right] \tag{1.34}$$

$$\Gamma_I^{PS} = \frac{\nu_{iI} \rho_i^2}{2 Z_I T} \left[2q^2 \left(\frac{\partial P_i}{\partial r} - \frac{n_i}{Z_I n_I} \frac{\partial P_I}{\partial r} \right) - 3q^2 n_i \frac{\partial T}{\partial r} \right]. \tag{1.35}$$

Here the ions have been assumed to be strongly coupled, so that $T_i = T_I = T$. Γ^{CL} is the classical flux; Γ^P is the plateau flux, dominant for $\epsilon^{3/2} < \epsilon^{3/2} \nu_* < 1$; and Γ^{PS} is the Pfirsch-Schlüter flux, dominant for $\epsilon^{3/2} \nu_* > 1$. Here ϵ is the inverse aspect ratio, r/R, and ν_* is the collisionality parameter $\nu_* = \nu R q / v_T \epsilon^{3/2}$, with ν the total collision frequency for a particular species (See Eq. B.30).

It is important to emphasize that comparison between experiment and neoclassical theory is difficult and often impossible because of the necessary complexity of the model (*c.f.* Appendices A and B). Formally the fluxes from all collisionality regimes are present regardless of the actual collisionality. However it is difficult to accurately calculate the fluxes in the transition regions between collisionality regimes. Furthermore, sufficient experimental data is often not available to adequately calculate the neoclassical fluxes.

For example, to calculate the flux of a trace impurity in a plasma with another main impurity, one needs the ion temperature profile, the working ion density profile, the main impurity density profile, and the q profile. These are seldom completely known in a real tokamak plasma. All of these factors suggest caution when claiming experimental agreement or disagreement with neoclassical predictions.

1.5 Motivation for and Summary of Method on TEXT

The goal of this thesis was to measure the transport properties of a trace, non-recycling impurity species by measuring profiles of an injected species with good temporal and spatial resolution. X-ray imaging methods have proven useful for such measurements in the past [71,54,63]. Systems of x-ray imaging arrays with many channels can provide the desired spatial resolution (in TEXT, for example, $\delta r/a \sim 0.1$) and also high temporal resolution (again in TEXT, $\delta t \sim 50$ μs). Thus a large system of x-ray imaging arrays was constructed to study the transport of injected aluminum in TEXT.

Aluminum was chosen because of the specific energy of its strong resonance line radiation in the x-ray region. The He-like state radiates at about 1.61 keV, and the H-like state radiates at about 1.73 keV (see Appendix C). Using a combination of a soft x-ray filter and a novel krypton gas absorption filter, with an L-shell x-ray cross section edge at about 1.68 keV, the absolute densities of these two charge states could be separately measured. A hard filter that measured mostly recombination continuum emission could then be used to measure the fully stripped state density. (These three states are the dominant charge states in TEXT plasmas except near the very edge $r \gtrsim 20$ cm.) Thus x-ray imaging can give temporally resolved profiles of three aluminum species.

1.6 TEXT

The Texas Experimental Tokamak (TEXT) [72,73] is a medium-sized tokamak at the University of Texas at Austin. It has a major radius of 1 m and a minor radius of 26 cm, defined by a full poloidal aperture titanium carbide-coated graphite limiter. TEXT routinely achieves plasma densities of $\lesssim 1 \times 10^{20}$ m^{-3} and central electron temperatures on the order of 1 keV with a magnetic field of 2-3 T and a plasma current of $\lesssim 350$ kA. Fig. 1.2 shows a schematic view of TEXT. This tokamak is equipped with a valuable collection of plasma diagnostics, summarized in Table 1.1 [72]. These diagnostics are important for the study of the transport of plasma impurities. To perform such ex-

periments using soft x-ray intensity measurements, it is essential to have independent measurements of the electron density and temperature profiles. For performing detailed comparisons with transport theories it is also essential to have independent measurents of the main ion density and temperature profiles as well as density profiles for the intrinsic impurity species. Because TEXT is well-diagnosed and its plasmas are quite reproducible, it was a suitable site for the impurity transport experiments described herein.

1.7 Organization of the Thesis

This thesis is organized as follows. Chapter 2 describes the models used to calculate the total x-ray emissivity emitted by the plasma. Chapter 3 describes three arrays of soft x-ray detectors designed and constructed for impurity transport studies on TEXT. Chapter 4 outlines the methods used for measuring density profiles of aluminum injected into TEXT and most of the experimental results: a scaling of the aluminum confinement time, aluminum density profiles for several different plasma conditions, and comparisons between the measured charge state distribution and coronal equilibrium. Preliminary evidence of poloidal asymmetries in the impurity density profiles is also presented in chapter 4. Transport simulations for comparison with the data of chapter 4 are described in chapter 5. Chapter 6 contains a discussion of the results and comparison with other particle transport measurements undertaken on TEXT. Finally, the conclusions and some suggestions for future work are given in chapter 7. The appendices describe details of neoclassical particle flux calculations, atomic parameters for x-ray emissivity calculations, Abel inversion, a comparison of recombination rate coefficients for aluminum, and the relationship between the uncertainty in measured aluminum densities and uncertainties in the other plasma parameters.

A brief note on units is appropriate here. In keeping with the unfortunate long-standing tradition of plasma physics research, mixed units are used throughout this thesis. To a large extent theoretical discussions are in cgs units, and experimental results are given mostly in SI (mks) units. Wherever possible, the units used are explicitly stated.

Table 1.1: TEXT Diagnostics as of August 1989

Diagnostic	**# of Channels**	**Measured Parameter**
Rogowski coil	1	Plasma current I_p
Toroidal loop	1	Loop voltage V_l
Sine, cosine loops	several	Plasma position
H_β monitor	1	Ionization level
2 mm μ-wave interferometer	1	Central line-averaged electron density $\bar{n}_e$
Hard x-ray monitor	1	Plasma current I_p, radiation, suprathermals
Impurity monitor	10	Visible bremsstrahlung Z_{eff}
Residual gas analyzer	1	Vacuum condition
Far infrared interferometer	6	Electron density profile $n_e(r)$
Electron cyclotron emission	10	Electron temperature profile $T_e(r)$
Thomson scattering	1,scanning	Edge temperature and temperature profiles
MHD coil arrays	24	MHD m, n mode numbers
X-ray spectrometer	1	Electron temperature T_e, impurity identification
Vertical x-ray array	40	Internal modes, impurity transport
Horizontal x-ray array	40	Internal modes, impurity transport
45° x-ray array	12	Internal modes, impurity transport
Charge exchange	1, scanning	Ion temperature $T_i(r)$
Spectrometers	several	Electron temperature T_e, impurities, rotation
Probes	several	Density, temperature, and potential fluctuations
Bolometer array	10	Radiated power P_{rad}
Diagnostic neutral beam	-	Ion temperature profile, impurity profiles
FIR scattering	30	Density profiles and fluctuations
Heavy ion beam probe	-	Potential, density, B_r fluctuations
Impurity pellet injector	1	$q(r)$, impurity transport, suprathermals
Li beam	1	$q(r)$

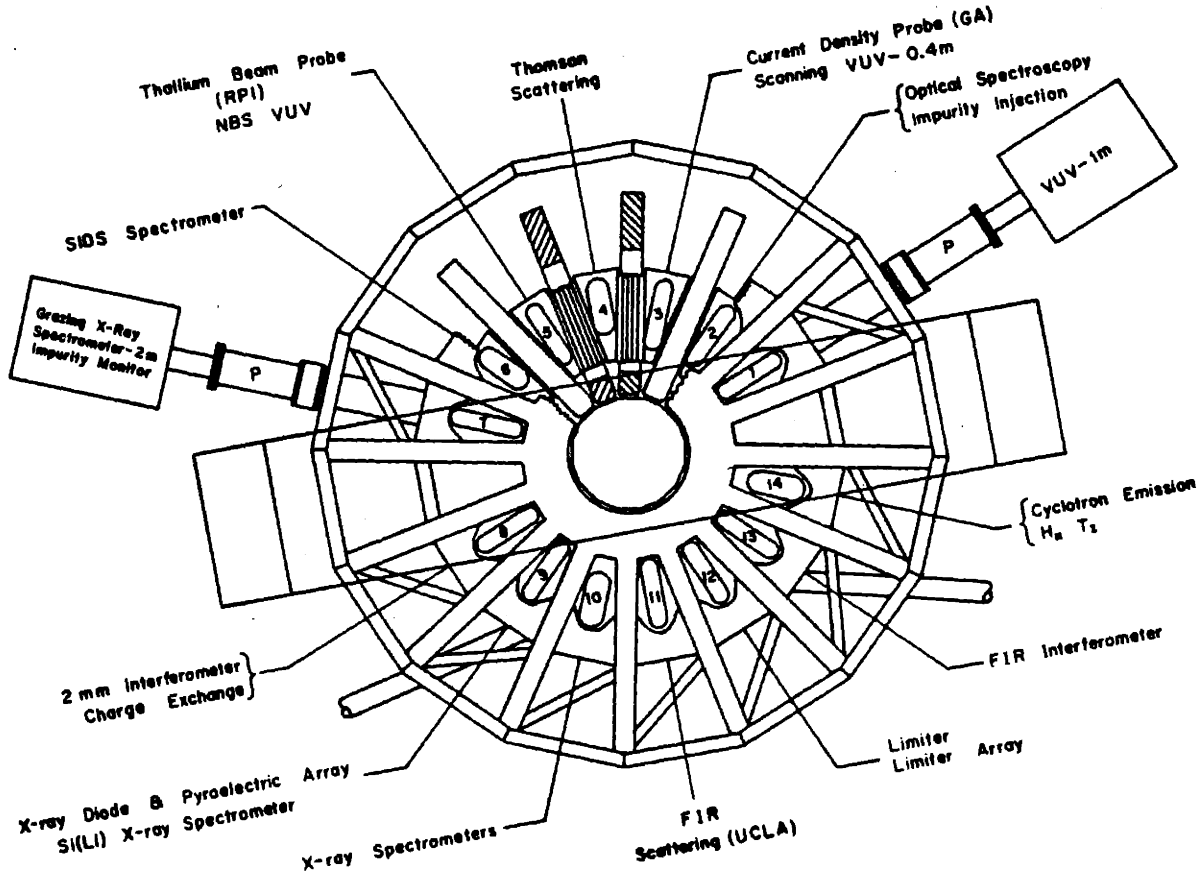

Figure 1.2: Schematic view of the Texas Experimental Tokamak. The major radius is 1 m and the minor radius is 0.26 m. The toroidal field is $\leq$3T and the plasma current is $\leq$350 kA.

Chapter 2

Modeling the Plasma X-Ray Emissivity

2.1 Introduction

The spectrum of the thermal radiation emitted by thermonuclear plasmas lies largely in the x-ray region because the electron temperature in most tokamaks is on the order of 1 keV or higher. The method for measuring impurity density profiles described in this thesis relies on the fact that the broadband x-ray power depends strongly on the impurity content of the plasma. In order to unfold the impurity density from measurements of the broadband x-ray emissions, it is necessary to have an accurate model for the total contribution to the x-ray spectrum from each impurity species. It is equally important to have independent measurements of the electron density n_e and electron temperature T_e, since the total broadband x-ray power varies roughly as $\sum_i n_e n_i T_e^{\alpha}$, where $1/2 \lesssim \alpha \lesssim 20$, depending on T_e and the particular radiating ion. This chapter describes the models used to calculate the total x-ray power from all relevant atomic processes.

Radial profiles of the x-ray brightness are measured with arrays of solid state photovoltaic detectors (discussed in detail in chapter 3). In TEXT, each detector views a chord through the circular plasma, resulting in a line integral measurement. Thus the signal current generated in a detector viewing a chord with impact radius p can be expressed as

$$I(p) = \int_{-\sqrt{a^2-p^2}}^{\sqrt{a^2-p^2}} \frac{A_d A(z)}{4\pi L(z)^2} \sum_i n_e(z) n_i(z) \left[\int_0^{\infty} \eta(h\nu) \frac{dP_{tot}(h\nu, T_e(z))}{dh\nu} dh\nu \right] dz. \quad (2.1)$$

In this equation A_d is the sensitive area of the detector, $A(z)$ is the area of the plasma subtended by the detector viewing geometry, $L(z)$ is the distance from the location z

along the chord in the plasma to the detector, and $\eta(h\nu)$ is the efficiency of the detector for a photon of energy $h\nu$, determined by any filters between it and the plasma. The quantity $A_d A(z)/4\pi L(z)^2$ is independent of z because $A(z)$ and $L(z)^2$ have the same dependence on z. Thus this quantity can be taken outside the chord integral.

The quantity described in this chapter, $dP_{tot}/dh\nu$, is the total radiation spectrum. The approach adopted in this chapter for calculating the quantity $dP_{tot}/dh\nu$ is to separate the distinct physical processes responsible for the production of x rays, calculate their contribution to the spectrum, and subsequently sum the individual terms.

In general the x-ray production mechanisms may be divided into two broad categories: continuum emission and line emission. The continuum portion may be further separated into contributions from bremsstrahlung and radiative recombination. The portion from lines may similarly be separated into line emission resulting from four different physical processes that populate excited states of an ion: electron impact excitation, dielectronic recombination, collisional inner shell excitation, and radiative recombination into upper levels. The methods for accurately calculating each of these components of the total emissivity from a given set of plasma parameters are discussed separately in detail in the following sections. First the two parts of the continuum are described in section 2.2, and then the four parts of the line radiation are described in section 2.3.

2.2 Continuum X-Radiation

In an ohmically heated tokamak plasma, the electrons are generally well-described by a Maxwellian velocity distribution characterized by the temperature T_e, and given by

$$f(v_e) = n_e \left(\frac{m_e}{2\pi T_e}\right)^{3/2} exp\left(\frac{-m_e v_e^2}{2T_e}\right). \tag{2.2}$$

Coulomb collisions between the electrons and either the background or impurity ions, during which the electrons lose some kinetic energy, give rise to the production of photons. (The ions may also radiate during collisions, but due to their much heavier mass, the overall contribution from ions to the x-ray power is negligible.) The two physical processes by which a continuum of photons is produced are bremsstrahlung (free-free radiation) and radiative recombination (free-bound radiation). These mechanisms lead to a continuous distribution of photon energies because of the characteristic distribution of initial electron kinetic energies (Eq. 2.2). Bremsstrahlung and radiative recombination are described separately in sections 2.2.1 and 2.2.2.

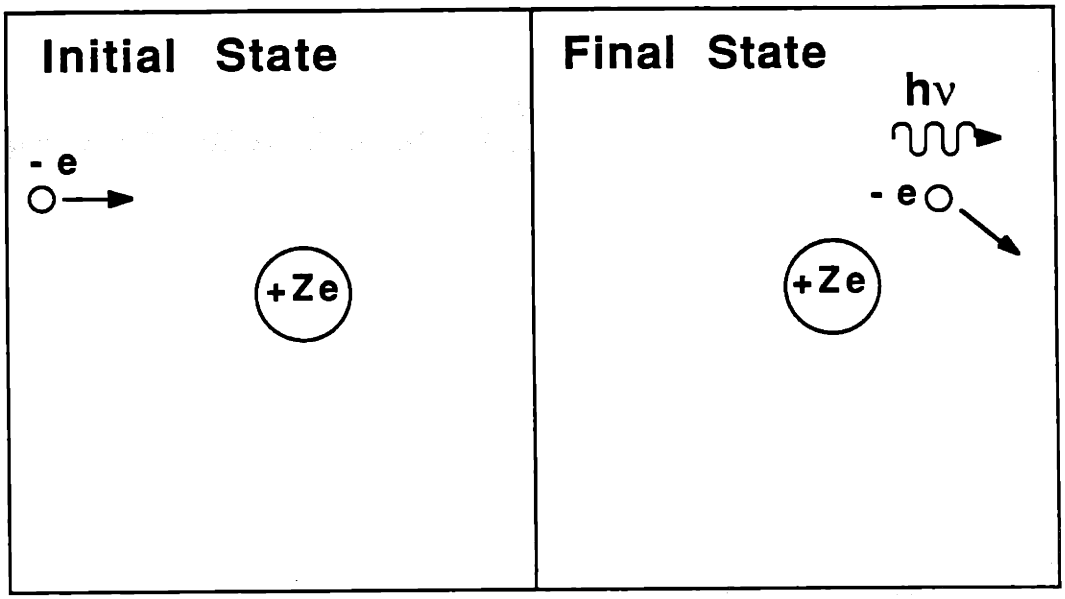

Figure 2.1: Bremsstrahlung radiation is produced when a free electron collides with an ion of charge $+Z$. The final state consists of a free electron with lower kinetic energy and a photon with energy $h\nu$ equal to the difference between the initial and final kinetic energies of the colliding electron.

2.2.1 Bremsstrahlung Radiation

Bremsstrahlung ("braking radiation" from German) occurs when a free electron collides with an ion, and its final energy state is also free—hence the designation free-free (see illustration in Fig. 2.1). During such a collision the electron is accelerated, consequently radiating a photon. In a plasma with electron density n_e (cm^{-3}), ion density n_j (cm^{-3}), and electron temperature T_e (keV), the x-ray spectrum emitted from bremsstrahlung is given by [19]

$$\frac{dP_b}{dh\nu} = 2.6 \times 10^{-14} n_e n_j \bar{g}_{ff} Z_j^2 \left(\frac{\chi_H}{T_e}\right)^{\frac{1}{2}} e^{-h\nu/T_e} \ \mathrm{keV/(keV cm^3 s)}, \tag{2.3}$$

where $\bar{g}_{ff}$ is the free-free Gaunt factor (the ratio of the bremsstrahlung intensity to the classical coulomb intensity) [74,75], Z_j is the ionic charge, and χ_H is the electron binding energy for the ground state of hydrogen (0.0136 keV).

Because of the simple form of Eq. 2.3, bremsstrahlung is the easiest component of the plasma x-ray emissivity to calculate. Therefore the ratio of the measured emissivity to the emissivity from only hydrogenic bremsstrahlung at the same temperature

and density is often used as a rough measure of its impurity content [76,71]. In this context, it is important to note that for temperatures above $\simeq$100 eV the contribution from radiative recombination to the spectrum emitted from a pure hydrogen plasma is negligible, as will be demonstrated in the next section. Thus a comparison of the measured emissivity to that expected from only hydrogen bremsstrahlung depends only on the level of impurities present, not on the contribution of radiative recombination from hydrogen relative to bremsstrahlung.

2.2.2 Radiative Recombination

The second mechanism responsible for producing continuous x radiation is radiative recombination, represented in Fig. 2.2. In this type of collision, the final state of the electron is a bound state in the ion (of initial charge state j, final charge state $j-1$) with binding energy χ_{j-1}. A photon with energy equal to the initial kinetic energy of the electron plus the binding energy of the final state is emitted. A simple energy balance shows that

$$\frac{mv_e^2}{2} = h\nu - \chi_{j-1}. \tag{2.4}$$

A continuous spectrum again results because of the distribution of the initial electron kinetic energies shown in Eq. 2.2. In contrast to bremsstrahlung, however, there is a distinct minimum in the energy of the photons emitted in the case of radiative recombination. This can easily be seen by setting to zero the initial energy of the colliding electron in Eq. 2.4, with the result that

$$(h\nu)_{min} = \chi_{j-1}. \tag{2.5}$$

This is the cause of discrete jumps (recombination edges) in the x-ray spectrum.

For the same plasma parameters used to calculate the bremsstrahlung power, the total power due to ions with charge state j from radiative recombination into charge state $j-1$ is given by [19]

$$\begin{aligned}\frac{dP_r}{dh\nu} &= 2.6\times10^{-14} g_{fb} n_e n_j \left(\frac{\chi_H}{T_e}\right)^{\frac{3}{2}} \left(\frac{\chi_{j-1}}{\chi_H}\right)^2 e^{-h\nu/T_e} \\ &\quad \left[\frac{\zeta_n}{n} e^{\chi_j/T_e} + \sum_{m=n+1}^{\infty} \frac{2}{m^3} e^{\chi_{j-1}/m^2 T_e}\right] \text{ keV}/(\text{keVcm}^3\text{s}),\end{aligned} \tag{2.6}$$

where g_{fb} is the free-bound Gaunt factor [74], χ_j is the ground state binding energy of the electron in the final state, n (m) is the principle quantum number of the ground (excited) state shell into which the electron recombines, and ζ_n is the number of vacancies

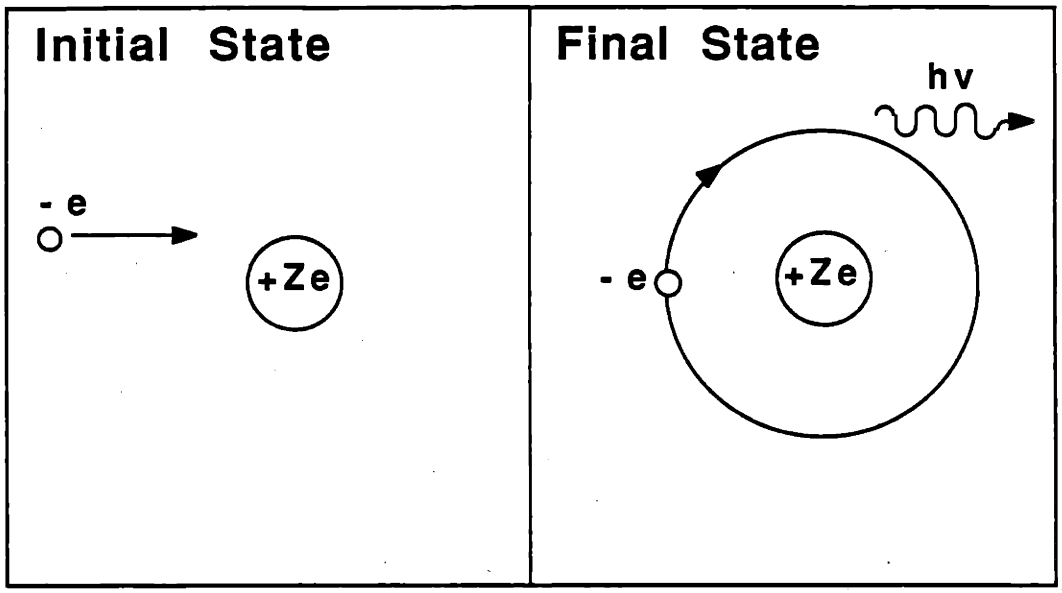

Figure 2.2: Radiative recombination radiation results when an initially free electron collides with an ion of charge Z and the final electron state is a bound state. The energy of the photon liberated during this process equals the initial kinetic energy of the electron plus the binding energy of the new bound state.

available in shell n that the electron may enter. The first term in the square brackets represents recombination into the ground state n of the ion and the second term represents recombination into higher levels with $m > n$. The former term dominates since the contribution from higher shells depends on $1/m^3$ and $e^{\chi_{j-1}/m^2 T_e}$. Thus for numerical calculations of the radiative recombination radiation, it is sufficient to cutoff the summation in the second term at $m \simeq n + 5$, and this has been done in the present work.

It is useful to compare the relative contributions from radiative recombination and bremsstrahlung to learn in which temperature regime each is most important. Setting the two powers equal and maintaining only the first term of P_r gives

$$n_e n_j \bar{g}_{ff} Z_j^2 \left(\frac{\chi_H}{T_e}\right)^{\frac{1}{2}} e^{\frac{-h\nu}{T_e}} = n_e n_j g_{fb} \left(\frac{\chi_H}{T_e}\right)^{\frac{3}{2}} \left(\frac{\chi_n}{\chi_H}\right)^2 \frac{\zeta_n}{n} e^{\frac{(\chi_n - h\nu)}{T_e}}. \tag{2.7}$$

Noting that for most plasmas of interest here, $\bar{g}_{ff} \sim g_{fb} \sim 1$, this becomes

$$1 = \frac{\chi_H}{T_e} \left(\frac{\chi_n^2}{Z^2 \chi_H^2}\right) \frac{\zeta_n}{n} e^{\chi_n / T_e}. \tag{2.8}$$

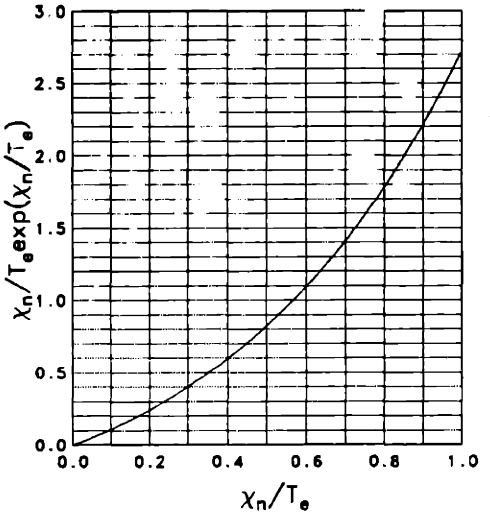

Figure 2.3: The quantity $\frac{\chi_n}{T_e} e^{\chi_n/T_e}$ is plotted as a function of χ_n/T_e. This parameter determines whether radiative recombination or bremsstrahlung is the dominant contributor to continuum x radiation.

Table 2.1: This table lists the temperatures where the bremsstrahlung and radiative recombination parts of the x-ray power are equal.

Charge state	n	ζ_n	T_e/χ
He-like	2	8	1.75
H-like	1	1	1.75
Fully stripped	1	2	2.84

Then since $\chi_n \simeq Z_j^2 \chi_H / n^2$, bremsstrahlung is dominant when

$$\frac{n^3}{\zeta_n} > \frac{\chi_n}{T_e} e^{\chi_n/T_e}. \tag{2.9}$$

Fig. 2.3 shows a plot of $(\chi_n/T_e)e^{\chi_n/T_e}$ vs. χ_n/T_e. The results are summarized in Table 2.1, which lists the ratios of electron temperature to binding energy where the bremsstrahlung power equals the radiative recombination power for the three highest charge states of any ion. For higher electron temperatures bremsstrahlung dominates. The H-like and He-like states have the same T_e/χ boundary because $n^3/\zeta_n = 1$ for both charge states.

To illustrate the characteristics of both the bremsstrahlung and radiative recombination emissions, calculated spectra for a hydrogen plasma with 2% carbon contamination are shown in Fig. 2.4. This impurity level is representative of typical low Z impurity

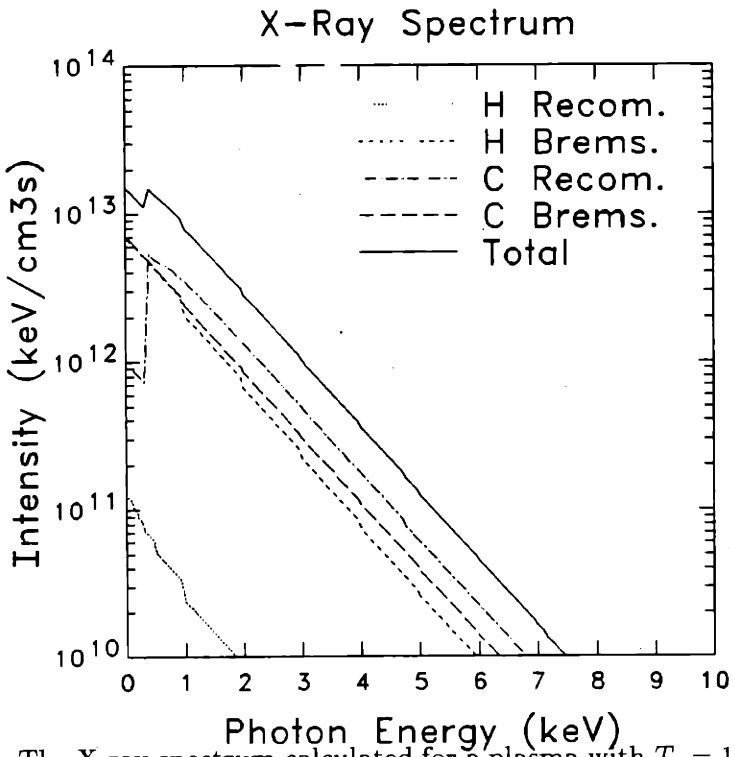

Figure 2.4: The X-ray spectrum calculated for a plasma with $T_e = 1$ keV, $n_e = 5 \times 10^{13}$ and 2% carbon contamination shows that the impurity radiation is the dominant contribution to the total, and radiative recombination is the dominant contributor for the carbon for photon energy greater than 480 eV. In contrast, bremsstrahlung dominates the hydrogen spectrum, since the binding energy in hydrogen is only 13.6 eV.

content in TEXT [77]. In this case it is clear that recombination due to fully stripped carbon dominates the x radiation for photon energies above 480 eV (the binding energy of the H-like carbon ion). However, if higher Z ions are present in the plasma (as they always are in TEXT), it will also be necessary to calculate the contribution from line radiation which may be comparable to or greater than the continuum sources in terms of the total power produced. The calculations necessary for line radiation are described in the next section.

2.3 Discrete Line Radiation

Jumps of electrons between bound orbitals result in the production of radiation at specific photon energies (equal to the difference between the binding energies of the

electron in the initial and final states) In a high temperature plasma several processes may contribute to the production of this line radiation by raising an electron to an excited orbital. The electron subsequently decays to a lower energy state and a photon is emitted. These processes include collisional excitation of outer shell electrons, dielectronic recombination, collisional excitation of inner shell electrons, and recombination into upper quantum levels. These three mechanisms are discussed separately in the following subsections. (The contribution from charge exchange recombination into upper levels is negligible, as will be shown in Section 4.2.3.)

2.3.1 Line Radiation after Electron Impact Excitation

The fundamental requirement for discrete line radiation to occur is that an electron falls from an excited orbit to a lower orbit (most often the ground state). One of several ways an electron may be elevated to the higher orbit is through electron impact excitation of an outer shell electron, represented schematically in Fig. 2.5. Initially, the bound electron resides in the ground state orbital, and it is subsequently raised to a higher energy bound state by an electron collision. The power emitted in line radiation from this process is then given by the photon energy times the rate at which the excited states are populated through collisions. The radiative decay time is much less than the collisional excitation time in low density plasmas, so the net rate of radiation is determined by the rate of population of the upper levels, given by [78,79]

$$X_{ij} = 5.06 \times 10^{-10} \frac{f_{ij} < g_{ij} > e^{-h\nu/T_e}}{h\nu\sqrt{T_e}} \ \mathrm{cm^3 s^{-1}} \tag{2.10}$$

where $h\nu$ and T_e are both in keV and i and j represent the initial (excited) and final bound states respectively, so $h\nu = E_i - E_j$. The power radiated is therefore simply

$$P_{ij} = 5.06 \times 10^{-10} \frac{f_{ij} < g_{ij} > e^{-h\nu/T_e}}{\sqrt{T_e}} \ \mathrm{keV cm^3 s^{-1}}. \tag{2.11}$$

In these expressions, f_{ij} is the absorption oscillator strength for the transition $i-j$ and $< g_{ij} >$ is the appropriate Gaunt factor averaged over the Maxwellian electron velocity distribution (for ions $< g_{ij} > \simeq 0.2$ [78]). Where available, oscillator strengths have been taken from measured values, otherwise theoretically calculated values are used. The complete set of specific transitions and the associated oscillator strengths for all impurity species considered in this work are tabulated in Appendix C.

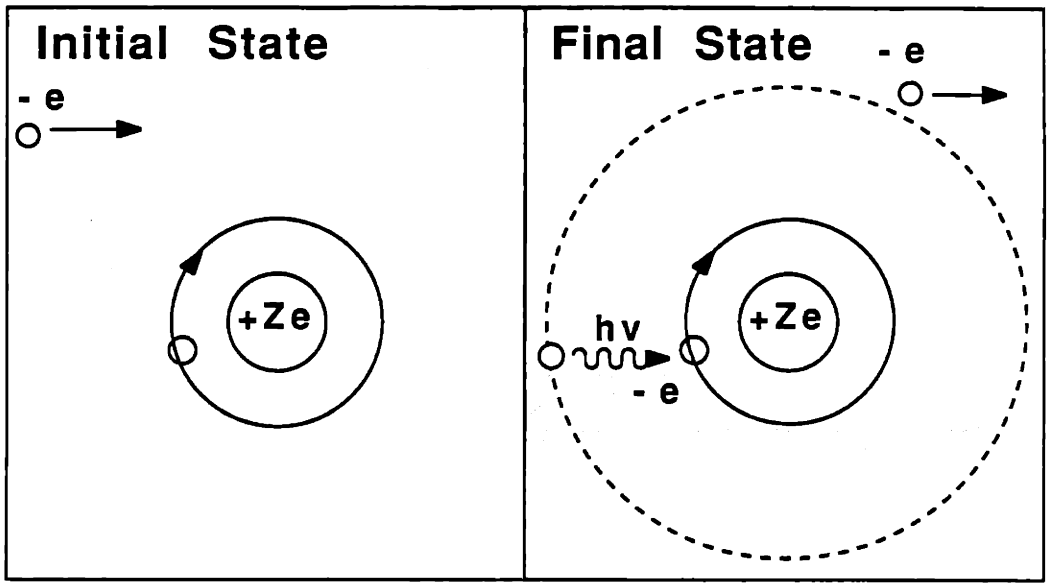

Figure 2.5: Line radiation results after an electron collides with a partially ionized ion. The bound electron is raised to an excited level (shown dashed in the right figure), which subsequently decays back to the initial state. A photon is emitted with energy equal to the difference between the two bound state energy levels. The colliding electron remains free.

2.3.2 Line Radiation after Dielectronic Recombination

Dielectronic recombination is the process by which an electron with kinetic energy just above the ionization threshold of the resultant ion enters a bound orbit and simultaneously raises another electron to an excited bound orbit. The excited electron then acts as a "spectator" electron when the recombined electron drops down to the ground state orbital as shown in Fig. 2.6. Because the spectator electron reduces the net Coulomb potential of the nucleus of the ion, the transition energy is slightly reduced, and the dielectronic lines appear as "satellite" lines on the long wavelength side of the resonance transition (resonance transitions are $1s - 2p$ for H-like systems and $2s^2 - 1s2p$ for He-like systems). Dielectronic recombination rates have been studied extensively from a theoretical viewpoint (especially, though not exclusively, for He-like iron) by Burgess [80,81], Shore [82], Gabriel and Bhalla [83,84,85], Bely-Dubau and Dubau [86,87,88], and Vainshtein and Safranova [89] and others. Dielectronic satellite line intensities have also been measured for various elements (mostly high Z elements: iron, titanium, nickel and chromium) by Bitter, *et. al.* [90,91,92], Bely-Dubau, *et. al.* [75,93,94], Källne,

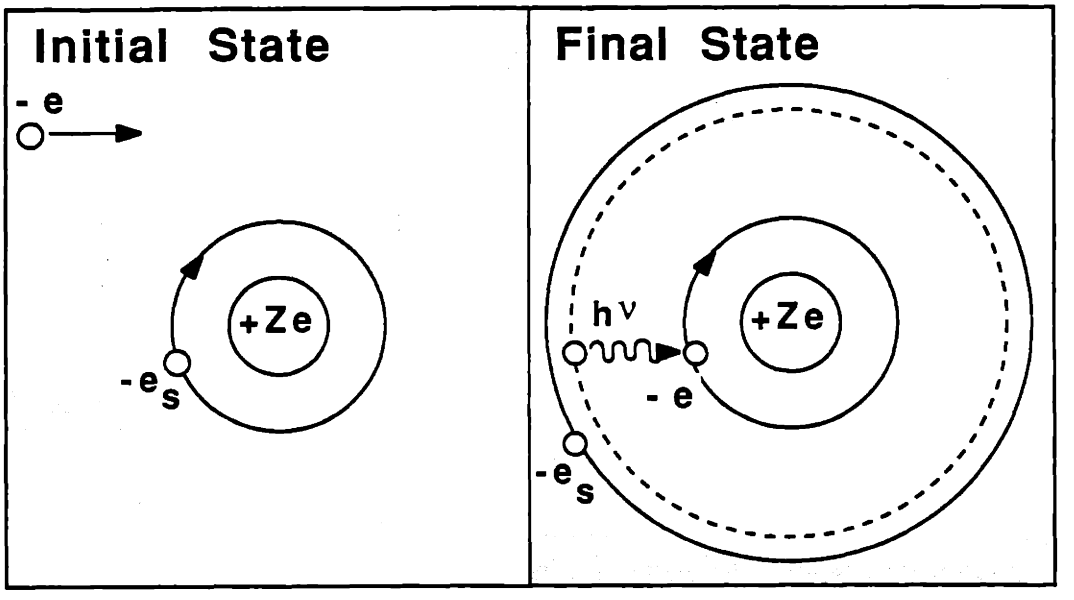

Figure 2.6: Dielectronic recombination results when an electron recombines into an excited state of a partially ionized atom, simultaneously exciting an initially bound electron (e_s) to a level above the ground state. The recombining electron then decays to a lower orbital. The line radiation resulting from this process is slightly shifted from the energy difference between the excited and final levels because of the presence of the spectator electron.

Källne and Rice [95,96], the TFR group [60], and Bartiromo, Bombarda and Gianella [97].

The satellite line intensity is given by [83,84]

$$P_d = \frac{5.23 \times 10^{-27} E_s}{T_e^{3/2}} \frac{g_s}{g_1} \frac{A_r A_a}{A_a + \sum A_r} e^{-E_s/T_e} \text{ keVcm}^3\text{s}^{-1}, \tag{2.12}$$

where E_s is the satellite transition energy (keV), g_s and g_1 are the statistical weights of the satellite level and the ground state level respectively (g_1=2 for H-like ions and 1 for He-like ions), and A_r and A_a are the radiative and autoionization transition probabilities.

As discussed above, line radiation resulting from dielectronic recombination manifests itself as lines very close to the resonance transition line. Therefore, since for the purposes of this work only the total power radiated in broadband x-ray emissions is the main quantity of interest, the dielectronic recombination radiation is treated as if it were at a single energy (taken to be the average of all the dielectronic satellite energies). The

total effective dielectronic recombination coefficient is therefore conveniently defined to be

$$Q_d = \sum_{\text{all satellites}} \frac{g_s A_r A_a}{A_a + \sum A_r}, \tag{2.13}$$

so that the total power from dielectronic recombination power at (or within $\simeq$0.05 keV of) the *average* satellite energy $\bar{E}_s$ is

$$P_d = 5.23 \times 10^{-27} \frac{\bar{E}_s Q_d}{g_1 T_e^{3/2}} e^{-E_s/T_e} \quad \text{keVcm}^3\text{s}^{-1}. \tag{2.14}$$

As in the case of lines from electron impact excitation, experimentally measured values of the dielectronic rate parameters have been used where available; otherwise the tabulated values of Vainshtein and Safranova [89] have been adapted for use in the form of Eq. 2.14. The specific values and references used to calculate the Q_d values for several impurity species are tabulated in Appendix C.

2.3.3 Line Radiation after Inner Shell Excitation

The third mechanism responsible for exciting electrons to higher orbits is collisional excitation of inner shell electrons. Because these electrons are screened by the outer shell electrons, the line intensities from this process are much lower than from collisional excitation of outer shell electrons. However, the same formalism may be used to calculate the radiation power emitted as was used in section 2.3.1 for collisional excitation of outer shell electrons. The transition energies and their oscillator strengths are listed in Appendix C.

2.3.4 Line Radiation after Recombination into Upper Levels

It was found that in the colder regions of Alcator-C, radiative recombination into upper levels ($n \geq 2$) was the dominant mechanism for populating these levels. When the recombined electron drops from the upper state to a lower state, line radiation is emitted. Thus it is often important to include this effect in the calculation of x-ray line radiation in H-like and fully stripped ions. The power emitted by this process can be expressed as

$$P_{l,r} = \sum_i \sum_j \alpha_{ri} b_{ij} E_{ij} \quad \text{keVcm}^3\text{s}^{-1}, \tag{2.15}$$

where α_{ri} is the total recombination rate into state i, b_{ij} is the branching ratio for the electron to decay to state j and E_{ij} is the energy released in the form of a photon during the transition.

The enhanced line radiation after radiative recombination and dielectronic recombination can be treated separately. Mewe has given rates from both processes [98]. The power of a particular line due to radiative recombination into upper levels is written [98]

$$P_{l,r} = \alpha_{z+1}^{RR} E_{ij} \ \ \mathrm{keV cm^3 s^{-1}}, \tag{2.16}$$

where α_{z+1}^{RR} is the effective recombination rate for enhancing the line, and is given by

$$\alpha_{z+1}^{RR} = 10^{-11} A_{REC} (z+1)^{2\eta+1} (T_e \times 1.1605 \times 10^7)^{-\eta} \ \mathrm{cm^3 s^{-1}}. \tag{2.17}$$

The parameters α_{z+1}^{RR} and η are given by Mewe for individual lines, and are listed in Appendix C for aluminum and silicon only. Similarly, the power of a particular line due to dielectronic recomination into upper levels is given by

$$P_{l,d} = \alpha_{z+1}^{DR} E_{ij}, \ \mathrm{keV cm^3 s^{-1}} \tag{2.18}$$

where

$$\alpha_{z+1}^{DR} = \frac{3.56 \times 10^{-17} (Z+1)^4 e^{-E_{DR}/T_e}}{T_e^{3/2}[1 + 5 \times 10^{-6}(Z+1)^4]} \ \mathrm{cm^3 s^{-1}} \tag{2.19}$$

for dielectronic recombination into the H-like state. In this expression Z is the nuclear charge. In the center of TEXT plasmas the x-ray power due to lines following recombination into upper levels is not important. However, farther out where $T_e \simeq 200 - 300$ eV this effect can increase the x-ray power from H-like aluminum by $\sim 70\%$.

2.4 Conclusion

The x-ray emissivity from bremsstrahlung, radiative recombination, collisionally excited lines dielectronic recombination and lines following recombination into upper levels can now be calculated for a Maxwellian plasma with electron temperature T_e and electron density n_e. As an example directly applicable to this study, the x-ray spectrum calculated for a plasma with 0.1% aluminum in coronal equilibrium is shown in Fig. 2.7. In this case $T_e = 1$ keV and $n_e = 3 \times 10^{13}$ cm^{-3}. Note the strong aluminum resonance lines at 1.61 and 1.73 keV from the He-like and H-like charge states. The recombination edge at 2.3 keV from the fully-stripped state is not evident.

Similar calculations for different impurity species and different x-ray filters give the power radiated per impurity ion. Results for impurities intrinsic to TEXT and injected into TEXT for impurity transport studies are shown in Appendix C. The next chapter describes the x-ray imaging systems used to measure the broadband x-ray power.

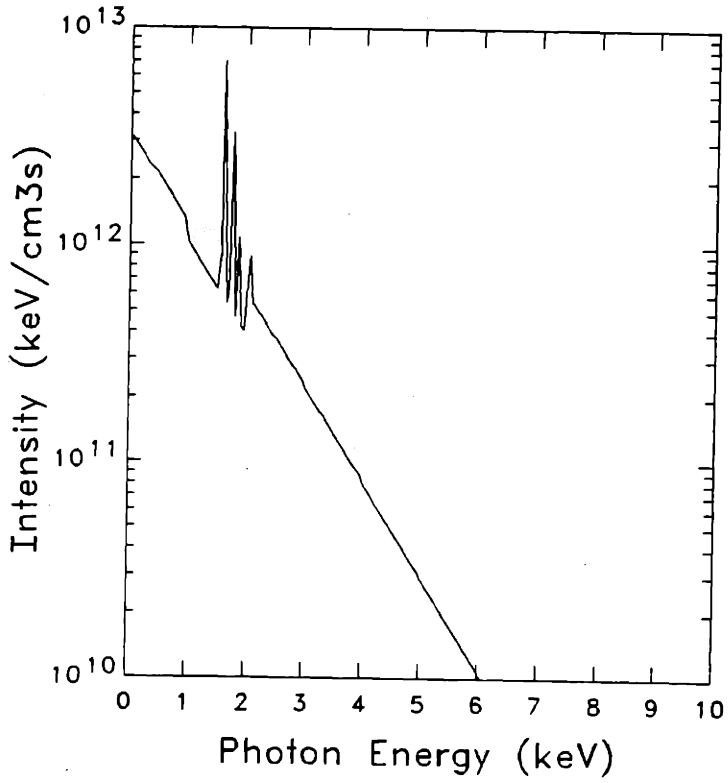

Figure 2.7: The x-ray spectrum from a plasma at $T_e = 1$ keV, and $n_e = 3 \times 10^{13}$ cm^{-3} with 0.1% aluminum density. The aluminum is assumed to be in coronal equilibrium. The two strongest lines are the aluminum resonance lines at 1.61 and 1.73 KeV from the He-like and H-like charge states respectively.

Chapter 3

X-Ray Measurement Systems on TEXT

3.1 Introduction

As emphasized throughout this thesis, x-radiation is emitted strongly from tokamak plasmas with temperatures greater than about 1 keV. Two main diagnostic methods have been developed for using this radiation to understand plasma parameters. First, x-ray spectroscopy provides high resolution in photon energy but usually low resolution in space and time. Second, broadband x-ray detection provides high temporal and spatial resolution, but low resolution in the photon energy. TEXT has both kinds of systems installed.

This chapter describes in detail a large system of broadband x-ray detector arrays constructed for impurity transport studies in TEXT [99]. The discussion introduces the fundamentals of solid-state photon detectors, their calibration in the x-ray energy region, and the design of a set of three absolutely calibrated x-ray arrays. Furthermore, a method of using krypton gas as an x-ray filter to improve the spectral resolution of these arrays is introduced. This filter was used to discriminate between the resonance line radiation of the He-like and H-like aluminum charge states.

3.2 Broadband X-Ray Detectors

Solid state semiconductor detectors, like other radiation detectors, convert photons into measurable electronic signals. This occurs when the photon interacts with the detector material and raises electrons from the lattice into the conduction band. The relationship between the deposited photon energy and the electrical signal produced can be found

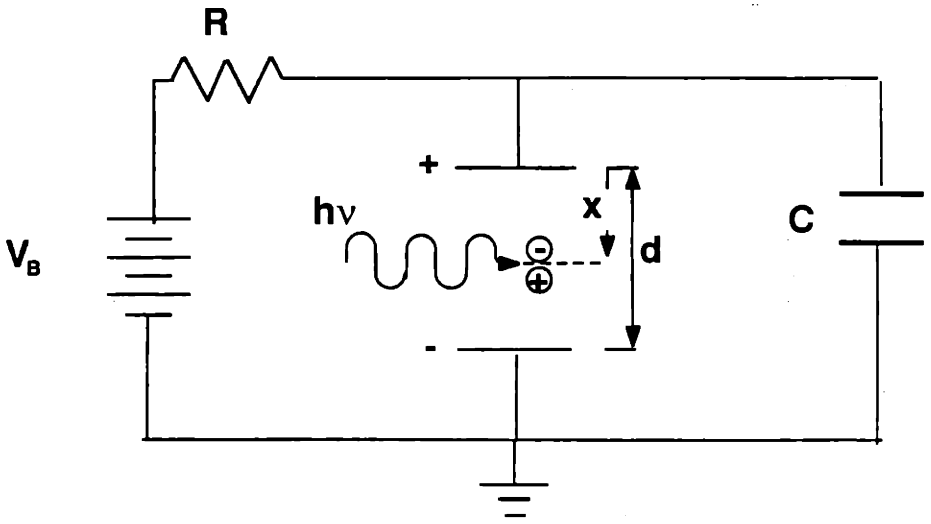

Figure 3.1: The equivalent circuit of a radiation detector is shown. The bias voltage, V_B is applied externally, and the detector can be represented by a large resistance R and some capacitance C. The detector has physical thickness d.

by considering the schematic of the equivalent electric circuit of a detector shown in Fig. 3.1 [100]. Here V_B is the externally applied bias voltage, R is the large detector resistance, C is the detector capacitance, and V_{out} is the desired signal. The photon detector, of physical thickness d, acts as a source of charge when a photon is deposited in the detector. In this case the photon is assumed to be completely absorbed a distance x from the anode.

The output voltage is found by considering the change in energy stored in the capacitor due to the change in voltage, $\frac{1}{2}C(V_f^2 - V_i^2)$, where V_f and V_i are the final and initial voltages across the capacitor respectively. The initial voltage is just V_B and the final voltage is $V_B + V_{out}$, so the energy change is $\frac{1}{2}C(V_B^2 + 2V_BV_{out} + V_{out}^2 - V_B^2)$, which is approximately CV_BV_{out} since V_{out} is typically much smaller than V_B. This change in energy goes into the change in kinetic energy of the photoelectrically produced charge carriers as they traverse the width of the detector in the electric field $E = V_B/d$. The total final kinetic energy of the charge carriers when they reach the electrodes is $\frac{1}{2}(n_e m_e v_{e,f}^2 + n_h m_h v_{h,f}^2)$, where n_e (n_h) is the number of electrons (holes) produced, m_e (m_h) is the electron (hole) mass, and $v_{e,f}$ ($v_{h,f}$) is the electron (hole) final velocity. The final velocities can be related to the electric field and the distance traveled: $v_{e,f} = \sqrt{2eV_Bx/dm_e}$ and $v_{h,f} = \sqrt{2eV_B(d-x)/dm_h}$. Substituting these velocities into

the expression for the kinetic energy, noting that the number of electrons and holes are equal ($n_e = n_h \quad n$), and equating the change in stored energy to the change in total kinetic energy gives

$$CV_B V_{out} = \frac{n}{2}\left[\frac{2xeV_B}{d} + \frac{2(d-x)eV_B}{d}\right] = neV_B, \tag{3.1}$$

or $V_{out} = ne/C$. Thus the signal voltage is proportional to the number of pairs of charge carriers produced in the detector, n, a quantity that depends directly on the energy of the absorbed photon and the energy required to create a charge pair in the specific detector material.

The detectors used for this work were mostly silicon surface barrier diodes (SBDs). General descriptions of SBDs are contained in References [101], [102] and [103]. These diodes consist of a metal-semiconductor interface forming a rectifying junction such that a reverse bias voltage generates an electric field, which in turn causes a region depleted of free charge carriers (the depletion depth, which has a thickness proportional to the square root of the bias voltage).

SBDs, though widely used for detecting charged [104,105,106,107,108,109] and neutral [110,111,112] particles, have also been extensively employed for detecting and imaging high intensity x emissions from laboratory plasmas [113,114,115,116], especially tokamak plasmas [56,117,118,119,71,120,121,122,123,41,124,125,126,127,128,129, 130,131,132,133,134,135,136,137,138]. Table 3.1 lists several representative experiments where SBDs (and PIN diodes, also a widely used junction-based detector) have been used for detecting x rays generated in plasma devices. SBDs are especially well-suited for imaging tokamak plasmas for three reasons: first, the detector x-ray sensitivity is quite flat between 1 and 8 kev; second, the core electron temperature in tokamaks often ranges between 1 and several keV, and as a consequence the x emissions fall mainly in this range; and finally, x-ray emission levels from tokamaks are of sufficient intensity that surface barrier detectors can be conveniently used as photovoltaic detectors [139] in the current mode.

3.2.1 Calibration and Response Measurements

SBD calibration measurements have previously concentrated largely on the energy range between 0.3 and 8 keV [113,119,154]. This section describes an improvement of these measurements at 8 keV and an extension to 17.5 keV, from which the high energy response of the detectors can be determined. This is an important issue if such detectors

Table 3.1 This table lists several representative plasma devices utilizing silicon surface barrier diodes (SBD) or *p-intrinsic-n* (PIN) diodes to detect x rays. The detectors are intended for either full (F) or partial (P) depletion; however diodes capable of fully depleted operation can be run underbiased such that full depletion is not attained; in such circumstances the diode is actually operating in a partially depleted mode. Note the wide range of plasma electron densities ($4 \times 10^{17} - 1 \times 10^{25}$ m^{-3}) and temperatures (0.2–400 keV) for which these silicon-based detectors are useful. (Device types are abbreviated as follows: T=tokamak, R=reversed field pinch, S=stellarator, M=mirror, DPF=dense plasma focus.)

Diode Type	Experiment	n_e (10^{19} m^{-3})	T_e (keV)	Refs.
SBD/F	ST (T)	~7	~0.8	[56]
SBD/F	PLT (T)	2~4	1~2	[117]
SBD/P	Tosca (T)	1.5	0.2	[118]
SBD/?	Pulsator (T)	≤ 10	~ 0.6	[40]
SBD/P	Alcator-A (T)	20~60	0.6~1.1	[119,71]
SBD/F	HBTX 1A (R)	2~20	~0.2	[113]
SBD/P	TEXT (T)	1~9	0.7~1.1	[120,121,122]
SBD/?	TFR (T)	~10	1	[123]
SBD/P	Alcator-C (T)	10~100	1~3	[41]
SBD/P	ISX-B (T)	0.5~9	0.5~2.2	[124,125,126]
SBD/P	HT-6B (T)	0.7~1.2	0.1~0.12	[127]
SBD/P	ZT-40M (R)	~2	0.2	[114]
SBD/P	TFTR (T)	~2	1~7	[128,129,130,131]
SBD/P	W VIIA (S)	5–10	0.4~0.6	[115,140]
SBD/F	Constance (M)	~0.04	~400	[116]
SBD/P	Varennes (T)	~5	~1	[132,133]
PIN/F	TFTR (T)	~2	1~2	[141, †]
PIN/F	DPF	$\lesssim 10^6$	~1	[142]
PIN/P	Ormak (T)	2~4	1~1.5	[143,144]
PIN/F	Z pinch	$10^5 \sim 10^6$	6~9	[145]
PIN/P	Alcator-C (T)	10~100	1~3	[146,147]
PIN/F	JET (T)	~1.6	3~4.5	[148,149,150]
PIN/P	JT-60 (T)	1~10	1~6	[151,152]
PIN/F	DPF	$\sim 10^6$	0.2~0.5	[153]

† The PIN array on TFTR was not operational for the "supershots" for which the electron temperature was ~7 keV.

are to be used to accurately quantify high intensity x-ray sources with photon energies approaching and exceeding 10 keV. For example, SBDs and PINs are currently used for imaging high temperature tokamak plasmas for which $T_e \gtrsim 5$ keV [130,131,148, 149,150,151,152], and thus a significant fraction of the x emission is at or above 10 keV. In addition the high energy response becomes critically important in this imaging application if spatially and temporally resolved plasma thermometry [71,128,130,131] is attempted on high temperature plasmas.

To address this issue, it is essential to know what constitutes the x-ray sensitive depth in a partially depleted SBD. For charged particle detection it is the depletion layer depth, proportional to the square root of the bias voltage, that determines the sensitive depth [105,106,101]. In contrast measurements of the x-ray response at 17.5 keV, for which the detectors are not optically thick, strongly indicate that it is predominantly the physical thickness of the SBD that determines the x-ray sensitive region [155]. (The optical thickness is defined as $\mu\rho\tau$ where μ is the mass absorption coefficient, ρ is the density, and τ is the thickness of the silicon.) This is at least superficially surprising since outside the depletion layer there is ostensibly no electric field to sweep out charge carriers generated by the x rays. In addition one might expect the x-ray and β-particle responses of SBDs to be similar. This is because the x-ray attenuation, dominated by the photoelectric effect below ~30 keV and the Compton effect above that, results in an ionizing electron that is effectively a low energy β-particle, albeit one that has been created well inside the detector. Confusion has therefore understandably prevailed over this issue; and many workers have assumed, apparently in error, that the depletion depth constitutes the x-ray sensitive depth [113].

Indeed it would be extremely important if the x-ray sensitive depth were the depletion depth and could be trivially set by adjusting the bias voltage. Then, for example, plasma x-ray thermometry [71,128,130,131] could be much more simply, accurately and quickly accomplished by modulating the bias voltage. In fact it was with this in mind that Petrasso *et. al.* searched for, but failed to find, a bias-dependent effect with 8 keV x rays [119]. One of the major aims of the response measurements described herein was to search for a bias-dependent effect which should clearly manifest itself at higher x-ray energies. This failing, it was necessary to test whether the detector thickness was of central importance, as was suggested early on [156].

It is important to note that the question of x-ray sensitive depth in an SBD is

also valid for diodes intended for fully depleted[1] operation. If such diodes are run with a sufficiently low bias voltage, they are in actuality partially depleted. To avoid confusion, SBDs capable of operation in the fully depleted mode are referred to as "fully depleted." (Of course there is no distinction between the depletion depth and the physical thickness of an SBD that is actually operated in a fully depleted mode.) In addition, the problem of the x-ray sensitive depth also applies to PIN diodes, another photovoltaic diode characterized by a bias-dependent depletion depth as well as partially and fully depleted operation.

The particular SBDs used for the response measurements were 18 EG&G Ortec ruggedized model BR-017-050-100 partially depleted diodes ranging in age from a few months to over 10 years (Table 3.2). Eleven of these SBDs are the same diodes used for numerous imaging studies of the x emissions from the Alcator-A [71] and Alcator-C [41] tokamaks, and, of particular importance here, for earlier absolute x-ray response measurements [119]. All 18 of these detectors have 1500 Å of aluminum deposited on the front surface of a silicon wafer that ranges in nominal thickness from 296 μm to 544 μm [157]. EG&G Ortec specifies that a bias voltage of ~70 V creates a depletion layer thickness of 100 μ or greater, the exact value depending on the silicon resistivity and the applied bias voltage [105,106].

Four Tennelec partially depleted model PD-50-100-17 diodes [158], and two United Detector Technology (UDT) model PIN-8LC Schottky barrier diodes [159] (Table 3.2) were also studied. The Tennelec detectors have a 250 Å gold front surface on ~400 μm thick silicon wafers, such that a bias voltage of ~80 V creates a depletion layer thickness of ~100 μm. These detectors are the same as those used in the construction of the horizontal x-ray array (Array B) on TEXT, described in the next section. The UDT diodes have 200 Å of gold over ~250 μm thick silicon such that a bias voltage of ~85 V creates a depletion layer thickness of ~100 μm. Because the UDT detectors are primarily intended for use as optical photodiodes, the entire assembly is covered with ~600 μm of standard borosilicate glass, rendering them blind to soft x rays; however they do respond to the higher energy x rays at 8 and 17.5 keV.

The x-ray source used for these measurements was a Norelco model 12045 x-ray diffractometer. Either a copper or molybdenum anode tube was used with a fixed

[1]Detectors constructed for fully depleted operation are normally more expensive than partially depleted detectors (by about a factor of 2) because of the need for three additional features: first, two contacts capable of supporting an electric field; second, higher resistivity silicon; and third, closer tolerance on the silicon wafer thickness.

Table 3.2: This table lists the partially depleted silicon surface barrier diodes (SBD) used for the measurements reported herein. Eleven of the SBDs(*) are the same diodes used in References [119,71] and [41]. The nominal physical thickness of the silicon and its resistivity (which, in combination with the bias voltage, determines the depletion depth) are also listed [157,158,159].

Diode #	Thickness (μm)	Resistivity Ω-cm)
EG&G Ortec:		
16-846F*	296	6800
16-663I*	321	3000
16-663F*	321	3000
18-365G	322	2500
16-662H	335	3000
16-662D*	335	3000
16-662C*	335	3000
17-230E*	347	4000
16-675C	347	3700
16-675B*	347	3500
16-850J*	347	3500
18-312C	484	3000
16-821A*	544	3500
16-821C*	544	3500
16-821J*	544	3500
26-454B	530	15700
26-454C	530	15700
26-454F	530	15700
Tennelec:		
4226-5	400	2100~3000
4013-9	400	2100~2400
4020-14	400	2100~2400
4170-11	429	2100~2400
UDT:		
PIN-8LCA	250~380	2500~4000
PIN-8LCB	250~380	2500~4000

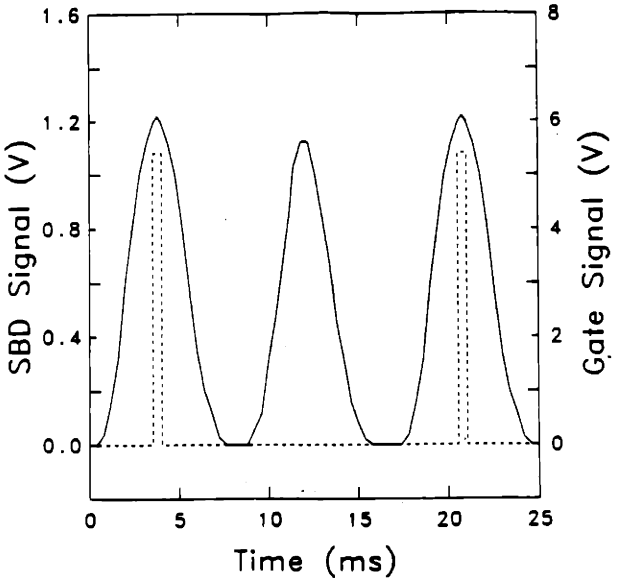

Figure 3.2: This plot shows typical SBD response to the Norelco diffractometer with the copper tube installed. The high voltage of the diffractometer is full-wave rectified, generating two distinct 60 Hz x-ray peaks of slightly different amplitude. The square wave (dashed) is triggered on the larger SBD signal; it is subsequently used to gate a Si(Li) spectrometer so that it only counts photons during the 0.5 ms period during the peak of the x-ray emission.

mica window (nominally 13 μm thick) to produce predominantly CuKα and Kβ x rays at 8.05 and 8.9 keV respectively, or MoKα and Kβ x rays at 17.48 and 19.6 keV respectively. The high voltage was full-wave-rectified such that the diffractometer produced two distinct 60 Hz x-ray peaks (Fig. 3.2). The voltage could be varied up to 40 kV, and the emission current ranged from 1 to 15 mA.

The unfiltered spectrum from the diffractometer, as viewed directly through the mica window, consisted of the Kα and Kβ lines of the anode material as well as a significant amount of thick target bremsstrahlung. To provide "clean" spectra (*i.e.*, mainly K lines) for the calibration measurements, the diffractometer was filtered with the same material as the anode (33 mg/cm^2 copper foil for the Cu tube; 191 mg/cm^2 molybdenum foil for the Mo tube). The K lines thus obtained made up at least 90% of the total number of photons collected (Fig. 3.3). The intensity of these lines was also determined to be linear with the diffractometer emission current (Fig. 3.4), an important consideration which subsequently bears upon the SBD linearity with x-ray intensity.

The intensity of the x-ray spectrum, shown in Fig. 3.3, from the diffractometer was measured using either an EG&G Ortec or a KeVex Si(Li) x-ray spectrometer. The

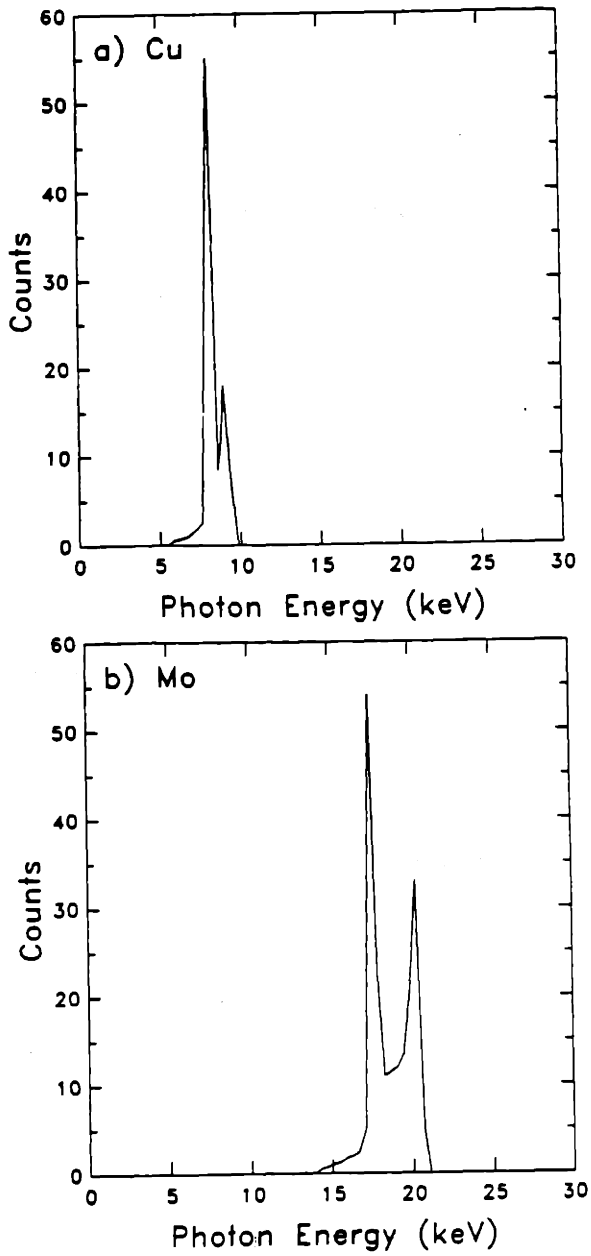

Figure 3.3: Spectra used for the SBD calibrations as measured by a Si(Li) spectrometer. a) The copper K lines made up about 90% of the total counts when the diffractometer was run at 15 kV and filtered with 33 mg/cm^2 copper foil. b) The molybdenum K lines comprised about 90% of the total number of photons when the diffractometer was run at 40 kV and filtered with 191 mg/cm^2 molybdenum foil.

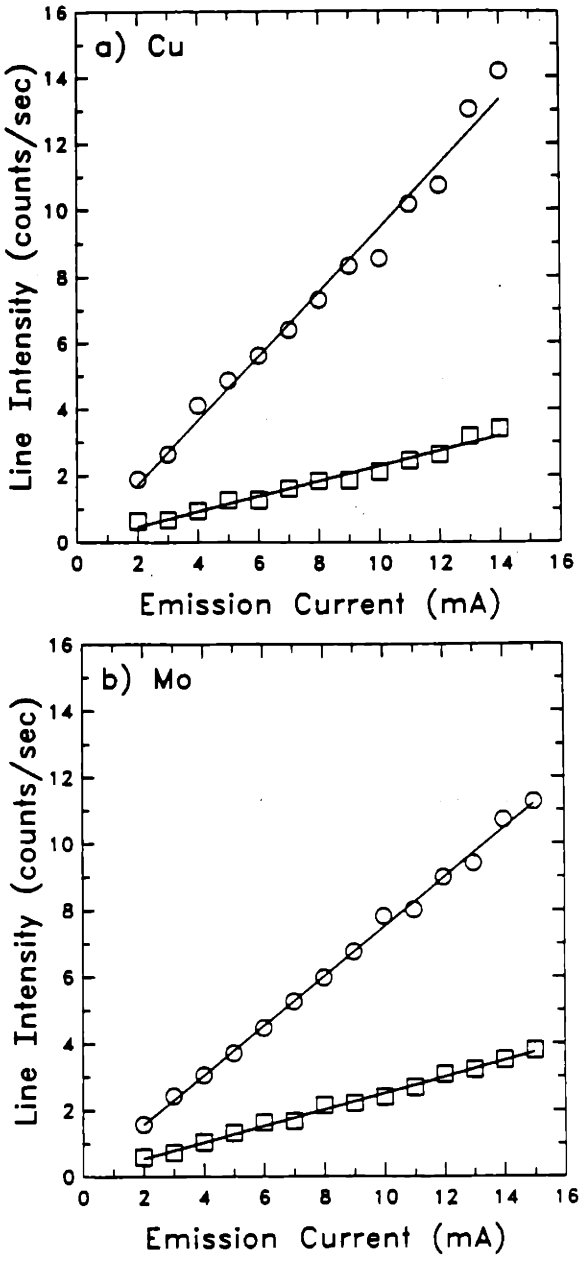

Figure 3.4: The intensity of the spectra used for the absolute SBD calibrations was linear with the diffractometer emission current, an important factor used later to determine the SBD signal linearity with x-ray intensity. a) Linearity of the CuKα (circles) and Kβ (squares) lines when the diffractometer is run as described in Fig. 3.3a. b) Linearity of the MoKα (circles) and Kβ (squares) lines when the diffractometer was run as in Fig. 3.3b.

spectrometer was gated to collect photons only during a 0.5 ms period at the larger of the two peaks (see the dashed gating signal in Fig. 3.2). The signal to gate the spectrometer was taken from a "monitor" SBD, which also served to assure a steady source strength over time. To avoid dead-time effects in the spectrometer counting system, the Si(Li) detector was filtered with material of known transmissivity. During the 8 keV measurements the spectrometer was covered with 233 $\pm$3.5 mg/cm^2 copper foil, while during the 17.5 keV work it was covered with 636$\pm$15 mg/cm^2 molybdenum foil. (These thicknesses were determined by x-ray transmission measurements, using the absorption cross sections from references [160] and [161].)

The x-ray response current of the SBDs was measured using the two circuits shown in Fig. 3.5. The circuit of Fig. 3.5a is a low-noise current-to-voltage amplifier with the gain set by the 1 MΩ feedback resistor. The SBD bias voltage is fixed by the Zener diode to be -9 V. This circuit is convenient for plasma x-ray imaging systems [120,121], and for making the absolute SBD response measurements reported herein. It is also the circuit used as the preamplifier in the vertical array (Array A) on TEXT. The rms noise level of this SBD/circuit combination is in the range of 1 nA (corresponding to $\sim$.02 μW of incident x-ray power or $\sim 1.4 \times 10^7$ photons/sec at 8 keV).

The simple circuit of Fig. 3.5b was used for establishing SBD linearity and the effects of varying the detector bias voltage. For example the value of the bias voltage was easily varied over a wide range up to the maximum recommended by the manufacturer ($\sim$70 V); in addition the bias polarity could be trivially switched for use with different diodes (the Ortec diodes require a negative bias [p-type silicon]; the Tennelec and UDT diodes require positive bias [n-type silicon]).

The responses of the 18 Ortec diodes to 8 keV x rays were comparatively uniform. The maximum variation between the diodes was $\sim$12% (Fig. 3.6a).[2] The signal current of each diode also exhibited a linear behavior from 0.1 to 150 μA with source intensity. (The 150 μA response corresponds to the maximum flux of x rays the diffractometer could generate.) Figures 3.7a and 3.7b show this linearity for two different filters and source voltages. The response of all these diodes was also independent of the bias voltage from the maximum recommended by the manufacturer down to about 1 V (Fig. 3.8a).

The Tennelec and UDT diodes were also very uniform at 8 keV. The maximum

[2]Differences larger than $\sim$5% between the diodes are real and unexplained. Since 8 keV x rays easily penetrate the front diode surface, it is unlikely that the differences seen at this energy can be accounted for by differences in the front surface transmissivity. On the other hand, the optical depth is so large that the differences are not due to differences in the physical thickness either.

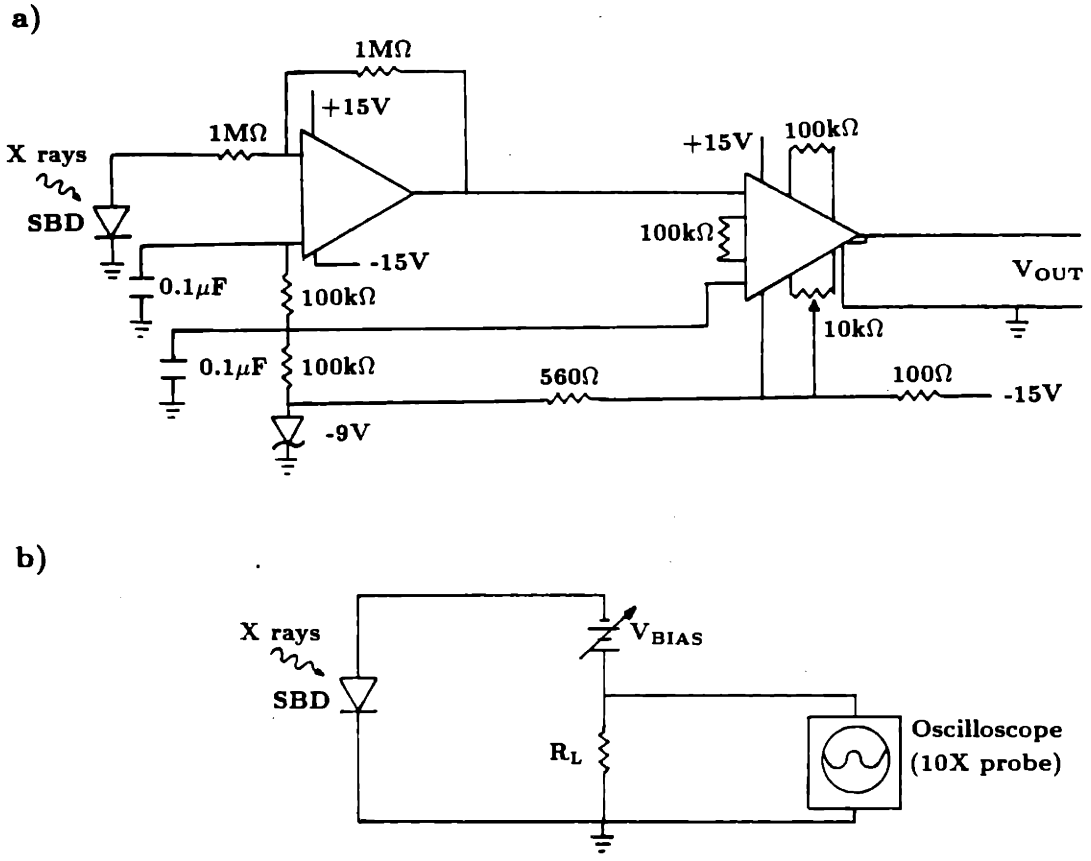

Figure 3.5: Two circuits used to measure the SBD response current. a) This circuit was used for the vertical x-ray imaging array (Array A) on TEXT [120,121], and for all absolute SBD calibration measurements reported herein. b) This simple circuit was used for making linearity measurements (where a wide range of response currents made it desirable to change the gain [R_L] easily), and for examining the effects of changing the SBD bias voltage (though not the results shown in Fig. 3.8). In this configuration, it is important that V_{BIAS} exceed the voltage drop across the load resistor; this guarantees a non-zero effective bias voltage on the SBD. For the linearity measurements the gain was adjusted so as to insure the voltage drop across the load resistor was much smaller than the applied bias voltage.

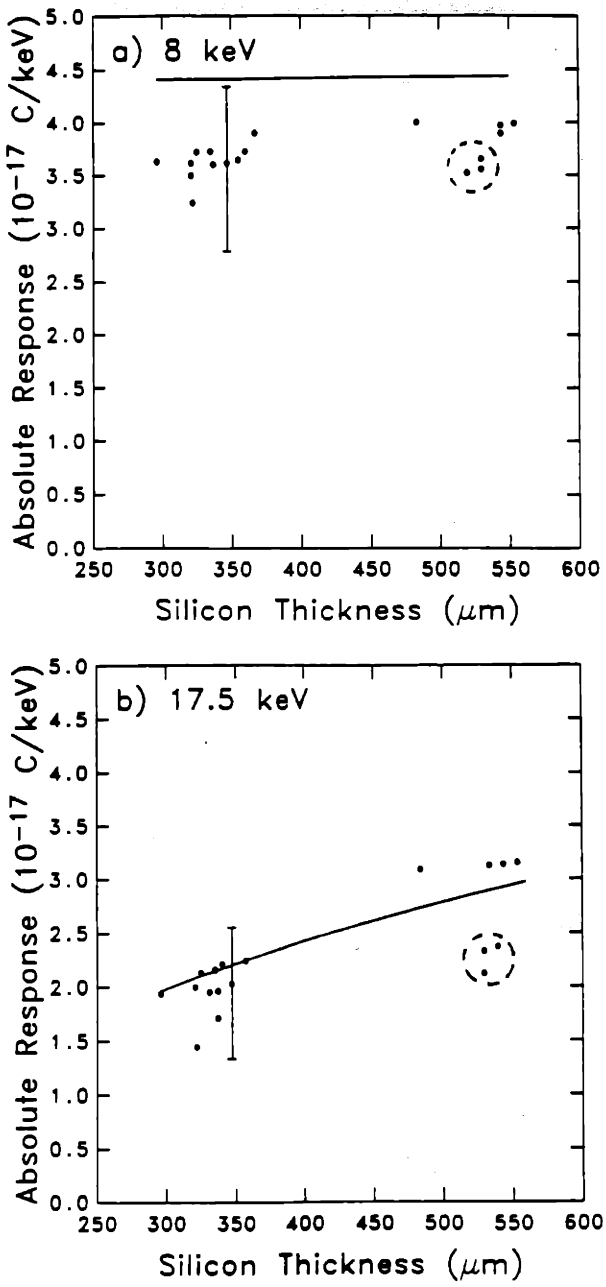

Figure 3.6: The measured absolute responses (points) are compared to predicted responses (lines) based on the physical thickness of the SBD, not the depletion depth, and assuming 3.6 eV in order to create an electron-hole pair [162,163,164,165,166,167]. The predicted response is proportional to $(1 - e^{\mu\rho r})$ which is $\simeq 1$ and nearly constant at 8 keV; but at 17.5 keV it varies rapidly with thickness. Relative differences greater than ~5% between diodes are real. The repeatability of an entire set of measurements (all 18 diodes) is ±10%. Some of the data points have been displaced from their nominal thickness by up to 20 μm to avoid overlap. a) Absolute response to CuK x rays (spectrum of Fig. 3.3a). b) Absolute response to MoK x rays (spectrum of Fig. 3.3b).

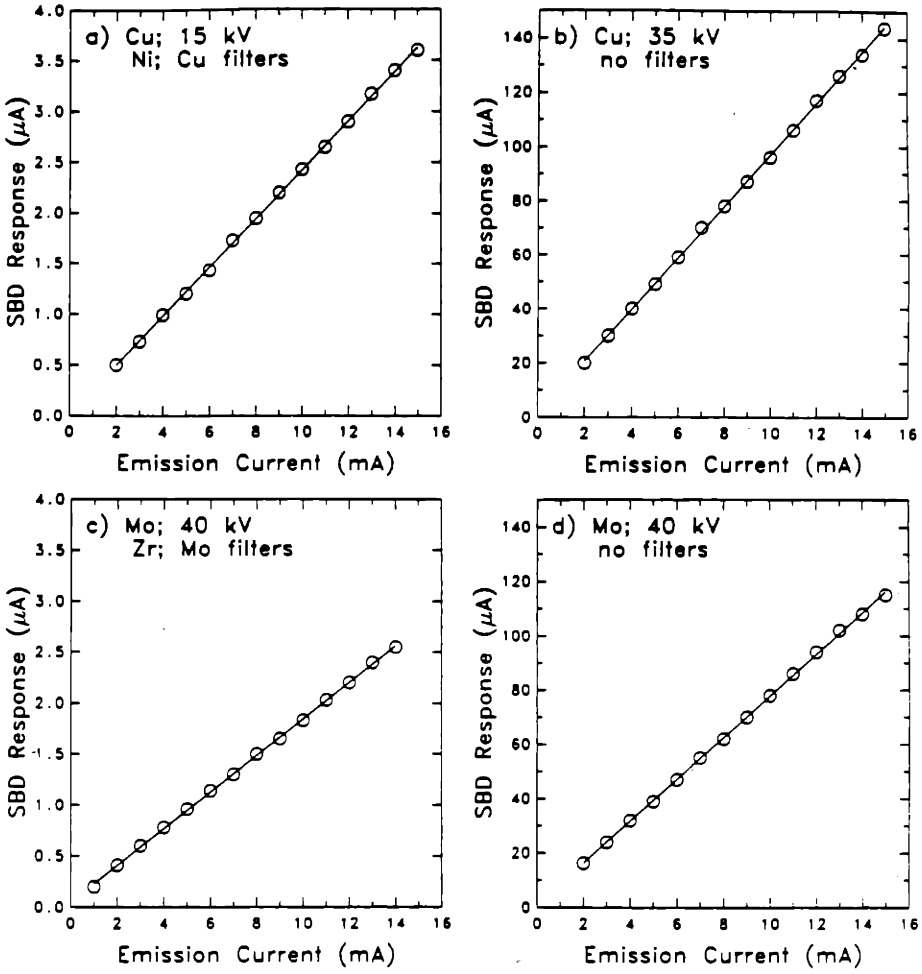

Figure 3.7: The SBD signal current is linear with the diffractometer emission current, and therefore with incident x-ray power (see also Fig. 3.4). a) Linear response when the diffractometer has the copper tube installed, when it is run at 15 kV and is filtered with 17 mg/cm^2 nickel and 33 mg/cm^2 copper foil. b) Linearity when the diffractometer has the copper tube installed, when it is run at 35 kV, and with no filtering except the fixed mica window of the tube. 150μA is the maximum signal current that can be generated using the diffractometer as the source. c) Linear response when the diffractometer has the molybdenum tube installed, when it is run at 40 kV and is filtered with 66 mg/cm^2 zirconium and 64 mg/cm^2 molybdenum foil. d) Linearity when the diffractometer has the molybdenum tube installed, when it is run at 40 kV with no filtering except the fixed mica window of the tube.

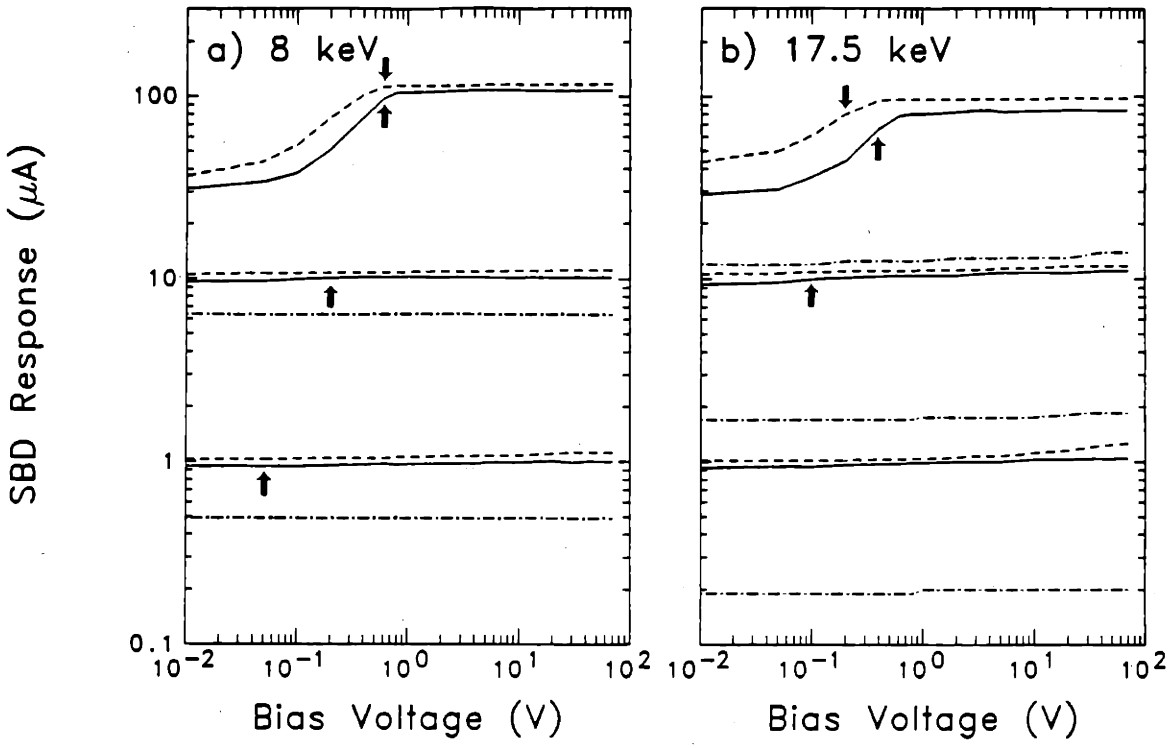

Figure 3.8: Using a circuit similar to that shown in Fig. 3.5a, but for which the bias could be easily varied, the effect of large changes in the bias voltage on x-ray response was measured for three SBDs: EG&G Ortec #16-675C (solid line); Tennelec #4226-5 (dashed line); and UDT # PIN-8LCA (dot-dashed line). The Ortec and Tennelec diodes were examined for nominal signal currents of about 100, 10 and 1 μ A (at 70 V bias). The corresponding UDT response ranged from 10 to 0.1 μA. The vertical arrows indicate bias voltage below which the response signal became distorted for the Ortec ($\uparrow$) and Tennelec ($\downarrow$) diodes; the UDT diodes did not exhibit any distortion in this range of signal currents. a) The response of the SBDs to 8 keV x rays was independent of bias voltage between ~1 and 70 V. A signal-dependent decrease in the response current was observed below a bias voltage of about 1 V. b) The response of the SBDs to 17.5 keV x rays changed by $\leq$10% as the bias changed from 1 to 70 V. A signal-dependent decrease was again observed below about 1 V. The relative invariance of the SBD signal with such a large change in the bias voltage is in contrast to the behavior expected if the x-ray sensitive depth were the depletion depth, which would give roughly a $\sqrt{V_{BIAS}}$ dependence for the SBD response.

variation between the 4 Tennelec diodes was ~3%, and the 2 UDT diode responses were essentially identical to each other. The Tennelec SBDs also exhibited linear response (0.1 to 160 μA) with the diffractometer emission current, and the responses of both the Tennelec and UDT detectors were again independent of the bias voltage above 1 V (Fig. 3.8a).

The responses of the 18 Ortec SBDs to 17.5 keV x rays were much less uniform than at 8 keV. The maximum variation between the diodes at this higher energy was ~100% (Fig. 3.6b), which is attributed largely to differences in the physical thickness of the diodes. The SBD current was linear from 0.1 to 100 μA with the diffractometer emission current (Figs. 3.7c, 3.7d), and again independent of the bias voltage from 1 to 70 V (Fig. 3.8b). The comparative invariance of SBD responses with changes in bias voltage is particularly significant at 17.5 keV; the signal current should change drastically (by a factor of ~5) as the bias is varied from 1 to 70 V if the x-ray sensitive depth were determined by the depletion depth. Instead it changes by less than 10%.

The Tennelec diodes exhibited larger variations in response to the higher energy x rays as well, while the 2 UDT diode responses were again virtually identical to each other. The maximum variation between the Tennelec diode responses to 17.5 keV x rays was ~15%. The responses of the Tennelec (at least 0.1 to 120 μA) and the UDT (at least 0.1 to 20 μA) SBDs were also linear with the diffractometer emission current. The diode currents were again comparatively invariant to large changes in the effective bias voltage (Fig. 3.8b).

The absolute response (defined as the current produced per incident power) of the 18 Ortec SBDs was measured at 8 and 17.5 keV. The intensity and spectra were measured with a Si(Li) spectrometer described previously, and the response of the SBD was measured at the same physical location. At these photon energies it was necessary to aperture the SBDs with stainless steel washers to prevent the x rays from penetrating the epoxy which defines the outer edge of the active area of the diode (specified as 0.5 cm^2 by the manufacturer). Penetration of the epoxy would increase the effective area of the SBD. In particular, an increase of ~30% in the response at 8 keV was measured when the diodes were not apertured and the epoxy penetration was not accounted for.

The uncertainty in absolute response measurements arose from three main sources: spectral purity, the reproducibility of a set of measurements, and uncertainty in the transmissivity of the material used to filter the spectrometer. The uncertainty due to spectral purity (whether the SBD and spectrometer were responding to the same

spectrum) was determined by taking measurements with and without a filter of known transmissivity that was sufficiently attenuating to reduce the incident x-ray power by a factor of 2. The difference between such filtered and unfiltered responses of the SBD and spectrometer always agreed within ±10%. The reproducibility between sets of measurements (*i.e.*, all 18 diodes) was also always within ±10%. The uncertainty in the filter transmissivities for the Si(Li) spectrometer led to the largest uncertainties in absolute responses (+16%, −20% at 8 keV; and +24%, −32% at 17.5 keV). The overall uncertainty (taken to be the square root of the sum of the square of these contributions) was then +21%, 25% at 8 keV; and +28%, −35% at 17.5 keV.

In Fig. 3.6 the measured absolute responses are shown as a function of detector physical thickness, and in Fig. 3.9 as a function of photon energy (for comparison, responses of many of the same SBDs from the reference [119] are included. The measured responses agreed well with predicted responses at 8 and 17.5 keV if the sensitive thickness was taken to be the physical thickness of the device; they did not agree if the sensitive region was taken to be the depletion layer thickness as determined by the bias voltage. These results are also directly relevant to fully depleted SBDs operated in an underbiased mode, since such detectors are, as mentioned, then partially depleted in actuality.

The response of the SBDs to x rays at 8 and 17.5 keV was found to be linear from 0.1 μA to at least 100 μA. This agrees qualitatively with the results of reference [119] where the SBD response to 1.5 keV x rays was shown to be linear over a factor of 4 in the 10 nA region. When incorporated with the results presented here, this indicates SBDs are likely to have a linear behavior from ~10 nA to 100 μA. Diode linearity was found to be invariant to large changes in the bias voltage, and the smaller the signal current, the lower the bias could be set before bias-dependent effects became prominent (Fig. 3.8). It is interesting to note, however, that a bias-dependence was observed in the SBD response to fast (~50 ns) pulses of broadband x rays in the 50–100 keV range.[3] It is believed that this result is primarily caused by a frequency cutoff due to the bias-dependent capacitance of the SBDs, particularly because there was no such bias-dependence for the response of the same diodes to 17.5 keV x rays modulated at

[3]Using diodes #18-365G and #16-661G, Dr. Ruth Shefer of Science Research Laboratory has observed a bias voltage dependence of the SBD response to extremely fast (characteristic time ~20 ns; total signal duration ~ 140 ns) pulses of broadband X rays with energies greater than about 50 keV. This is due to a frequency cutoff effect due to the capacitance of the diode, which varies as $1/\sqrt{V_{BIAS}}$. With the 50 Ω load resistor used by Dr. Shefer, the 3 db attenuation frequency of these diodes is ~ $10\sqrt{V_{BIAS}}$ MHz. Furthermore, using the same diodes, there are no such bias-dependence in the response to 17.5 keV x rays modulated at 120 Hz.

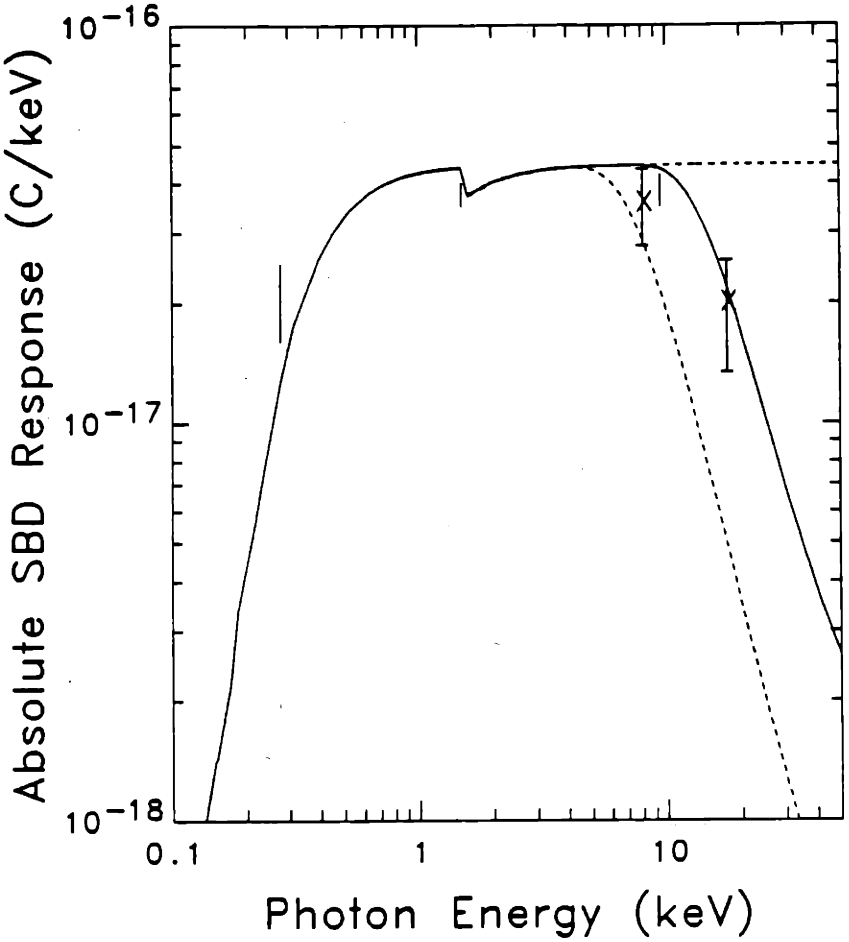

Figure 3.9: Measured absolute responses are compared with predicted absolute responses as a function of photon energy. The two data points with error bars are the responses measured for the representative Ortec diode #16-675C. The solid vertical lines represent the range of results measured for many diodes in reference [119]. At 8 keV these results have been reduced by 30% to correct for penetration of the edge epoxy, an effect not taken into account in that work (the 8 keV data is also offset to 10 keV for clarity). The solid curve is the response predicted for a 347 μm thick detector (see Table 3.2). The upper dashed line is the predicted response for a detector of infinite thickness, and the lower dashed line is the predicted response for a 20 μm thick detector (the depletion layer thickness of detector #16-675C at a bias of 1 V). The measured responses agree best with the theoretical response based on the physical thickness of the SBD.

120 Hz.

The lack of significant bias dependence at 8 and 17.5 keV also has important implications for practical operational aspects. The leakage current, which often must be compensated for to maintain the maximum electronic dynamic range [128,129,130,131], increases with bias (approximately as $\sqrt{V_{BIAS}}$). Therefore it is desirable to operate at a low bias to avoid a high leakage current due, for example, to an elevated diode temperature or diode degradation.[4] This work shows that low bias operation of partially depleted SBDs is in principle viable, and might be an acceptable means of reducing leakage current without affecting the high-energy x-ray response.[5]

Differences between SBD responses were comparatively small at 8 keV due to the large optical thickness of the diodes at this energy. The differences at 17.5 keV, however, were significant, because the diodes were not optically thick to photons of this energy. The absolute response measurements agreed well with predicted responses if the x-ray sensitive thickness was assumed to be the physical thickness of the SBD (not the depletion layer thickness) and that the energy necessary to create a charge pair is 3.6 eV [162,167]. The absolute responses at 8 keV also agreed well with those of reference [119] reduced by 30% to correct for the effect of epoxy penetration discussed earlier. This indicates a notable stability of the diodes over a period of 10 years. (The effect of x-ray penetration of the epoxy does not occur for the measurements at 0.282 and 1.5 keV of reference [119].)

While agreement with predicted responses was within the errors for all 18 diodes, 3 new diodes in this group (26-454B, 26-454C and 26-454F; circled in Fig. 3.6) exhibited responses lower than expected based on their nominal thicknesses[6] ($\sim$10% at 8 keV and $\sim$25% at 17.5 keV). One obvious difference between these diodes and the others was that their resistivity was typically a factor of 5 higher (Table 3.2), which implies a depletion layer of about a factor of 2 greater [105,106]. It is not clear why these diodes had lower responses, but it is of central importance that this provided additional evidence that the

[4]Among many other reasons, diode degradation can be caused by operating in a hydrogenated (reducing) atmosphere, or caused by radiation damage resulting in lattice defects. Degradation of SBDs due to neutron-induced damage from high temperature plasmas may possibly be avoided by using reflective optics. Annealing SBDs is not currently a useful method to remedy radiation damage because the epoxy used to construct the diodes cannot withstand elevated temperatures [157]. A. W. Edwards, *et. al.* found that most neutron damage in PIN diodes could be overcome by annealing.

[5]Two conditions must be met to allow low-bias operation of SBDs; 1) the x-ray signal must not have a characteristic frequency greater than the cutoff frequency of the SBD; and 2) the signal amplitude cannot be so large that bias-dependent effects are prominent at low bias voltages (Fig. 3.8).

[6]The 26-series of Ortec SBDs have reported nominal thicknesses of 530 μm [157]. Using transmission of the 17.5 keV Mo Kα line we measured the thickness of diodes #26-454C to be 495$\pm$15 μm.

depletion depth is not the critical parameter in determining the x-ray sensitive region of SBDs.

That the sensitive depth is the physical depth can be understood physically by comparing the characteristic charge carrier diffusion time to the characteristic time for electron/hole recombination [168]. In silicon the diffusion coefficient is related to the electron (hole) mobility μ by $D(cm^2/s) = \mu kT/q$, where kT/q is expressed in volts. The mobility for silicon is 1350 cm^2/Vs (480) for electrons (holes) [105]. Therefore at room temperature typical diffusion times to transverse a 500 μm detector are $t = L^2/D =$ 70 μs (200 μs). For comparison the typical lifetime before recombination is 1-10 ms [168]. The detector sensitive thickness should therefore be expected to depend on the physical detector thickness, and not the depletion depth, because the charge carriers have ample time to diffuse to the electrodes before recombination occurs.

There are several issues which need to be addressed in future work. First, the logical extension of these results is to measure the response of SBDs to higher energy monochromatic x rays ($h\nu \simeq$ 25-100 keV), again searching for any bias-dependence of the SBD signal. Second, it would be useful and interesting to directly test whether, as expected, fully depleted SBDs with a lower applied bias respond in the same fashion as partially depleted diodes, a comparison currently relevant to ongoing fusion experiments (Table 3.1). Third, a comparison of the behavior of PIN and SBD diodes, specifically an examination of what constitutes the sensitive thickness of a PIN diode, will be important for future fusion experiments[7][8]

3.3 Array Systems Installed on TEXT

A set of three x-ray imaging arrays was constructed to perform impurity transport studies in TEXT. With the objective of measuring impurity density profiles $n_Z(r)$ we can, with independent and simultaneous measurements of $n_e(r)$ and $T_e(r)$ as well as some qualitative knowledge of the impurities, begin to infer the level of impurities in the plasma from a single measurement of the broadband x-ray brightness profile [76,71]. This method can be refined through the use of multiple arrays of detectors with dif-

[7]Measurements of absolute x-ray response of fully depleted PIN diodes have previously been made at several photon energies. Ebert and coworkers did not examine the effect of varying the bias voltage. Private communications, 1987 and [169].

[8]In so far as the low energy x-ray response ($\leq$2 keV) is unimportant in an experiment, PIN diodes may be preferable to SBDs because of their inherently faster time response and their capacity for annealing [150].

ferent absorption filters to yield some spectroscopic resolution, and thus discrimination between different ionization states of a single impurity [54,170], or different impurity species [41,149]. In certain circumstances this information can be used to estimate the average ionic charge (Z_{eff}) of the plasma. This is an especially important quantity because, as described in chapter 1, it can often determine at least four important properties of the plasma: 1) the radiative component of the power balance; 2) the current density profile in a tokamak; 3) the extent to which the fuel ions (hydrogen) are diluted; and 4) the efficacy of auxiliary heating methods. In addition to the behavior of impurities intrinsic to the tokamak, we may study general impurity transport by injecting, via laser ablation [171] or pellet injection [172,173], small amounts of known elements into the plasma [54,170,37,35,65]. In this sort of experiment confusion over the source of particles is reduced, because the injection is temporally well defined and trace, non-gaseous, elements injected by laser ablation are less likely to recycle once they have escaped the bulk plasma [171].

The x-ray imaging system described herein was constructed in order to measure impurity density profiles with good spatial and temporal resolution using multiply filtered arrays on TEXT. This tokamak is especially well-suited for this type of experiment because of the availability of a large number of independent diagnostics for measuring profiles of many other plasma parameters in addition to the x-ray emission (see Table 1.1). Of particular importance to impurity transport studies using x-ray arrays is the availability of time resolved n_e and T_e profiles for each discharge. In TEXT the electron density was obtained with a six channel far infrared interferometer [72], and the temperature was measured with a ten channel Electron Cyclotron Emission (ECE) grating polychromator [174]. The ECE system was calibrated against a scanning single spatial channel ruby laser Thomson scattering diagnostic [175]. Other important diagnostics included monochromators in the visible through UV wavelength regions [35,65], an x-ray spectrometer [176], and a ten channel bolometer array for measuring time dependent profiles of the total radiated power [177].

In addition to the application described above, the x-ray imaging arrays on TEXT are useful for studying several other aspects of plasma behavior. For example, the high frequency response ($\lesssim$ 100 kHz cutoff) of the system provides an excellent means for examining fast magnetohydrodynamic (MHD) instabilities in the plasma [178,179], as well as sawtooth oscillations [56,57]. These instabilities are clearly manifested through changes in the broadband x-ray signals because of their perturbations on the electron

temperature, density, and impurity profiles. A further use of the x-ray imaging system is the tomographic reconstruction of the plasma x-ray emissivity from the three poloidal sets of x-ray brightness profiles [180,181,182,183]. For this application, the imaging system provides a practical compromise between radial and poloidal resolution; *i.e.*, poloidal modes with mode numbers $m \leq 2$ can be resolved, and the radial resolution is $\delta r \lesssim 2.5$ cm ($\delta r/a \simeq 0.1$).

This section describes the major components of the system, including the detectors and their spectral sensitivities, the associated electronics for signal processing and data acquisition, and the vacuum system. A description of a unique krypton gas edge absorption filter and some preliminary data from aluminum injection experiments is included.

3.3.1 X-Ray Imaging System Components

Fig. 3.10 shows a schematic of the complete x-ray imaging system as configured on TEXT. The entire system consists of a total of 92 x-ray detectors, distributed among two multichannel arrays of SBD x-ray detectors and one array of *p-i*ntrinsic-*n* (*pin*) diodes. The two SBD arrays are Array A (Fig. 3.11), a vertically-viewing 40-channel array, and Array B (Fig. 3.12), a horizontally-viewing 40-channel array. Array B is arranged in two columns of 20 detectors each. These two columns form separate arrays viewing essentially the same plasma and may be filtered differently. Array C (Fig. 3.13) is a 12-channel *pin* array located at an angle of 45° between the vertical and the horizontal midplane. Array A views chords across the entire plasma cross section from −26 cm to +26 cm (inside to outside) with a spatial resolution of ≃1.3 cm. Array B views chords from −23 cm to +25 cm (bottom to top) with a spatial resolution of ≃2.4 cm[9] Array C views only the top one-quarter of the plasma from 0 cm to +15 cm with a spatial resolution of ≃1.3 cm. All three arrays view the plasma from the same toroidal location, and each is housed in a stainless steel vacuum enclosure that is separated from the TEXT vacuum system by a beryllium window 25 μm (1 mil) thick. This window also completely attenuates visible light generated in the plasma, to which the detectors are also sensitive.

[9]Arrays A and B have different spatial resolutions because Array B was constructed to include the two independently filtered 20-channel arrays that both viewed the entire plasma. Thus the distance between adjacent chords for Array B is twice that of Array A. See Figs. 3.11 and 3.12 for the major differences.

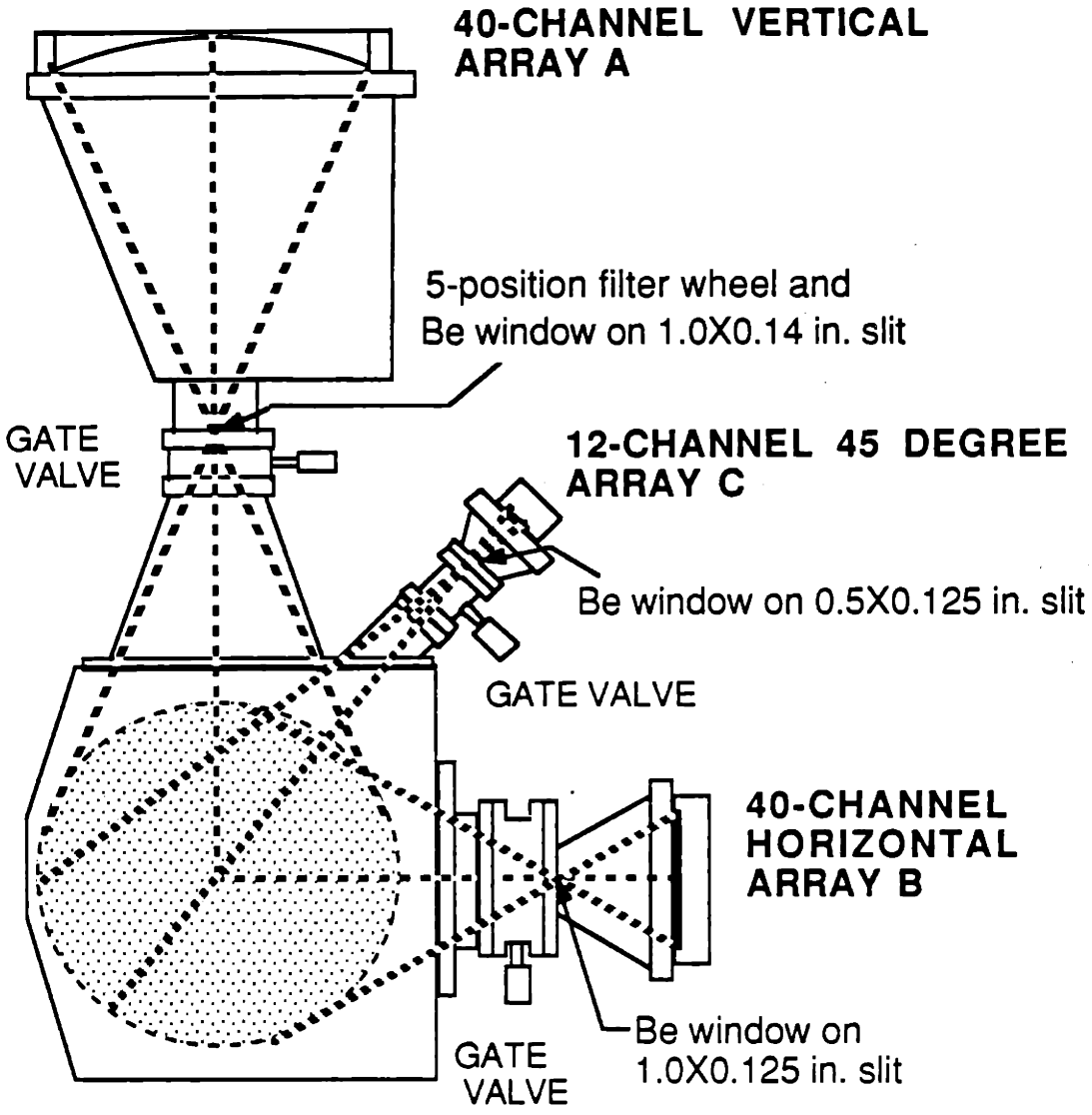

Figure 3.10: The TEXT soft x-ray imaging system has a total of 92 detectors in three separate arrays viewing poloidal cross sections of the plasma at the same toroidal location. Array A is a rebuilt version of the 40-channel SBD array that was originally installed [184]. Array B is a 40-channel SBD array divided into two 20-channel columns that may be independently filtered. Array C, a 12-channel *pin* diode array, views only the top quarter of the plasma from a 45° angle. All three arrays are separated from the main TEXT vacuum by 25 μm (1 mil) thick beryllium windows. See Fig. 3.11–3.13 for a detailed picture of the individual arrays. (The long dimension of each slit is in the toroidal direction, and the plasma minor radius is 26 cm.)

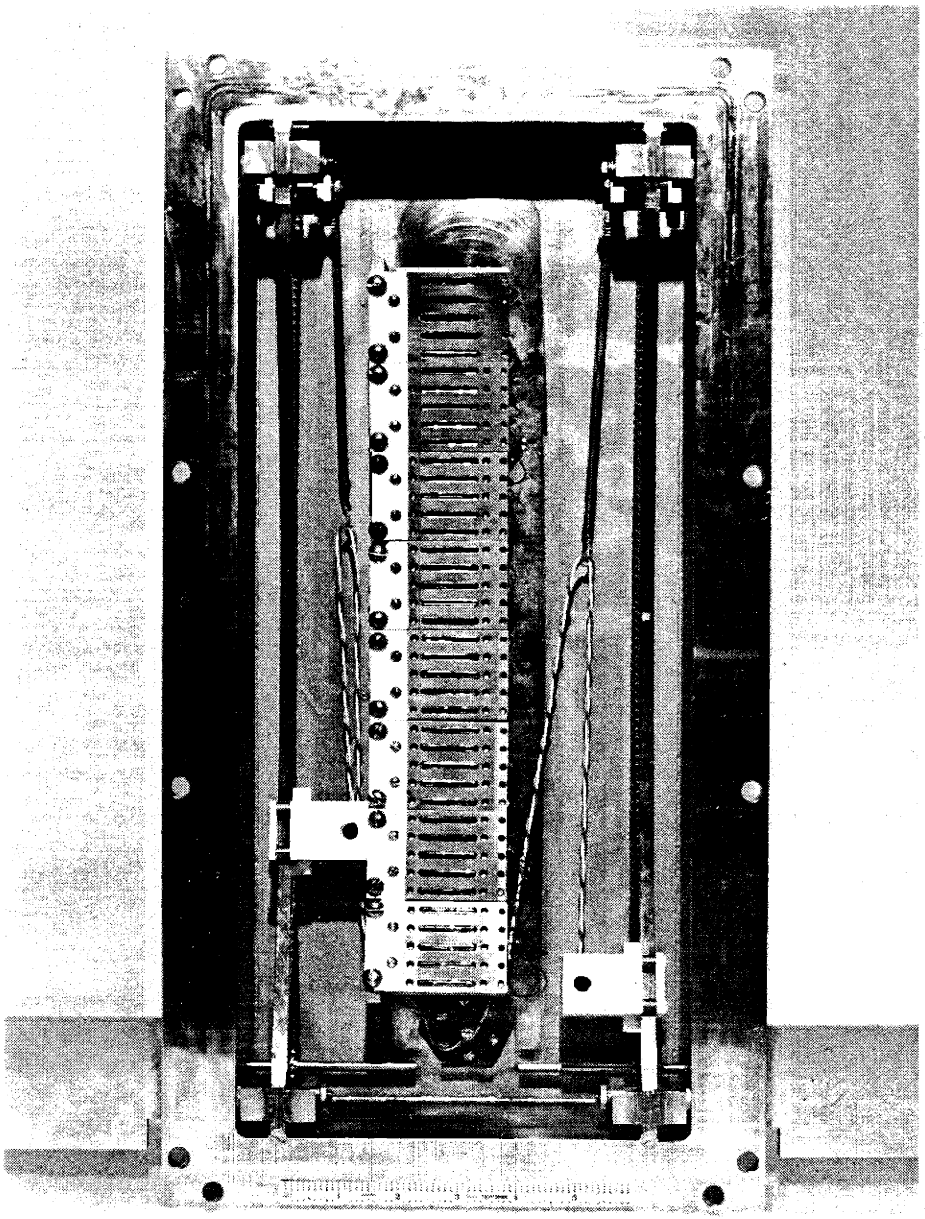

Figure 3.11: Array A, the 40-channel, vertically viewing set of rectangular SBDs. Note the two round SBDs in square white polyethylene holders that could be positioned adjacent to any rectangular main array diode for relative calibration during a TEXT discharge. (The scanning diodes were stationary during a given discharge.)

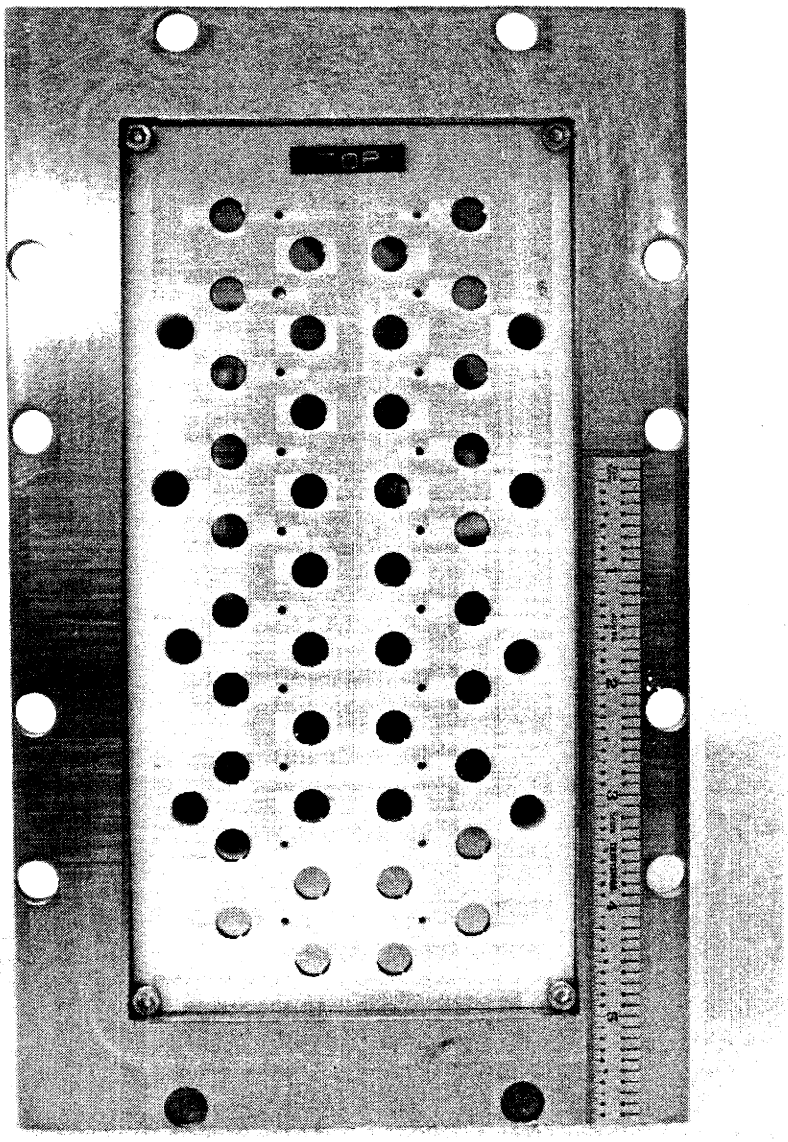

Figure 3.12: Array B, the 40-channel, horizontally viewing set of SBDs. The two columns of 20 detectors each could be independently filtered. (The four holes on each side of the column of detectors are to allow vacuum pumping in the section of the box behind the solid polyethylene detector support structure.)

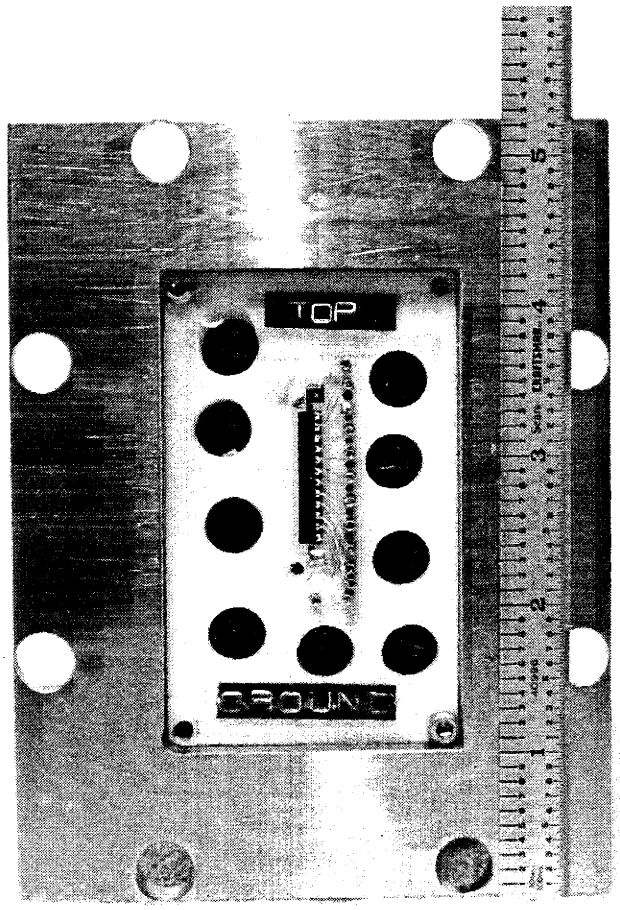

Figure 3.13: Array C, the 12-channel set of *pin* detectors that views the plasma from a 45° angle. (Again, the large holes were to allow both sections of the box to be pumped out.) Note the different scales on Figs. 3.11–3.13; the ruler in all three photographs is six inches long.

An original version of Array A was installed on TEXT several years ago, and was described in detail elsewhere [184]. In the context of the work presented here, three major improvements were been made to this array [185]: 1) an *in situ* relative calibration of the rectangular diodes against absolutely calibrated diodes (the response of the Array A diodes was measured relative to the response of round diodes that could be positioned adjacent to any Array A diode, as shown in Fig. 3.11); 2) the modification of the vacuum box to allow the entire plasma cross section to be viewed ($\pm$26 cm instead of $\pm$21.5 cm previously allowable); and 3) the addition of the beryllium window to physically divide the array vacuum system from that of TEXT.

The detectors in Array A were p-type SBDs, those in Array B were n-type, and the detectors used in Array C were *p-i*ntrinsic-*n* diodes. The smaller *pin* diodes were chosen for Array C because of size constraints imposed by the TEXT torque frame. Small diodes from United Detector Technology (model A4V-12PL) [10] were found to be sufficiently compact for use in this experiment, and were similar to those diodes used for x-ray tomography experiments on Alcator-C [180] and the Missouri Mirror Experiment [186]. The total size of a set of 12 *pin* detectors is approximately one inch long by one-half inch wide, as shown in Fig. 3.13. This size made these detectors ideal for use in a small vacuum box. The advantages of small size and low cost of the *pin* diodes would not necessarily justify their use for all three arrays on TEXT; the geometry of Array C resulted in a small solid viewing angle. (The detector active area A_d=0.152 cm$\times$0.279 cm = 0.042 cm^2, the detector-to-slit distance L_s = 8.6 cm, and the detector-to-plasma distance L_p = 69.6 cm.) This had the consequence of a small response signal, and the signal-to-noise ratio was much smaller for Array C than it was for Array A (A_d = 0.75 cm^2, L_s = 44.0 cm, and L_p = 122.6 cm) or Array B (A_d = 0.5 cm^2, L_s = 17.0 cm, and L_p = 70.5 cm). The noise from all three arrays was dominated by the detector/preamplifier combination rather than detector response to extraneous radiation. With 1 $M\Omega$ feedback resistors typical signal/noise levels from the preamplifiers were, from Array A, $0.1\mu A/0.003\mu A$; from Array B, $0.65\mu A/0.02\mu A$; and from Array C, $0.08\mu A/0.02\mu A$.

Severe size restrictions, as mandated for Array C, were not imposed on the vacuum boxes for Arrays A and B. The detectors in Array A were Ortec model ARXX-3X25-100S partially-depleted SBDs [184,187], those in Array B were Tennelec model PD-50-100-17 partially depleted SBDs [158]. The Tennelec diodes have been absolutely calibrated as

[10] United Detector Technology, Hawthorne California.

described in section 3.2.1 and Ref [155].

Despite physical differences in their front surfaces, the diodes had similar low energy spectral responses in the x-ray wavelength range when they viewed the plasma through the 25 μm beryllium window. This is because the low-energy response was dominated by the beryllium absorption. The front of the Ortec diodes (Array A) consisted of $\sim$2500 Å aluminum, that of the Tennelec diodes (Array B) was $\sim$250 Å of gold, and that of the UDT diodes (Array C) was $\sim$700 Å of SiO_2. The x-ray transmissivities for these materials are shown in Fig. 3.14a for the energy range between 50 eV and 5 keV. (The absorption cross sections were taken from Refs. [161,160].) On the high energy side of the spectrum, the response of all the diodes is nearly the same because it was determined predominantly by the total physical thickness of the silicon used for the detectors, not the depletion depth [155]. The detectors in Arrays A, B and C had physical thicknesses $\sim$300 μm, $\sim$400 μm, and $\sim$250 μm respectively. The total response for all three arrays when they view the plasma through the beryllium window is shown in Fig. 3.14b. From this figure, it is seen that they all have nearly identical responses over the energy range of interest (*i.e.*, $\sim$1 keV to 20 keV). Indeed the brightness profiles measured by the three arrays agreed to within $\lesssim$10% when they were filtered with only their permanent front surfaces and the intervening 25 μm Be. This feature would be particularly important for the application of x-ray tomography.

The signal current from the detectors (proportional to the total incident x-ray power) was converted to a voltage signal in preamplifier boards directly adjacent to the array vacuum boxes. The signal was then amplified and analog filtered in the tokamak enclosure before being sent to the TEXT data room for digitization. This overall signal processing scheme is shown schematically in Fig. 3.15a. Array A had slightly different electronics [184] than Arrays B and C (the preamplifier circuit used for absolute calibration measurements and shown in Fig. 3.5 was used for Array A); the discussion below is limited to the electronics of Arrays B and C. The general characteristics of all three arrays are, however, quite similar.

The detector signal currents, typically on the order of a few microamps for the central channels and decreasing rapidly for channels viewing chords farther from the plasma center, were transmitted via Physicon vacuum feedthroughs to the AC-coupled preamplifier stage illustrated in Fig. 3.15b. An AC-coupled preamp design was used in order to allow the bias voltage for the Array B diodes to be easily varied over a wide range, up to the maximum suggested by the diode manufacturer ($\sim$ +70V). The diodes

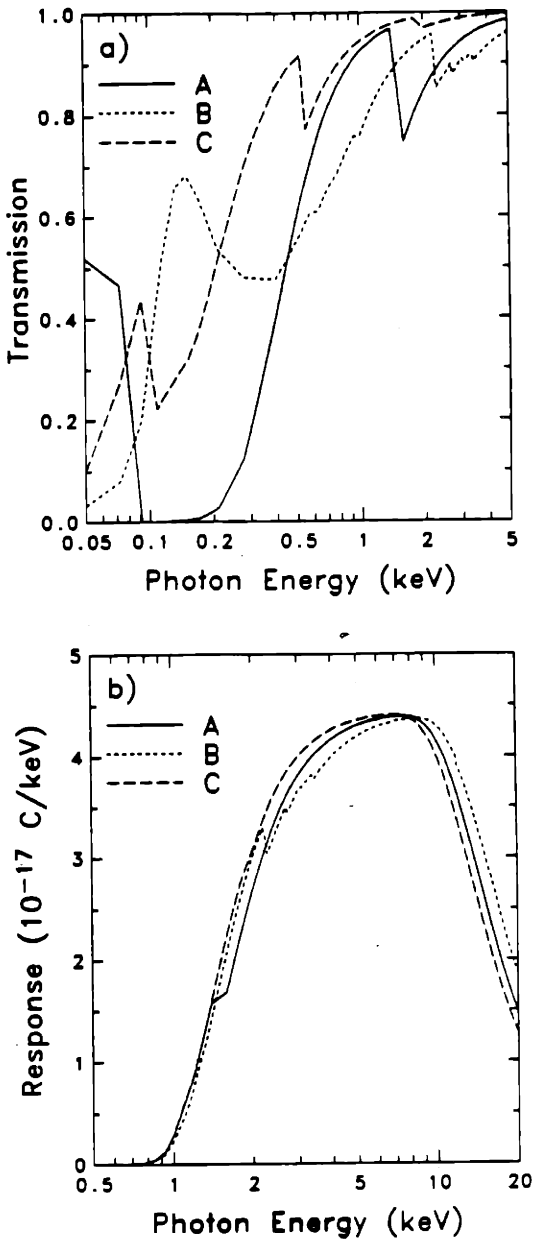

Figure 3.14: a) X-ray transmissivities for the front surfaces of the three types of diodes used in imaging Arrays A, B and C. The solid line is for 2500 Å of Al (front of Ortec diodes; Array A); the small dashed line is for 250 Å gold (front of the Tennelec diodes; Array B); and the large dashed line is for 700 Å of SiO_2 (front of UDT diodes; Array C). Note the strong effects of K-edges at 0.53 keV for oxygen in SiO_2 and at 1.56 keV for aluminum. The M-edge of gold is also apparent at about 2.3 keV. b) The total response is shown for the three types of diodes, including the important effect of the 25 μm beryllium window which separates the tokamak vacuum from that of the x-ray detectors. It is important to note how the addition of the beryllium brings the low-energy cutoff up to $\sim$1 keV, resulting in similar spectral response for all three types of detectors. The high energy response is determined by the detector physical thickness ($\sim$300, 400 and 250 μm respectively).

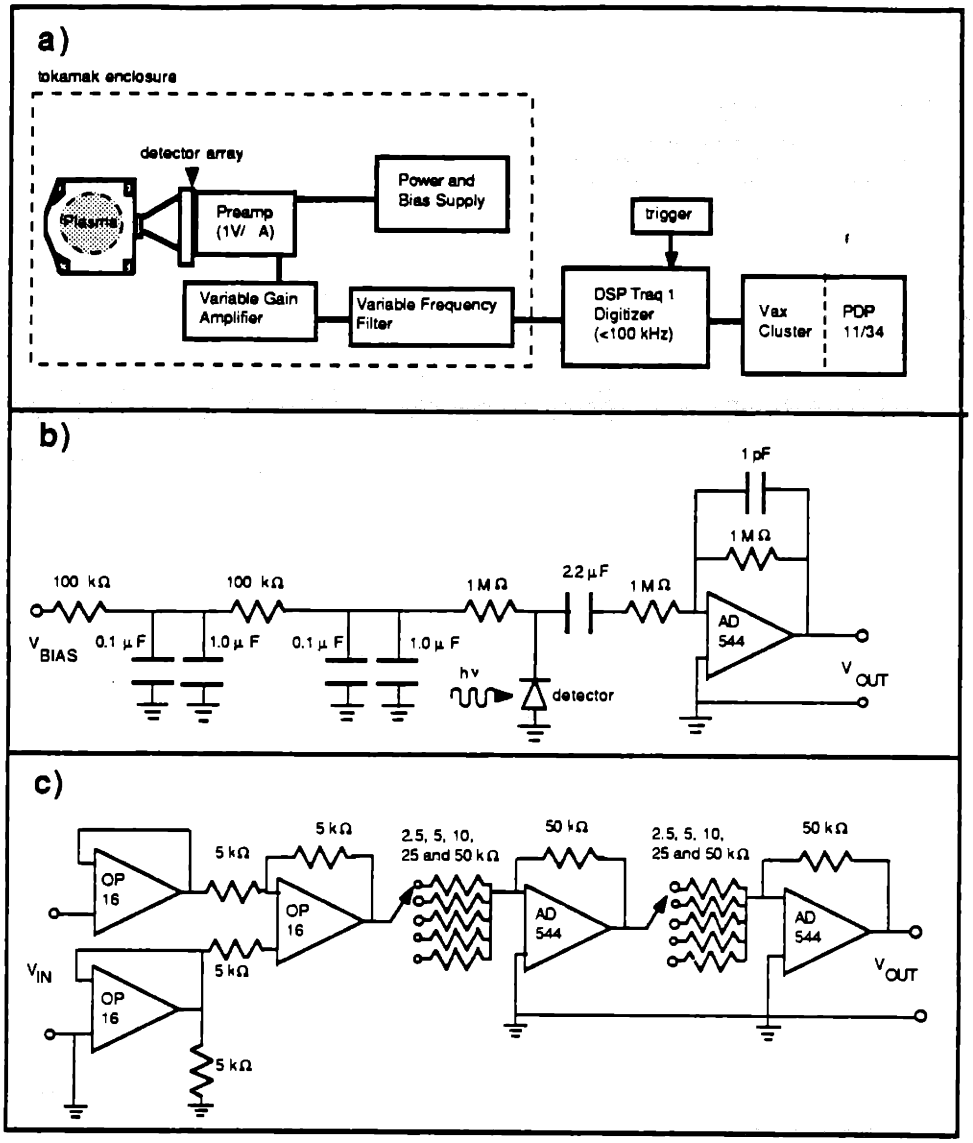

Figure 3.15: a) An overall schematic of the data acquisition for Arrays B and C. (Array A had slightly different preamplifiers and amplifiers [184].) The signal was converted from a current to a voltage in the preamplifier, subsequently it was amplified, filtered, and finally sent to the TEXT data room for digitization and storage. b) The preamplifier circuit used for Array B was AC-coupled to allow the bias voltage to be easily varied and to avoid long time scale and DC changes in signal levels. (The Array C preamp was also AC-coupled, but the bias voltage was a fixed -15 V.) With an AC-coupled circuit no compensation for the leakage current was required. The typical pulse length on TEXT was 500 ms, and the RC time constant of the preamp was $\simeq 1M\Omega \times 2.2\mu F = 2.2$ s. c) The amplifier circuit could achieve voltage gains of 1, 2, 4, 5, 10, 20, 25, 40, 50, 100, 200, and 400, by combining different gains of the two gain stages. The signal level could then be easily set to match the dynamic range of ± 5 V of the digitizers. For channels with the weakest signals (the outer-viewing channels in Fig. 3.10) the maximum gain used was rarely above 25.

of Array C were simply biased at a constant 15 V taken from the power supply leg of the operational amplifier; this avoided the need for a separate power and bias voltage supply for this array. (The Array B diodes [n-type silicon] required a positive bias voltage, but the Array C diodes [p-type silicon] required a negative bias voltage.) In the preamps for all the arrays, the signal current was converted to a voltage by the 1 MΩ feedback resistor across an Analog Devices AD-544 operational amplifier (PMI OP27 or OP37 op-amps worked equally well). This provides a gain of 1V/μA, so signal levels at the output of the preamplifier were typically a few volts for the central channels. (The profiles of chord-integrated signals were usually approximately Gaussian, similar to the temperature profile, with an e^{-1} width varying from 3 cm to 10 cm. This width depended strongly on the combination of plasma current and toroidal magnetic field confining the plasma [188].)

After the preamplifier stage, the signals were passed through twinax cables to amplifier modules with variable gains ranging from 1 to 400. By changing the amplifier gain the user could easily compensate for the different signal levels between array channels and provide adequate signal levels for digitization. (The digitizer input voltage limits were ±5 V.) A schematic of the two-stage amplifier circuit is shown in Fig. 3.15c. The frequency responses of the preamplifier and amplifier, determined using a sine wave input from a signal generator, are shown in Figs. 3.16a and 3.16b respectively. This figure shows that the overall response of the preamplifier/amplifier combination was constant up to about 20 kHz, depending on the amplifier gain. (In practice, we rarely run with any gains exceeding 25).

After amplification the signals were filtered by variable-frequency/variable-gain filters. These modules had high frequency (3db) cutoffs of 2, 4, 8, 20 and 40 kHz, and a variable gain of either ±1 or $\pm\frac{1}{2}$. The filter frequency was normally chosen to coincide with half the digitization frequency in order to satisfy the Nyquist sampling theorem and thereby reduce the chance of frequency aliasing.

The signal was converted from the analog output of the filter module to digital data by a DSP Technology Transiac Traq I system [189]. This system was capable of digitizing at a rate up to 100 kHz with 12-bit resolution. For normal TEXT runs, the signal was digitized at 20 kHz. This frequency was sufficient to resolve sawtooth and MHD activity because the sawtooth frequency ranges between 140 Hz and 1 kHz and the characteristic MHD frequency is ~5 kHz. For experiments designed specifically to study fast MHD oscillations, the data was digitized at 50 kHz.

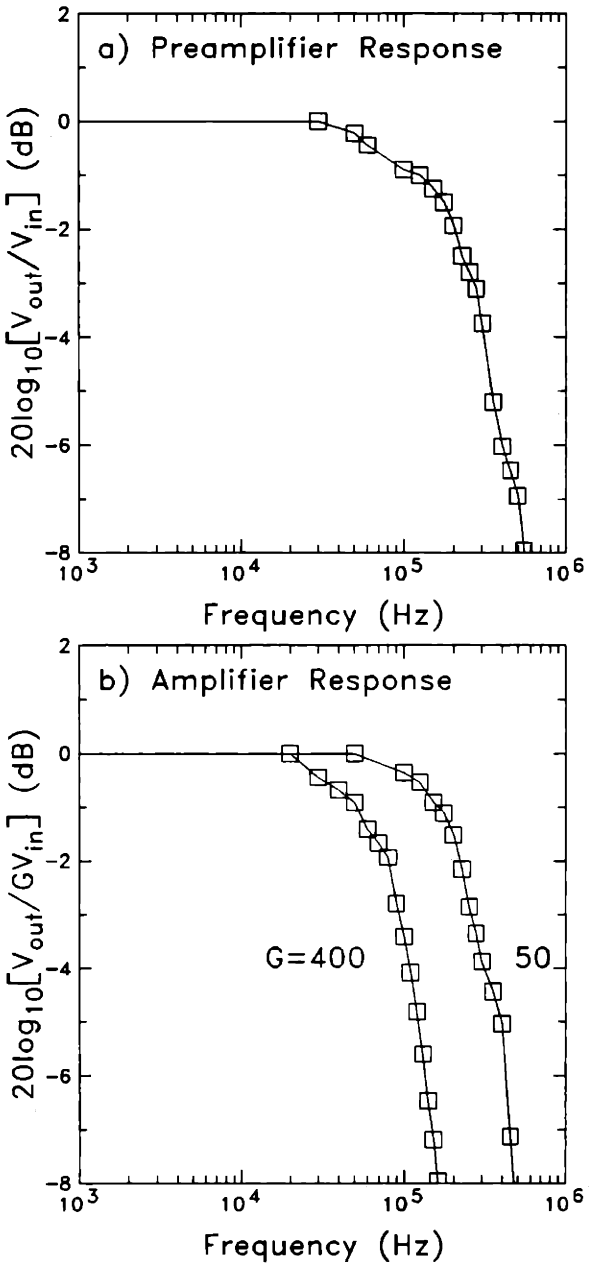

Figure 3.16: The frequency response of the electronics used for data processing was measured using a sine wave generator. a) The preamplifier response had a 3dB rolloff at ~250 kHz; and b) the amplifier response for gains of 50 and 400 had 3 dB rolloffs of ~ 250 kHz and 100 kHz respectively. Since the highest gain used was rarely above 25, the high frequency cutoff for all channels was always above 100 kHz.

As previously mentioned, each array was housed in a stainless steel box separated by a 25 μm thick beryllium window from the main vacuum of TEXT (nominally $\sim 10^{-8}$ torr after discharge cleaning [35,65]). This window was simply glued with Torr seal epoxy[11] over a narrow slit cut into each array's mounting flange. An advantage of separating the tokamak and array vacuums was that a dedicated pump was then unnecessary to maintain high vacuum in the array boxes. An additional advantage was that the boxes could be easily backfilled with various gases for use as x-ray filters. A specific example of this technique, using krypton as an x-ray filter, is described next.

3.3.2 Krypton Filtering and Preliminary Results

In order to measure the charge state distribution (chapter 4) and transport properties (chapter 5) of aluminum injected into TEXT, a set of filters was developed to discriminate between x radiation from the three highest charge states of aluminum. (He-like Al^{+11}, H-like Al^{+12} and fully stripped Al^{+13} are predicted in coronal equilibrium to be the predominant three charge states in plasmas with characteristic TEXT parameters [190].) The three main filters used for this purpose were Filter A, consisting of 4.6 mg/cm^2 Be alone; Filter G, consisting of 4.6 mg/cm^2 Be plus 1.52 mg/cm^2 krypton; and Filter D, consisting of 4.6 mg/cm^2 Be plus 30.5 mg/cm^2 carbon. (Another filter, designated Filter H, was sometimes used instead of Filter G. It was very similar to Filter G; see Appendix C.) The x-ray spectral response for all three of these filters is shown in Fig. 3.17. Filter A responded primarily to the strong $1s - 2p$ resonance transition lines from both He-like and H-like aluminum at 1.61 keV and 1.73 keV respectively. Filter G responded mostly to the He-like line at 1.61 keV because of the strong L-shell absorption edge in krypton that begins at 1.675 keV [160]. Thus this filter performed the quantitative discrimination between the He-like and H-like charge state densities. Filter D cut out all the lines of both the He-like (binding energy χ=2.09 keV) and H-like (χ=2.30 keV) states due to its low energy cutoff at about 3 keV. This filter was therefore responsive mainly to the continuum from radiative recombination into the ground state of the fully stripped aluminum [54].

Typical time histories of the central chord-integrated x-ray signals are shown in Fig. 3.18 for an ohmically heated discharge with a toroidal field B_T=2.8 T, plasma current I_p=320 kA, and a central line-averaged electron density $\bar{n}_e = 6.0 \times 10^{13}$ cm^{-3}. In this particular shot aluminum was injected, using the TEXT laser ablation system

[11] Torr seal (Varian)

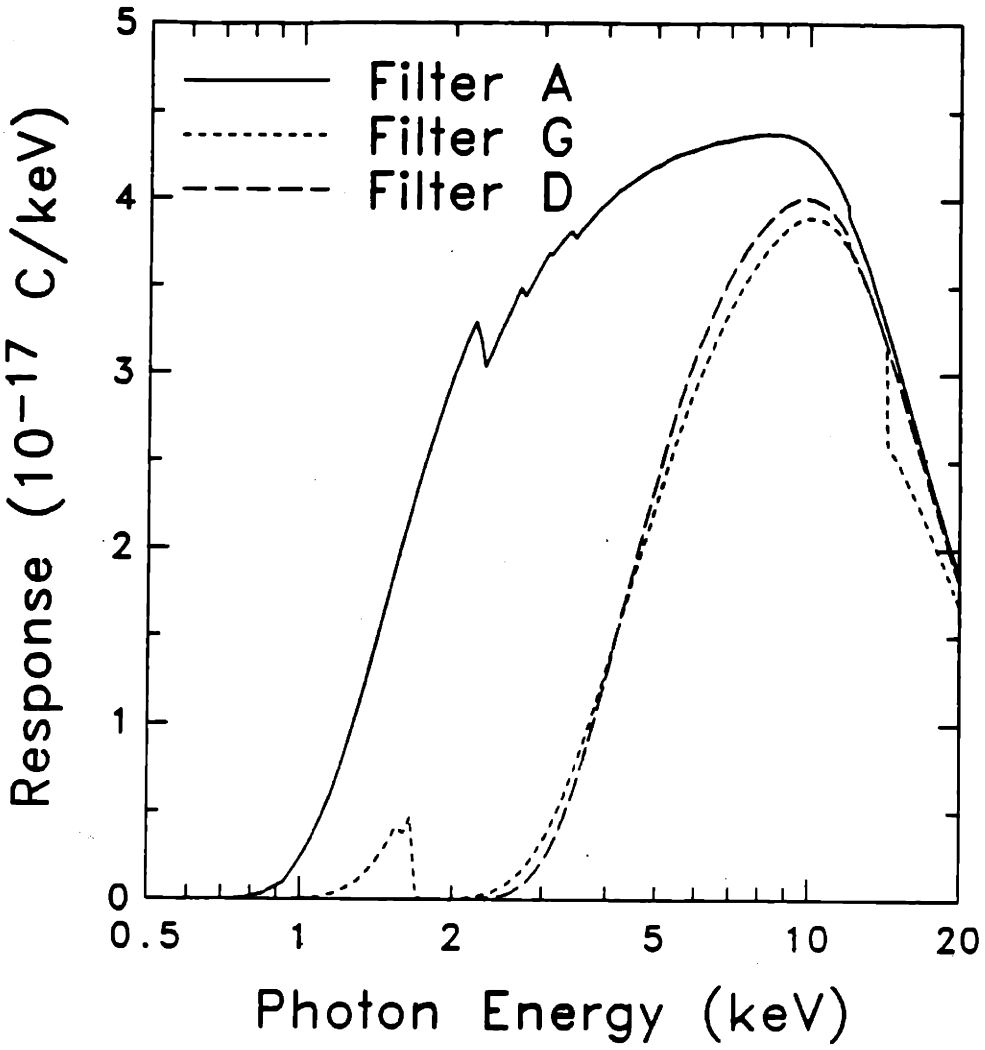

Figure 3.17: The response of the filter/detector combinations used for measuring the charge state distribution of injected aluminum are shown (also used for the data of Fig. 3.18). The low-energy response of the detectors was determined by the three different filters, and the high energy response was determined mainly by the physical thickness of the silicon detectors [155]. The three filters were comprised of 4.6 mg/cm^2 beryllium (Filter A); 4.6 mg/cm^2 beryllium and 1.52 mg/cm^2 krypton (Filter G); and 4.6 mg/cm^2 beryllium plus 30.5 mg/cm^2 carbon (Filter D). The low-energy cutoffs for Filters A and D were 1.0 and 3.0 keV respectively; Filter G had a small response between 1.3 and 1.675 keV, and then again above 3.0 keV. The strong absorption edge of Filter G at 1.675 keV discriminated between the He-like and H-like resonance lines of aluminum at 1.61 and 1.73 keV respectively. The higher energy cutoff of Filter D eliminates all the lines from these two states, so the response for this filter was mainly to the continuum recombination radiation from the fully stripped state [54].

[191], at 325 ms in order to study its charge state distribution and transport using the three differently filtered arrays described above. The three signals shown are from three differently filtered detectors all with lines of sight through the plasma center: one horizontal channel with only the beryllium window (Array B, Filter A), another horizontal channel with an additional 400 μm carbon (Array B, Filter D), and the central vertical channel with the 25 μm beryllium and 44.0 cm of krypton at a pressure of 7 torr (Array A, Filter G). Note that the response of Filter A to the aluminum is about 7 times that of Filter G and 100 times that of Filter D. This already shows, qualitatively, that the fully stripped state was not present in large amounts.

Radial brightness profiles taken at 372 ms during the same discharge, after subtracting the pre-injection signal levels, are shown in Fig. 3.19. The data from Array A (squares) is shifted outward with respect to the Array B data because of the normal horizontal shift of the plasma column (the Shafronov shift) [192] due to the toroidal plasma equilibrium. The imaging system thus gave a direct measurement of the position of the plasma center which has been used to correct magnetic measurements of the horizontal plasma position. There was no apparent vertical shift of the plasma as reflected by the profiles from Array B, and all the profiles from Arrays A and B appear nearly symmetric about their respective centers. An important conclusion regarding the degree of aluminum ionization that can be drawn from comparison of the shapes of the profiles taken with Filters A and G is that He-like aluminum was the dominant charge state in this discharge, because both filters gave profiles of nearly identical shape. If, on the other hand, the H-like state were dominant in the central hot region of the plasma the Filter G profile would be significantly broader than that from Filter A. This is because the He-like ions (again, the dominant contributor to the signal of Filter G) would be depleted in the central region. More quantitative analysis is presented in the next chapter.

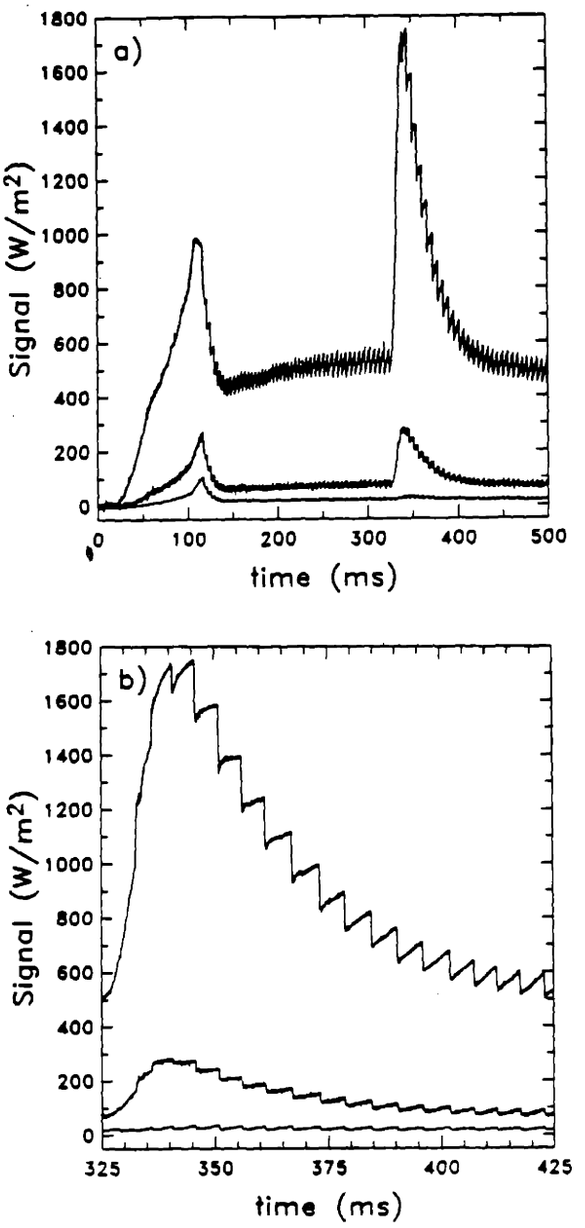

Figure 3.18: Data from a high-density TEXT shot from three differently filtered detectors viewing central chords through the plasma: an Array B channel with Filter A (top trace); an Array A channel with Filter G (middle trace); and an Array B channel with Filter D (bottom trace). (See Fig. 3.17 for the corresponding energy response curves.) a) Time traces throughout the entire discharge; and b) an expansion of the data around the injection at 325 ms clearly shows the characteristic sawtooth oscillations, and the strong effect of laser ablation of aluminum into the plasma for impurity transport studies.

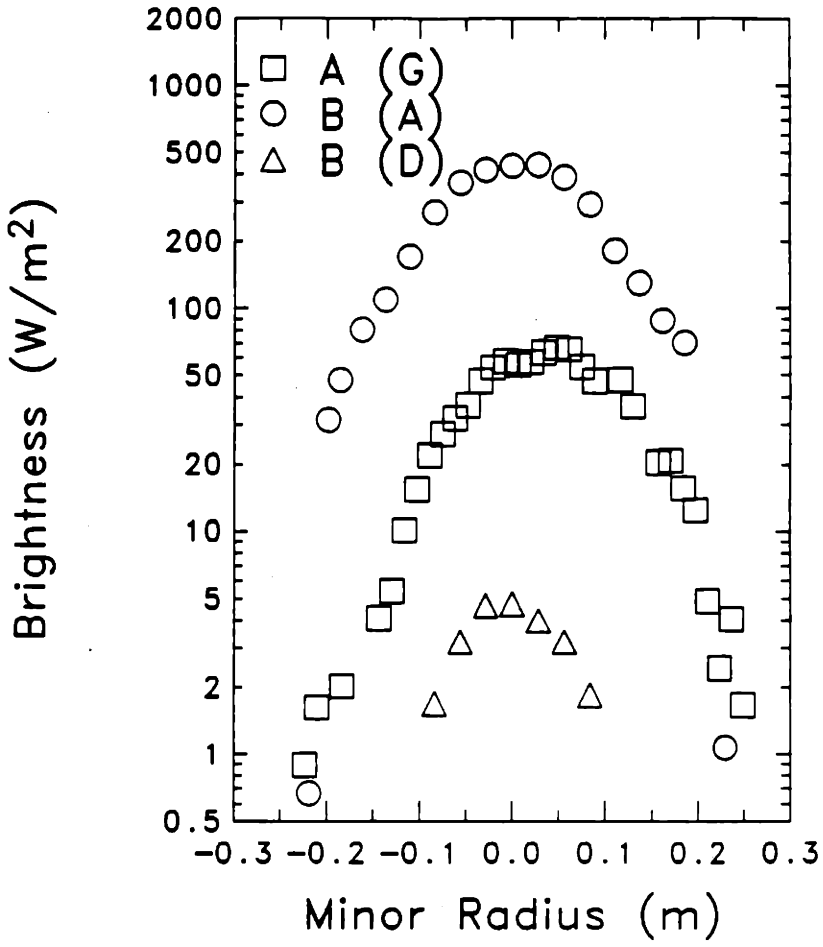

Figure 3.19: a) Brightness profiles taken at 372 ms of shot #144004, using the filters described in Fig. 3.17 (see also Fig. 3.18 for the time history of the central channel raw data). The first letter in the legend indicates the array used to take the data, and the letter in parentheses indicates the filter used. Note that the Array A profile is shifted outward due to the normal Shafronov shift, and all the profiles are nearly symmetric about their centers. The very small amplitude of the Filter D signal indicated qualitatively that the fully stripped density was small. Furthermore, the similarity in shape of the profiles from Filters A and G indicated that the He-like charge state was dominant in the plasma.

Chapter 4

Measurements of the Transport of Injected Aluminum in TEXT

4.1 Introduction

This chapter describes the experimental aspects of the impurity transport studies performed on TEXT. Aluminum was injected into TEXT in order to study the transport properties of a trace, non-recycling impurity. Aluminum confinement times were measured for many different discharges, and an approximate scaling formula for the confinement time in terms of some global parameters was developed from general trends in the data. A somewhat more accurate scaling in general agreement with the approximate result was established by performing a regression analysis on the data. Radial profiles of the ions averaged over a sawtooth period were also measured in several discharges using the three differently filtered x-ray arrays described in chapter 3. The charge state distribution profiles obtained from the density profiles were compared to the predictions of coronal equilibrium. Sawtooth-induced changes in the density profiles were found also for a few of the discharges. This chapter describes the method of data analysis to obtain the aluminum density profiles and discusses the results.

4.2 Experimental Method

4.2.1 Injection Techniques

Aluminum was injected into TEXT by one of two methods: laser ablation [171] or pellet injection [172,173]. The TEXT laser ablation system [191] uses a 5 J Q-switched ruby laser to ablate material from a glass slide approximately 61 cm below the plasma center. The injected particles were thus deposited primarily near the edge of the plasma with

some small inward velocity. In contrast, the TEXT impurity pellet injector system [193,194] can deposit impurities much farther into the plasma. The radial location of maximum material ablation depends on the Z of the material (more accurately, the heat of sublimation), the pellet size and velocity, and the plasma temperature and density. At the maximum attainable pellet velocity ($v_p \lesssim 250$ m/s), photographs of the pellet entering the plasma in low current, low density discharges indicated that aluminum ($Z = 13$) was deposited mostly near $12 \lesssim r \lesssim 14$ cm, about half way out from the plasma center (see Fig. 4.1). In more robust high current, high density discharges, the pellet was deposited mostly near $16 \lesssim r \lesssim 19$ cm (see Fig. 4.2).

Pellet injection had the advantage of smaller perturbations to the edge plasma than laser ablation of an equivalent number of particles, because the pellet did not begin to ablate significantly until it reached the hotter part of the plasma. However, laser ablation was capable of much smaller injections than that attained with pellets; the smallest cylindrical aluminum pellet was 0.005 in diameter by 0.007 in long ($\sim 5.4 \times 10^{17}$ atoms). In order for the x-ray arrays to see the injected aluminum from laser ablation, an amount comparable to these small pellets was injected. Soft x-ray signals after laser ablation and pellet injection in deuterium discharges are compared in Fig. 4.3. In this case the pellet injection was much bigger than the laser ablation. Note that in the pellet case the signal rose much more rapidly than in the case with laser ablation, but the ultimate decay of the two signals was the same.

4.2.2 Diagnostics

The primary diagnostic used for these measurements was the set of three differently filtered x-ray arrays described in chapter 3. Other plasma parameters were measured with some of the diagnostics listed in Table 1.1. The electron density profile was obtained with the TEXT six-channel far infrared interferometer system (FIR) [72]. The electron temperature profile was obtained with the Auburn ten-channel Electron Cyclotron Emission (ECE) grating polychromator [174]. The chord-integrated intensity of the $2s - 2p$ transition of the Li-like (Al^{+10}) aluminum ion at 568Å was monitored with a McPherson model 225 normal incidence monochromator 22.5° toroidally away from the laser ablation system. This monochromator was also used, during different discharges, to monitor lines from intrinsic impurities during Al injections. Temporal evolution of the raw data taken around the time of an injection from the x-ray arrays, the monochromator, the ECE system, and the FIR system are shown in Fig. 4.4.

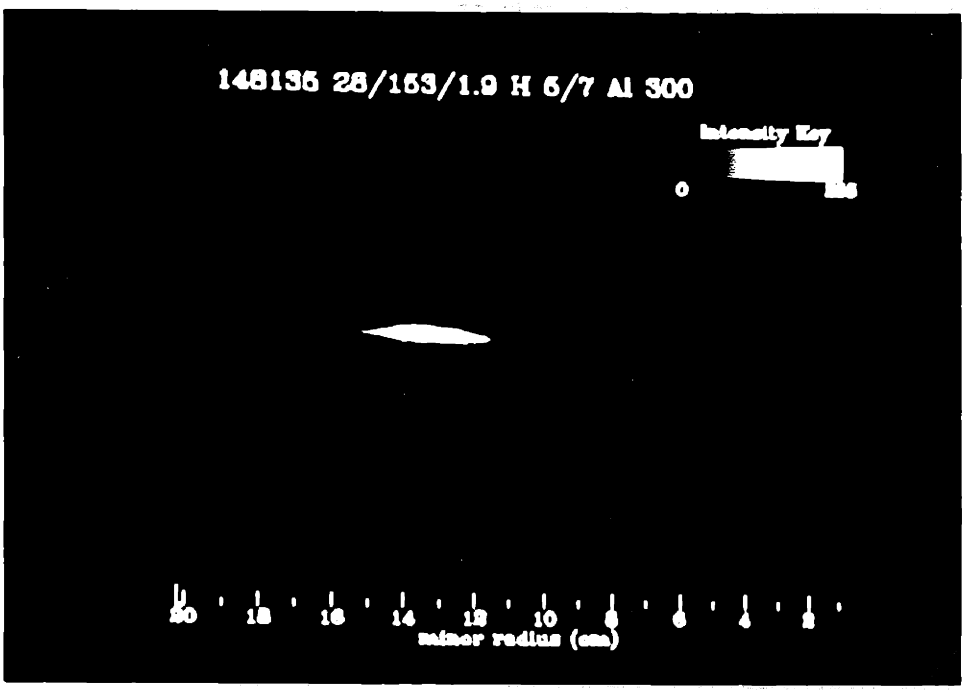

Figure 4.1: This photograph of an aluminum pellet shows that the pellet is deposited mostly near $r = 14$ cm in a discharge with $I_P = 153$ kA and $n_e = 1.9 \times 10^{13}$ cm^{-3}.

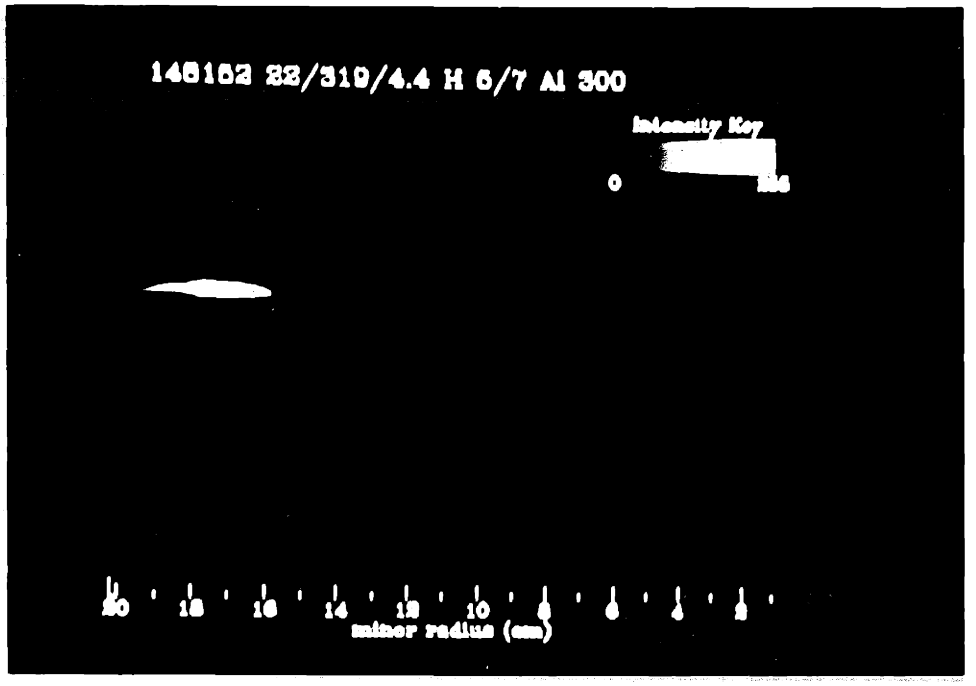

Figure 4.2: This photograph of an aluminum pellet shows that the pellet is deposited mostly near $r = 21$ cm in a discharge with $I_P = 319$ kA and $n_e = 4.4 \times 10^{13}$ cm^{-3}.

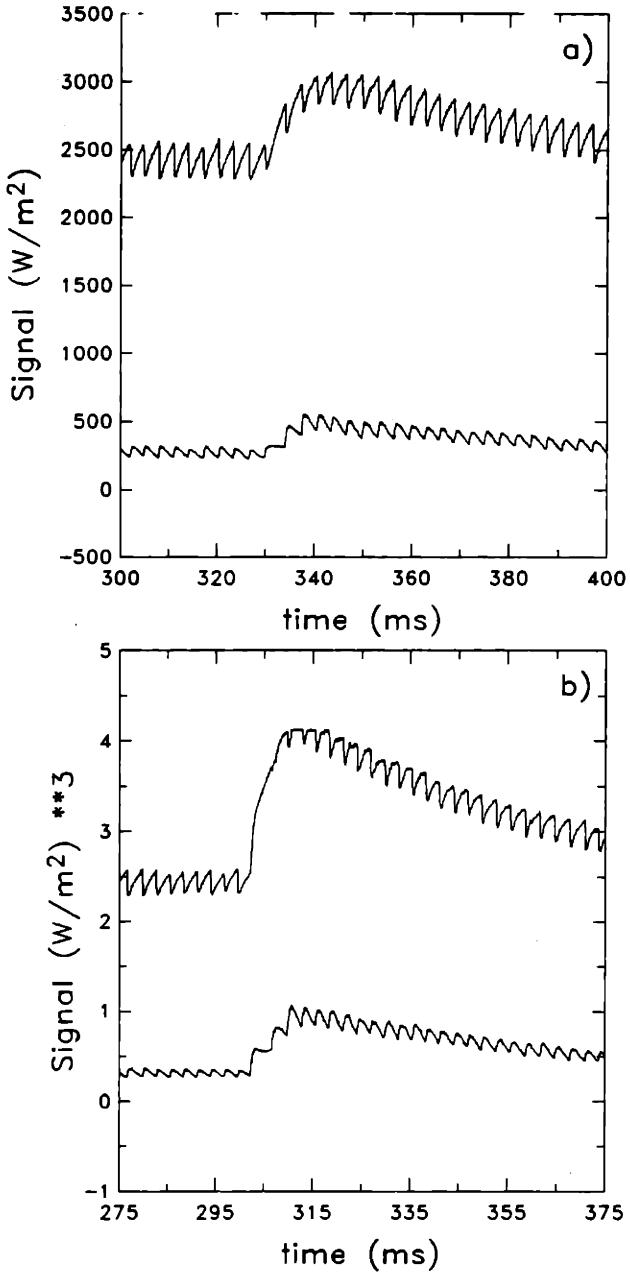

Figure 4.3: This figure compares some soft x-ray signals after laser ablation and pellet injection. The plasma conditions in both discharges were 2.8/320/4D. a) With laser ablation, at 325 ms, the initial rise was comparatively slow, peaking at about 18 ms after injection; b) With aluminum pellet injection, at 300 ms, the initial rise was quite fast, peaking after only about 10 ms, but the ultimate decay time of the signals obtained with either injection technique was the same. The two traces in each plot are the central filter A signal (top traces) and a filter A signal with chord radius equal to 15.4 cm.

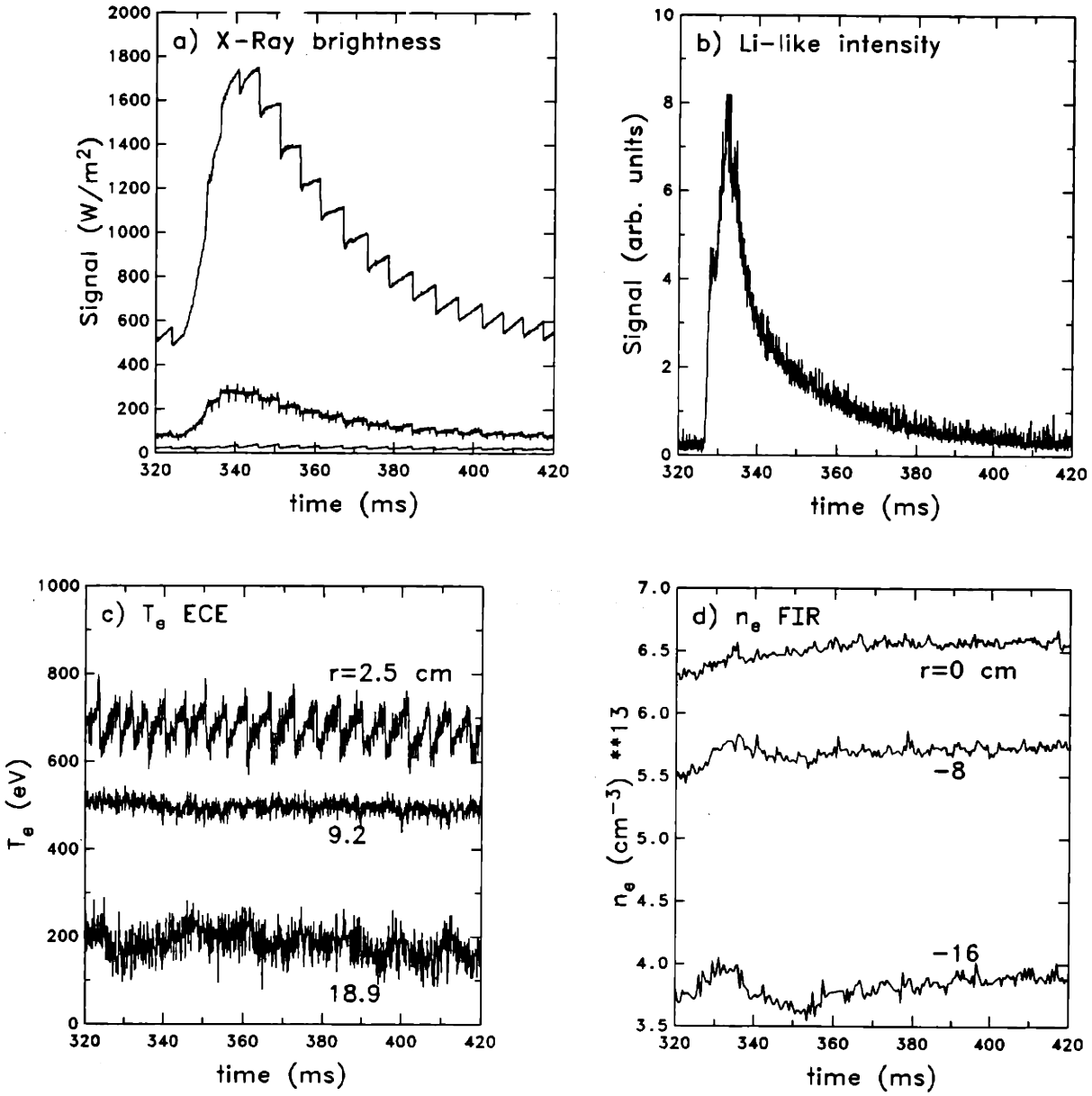

Figure 4.4: Temporal behavior of several signals during aluminum injection. Discharge conditions were $B_T = 2.8\ T$, $I_p = 320\ kA$ and $\overline{n}_e = 6\ \times 10^{13}$ cm^{-3} (2.8/320/6H), with injection at 325 ms. a) Three differently filtered x-ray detectors viewing central chords through the plasma. Filters A, G and D were used, as described in chapter 3. b) Li-like $2s - 2p$ intensity at 568 Å peaked after 5 ms and decayed rapidly thereafter. c) Three channels of the ECE temperature diagnostics at different radii. The perturbation due to the injection was very small. d) Three FIR density signals at different radii. Perturbations in the central chord-averaged electron density were kept below 5% during these injection experiments.

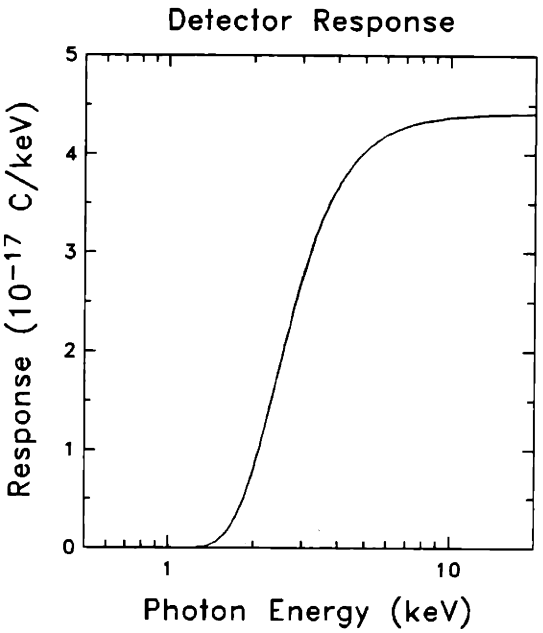

Figure 4.5: X-ray response function for the intrinsic germanium x-ray spectrometer system. The low energy response, fixed by a 5 mil beryllium window, had a low energy cutoff of about 2.2 keV.

Several other diagnostics were also used to measure quantities in support of this work. A ten-channel bolometer array [177] obtained profiles of the total radiated power. Changes in the radiated power profile due to the Al injections were very small. An intrinsic germanium x-ray spectrometer/pulse height analysis system obtained the x-ray spectrum every 20 ms. The low energy response of this system, determined by its 5 mil beryllium window, was about 2.2 keV (see Fig. 4.5). Thus the aluminum resonance lines at 1.62 and 1.73 keV could not be accurately resolved, nor could the recombination edge from fully-stripped aluminum at 2.3 keV. Finally, in some discharges the central ion temperature was obtained from a charge exchange neutral energy analyzer.

4.2.3 X-Ray Data Analysis

Aluminum density profiles were found from the x-ray data, the electron temperature profile, and the electron density profile. The starting point for the analysis was the solution of three equations describing the local x-ray emissivity measured with three different filters (A, G, and D):

$$\epsilon^A = n_e \left[n_{11} P_{11}^A(T_e) + n_{12} P_{12}^A(T_e) + n_{13} P_{13}^A(T_e) \right] \quad (4.1)$$

$$\epsilon^G = n_e \left[n_{11} P_{11}^G(T_e) + n_{12} P_{12}^G(T_e) + n_{13} P_{13}^G(T_e) \right] \quad (4.2)$$

$$\epsilon^D = n_e \left[n_{11} P_{11}^D(T_e) + n_{12} P_{12}^D(T_e) + n_{13} P_{13}^D(T_e) \right]. \quad (4.3)$$

The three unknowns, n_{11}, n_{12}, and n_{13}, are the He-like, H-like and fully-stripped aluminum densities respectively. ϵ^A, ϵ^G, and ϵ^D are the net local x-ray emissivities from aluminum measured using filters A, G and D described in chapter 3. The power functions P_j^k for filter k and ion j were calculated as described in chapter 2, and they are shown for filters A, G, and D in Appendix C.

The emissivity profiles were found by first subtracting the background x-ray brightness profiles, obtained prior to the injection, from the total profile obtained after the injection and then Abel inverting the net brightness profile. In some cases with very small brightness signals the x-ray profiles were Abel inverted then subtracted. The results from subtraction prior to inversion and inversion prior to subtraction are compared in Fig. 4.6. The uncertainty due to this procedure was the primary source of uncertainty in the measurement, and was largest for the filter D signal since it always had the smallest signal. Thus the density of the fully-stripped state was the least accurately known. (See Appendix D on Abel inversion.) It was important, when performing the subtraction of the background brightness profile, to be aware of the phase of the sawtooth oscillation. The brightness profile could change shape drastically during the sawtooth crash (especially for very low q_a discharges), so for example subtraction of a background profile obtained just before a sawtooth crash from a total profile obtained just after a sawtooth crash would lead to an erroneously hollow net brightness profile.

Another correction was required before background subtraction. This was to properly take into account the small increase in the electron density due to the injection. The increasing density caused enhanced background radiation because the x-ray emissivity from all species is proportional to n_e (*e.g.*, see Eqs. 2.3 and 2.6). Thus the background brightness profile was multiplied by $(1 + \Delta\bar{n}_e/\bar{n}_e)$ before performing the background subtraction. $\Delta\bar{n}_e$ was the change in the central chord averaged electron density. The three central-most interferometer chords typically gave values of $\Delta\bar{n}_e/\bar{n}_e$, in agreement within about 1% (*e.g.*, the FIR chord at -8 cm might give $\Delta\bar{n}_e/\bar{n}_e = 4\%$; that through the plasma center, 5%; and that at +8 cm, 3%). This introduces another uncertainty in the emissivity profiles. Again the uncertainty was largest in the filter D signals.

Most profiles shown in this chapter were averaged over one sawtooth period; therefore the proper background subtraction procedure was to average both the total and

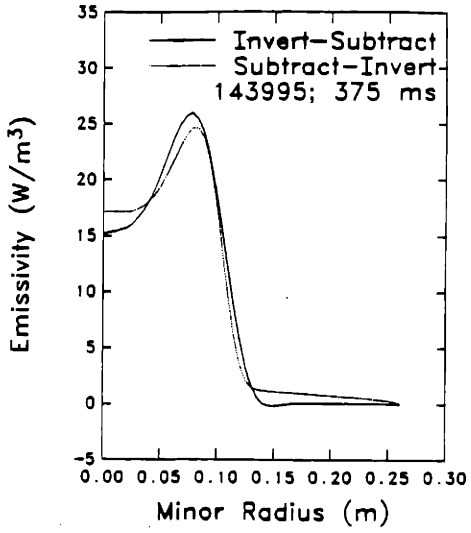

Figure 4.6: The emissivity profiles from filter D have been obtained by either Abel inverting then subtracting the background (solid line) or by subtracting the background then Abel inverting (dashed line). The resultant uncertainty is $\lesssim$ 10% inside 11 cm, but increases to $\gtrsim$ 50% between 11 and 15 cm.

background profiles over a sawtooth period. However, in cases where changes in the density profile during the sawtooth oscillation were of interest, the background subtraction was somewhat more difficult. To alleviate this problem a sawtooth-phase-locked background subtraction algorithm was developed. The method worked as follows. A particular single sawtooth period was chosen and then the signal from that period was subtracted from all other sawtooth periods on the same data channel. The sawtooth crash times were determined using a reference channel (normally the hard-filtered central x-ray channel). The time derivative of this signal was calculated, and those times when the derivative exceeded a threshold value chosen by the user were defined to be the sawtooth crash times. For example, Fig. 4.7 shows the central hard-filtered x-ray signal and its time derivative for a typical discharge with aluminum injection at 325 ms. In this case the threshold for sawtooth detection would be set at about -0.4 (in order to pick up the smallest sawtooth at 332 ms), and the background sawtooth period would normally be chosen to be that between 316.15 and 321.7 ms, because this was the last complete sawtooth period prior to the impurity injection. The algorithm then stepped through all active x-ray channels for the particular discharge and subtracted the background sawtooth. Fig. 4.8 shows the central x-ray brightness evolution from filter A

(the soft filter) before and after application of this sawtooth-phase-locked background subtraction. This procedure was also used to obtain all time dependent brightnesses for comparison to numerical transport simulations in chapter 5.

The final result of background subtraction and Abel inversion was a set of three emissivity profiles. Figs. 4.9–4.11 show net emissivity profiles, and the brightness profiles from which they were calculated, for a TEXT discharge with aluminum injection. The solid lines in the brightness profile plots were obtained by integration of the emissivity profile. The agreement was good for all three filters.

With the x-ray emissivity profile and the electron temperature and density profiles, Eqs. 4.1–4.3 could be solved to obtain an initial estimate of the aluminum charge state densities. The method of solution took advantage of the unique filter combination used in these experiments. The relative error for all three filters was defined as

$$\Delta^A \equiv \left[\epsilon^A - n_e\left(P^A_{11}n_{11} + P^A_{12}n_{12} + P^A_{13}n_{13}\right)\right]/\epsilon^A \tag{4.4}$$

$$\Delta^G \equiv \left[\epsilon^G - n_e\left(P^G_{11}n_{11} + P^G_{12}n_{12} + P^G_{13}n_{13}\right)\right]/\epsilon^G \tag{4.5}$$

$$\Delta^D \equiv \left[\epsilon^D - n_e\left(P^D_{11}n_{11} + P^D_{12}n_{12} + P^D_{13}n_{13}\right)\right]/\epsilon^D. \tag{4.6}$$

Eqs. 4.1–4.3 were then solved with three constraints: first, none of the aluminum densities were allowed to become negative; second, the sum of the relative errors squared was minimized; and third, the relative error for all three filters was less than 10%. In some cases these constraints could not all be satisfied; usually because the filter D signal was too low. When this occurred, the fully stripped density was assumed to be zero and Eqs. 4.1 and 4.2 were straightforwardly solved to obtain n_{11} and n_{12}.

The direct solution of Eqs. 4.1–4.3 yields only an initial approximation for the aluminum density because in some situations this solution is not very accurate. Specifically, for temperatures below about 450 eV, the solution to the three emissivity equations becomes extremely sensitive to small changes in measured emissivities and the x-ray power functions (see Appendix F). The underlying physical reason for this behavior was that the contribution to the krypton filter signal from the H-like state increased strongly with decreasing temperatures because of line radiation following recombination into excited levels (see Sec. 2.3.4). This process effectively made H-like ions act as a source of the He-like resonance line, so the filter combination could no longer effectively discriminate between the H-like and He-like charge state densities. (In essence, the contrast between the two imaging systems was degraded for temperatures below 450 eV. Unfortunately in many TEXT discharges about half the plasma was in this temperature range.)

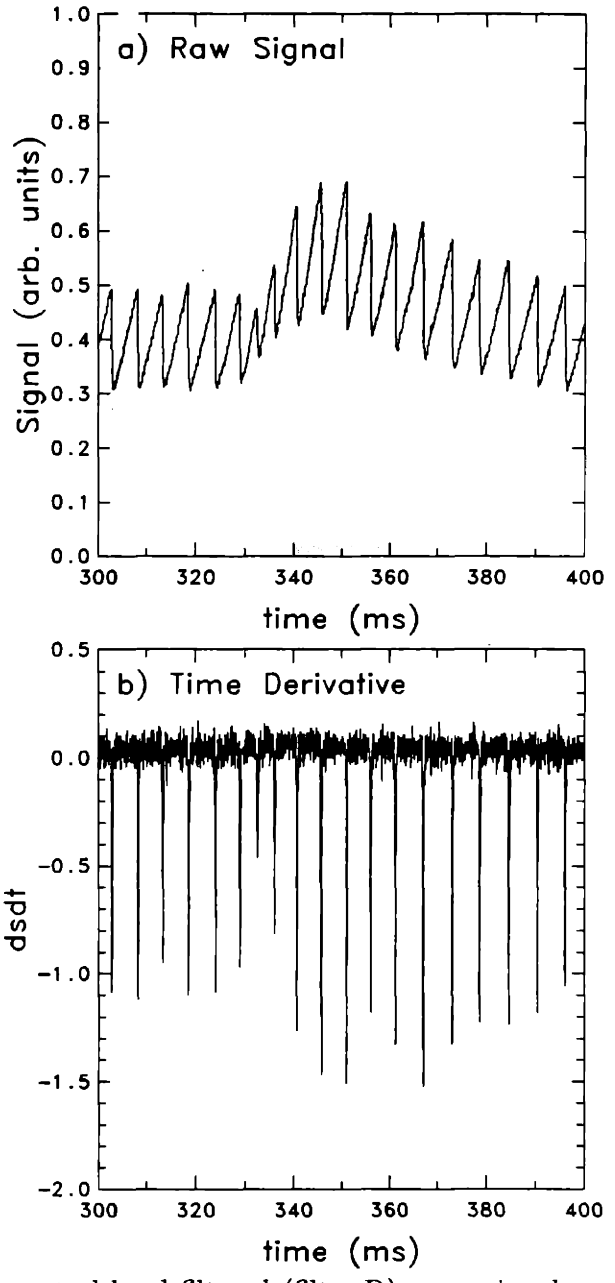

Figure 4.7: The central hard filtered (filter D) x-ray signal was normally used to determine the sawtooth crash times, because it typically had the smallest overall change due to the impurity injection. It also often had the largest sawteeth relative to its total signal because of the strong temperature sensitivity of the radiative recombination to which it is most responsive. a) The central filter D signal during the same shot shown in Fig. 4.4; and b) its time derivative, clearly showing large negative spikes used to define the sawtooth crash times.

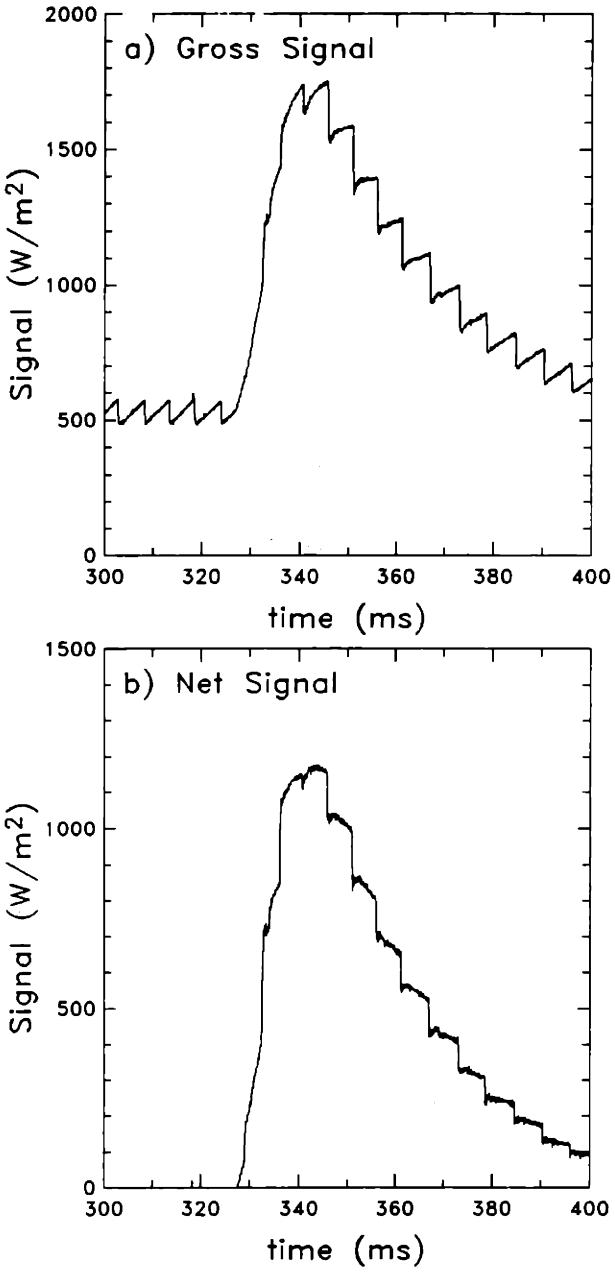

Figure 4.8: The evolution of the soft x-ray brightness profile from filter A (the soft filter) a) before and b) after sawtooth phase-locked background subtraction.

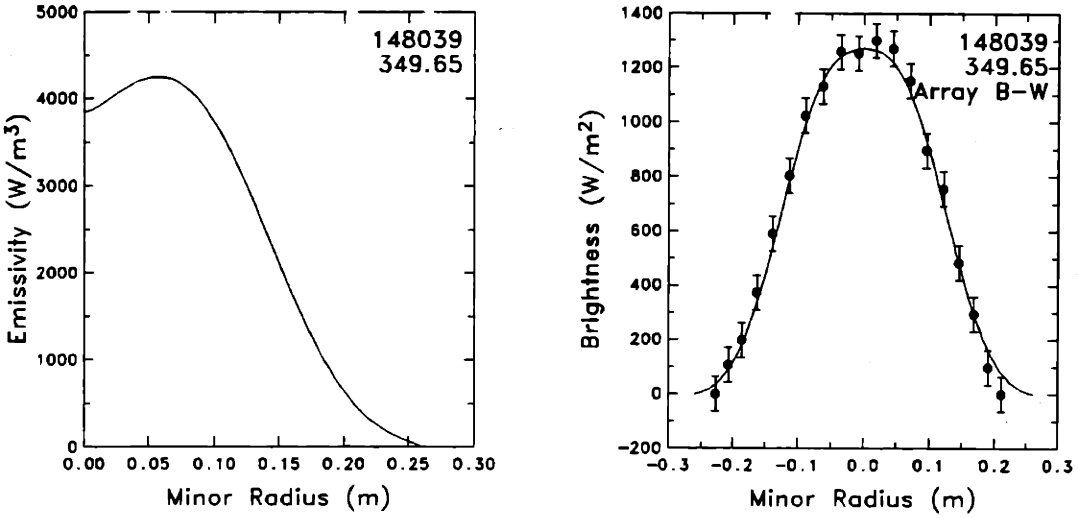

Figure 4.9: a) The emissivity profile from filter A obtained around 350 ms during TEXT shot 148039, about 25 ms after aluminum laser ablation and averaged over a single sawtooth period. b) The brightness profile used to obtain the emissivity in a). The solid line is the result of reintegrating the emissivity in a).

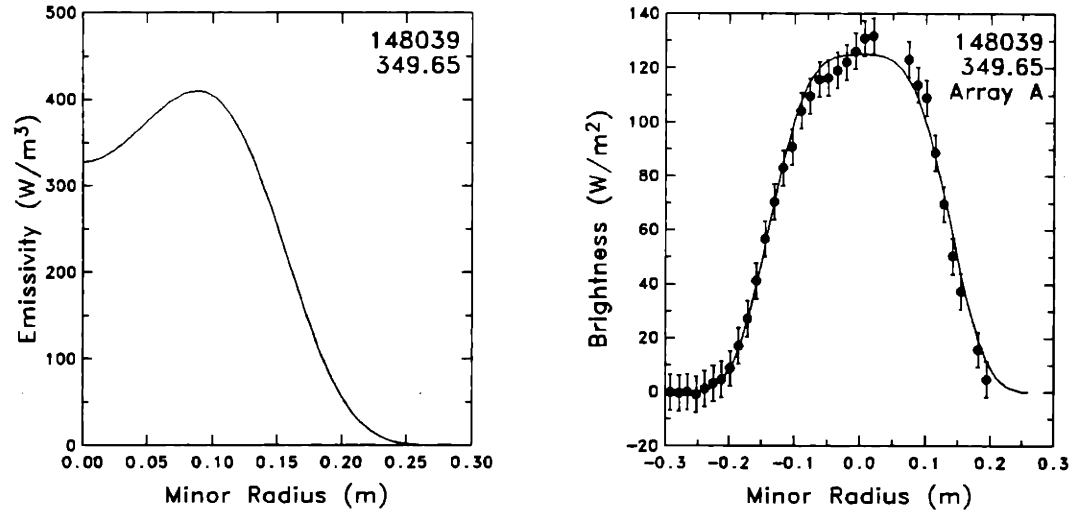

Figure 4.10: a) The emissivity profile from filter G obtained around 350 ms during TEXT shot 148039, about 25 ms after aluminum laser ablation and averaged over a single sawtooth period. b) The brightness profile used to obtain the emissivity in a). The solid line is the result of reintegrating the emissivity in a).

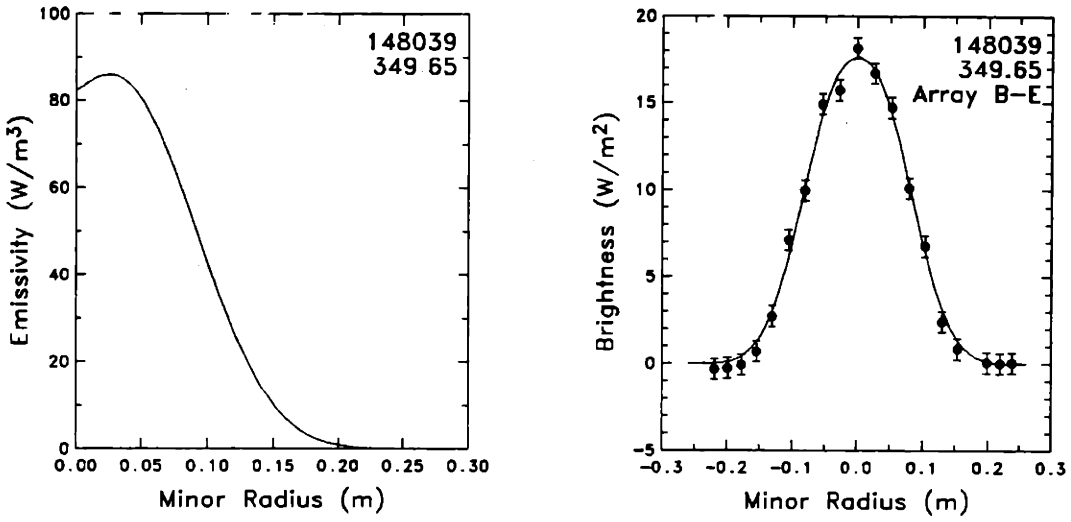

Figure 4.11: a) The emissivity profile from filter D obtained around 350 ms during TEXT shot 148039, 25 ms after aluminum laser ablation and averaged over a single sawtooth period. b) The brightness profile used to obtain the emissivity in a). The solid line is the result of reintegrating the emissivity in a).

An aluminum density profile obtained by simply solving the three emissivity equations is shown in Fig. 4.12. This discharge was run with conditions 2.8/160/3H. The resultant aluminum profile was centrally peaked, but increased outside $r \simeq 10$ cm, where the temperature was about 450 eV. This increase in the outer plasma was characteristic of most aluminum density profiles obtained by direct solution of the three equations. In an effort to understand this behavior, other potential sources for large x-ray emissivity in the outer plasma were examined.

One possible source of large x-ray signals in the colder plasma is charge exchange recombination into upper levels. In this process a neutral hydrogen atom gives its electron to another ion:

$$H^0 + A^{+Z} \longrightarrow H^{+1} + A^{+Z-1}. \tag{4.7}$$

If the electron is captured in a quantum state other than the ground state, the resultant ion can de-excite by emitting a photon, directly analogous to line radiation following recombination into upper levels described in Sec. 2.3.4. In the case of fully-stripped aluminum, the emissivity radiated by this process can be expressed as

$$\epsilon_{CX} = \sum_i \sum_j n_{H^0} n_{13} < \sigma v >_{CX,i} E_j, \tag{4.8}$$

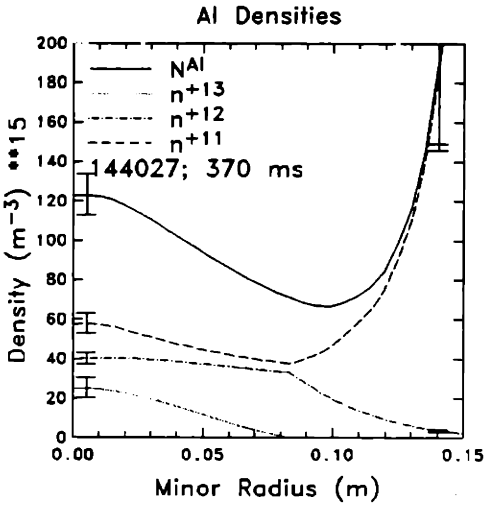

Figure 4.12: The aluminum density profile for a high q_a shot was determined by simply solving Eqs. 4.1–4.3. Note the strong increase in density outside of $r \simeq 10$ cm.

where n_{H^0} is the neutral hydrogen density and E_j represents all the possible transitions after the electron has been captured into the state i. The reaction rate $< \sigma v >_{CX}$ is obtained by averaging the cross section over a Maxwellian velocity distribution,

$$< \sigma v >_{CX} = \frac{\int_0^\infty \sigma(v) v f(v) v^2 \, dv}{\int_0^\infty f(v) v^2 \, dv}, \tag{4.9}$$

and $f(v)$ is taken from Eq. 2.2. To estimate the importance of charge exchange recombination for the x-ray power, the neutral hydrogen density was calculated using the neutral transport code ANTIC [195]. The neutral source was modeled by assuming neutrals were born at the limiter and the wall with energies of either 1 or 10 eV, and the total magnitude of the source was chosen to match the source measured with H_α diagnostics [196]. The measured electron density and temperature profiles were also used in the calculation of the neutral particle transport. The calculated neutral particle density is shown in Fig. 4.13. The charge exchange cross section was obtained from Ref [197]. To approximate the x-ray power from charge exchange recombination, two simplifying assumptions were made: first, the total cross section $\sigma(v)$ was assumed to be independent of velocity and equal to its maximum value $\sigma_{CX}^{max} \simeq 1.5 \times 10^{-19}$ m^2; and second, all charge exchanges with fully stripped aluminum were assumed to generate a photon with the same energy as the H-like resonance transition. The first of these assumptions implies that the calculation for the reaction rate in Eq. 4.9 will provide

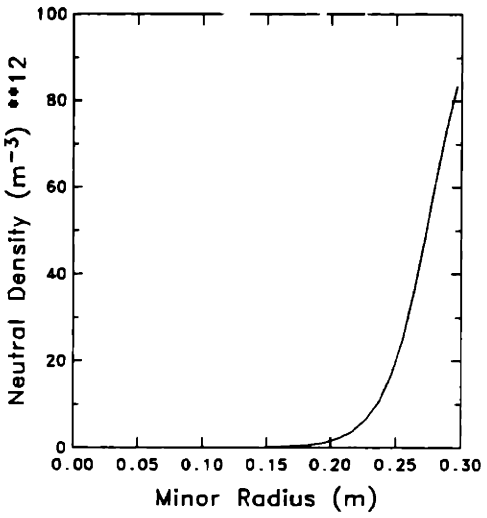

Figure 4.13: The total density of neutral hydrogen was calculated using the ANTIC neutral transport code [195].

an upper limit for the total charge exchange reaction rate because the cross section actually decreases with increasing relative velocity. The second assumption implies that all captured electrons eventually make the transition from the $n = 2$ level to the $n = 1$ level. This assumption will also overestimate the x-ray power from this process because some electrons captured in elevated levels ($n \geq 3$) will be removed by collisions before they can cascade down to the $n = 2$ level, and other electrons may be captured in the ground state, and thus will not yield any line radiation. The charge exchange x-ray emissivity obtained here is therefore an upper bound.

The charge exchange recombinatio rate from Eq. 4.9 is now given by $< \sigma v >_{CX} = 2\sigma_{CX}^{max} v_{th,i}/\sqrt{\pi} = \sigma_{CX}^{max}\sqrt{8T_i/\pi m_i}$, and the resultant x-ray emissivity is

$$\epsilon_{CX} = n_{H^0} n_{13} h\nu \sigma_{CX}^{max} \sqrt{8T_i/\pi m_i} \tag{4.10}$$

where $h\nu$ is the resonance line energy (1.73 keV for H-like aluminum). For example at $r \simeq 15$ cm in a high density, high current discharge, $n_{H^0} \simeq 3 \times 10^{11}$ m^{-3} and $T_i \simeq 150$ eV, so $\epsilon_{CX} = 2.4 \times 10^{-18} n_{13}$ (m^{-3}) Wm^{-3}. The measured soft filter emissivity at this location after an aluminum injection is typically 1000 Wm^{-3}. If this emissivity were only from charge exchange recombination, it would require a fully stripped aluminum density of 4.2×10^{20} m^{-3}, about 40 times the electron density.

It is informative to write the charge exchange power in the form of an x-ray power

function for comparison with the x-ray power functions found in chapter 2 and Appendix C. Note the x-ray emissivity is usually written in terms of the power function as $\epsilon = n_e n_i P_i(T_e)$. By comparing Eq. 4.10, the effective charge exchange recombination power function can be written

$$P_{CX} = \left(\frac{n_{H_0}}{n_e}\right) h\nu\sigma_{CX}^{max} \left(\frac{8T_i}{\pi m_i}\right)^{1/2}. \tag{4.11}$$

In this case, the power function depends on the ion temperature, not the electron temperature. At an ion temperature of 100 eV and $n_{H_0}/n_e = 5 \times 10^{-9}$ (typical TEXT value), $P_{CX} = 3.2 \times 10^{-38}$ Wm^3. For comparison the filter A power function for fully stripped aluminum at $T_e = 100$ eV is 1.45×10^{-33} Wm^3, more than four orders of magnitude larger. Furthermore, if the charge exchange contribution to the x-ray signal were dominant, one might expect the x-ray brightness to increase in the outermost channels because the quantity n_{H_0}/n_e increases very rapidly in the outer part of the plasma (see Fig. 4.13). Thus based on the calculation of an upper bound for P_{CX} and the fact that the x-ray brightness levels decrease toward the plasma edge, the conclusion is that charge exchange contributes negligibly to the x-ray signals in TEXT.

Another possible cause for large x-ray signals in the outer plasma is the finite viewing volume of the x-ray detectors. Since there are radial temperature and density gradients in the plasma, the finite swath of a viewing chord is weighted somewhat toward the plasma center, where the x-ray emissivity tends to be larger. This effect would tend to move the effective impact radius of each chord inward, essentially peaking the brightness profiles. Thus if this effect were significant and not properly taken into account, the Abel inverted emissivity profiles would be broader than the true profile, and the resultant impurity density profiles would also be inaccurately large for large minor radii.

To determine the importance of this effect for TEXT, the effective impact radii of the soft-filtered x-ray channels were varied numerically, and the resultant emissivity profiles were compared. Fig. 4.14 compares inversions from three cases: 1) the chord radii were moved inward by 0.0125 m (about half the swath width); 2) the chord radii were held at the original positions; and 3) the chord radii were moved outward by 0.0125 m. The emissivity obtained from the most peaked brightness profile was also the most peaked, as expected, but the emissivity near 0.15 m only decreased by $\sim$ 25%, not a large amount. The amount of the radial shift used for this calculation, 0.0125 m, was chosen arbitrarily. A more accurate value for this shift was therefore sought from the measured emissivity profiles. An effective chord shift was calculated by weighting the

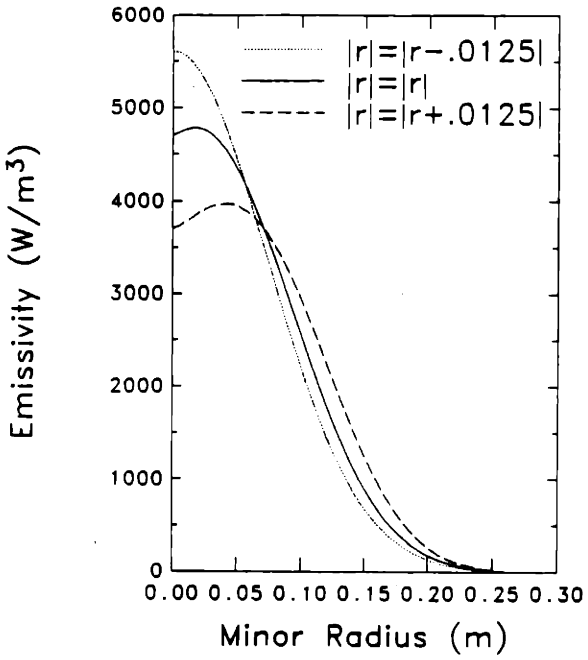

Figure 4.14: The Abel inverted x-ray emissivity profiles from three different inversions are shown. The peaked profile (dotted) was inverted from data moved inward by 0.0125 m, the solide profile was from an inversion using the actual impact chords, and the hollow (dashed) profile resulted from an inversion with the chords moved outward by 0.0125 m. The emissivity at $r = 0.15$ m changed by less than 50%.

local radius with the measured emissivity from case 2) above, so that

$$p_{eff} = \frac{\int_{p-\Delta p}^{p+\Delta p} \epsilon(r) r \, dr}{\int_{p-\Delta p}^{p+\Delta p} \epsilon(r) \, dr}, \tag{4.12}$$

where p is the impact radius and Δp is the swath half-width.

The calculated shift for each radius, $p_{eff} - p$, is shown in Fig. 4.15. The shift of the chord radii was smaller than 0.004 m across the entire plasma. This implies that the comparison in Fig. 4.14 gives an extreme upper bound on the change in emissivity due to the finite swath width effect since it assumed a shift three times the maximum value. The conclusion from this discussion is that the finite spatial resolution of the system did not artificially enhance the x-ray emissivity in the outside of the plasma.

Thus the large x-ray signals beyond $r \simeq 10$ cm were assumed to be real and due to those atomic processes described in chapter 2. However the large aluminum density obtained in this region by direct solution of Eqs. 4.1–4.3 was probably specious, because

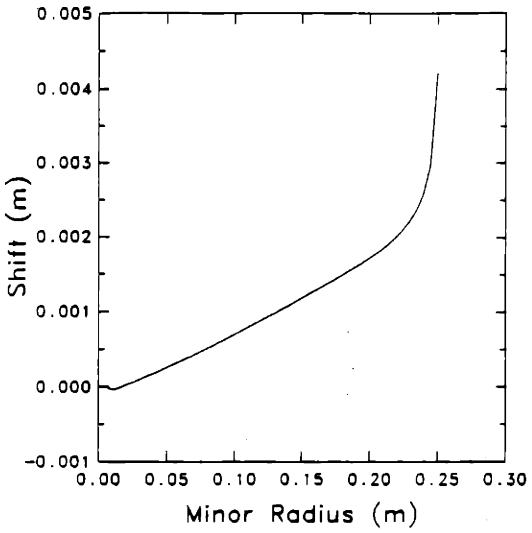

Figure 4.15: The shift of the viewing chord radius was calculated using Eq. 4.12. The important result was that the maximum shift was less than .004 m.

it would imply a tremendous change in Z_{eff} outside of $r \simeq 0.15$ m (*e.g.*, in the case of Fig. 4.12 $\Delta Z_{eff} \gtrsim 2.5$ for $r \gtrsim 0.155$ m). Such a large change in Z_{eff} should significantly change the temperature profile, probably enough to disrupt the plasma. This was not observed in the experiments. The large upturn in impurity density was thus thought to be due to the lack of contrast in the imaging system.

To overcome the contrast problems in Eqs. 4.1–4.3 aluminum density profiles without large densities in the edge region were sought. The x-ray brightness profiles were calculated from modeled aluminum density profiles for comparison to the measured brightness profiles. The aluminum density profiles were parameterized in the form[1]

$$n(r) = n_0(1 - (r/a)^2) \exp\left[-\left(c_1(r/a)^2 + c_2(r/a)^4\right)\right]. \tag{4.13}$$

The solution obtained from Eqs. 4.1–4.3 was used as an initial guess, and subsequently the fit parameters n_0, c_1 and c_2 were varied until good agreement with the experimental data was obtained. In some cases this model allowed the extremely large edge aluminum densities to be avoided, but in others slightly hollow aluminum profiles were still required to match the data. Several profiles obtained in this manner are exhibited in the next section.

[1]This is the same functional form used for density and temperature profiles in E. A. Chaniotakis' work on variational transport codes [E. A. Chaniotakis, private communications, 1989].

4.3 Experimental Results

Using the x-ray imaging system described in chapter 3, four facets of the injected aluminum transport were measured the impurity confinement time, sawtooth period-averaged aluminum density profiles, the charge state distribution of aluminum ions near the plasma center, and sawtooth-induced changes in the aluminum density profiles. Two empirical scalings for the impurity confinement time were constructed from these measurements in several different types of discharges (see Table 4.1). One scaling was based simply on general trends in the data, and the other was obtained by performing a regression analysis on the data. The two results were in good agreement. Aluminum density profiles averaged over a sawtooth period were measured during several of the same discharges. The resultant aluminum charge state distribution was then compared to the predicted charge state distribution under the assumption of coronal equilibrium, and the effect of sawteeth on the charge state profile was examined. Finally, changes in the absolute density profiles during sawtooth crashes were found for a few discharges. The results of these measurements are described in the next four sections.

Before presenting these results, some nomenclature should be introduced. TEXT discharges were typically described in terms of the nominal values of the toroidal magnetic field, the plasma current, and the central line averaged electron density and the working isotope. A shorthand notation will be used henceforth to describe these TEXT parameters in units of T, kA, and 10^{19} m^{-3}. For example, a hydrogen discharge with B_T=2.8 T, I_P= 160 kA, and $\bar{n}_e = 2.0 \times 10^{19}$ m^{-3} will be denoted as 2.8/160/2.0H.

4.3.1 Aluminum Ion Confinement Time Scalings

In an effort to understand the dominant transport mechanisms operative for impurity ions in TEXT, and for comparison with previous impurity transport studies [34,38,65], the aluminum confinement time was measured under several different plasma conditions. The main parameters varied were the electron density, the plasma current, the background gas, and the plasma cleanliness. The tokamak geometry (R_0 and a) was not varied in this study.

Table 4.1:
Discharge Parameters for Aluminum Confinement Time Scaling

Shot	B_T (T)	I_P (kA)	$\bar{n}_e$ (10^{19} m^{-3})	Z_{eff}	Z_i	m_i (amu)	τ_c (ms)	q_a
143027	2.8	320	4.8	1.28	1.0	1.0	24.2	2.60
143030	2.8	320	4.2	1.23	1.0	1.0	21.2	2.65
143032	2.8	320	4.2	1.28	1.0	1.0	21.9	2.65
143033	2.8	320	4.3	1.28	1.0	1.0	22.4	2.65
143039	2.8	320	4.4	1.23	1.0	1.0	22.7	2.65
143046	2.8	320	5.7	1.22	1.0	1.0	29.7	2.70
143047	2.8	320	5.9	1.18	1.0	1.0	29.8	2.70
143048	2.8	320	5.8	1.22	1.0	1.0	29.0	2.70
143052	2.8	320	5.9	1.25	1.0	1.0	33.2	2.70
143053	2.8	320	5.9	1.25	1.0	1.0	30.2	2.65
143054	2.8	320	6.2	1.25	1.0	1.0	29.6	2.70
143055	2.8	320	6.1	1.30	1.0	1.0	30.4	2.70
143058	2.8	320	5.8	1.30	1.0	1.0	29.1	2.65
143059	2.8	320	6.1	1.30	1.0	1.0	30.1	2.70
143062	2.8	320	5.9	1.30	1.0	1.0	31.2	2.70
143079	2.8	320	2.8	1.88	1.0	1.0	19.6	2.72
143105	2.8	320	2.2	2.14	1.0	1.0	20.4	2.75
143117	2.8	160	2.0	1.39	1.0	1.0	18.6	5.40
143118	2.8	160	2.1	1.39	1.0	1.0	19.9	5.25
143124	2.8	160	1.9	1.39	1.0	1.0	18.2	5.45
143309	2.8	240	2.3	2.15	1.0	1.0	29.4	3.63
143310	2.8	240	2.2	2.15	1.0	1.0	26.0	3.65
143311	2.8	240	2.3	2.15	1.0	1.0	26.8	3.60
143312	2.8	240	2.3	2.09	1.0	1.0	31.7	3.57
143313	2.8	240	2.2	2.15	1.0	1.0	28.5	3.58
143314	2.8	240	2.1	2.04	1.0	1.0	28.3	3.60
143315	2.8	240	2.2	2.04	1.0	1.0	29.2	3.53
143317	2.8	240	2.1	2.09	1.0	1.0	31.1	3.62
143322	2.8	240	2.9	2.05	1.0	1.0	34.4	3.50
143328	2.8	240	3.2	1.94	1.0	1.0	34.4	3.40
143329	2.8	240	3.0	2.11	1.0	1.0	33.3	3.20
143331	2.8	240	3.0	2.11	1.0	1.0	38.5	3.30
143333	2.8	240	3.0	2.00	1.0	1.0	30.9	3.55
143354	2.8	160	1.2	2.69	1.0	1.0	20.4	5.30
143355	2.8	160	1.1	2.55	1.0	1.0	18.6	5.40
143357	2.8	160	1.2	2.55	1.0	1.0	24.5	5.27
143362	2.8	160	1.2	2.52	1.0	1.0	21.1	5.10
143366	2.8	160	1.1	2.66	1.0	1.0	23.8	5.20
143367	2.8	160	1.1	2.62	1.0	1.0	23.3	5.45

Shot	B_T (T)	I_P (kA)	n_e (10^{19} m^{-3})	Z_{eff}	Z_i	m_i (amu)	τ_c (ms)	q_a
143982	2.8	320	2.9	1.57	1.0	1.0	18.9	2.70
143983	2.8	320	3.0	1.57	1.0	1.0	20.2	2.67
143989	2.8	320	4.1	1.37	1.0	1.0	20.5	2.70
143990	2.8	320	4.2	1.37	1.0	1.0	19.5	2.70
143993	2.8	320	5.3	1.37	1.0	1.0	28.5	2.72
143994	2.8	320	4.9	1.19	1.0	1.0	25.1	2.70
143995	2.8	320	5.1	1.26	1.0	1.0	29.2	2.75
144001	2.8	320	6.0	1.20	1.0	1.0	29.4	2.70
144002	2.8	320	6.3	1.17	1.0	1.0	32.6	2.68
144003	2.8	320	6.1	1.17	1.0	1.0	25.4	2.70
144004	2.8	320	6.3	1.17	1.0	1.0	28.0	2.68
144026	2.8	160	3.0	1.24	1.0	1.0	22.5	5.30
144027	2.8	160	2.9	1.20	1.0	1.0	23.7	5.20
148014	2.8	320	2.1	2.85	1.0	1.0	23.8	2.80
148016	2.8	320	2.1	2.72	1.0	1.0	20.6	2.75
148022	2.8	320	2.2	2.85	1.0	1.0	21.0	2.72
148026	2.8	320	3.7	1.87	1.0	1.0	26.8	2.62
148027	2.8	320	3.7	1.87	1.0	1.0	27.7	2.63
148029	2.8	320	4.1	1.82	1.0	1.0	29.2	2.60
148030	2.8	320	3.8	1.82	1.0	1.0	27.3	2.60
148031	2.8	320	3.9	1.97	1.0	1.0	25.4	2.60
148033	2.8	320	4.0	1.82	1.0	1.0	31.1	2.62
148034	2.8	320	4.0	1.82	1.0	1.0	30.5	2.63
148039	2.8	320	5.8	1.67	1.0	1.0	40.6	2.65
148041	2.8	320	5.9	1.67	1.0	1.0	42.9	2.60
148107	2.8	160	2.0	2.15	1.0	1.0	33.1	5.30
148108	2.8	160	2.0	2.21	1.0	1.0	28.9	5.35
148109	2.8	160	2.0	2.15	1.0	1.0	31.4	5.25
148110	2.8	160	2.2	2.21	1.0	1.0	31.8	5.25
148115	2.8	150	2.2	1.79	1.0	1.0	25.4	5.75
148126	2.8	150	1.9	1.84	1.0	1.0	31.3	5.65
148127	2.8	150	2.1	1.70	1.0	1.0	32.6	5.65
148131	2.8	150	2.2	1.75	1.0	1.0	30.5	5.70
148135	2.8	150	2.1	1.85	1.0	1.0	33.2	5.65
148192	2.8	320	2.0	3.00	1.0	2.0	30.1	2.77
148193	2.8	320	1.9	3.00	1.0	2.0	26.8	2.80
148194	2.8	320	1.9	3.08	1.0	2.0	37.2	2.80
148196	2.8	320	2.1	3.00	1.0	2.0	39.1	2.75
148197	2.8	320	2.0	2.85	1.0	2.0	32.6	2.70
148198	2.8	320	2.0	2.70	1.0	2.0	31.2	2.75

Shot	B_T (T)	I_P (kA)	$\bar{n}_e$ (10^{19} m^{-3})	Z_{eff}	Z_i	m_i (amu)	τ_c (ms)	q_a
148199	2.8	320	1.9	3.00	1.0	2.0	37.2	2.75
148200	2.8	320	2.1	2.85	1.0	2.0	31.8	2.75
148237	2.8	320	4.0	1.95	1.0	2.0	96.0	2.70
148313	2.8	320	2.0	4.21	2.0	4.0	48.7	2.70
148318	2.8	320	2.0	4.68	2.0	4.0	51.8	2.70
148329	2.8	320	4.0	2.89	2.0	4.0	83.1	2.60
148337	2.8	320	4.1	2.83	2.0	4.0	83.4	2.70
148338	2.8	320	3.8	2.89	2.0	4.0	70.6	2.67
148340	2.8	320	3.7	2.89	2.0	4.0	65.7	2.65
148341	2.8	320	4.1	2.89	2.0	4.0	76.9	2.65
148411	2.8	150	2.2	2.11	2.0	4.0	33.7	5.30
148412	2.8	150	2.0	2.11	2.0	4.0	40.5	5.20
148413	2.8	150	2.4	2.11	2.0	4.0	44.7	5.20
148414	2.8	150	2.2	1.99	2.0	4.0	50.9	5.15
148416	2.8	150	2.2	2.11	2.0	4.0	41.4	5.10
148424	2.8	150	4.0	1.74	2.0	4.0	86.5	5.30
148426	2.8	150	3.8	1.84	2.0	4.0	112.5	5.35
148427	2.8	150	3.9	1.65	2.0	4.0	80.7	5.55
149965	2.8	320	4.1	2.36	1.0	2.0	57.8	2.60
149966	2.8	320	3.7	2.30	1.0	2.0	55.6	2.65
149972	2.8	320	3.9	2.24	1.0	2.0	52.1	2.65
149976	2.8	320	4.0	2.24	1.0	2.0	56.3	2.67
149996	2.8	150	2.2	2.08	1.0	2.0	47.6	5.45
149997	2.8	150	2.2	2.19	1.0	2.0	42.6	5.30
149999	2.8	150	2.0	2.02	1.0	2.0	37.5	5.50
150004	2.8	150	1.7	2.02	1.0	2.0	33.8	5.65

The impurity confinement time, τ_c, was defined to be the exponential decay rate of the softest filtered x-ray signal after aluminum injection (filter A). In the discharges considered here the decay of this signal was indicative of the injected impurity transport, and not changes in other plasma parameters, because other parameters were not allowed to vary by more than 5% due to the injections (the change in the soft x-ray signal due to aluminum injection was typically at least a factor of two). Furthermore, spectroscopic data indicated that intrinsic impurity transport was not affected by the small aluminum injections [198]. To find τ_c from the x-ray signal the data were fit to a function of the form

$$B = B_0 + B_1 e^{-t/\tau_c} \tag{4.14}$$

using the nonlinear regression analysis routine RNLIN from IMSL.[2] As examples, the signal and fit function from a typical high current, high density discharge is shown in Fig. 4.16a, and the signal and fit from a typical low current, low density discharge are shown in Fig. 4.16b. The signal was fit from the time the signal had dropped to 80% of its maximum value to the time it had dropped to 10% of its maximum (the same limits were used by Marmar, *et. al.* [34] and by Leung *et. al.* [65,35]).

The scaling described below was based on 105 discharges described in Table 4.1. The table lists for each discharge the nominal global plasma parameters: the toroidal field (B_T in T), the plasma current (I_P in kA) and the central line-averaged electron density ($\bar{n}_e$ in 10^{19} m^{-3}). Also shown, Z_{eff} was calculated from the loop voltage and the electron temperature profile assuming Spitzer resistivity [22], radially constant toroidal electric field, $E_t = V_l/2\pi R_0$, and flat Z_{eff} profiles (V_l is the measured loop voltage and $dI_P/dt = 0$). The table also lists the background gas charge (Z_i) and its mass (m_i), the impurity confinement time (τ_c), defined through Eq. 4.14, and the measured magnetic safety factor at the limiter radius (q_a; the measured value is listed because it differs slightly from that calculated from the nominal B_T and I_P). All the discharges considered were sawtoothing after the aluminum injection.

Several density scans at constant q_a and approximately constant Z_{eff} ($1.2 \lesssim Z_{eff} \lesssim 1.6$) indicated that the aluminum confinement time increased with increasing density. (The values of Z_{eff} and $\bar{n}_e$ are not strictly independent, because plasmas with higher density tended to be cleaner.) Furthermore discharges with higher Z_{eff}, taken after an accidental vent or after installation of a new TiC-coated graphite limiter, indicated that the aluminum confinement time also increased with Z_{eff}. Fig. 4.17 shows the measured τ_c as a function of the product $Z_{eff}\bar{n}_e$ for hydrogen working gas and two different values of q_a. This plot shows that τ_c was approximately linear with $Z_{eff}\bar{n}_e$ at least over the range $3 \lesssim Z_{eff}\bar{n}_e \lesssim 10$. The larger spread in the data taken at higher q_a occurs because the temperature profile was always much more peaked in high q_a discharges. The limited spatial resolution of the ECE temperature diagnostic thus caused larger uncertainties in the temperature profiles, and therefore the calculated value of Z_{eff} was much less certain than in the lower q_a case. Nonetheless, it is important to note that only one data point lies outside the $\pm 25\%$ uncertainty level indicated by the dashed lines in Fig. 4.17b. No points are outside the $\pm 25\%$ uncertainty in the low q_a case, Fig. 4.17a.

The linear dependence on $Z_{eff}\bar{n}_e$ is similar to some previous transport results. The

[2]International Math and Science Library, Houston, TX 77036.

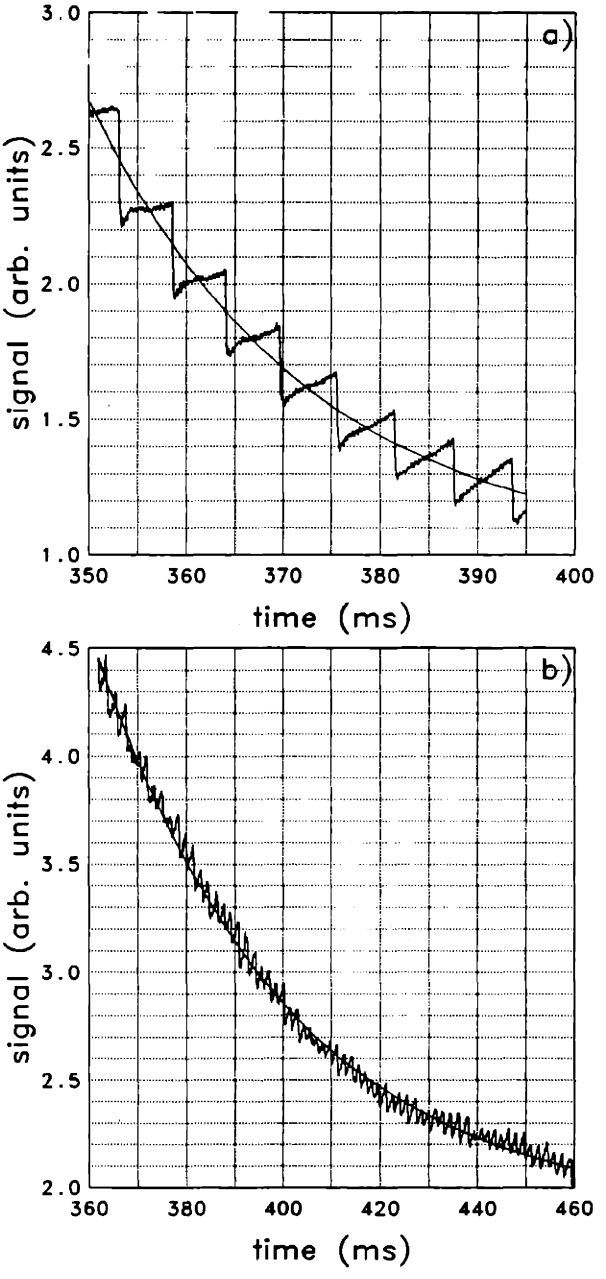

Figure 4.16: The exponential decay of the central soft x-ray brightness was fit to a function of the form $B = B_0 + B_1 e^{-t/\tau_c}$ to define the impurity confinement time τ_c. a) The smooth curve shows the fit; the x-ray data shows the large sawteeth characteristic of a high current, high density hydrogen discharge (2.8/320/6.1H). The fit decay time was 22.7 ms. b) The exponential fit for a lower current, lower density hydrogen plasma. Note that the sawteeth were very small with a high frequency during the decay of the soft x-ray signal (2.8/150/2.0H). The fit decay time was 39.4 ms.

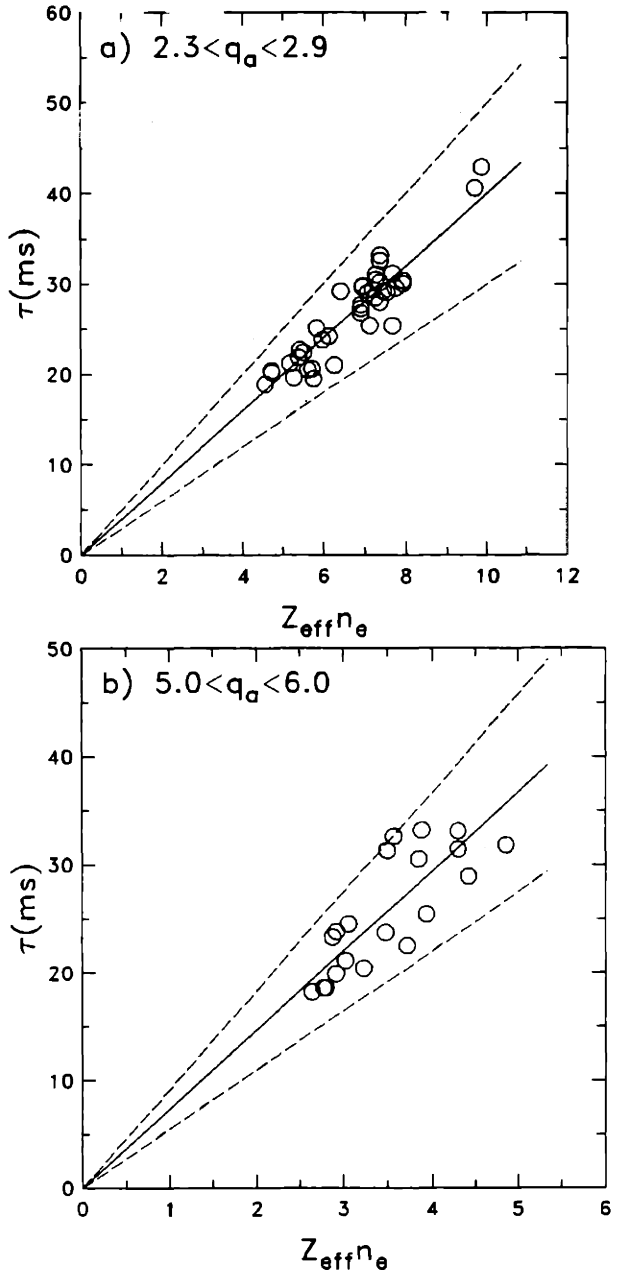

Figure 4.17: The measured impurity confinement time is shown as a function of the product $Z_{eff}\bar{n}_e$ for two different q_a values in hydrogen plasmas: a) $B_T = 2.8\ T$, $300 \simeq I_P \simeq 320$ kA, and $2.3 \simeq q_a \simeq 2.9$; and b) B_T=2.8 T, $150 \leq I_P \leq 160$ kA, and $5.9 \lesssim q_a \lesssim 6.3$. The data were approximately linear with $Z_{eff}\bar{n}_e$ within 25% indicated by the dashed lines.

Z_{eff} dependence was reported earlier from impurity injection experiments in TEXT with scandium, titanium and iron [66]. The linear dependence on electron density is also similar to the dependence found for the working particle confinement in TEXT [196] and the energy confinement in many tokamaks including TEXT [199] and Alcator-C [200]. The linear dependence on Z_{eff} is also the same as that found for impurity confinement in Alcator-C [34].

However, there are also differences between the τ_c scaling found here and the results of previous transport experiments. First, the working particle confinement time and the energy confinement time were found to saturate at some density in TEXT [196,199], and the energy confinement time also saturated with increasing density in Alcator-C [200]. (Specifically, for low q_a discharges, τ_p saturated at about 5×10^{19} m^{-3} in TEXT, τ_E also saturated at about 5×10^{19} m^{-3} in TEXT, and τ_E saturated at about 2.0×10^{20} m^{-3} in Alcator-C.) No such saturation was apparent for the aluminum confinement in TEXT up to the maximum density achieved, 6.3×10^{19} m^{-3}. Second, in Alcator-C the working particle confinement time decreased with increasing electron density [201]. Third, impurity confinement studies in Alcator-C showed no dependence on electron density, except in the case of very low density, where the impurity confinement increased with decreasing $\bar{n}_e$. This was attributed not to changes in $\bar{n}_e$ itself, but rather to increasing Z_{eff} as the electron density decreased [34]. Fourth, the impurity confinement time decreased with density in the TJ-1 tokamak [38]. These various results may imply that the impurity confinement in Alcator-C was in a saturated regime, whereas the density in TEXT was too low to have reached saturation.

Once the dependence on Z_{eff} and $\bar{n}_e$ was established, the dependence on the mass and charge of the working gas was studied. Aluminum was injected into deuterium and helium plasmas with the same global conditions as the hydrogen experiments. Fig. 4.18 shows the resultant confinement times normalized to $Z_{eff}\bar{n}_e$ as a function of m_i/Z_i and $\sqrt{m_i/Z_i}$ for two q_a values. The data were fit somewhat better by the line proportional to $\sqrt{m_i/Z_i}$ (Figs. 4.18c and 4.18d) if the line is assumed to pass through the origin. The $\sqrt{m_i}$ dependence is the same as previously reported for scandium, titanium and iron in TEXT [66]. It is only qualitatively similar, however, to the result found in Alcator-C [34], where the impurity confinement time scaled as m_i/Z_i. The dependence on working gas mass and charge appeared to be weaker in TEXT than in Alcator. The data of Fig. 4.18 is not sufficient to completely rule out a linear isotope scaling, but τ_c certainly increases with m_i/Z_i, and $\tau_c \propto \sqrt{m_i/Z_i}$ does fit the data a little better.

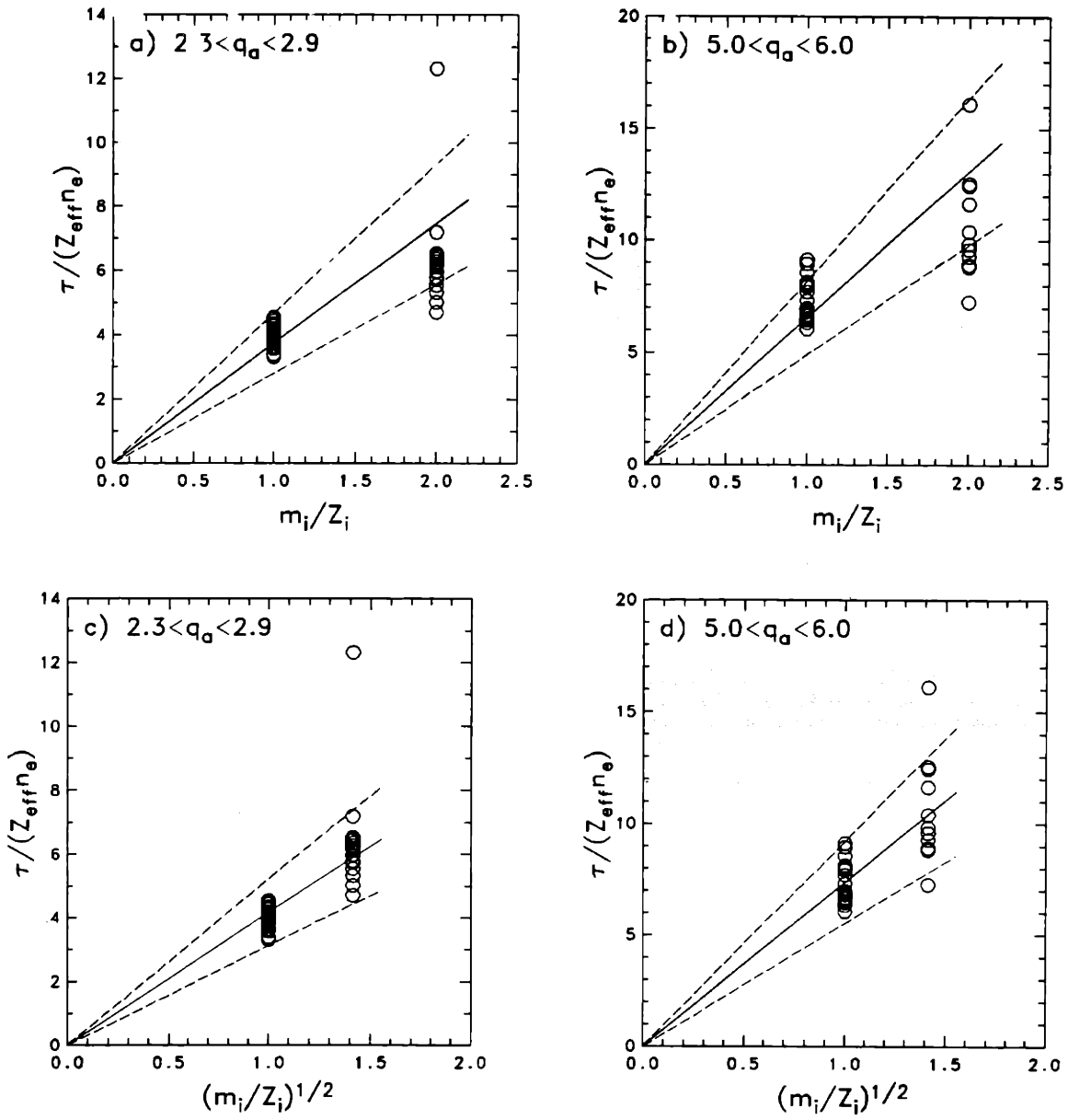

Figure 4.18: The confinement time of aluminum normalized to $Z_{eff}\bar{n}_e$ is shown as two different functions of m_i/Z_i for two different q_a values: a) From B_T=2.8 T, I_P=320 kA, $\tau_c/Z_{eff}\bar{n}_e$ vs. m_i/Z_i; b) From B_T=2.8 T, I_P=160 kA, $\tau_c/Z_{eff}\bar{n}_e$ vs. m_i/Z_i; c) From B_T=2.8 T, I_P=320 kA, $\tau_c/Z_{eff}\bar{n}_e$ vs. $\sqrt{m_i/Z_i}$; d) From B_T=2.8 T, I_P=160 kA, $\tau_c/Z_{eff}\bar{n}_e$ vs. $\sqrt{m_i/Z_i}$. The data were fit slightly better by $\tau_c \propto \sqrt{m_i/Z_i}$.

The dependence of τ_c on the plasma current was explored next. Discharges were run with currents of 150, 160, 280, 300 and 320 kA at a constant toroidal field of B_T=2.8 T. The result was that the confinement increased as the plasma current was decreased. The conclusion, born out in Fig. 4.19, is that the confinement time is approximately proportional to $1/I_P$. This also agrees with previous results on TEXT where the confinement time of scandium decreased with increasing plasma current [65]. This result is consistent with measurements of the working particle diffusion coefficient in TEXT from sawtooth density pulse propagation [58], where it was found that $D \propto 1/q_a$. For purely diffusive transport, this would give $\tau \propto 1/I_P$, since $\tau \sim a^2/D$ (and $q_a \simeq 2\pi a^2 B_T/\mu_0 R_0 I_P$). Furthermore, the impurity confinement scaling described herein is also qualitatively consistent with energy transport measured during sawtooth temperature pulse propagation [188]. In that case, χ_e was found to scale approximately as $1/q_a^{1.5}$, which would again result in τ_E increasing with q_a.

However, the TEXT I_P scaling of τ_c disagrees with Alcator-C results [34], where the impurity confinement time scaled as the inverse of q_a. (It was pointed out earlier by Leung [65] that the scaling of impurity confinement with plasma current was not the same in TEXT as in Alcator) The scaling of the impurity confinement time in TEXT with plasma current also disagrees with the working ion confinement time in TEXT, which increases with the plasma current [196]. Furthermore this scaling with q_a is also in contrast to the scaling found from iron injections in the low field TJ-1 tokamak [38], wherein the impurity confinement time was found to agree favorably with the neoclassical scaling of Rozhanskii [39],

$$\tau_c \text{ (ms)} = 5 \times 10^{+8} \frac{R_0 a^2 B_T^2}{q_0 T_i}. \tag{4.15}$$

In this formula R_0 and a are in m, B_T is in T, q_0 is the *central* safety factor, and T_i is the ion temperature in keV. The confinement scaling with q_a in TEXT disagrees with that found in both Alcator and TJ-1.

Finally all the TEXT scalings considered thus far can be combined into one formula:

$$\tau_c(\text{ms}) \simeq 1286 Z_{eff} \bar{n}_e \frac{1}{I_P} \sqrt{\frac{m_i}{Z_i}}. \tag{4.16}$$

In this equation $\bar{n}_e$ is in 10^{19} m^{-3}, I_P is in kA, and m_i is in amu. Eq. 4.16 was derived from 105 shots shown in Table 4.1 and the data is all shown in Fig. 4.19. The important note is that only 10 shots ($\sim$ 10% of the data) have confinement times more than 25% different than the prediction of Eq. 4.16. This equation should be compared to that

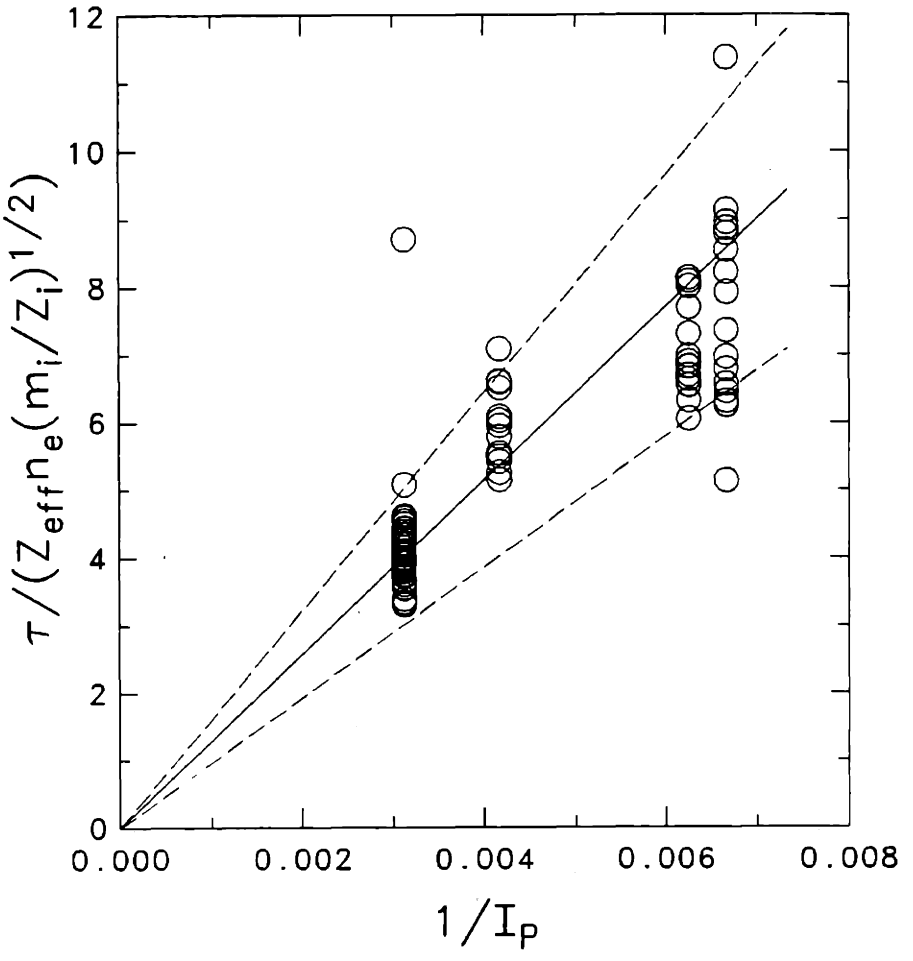

Figure 4.19: The confinement time normalized to $Z_{eff}\bar{n}_e\sqrt{m_i/Z_i}$ is shown as a function of $1/I_P$. Only 10 of the 105 data points lie further than 25% away from a linear dependence on $1/I_P$.

predicted by Rozhanskii, Eq. 4 15 [39] (in agreement with the data from TJ-1) and that derived to fit the Alcator-C data [34],

$$\tau_c(ms) = 0.075 a R_0^{0.75} \frac{Z_{eff} m_i}{q_a Z_i}. \tag{4.17}$$

It is difficult to completely reconcile the TEXT result with that of either Alcator-C or TJ-1 In the Z_{eff} scaling, τ_c in TEXT is the same as in Alcator-C. In both TEXT and Alcator-C, τ_c increases with m_i/Z_i, but more rapidly in Alcator-C. In TEXT, Alcator-C, and TJ-1, τ_c scales with q_a differently: $\tau_c \propto 1/I_P$ in TEXT, $\tau_c \propto 1/q_a$ in Alcator-C, and $\tau_c \propto B_T^2/q_0$ in TJ-1. The impurity confinement increases with $\bar{n}_e$ in TEXT, an effect not seen in Alcator-C and opposite of that found in TJ-1. Alcator may be operating in a regime where the impurity confinement time has saturated, but no saturation was seen in TEXT when it was run with densities up to 6.3×10^{13} cm^{-3}. TJ-1 may be in a completely different transport regime because its global parameters are so different from those of TEXT and Alcator-C (for example in TJ-1, $B_T \leq 1.5$ T, $I_p \leq 50$ kA, and $\bar{n}_e \leq 3 \times 10^{19}$ m^{-3}.) and comparisons between the TJ-1 scaling and the TEXT scaling are not transparent. A density dependence may be implicit in the $1/T_i$ term in the TJ-1 scaling of Eq. 4.15, because the electron temperature in most tokamaks increases with decreasing density, so the ion temperature may also increase as some function of $1/\bar{n}_e$; however, the electron-ion coupling also improves at high density, so the dependence of T_i on n_e is not simple. Artsimovich has given a simple formula to relate the ion temperature to other plasma parameters [202], valid for $1.6 \leq \frac{T_e}{T_i} \leq 10$,

$$T_i(\text{eV}) = 2.8 \times 10^{-6} \frac{1}{\sqrt{A_i}} (B_T I_P n_{e0} R^2)^{1/3}, \tag{4.18}$$

with B_T in T, I_P in kA, n_{e0} in 10^{19} m^{-3}, R in m, and A_i is the working ion atomic mass in amu. This formula has been shown to be valid in TEXT for densities below about 4×10^{19} m^{-3} [203]. However it is unclear whether it should hold under TJ-1 conditions, and if it were valid in TJ-1, it would not lead to the same scaling with q_a and $\bar{n}_e$ found in TEXT.

A somewhat more accurate scaling for the impurity confinement time in TEXT was found by performing a regression analysis on the data. Specifically, the data were fit to a function of the form

$$\tau_c = \theta_1 Z_{eff}^{\theta_2} \bar{n}_e^{\theta_3} I_P^{\theta_4} (m_i/Z_i)^{\theta_5}, \tag{4.19}$$

where the $\theta_i's$ were the fit parameters. The result was

$$\tau_c = 571 Z_{eff}^{1.16} \bar{n}_e^{1.25} I_P^{-0.93} (m_i/Z_i)^{0.57}. \tag{4.20}$$

This fit is shown in Fig. 4.20 The agreement between this result and that of Eq. 4.16 is quite good considering the limited database. The two points that are much higher than the regression analysis result were from discharges in which the x-ray signal only marginally returned to the pre-injection level.

The impurity confinement scaling developed here for TEXT is suggestive of the importance of sawtooth oscillations in overall impurity transport. The sawtooth period is an increasing function of electron density, and the sawtooth inversion radius increases with increasing I_P Thus, as the density increases, sawtooth crashes flatten the density profiles less often, and as I_P increases, more of the plasma volume is affected by the sawtooth crash. If the sawtooth were to mimic a purely diffusive process, one might expect an average diffusion coefficient that scaled with r_{inv}^2/τ_s, implying a confinement time on the order of $\sim a^2\tau_s/r_{inv}^2$. On the other hand, if the sawtooth behaved as a purely convective process, one might expect an average convective velocity that scaled with r_{inv}/τ_s, with a consequent confinement time on the order of $a\tau_s/r_{inv}$. The primary sawtooth parameters, r_{inv} and τ_s have been found to scale in TEXT as [188]

$$r_{inv} \sim I_p^{0.66}\bar{n}_e^{0.1}/B_T^{0.95} \tag{4.21}$$

and

$$\tau_s \sim B_T^{0.38}\bar{n}_e^{0.96}/I_P^{0.84}. \tag{4.22}$$

Combining these relations gives

$$\frac{a^2\tau_s}{r_{inv}^2} \sim \frac{a^2\bar{n}_e^{0.76}B_T^{2.28}}{I_P^{2.16}} \approx a^2\bar{n}_e^{0.8}\frac{B_T^{2.3}}{I_P^{2.2}}, \tag{4.23}$$

and

$$\frac{a\tau_s}{r_{inv}} \sim \frac{a\bar{n}_e^{0.86}B_T^{1.33}}{I_P^{1.5}} \approx a\bar{n}_e^{0.9}\frac{B_T^{1.3}}{I_P^{1.5}}. \tag{4.24}$$

Neither of these results agree completely with the scaling found here for τ_c, but they both give the qualitative behavior that τ_c increases with increasing $\bar{n}_e$ and decreases with increasing I_P. It is important to remember that the sawtooth crash is not the only driving mechanism for transport because the sawtooth oscillation clearly does not affect the entire plasma, and particle transport indeed occurs in non-sawtoothing plasmas. Thus other transport processes must also be present, especially in that fraction of the plasma outside the sawtooth mixing radius. It is interesting that the convective model of Eq. 4.24 gives better agreement to the experimental confinement scaling than the diffusive model. Models for sawtooth-induced transport using enhanced convection have

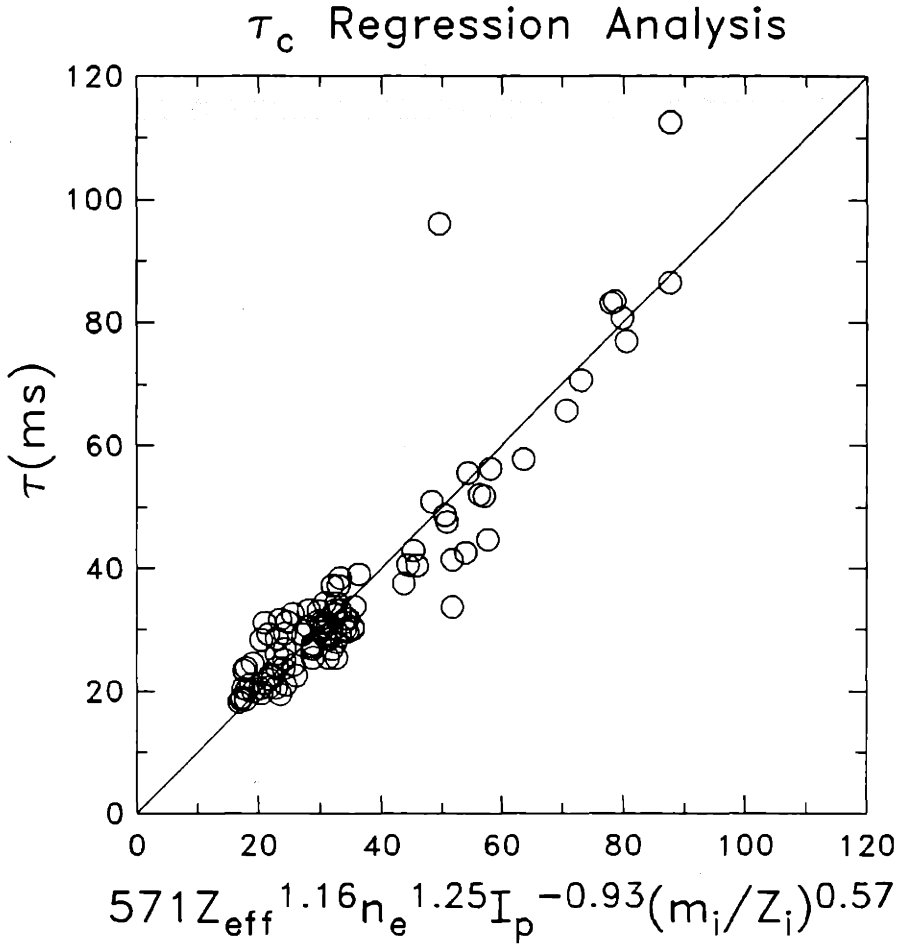

Figure 4.20: The confinement time data were fit to a function of Z_{eff}, $\bar{n}_e$, I_P, and m_i/Z_i. The result is shown as the x-axis label. The circles show 105 data points.

Table 4.2:
TEXT Discharges for Al Profile Measurements

Shot	B_T (T)	I_P (kA)	$\bar{n}_e$ (10^{19} m^{-3})	T_{e0} (keV)	gas	Inj.	time (ms)	τ_c (ms)	τ_s (ms)	τ_i (ms)
143989	2.8	320	4.1	0.86	H	l	365	20.5	4.0	20.9
143995	2.8	320	5.1	0.75	H	l	375	29.2	6.1	24.1
144004	2.8	320	6.3	0.68	H	l	370	28.0	5.7	28.0
144027	2.8	160	3.0	0.73	H	l	370	23.7	2.6	40.0
148034	2.8	320	4.0	0.96	H	l	350	30.5	3.6	14.7
148039	2.8	320	6.0	0.92	H	l	350	40.6	4.5	13.4
148135	2.8	150	1.9	0.97	H	p	350	33.2	0.8	28.6
148152	2.2	320	4.4	0.98	H	p	360	32.0	2.9	13.4
148237	2.8	320	3.8	1.16	D	l	350	96.0	3.1	11.0

also given better agreement with experimental results than enhanced diffusion models used in TFR [60] and ASDEX [48].

4.3.2 Aluminum Density Profiles

4.3.2.1 Sawtooth Period-Averaged Density Profiles

Aluminum density profiles measured in 9 discharges are shown in Figs. 4.21–4.29. These profiles were all from data averaged over a single sawtooth period sometime between 25–50 ms following the injection. The particular time for analysis was chosen to be after the small perturbation in the electron temperature profile and the plasma horizontal position had died away. Most of the discharges were hydrogen with $B_T = 2.8\ T$, $I_P = 320$ kA or 160 kA and various electron densities. The specific plasma conditions for each discharge are listed in Table 4.2. Also listed in this table are the measured confinement time τ_c, the sawtooth period τ_s, and the longest ionization τ_i, which is the time to ionize the H-like state to fully stripped aluminum.

The general characteristic of all high current ($I_P = 320$ kA; low q_a), low density hydrogen discharges was a centrally flat or slightly hollow aluminum density profile, probably due to the strong sawteeth in high current discharges (low q_a discharges have the largest inversion radii). Lower density discharges tended to exhibit more hollowness than their higher density couterparts, again probably because the sawtooth frequency was higher in low density discharges. In high current, high density plasmas (e.g., shot 144004) the aluminum density profile was typically slightly peaked or flat in the center, because of the long sawtooth periods in high density discharges relative to the lower density discharges. The exception to this generalization (shot 148039) showed a hollow

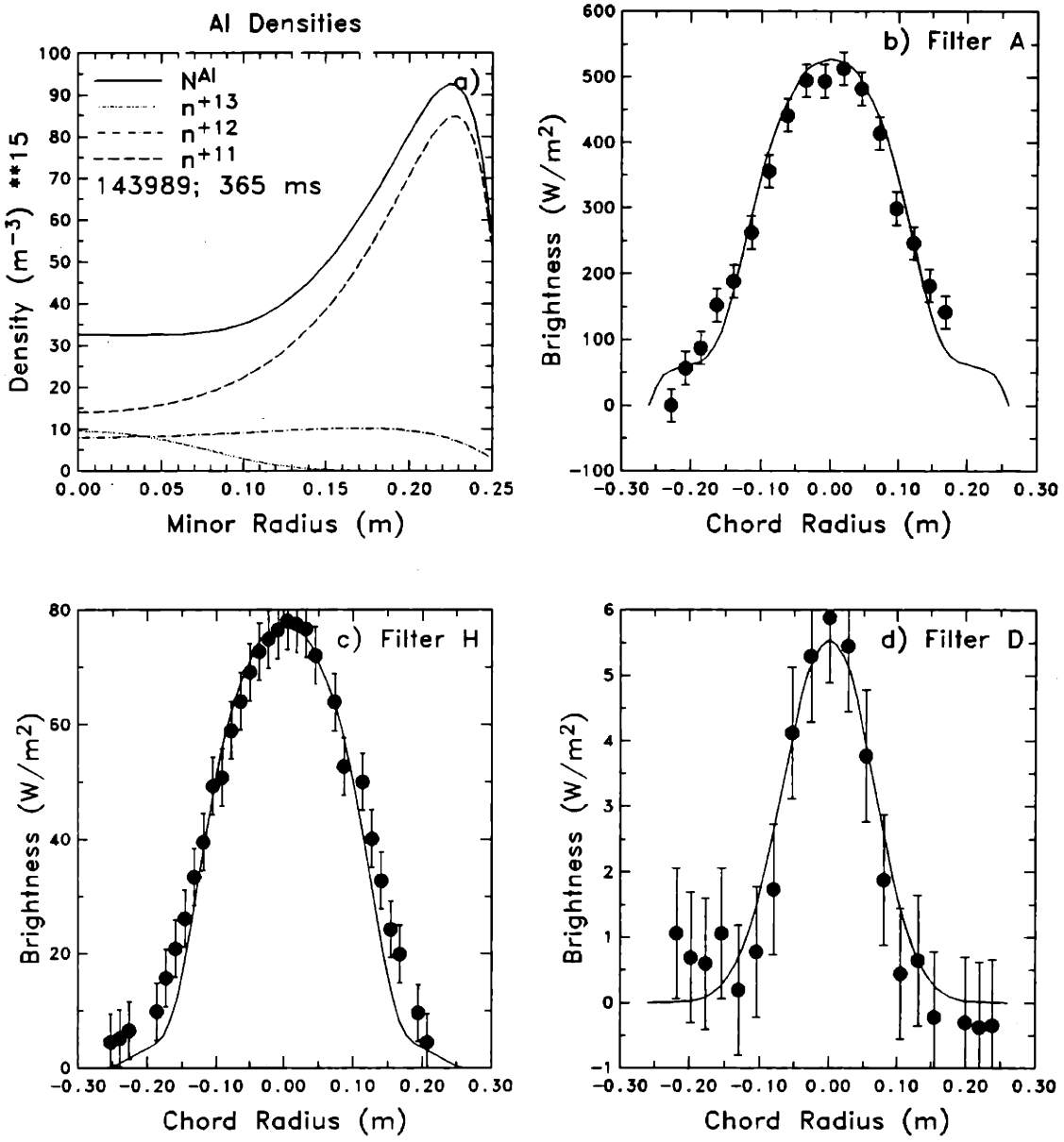

Figure 4.21: a) Aluminum density profiles from shot 143989; 2.8/320/4.1 H with laser ablation. The calculated x-ray brightness profiles (lines) from the aluminum profiles are compared to the data from three filters in b)-c).

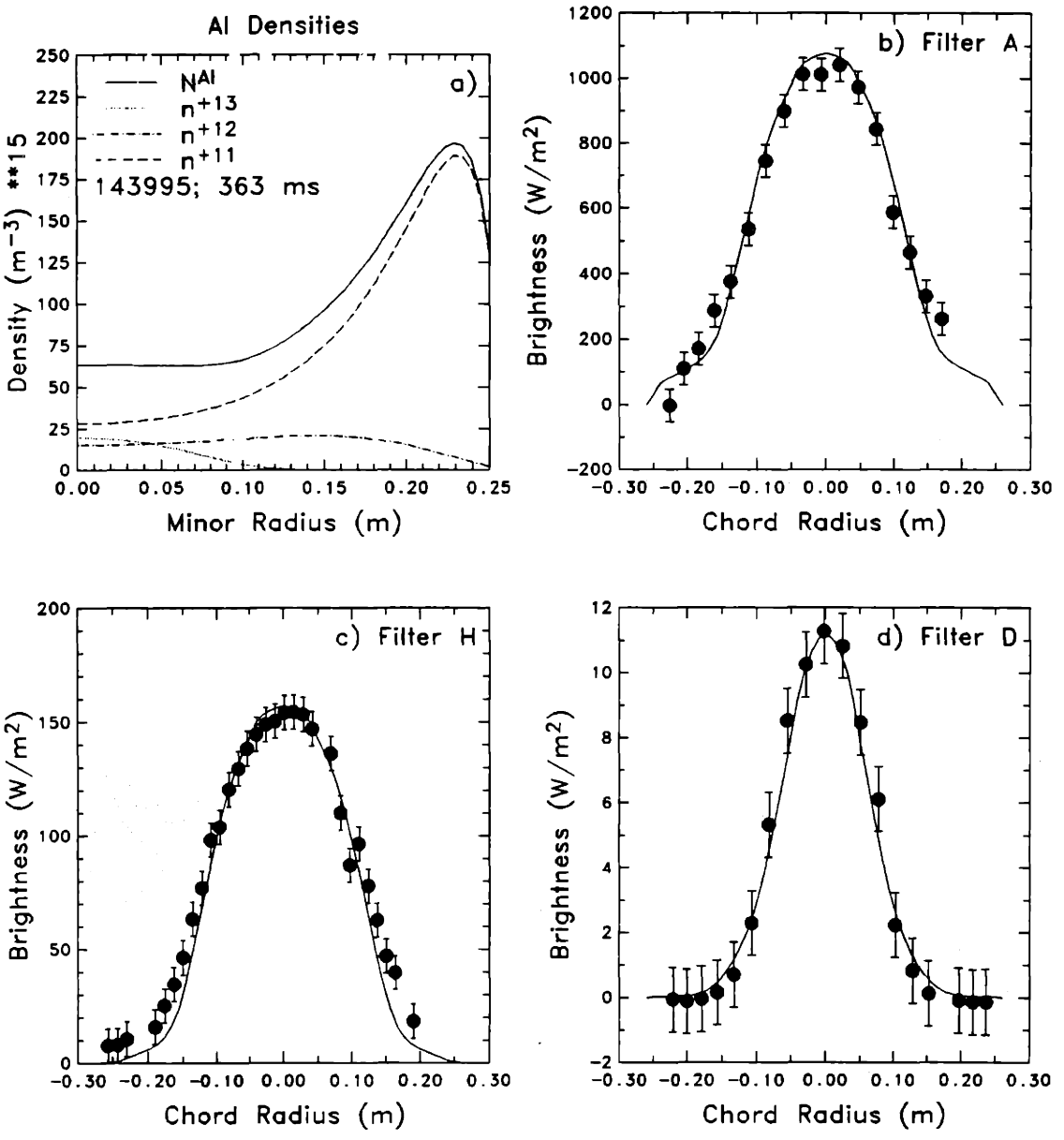

Figure 4.22: Aluminum density profiles from shot 143995; 2.8/320/5.1 H with laser ablation. The calculated x-ray brightness profiles (lines) from the aluminum profiles are compared to the data from three filters in b)-c).

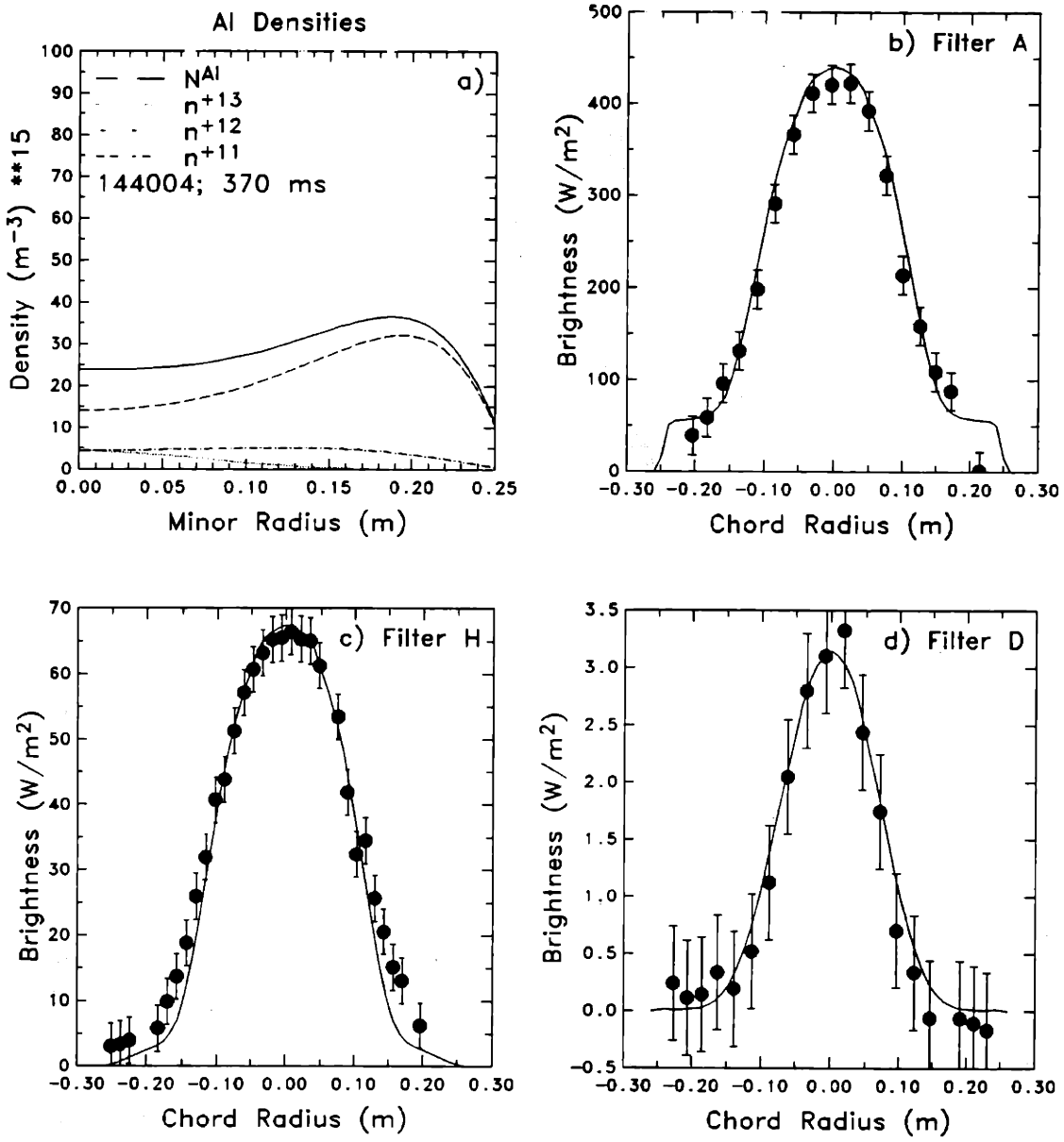

Figure 4.23: Aluminum density profiles from shot 144004; 2.8/320/6.3 H with laser ablation. The calculated x-ray brightness profiles (lines) from the aluminum profiles are compared to the data from three filters in b)-c).

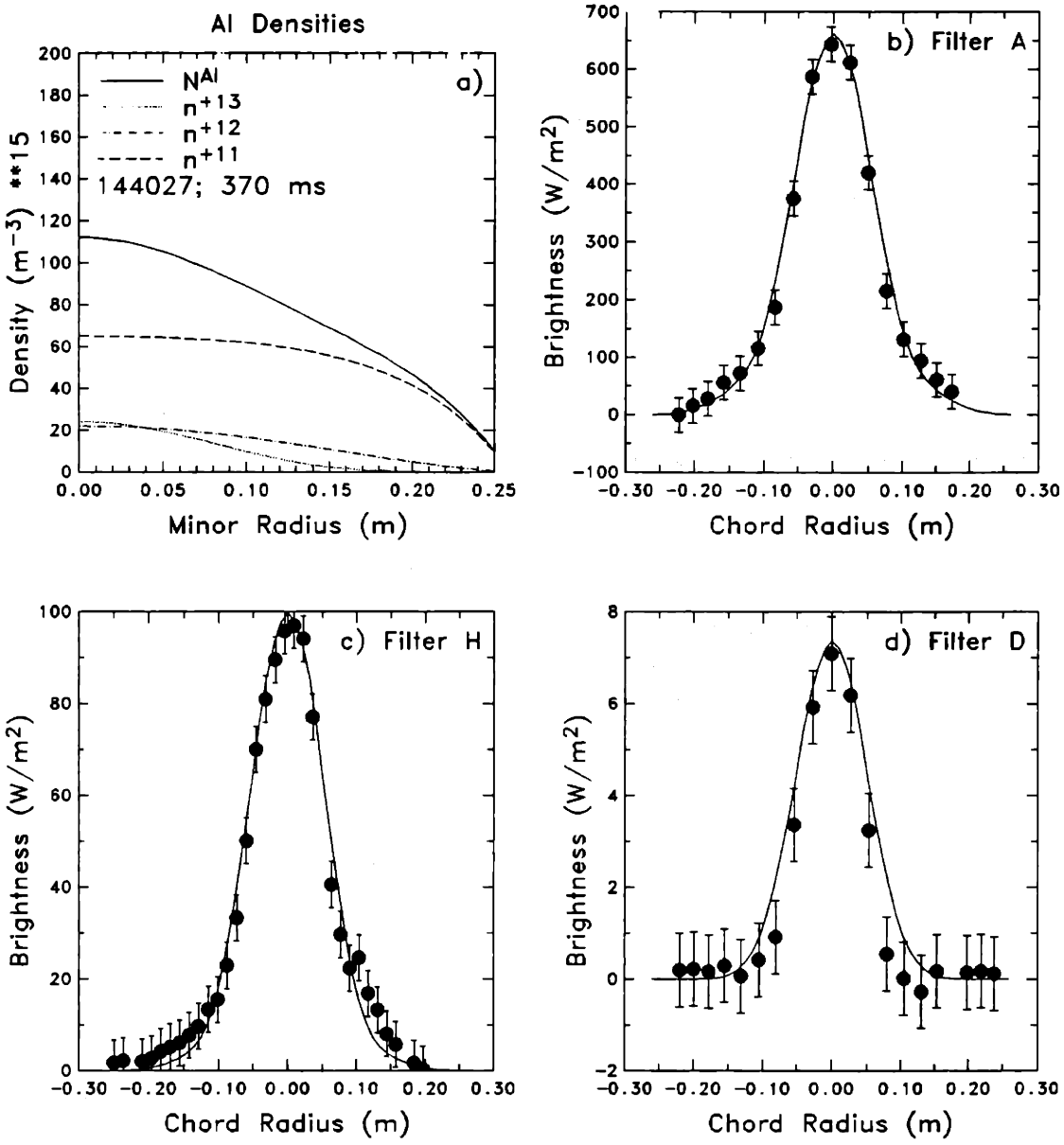

Figure 4.24: Aluminum density profiles from shot 144027; 2.8/160/3.0 H with laser ablation. The calculated x-ray brightness profiles (lines) from the aluminum profiles are compared to the data from three filters in b)-c).

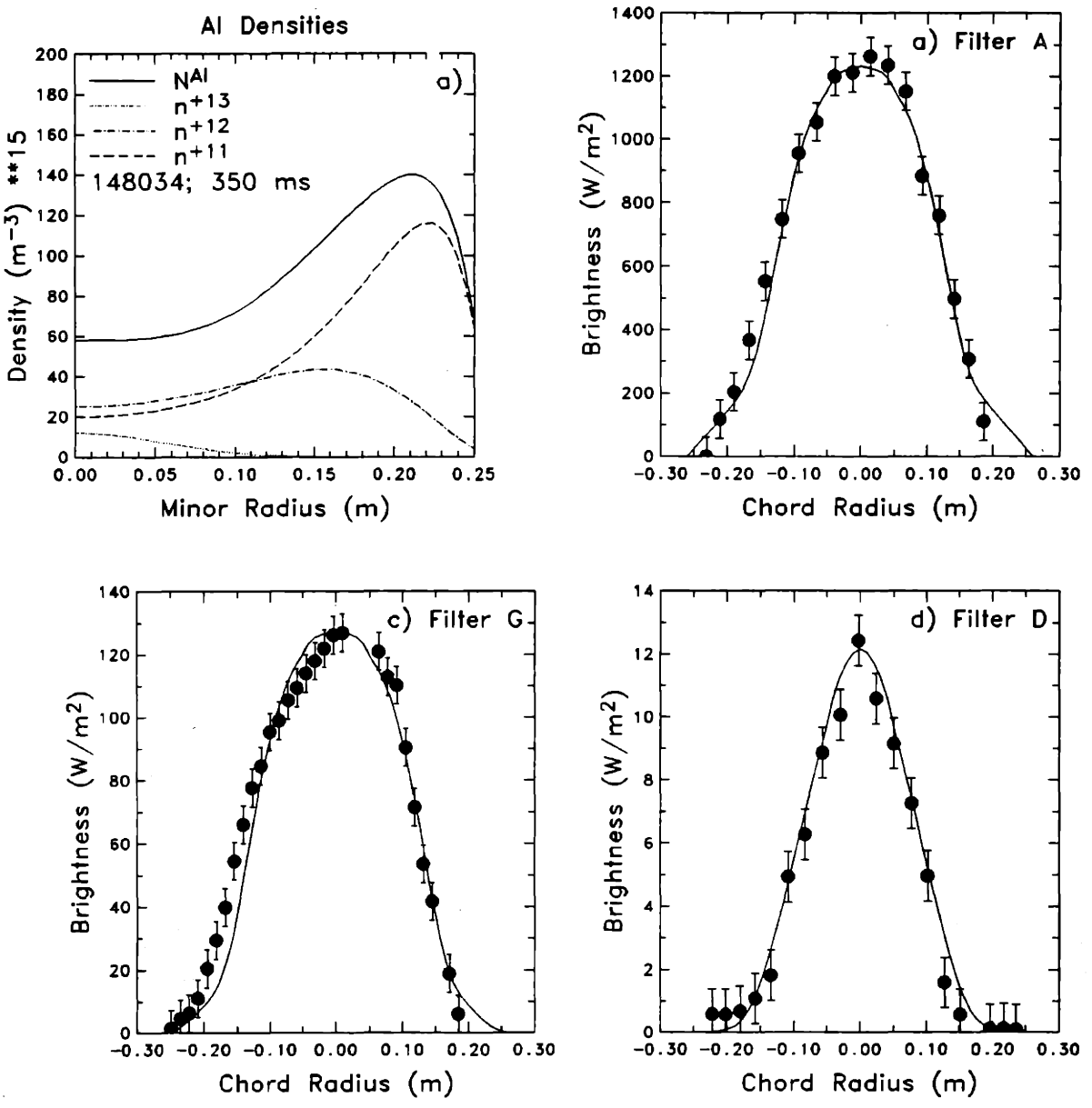

Figure 4.25: Aluminum density profiles from shot 148034; 2.8/320/4.0 H with laser ablation. The calculated x-ray brightness profiles (lines) from the aluminum profiles are compared to the data from three filters in b)-c).

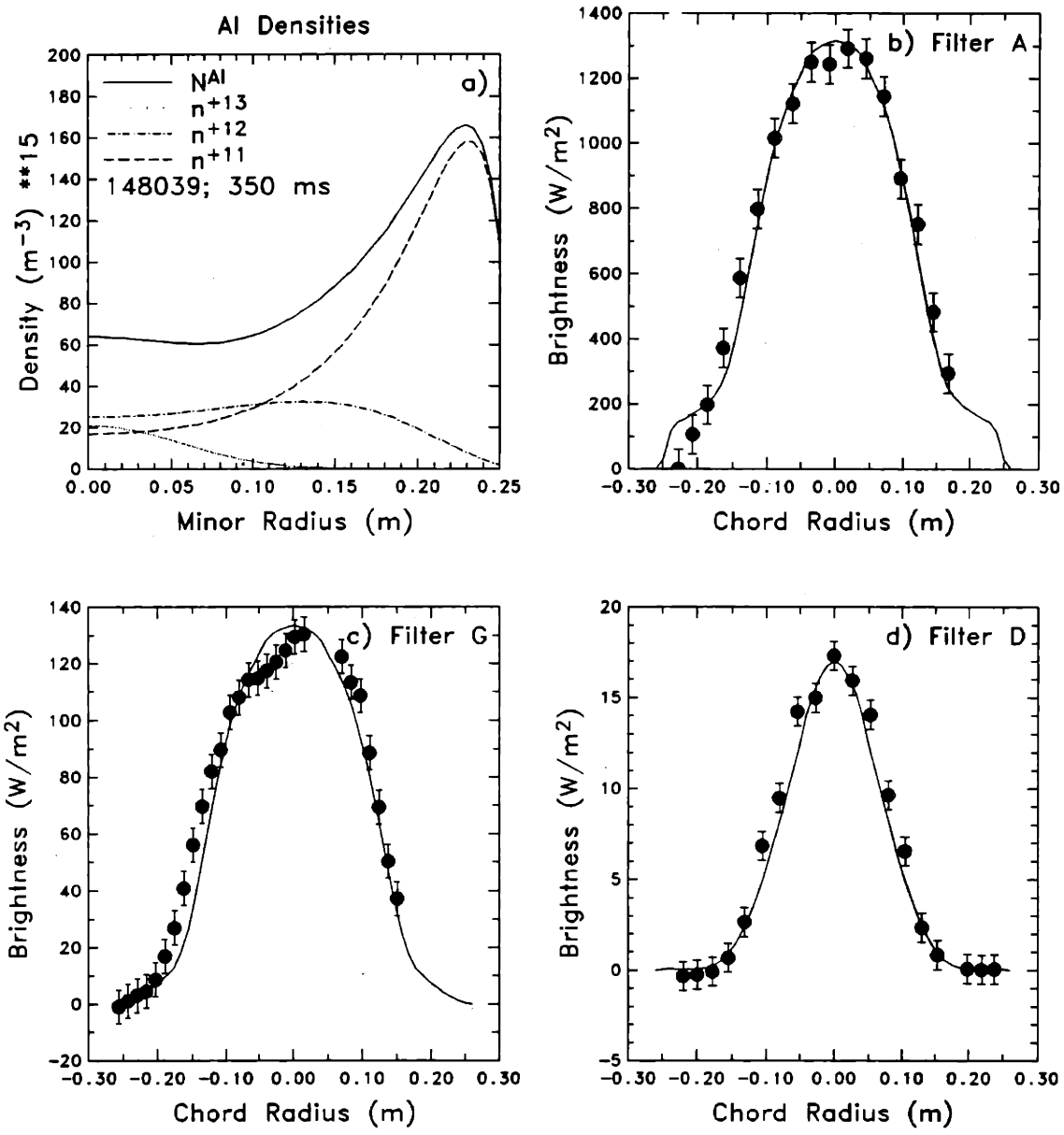

Figure 4.26: Aluminum density profiles from shot 148039; 2.8/320/6.0 H with laser ablation. The calculated x-ray brightness profiles (lines) from the aluminum profiles are compared to the data from three filters in b)-c).

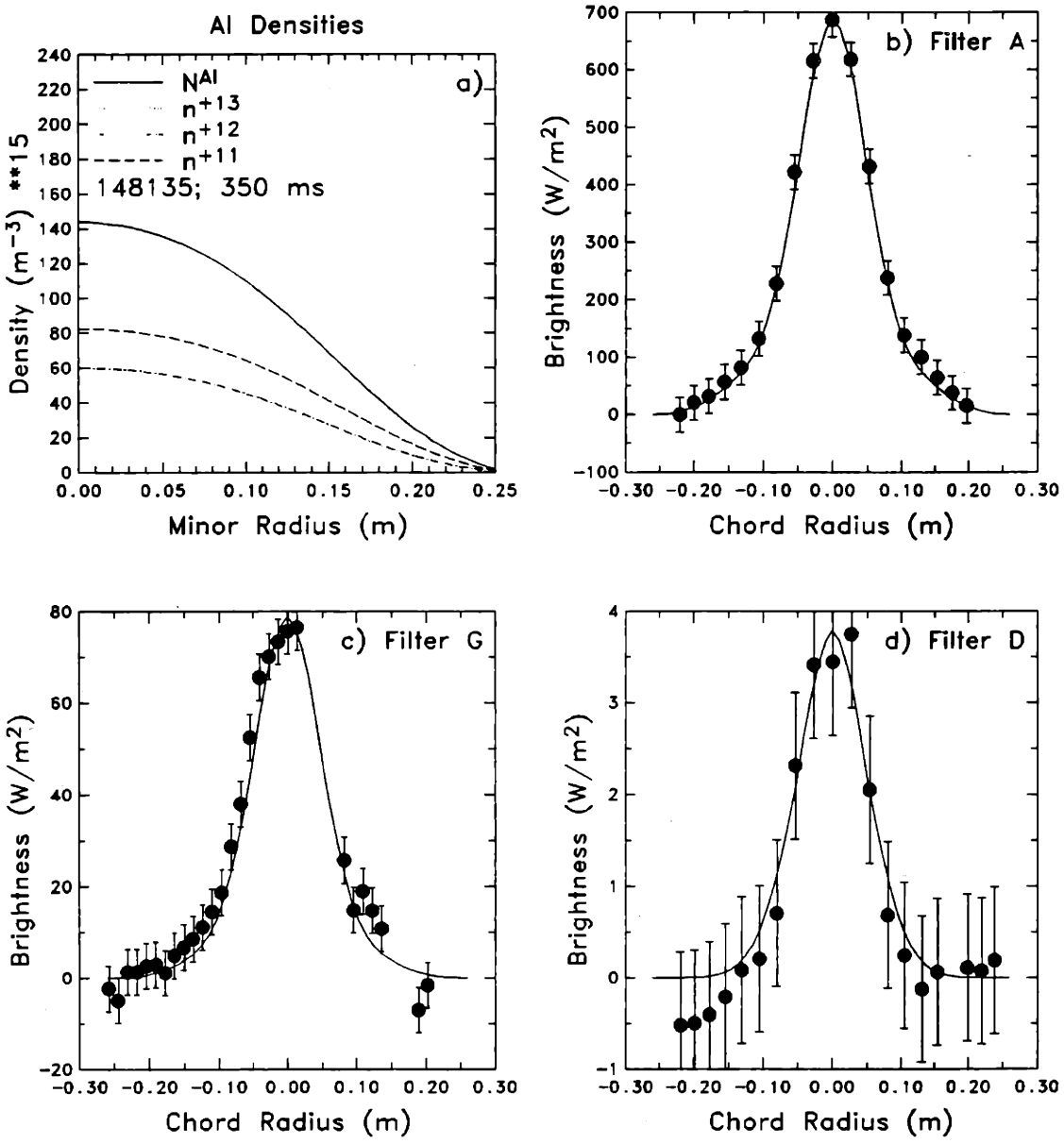

Figure 4.27: Aluminum density profiles from shot 148135; 2.8/150/1.9 H with pellet injection. The calculated x-ray brightness profiles (lines) from the aluminum profiles are compared to the data from three filters in b)-c).

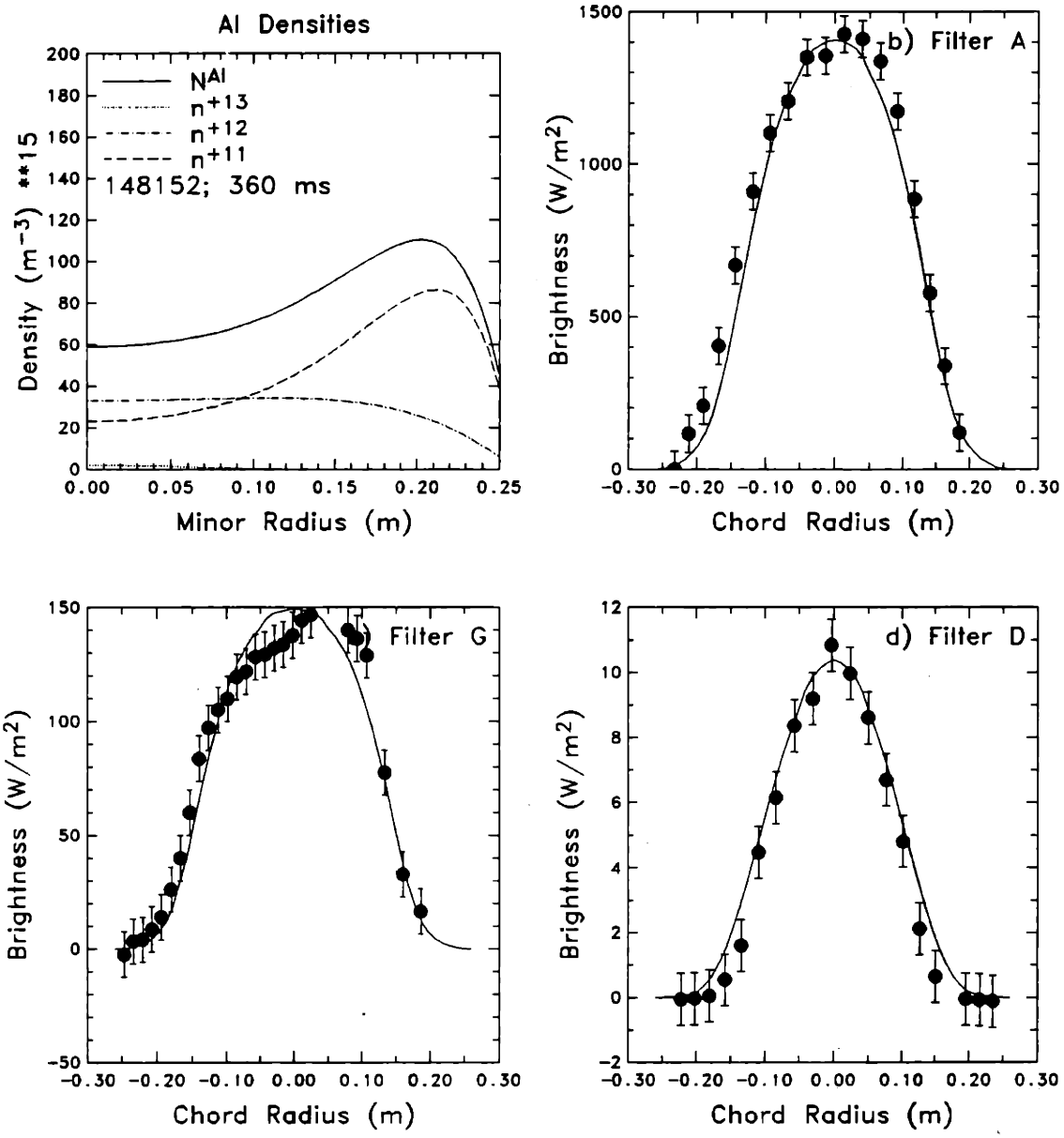

Figure 4.28: Aluminum density profiles from shot 148152; 2.2/320/4.4 H with pellet injection. The calculated x-ray brightness profiles (lines) from the aluminum profiles are compared to the data from three filters in b)-c).

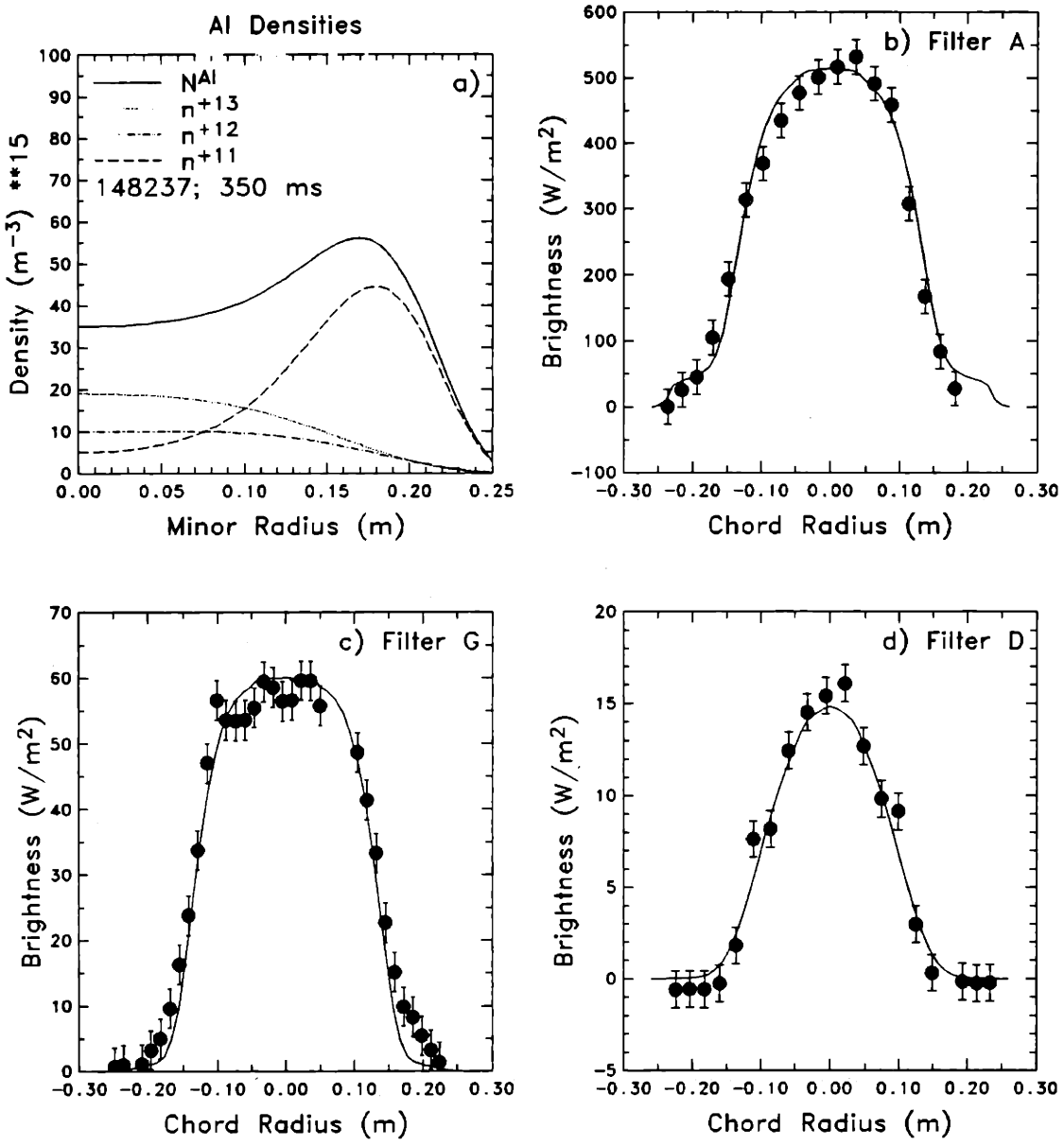

Figure 4.29: Aluminum density profiles from shot 148237; 2.8/320/3.8 D with laser ablation. The calculated x-ray brightness profiles (lines) from the aluminum profiles are compared to the data from three filters in b)-c).

aluminum density profile because it was taken only 25 ms after injection, so it had not yet had time to peak.

Low current discharges exhibited more peaked profiles than high current discharges. This may also be related to the sawtooth effect on the density profiles, because in the low current discharges, the sawtooth inversion radius and amplitiude were typically much smaller than in the high current shots. Furthermore, the measured change in impurity profiles due to sawteeth was much smaller in high q_a discharges, as will be shown in the next section.

4.3.2.2 Sawtooth-Induced Density Profiles Changes

The sawtooth oscillation plays an important role in impurity transport by fundamentally altering radial transport of both particles and energy. With the advent of high resolution x-ray tomography [146,148,182,183] the details of the sawtooth crash are becoming clearer, but they are still not completely understood. However, it is well known that at the time of the crash radial transport is greatly enhanced [54,63,60,48]. In TEXT sawteeth were found to significantly affect injected aluminum transport.

Immediately after an aluminum injection sawteeth can significantly magnify the impurity influx. For example Fig 4.30 compares the temporal behavior of the central soft x-ray signals during low q_a (large sawteeth) and high q_a (small sawteeth) discharges with the same nominal density. Note the different time behaviors; the strongly sawtoothing discharge reaches peak x-ray brightness about 12.5 ms after the injection, but the weakly sawtoothing discharge reaches maximum brightness after about 19.9 ms, $\sim$ 7.4 ms later than the low q_a discharge. Again, the sawteeth cannot be solely responsible for particle transport, but they can significantly increase particle flows as will be demonstrated below.

The effect of enhanced inward impurity flow due to sawteeth can be seen very clearly by comparing impurity density profiles just before and just after a sawtooth crash in the early soft x-ray rise phase following an aluminum injection. At this time, the aluminun density is still peaked near the plasma edge. Fig. 4.31a shows the central soft x-ray signal over a 20 ms period around the time of an injection into a high density, low q_a discharge (2.8/320/6H). The central electron temperature from the ECE diagnostic is shown for comparison in Fig. 4.31b. Normal sawteeth continued on the temperature signal throughout the rise phase of the soft x-ray signal. Note the extremely steep *rise* in the x-ray signal during the sawtooth crashes at 331 and 335 ms, despite the *drop* in the

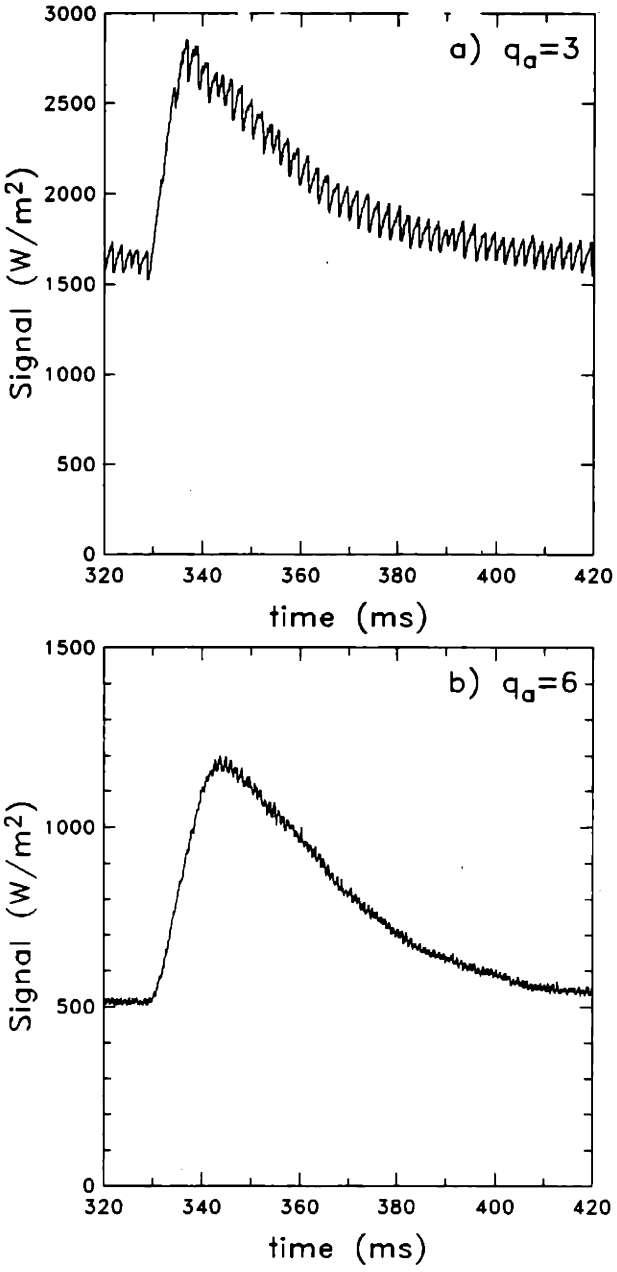

Figure 4.30: This figure compares the temporal behavior of the central soft x-ray signal around the time of aluminum injection at 325 ms for strongly and weakly sawtoothing discharges. a) The strongly sawtoothing discharge exhibited a peak x-ray brightness about 12.5 ms after injection; and b) a weakly sawtoothing discharge exhibited a peak x-ray brightness about 19.9 ms after the injection and a slightly slower overall decay in the signal. The sawteeth can play a strong role in enhancing the inward impurity transport immediately after the injection. (See also Fig. 4.32.)

electron temperature (the electron density change during these sawteeth was completely negligible in terms of its affect on the x-ray signal) An increasing x-ray signal during a sawtooth crash is in contrast to the x-ray behavior during normal sawteeth (for example, those before the injection), and is attributable to the rapid inflow of aluminum during the sawtooth crash. The aluminum density profiles measured just before and after the sawtooth at 331 ms are compared in Fig. 4.32. The density profile just before the crash (Fig. 4.32a) showed no aluminum in the plasma center (at least $\leq 5 \times 10^{14}$ m^{-3}), and a steep positive gradient outside of about $6 \sim 7$ cm. Just after the crash this gradient was greatly reduced; the density profile was nearly flat out to about 10 cm, outside of which the density increased again. A large amount of aluminum was transported into the plasma during the sawtooth crash. In fact the central aluminum density changed from essentially zero ($\lesssim 5 \times 10^{14}$ m^3) to $\sim 2.5 \times 10^{16}$ m^{-3}. Note also the rapid time scale for this change; the sawtooth crash duration was $\lesssim 0.5$ ms.

The x-ray brightness profiles calculated from these aluminum densities are shown in Fig. 4.33. The brightness fit is not exceptional for the data before the sawtooth crash (top pair of profiles), but the general trend of a hollow brightness profile is well matched. The important feature is that the brightness profiles, which are line integrated intensities, change from hollow to peaked during the sawtooth crash.

The sawtooth crash also strongly affected the impurity density profiles after the x-ray brightness peaked and began to decay again. Figs. 4.34, 4.35, and 4.36 compare aluminum density profiles before and after sawtooth crashes from three different discharge conditions: high density, low q_a; low density, low q_a; and low density, high q_a. The profiles from these discharges differed in the extent to which a sawtooth crash affected them. The high density discharge of Fig. 4.34 exhibited the largest change in total aluminum density, a ~30% drop in the central value. Changes in the individual charge state densities contributed separately to the total density change: the He-like state dropped by less than ~10%, the H-like state ~30%, and the fully stripped state by ~60%. By comparison, in the low density case shown in Fig. 4.35 the change in total aluminum density was smaller, only ~20%. In this case the contribution to the total change due to the He-like and H-like states were small, only about 5%. The fully stripped state dropped almost 100%. The fully stripped state did not accumulate in any significant amount in this discharge because the sawtooth frequency was ~0.5 kHz. Thus the fully stripped ions were ejected from the central plasma too often compared to the ionization rate to allow the fully stripped state to accumulate. In contrast to

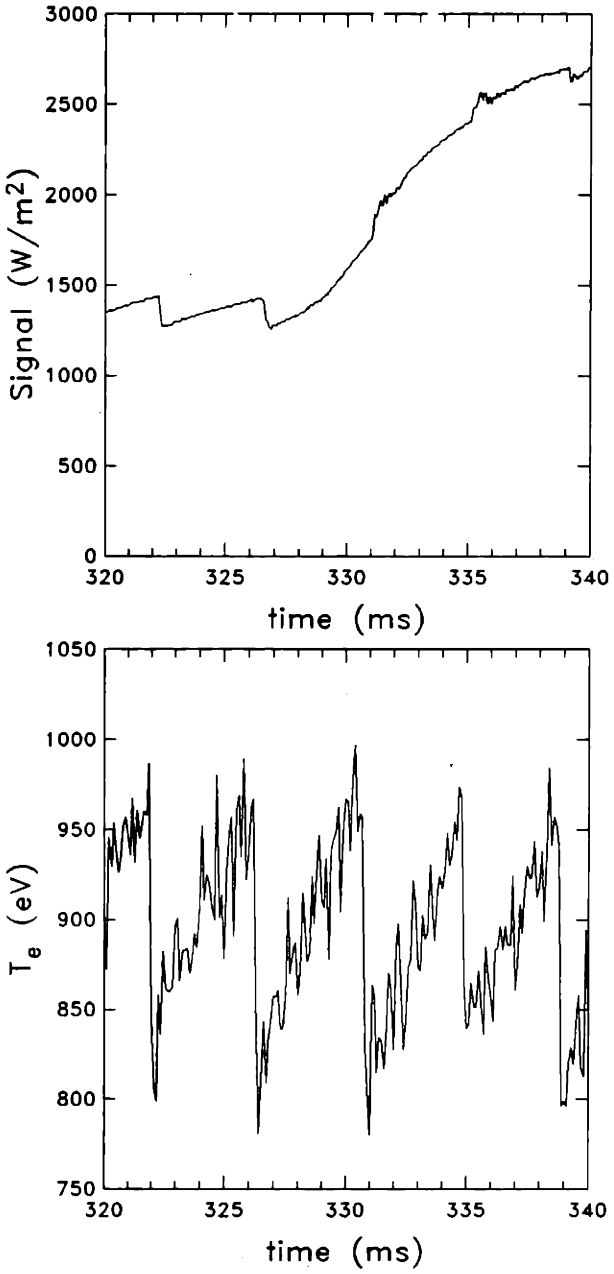

Figure 4.31: a) The central soft x-ray signal, and b) the central electron temperature signal from the ECE diagnostic are shown during a 20 ms period around the time of an aluminum injection. Normal temperature sawteeth continued after the injection, but the soft x-ray signal showed an uncharacteristic *rise* during the sawteeth at 331 and 335 ms. This is due to a rapid increase in the central aluminum density at each sawtooth crash. (The temperature and x-ray data are shifted by $\sim$ 0.5 ms with respect to one another because of differences in the digitization.)

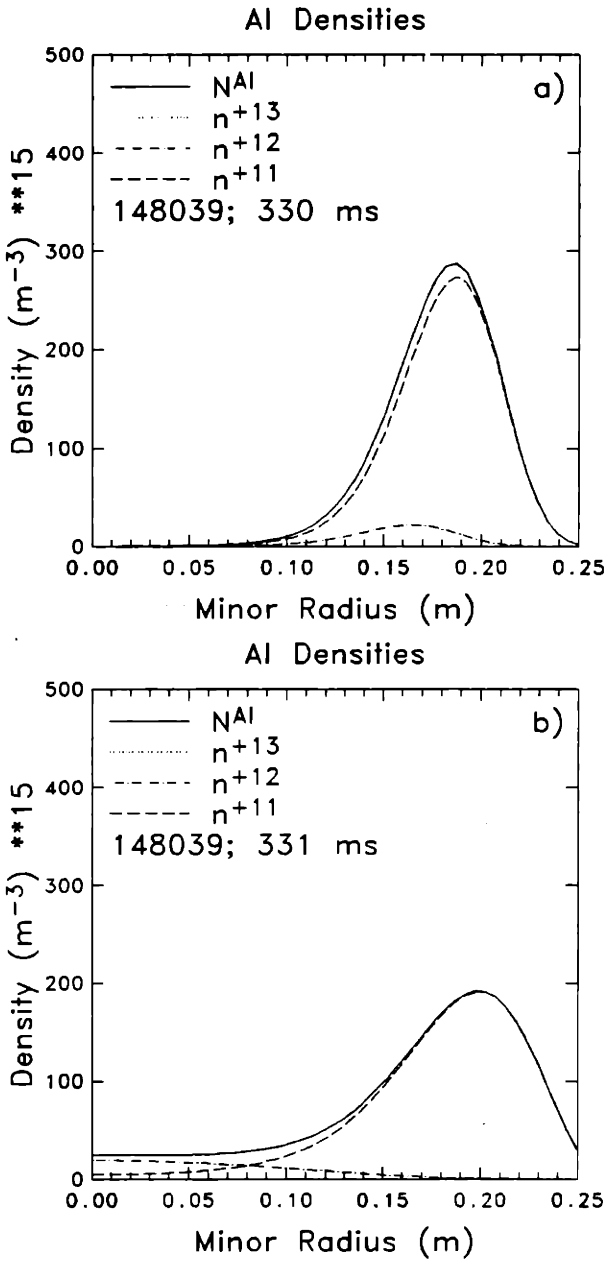

Figure 4.32: Aluminum density profiles just before and after a sawtooth crash in the early soft x-ray rise phase following impurity injection. a) The density profile is completely hollow before a sawtooth; there was almost no aluminum ($\simeq 5 \times 10^{14}$ m^{-3}) at the plasma center yet, and there was a strong positive density gradient outside of about 6–7 cm. b) After a sawtooth crash the profile was nearly flat from the center of the plasma to about 10 cm, outside of which there was a steep rise. During the crash the central aluminum density increased from zero to $\sim 2.5 \times 10^{16}$ m^{-3} in $\lesssim 0.5$ ms.

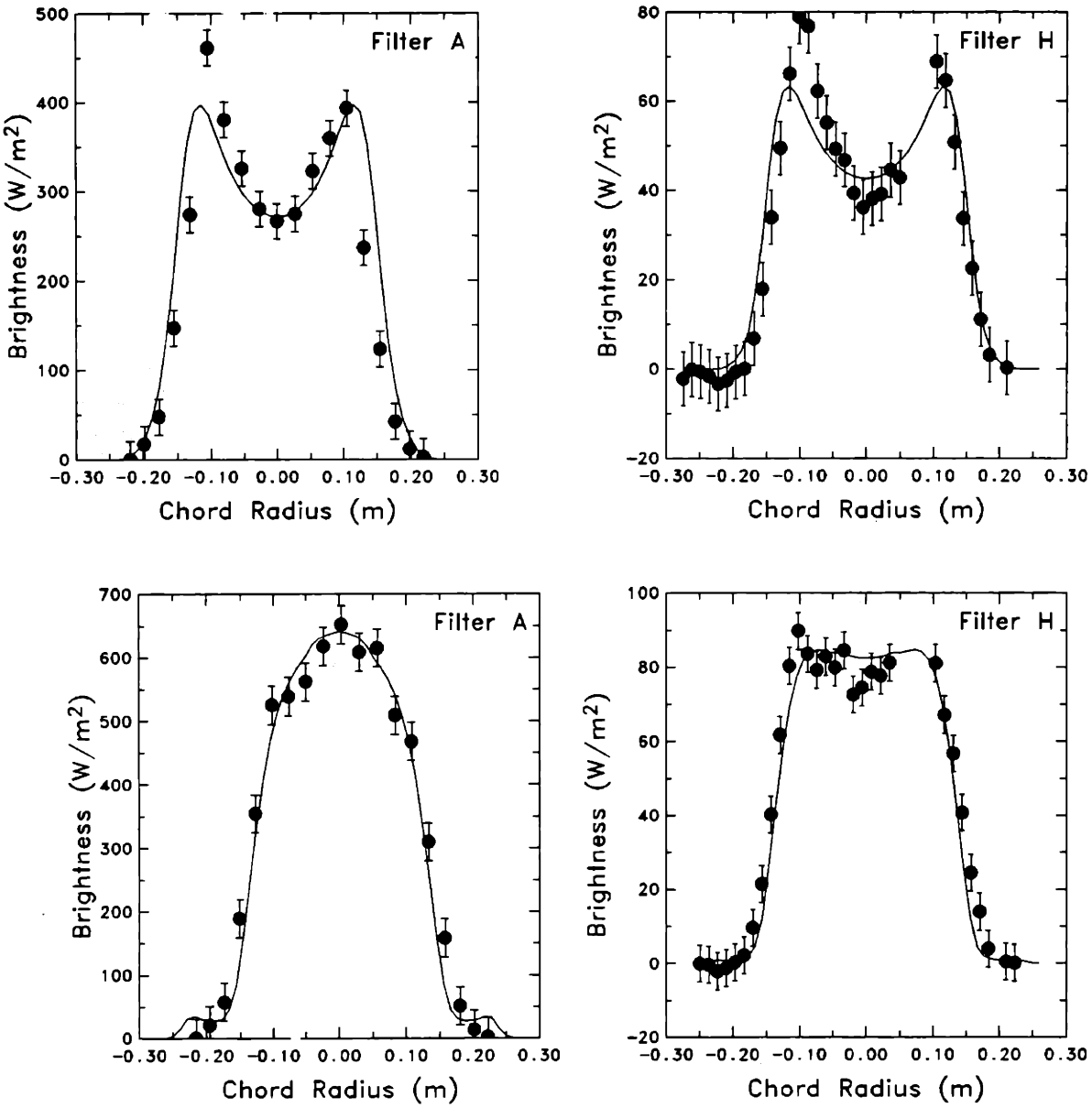

Figure 4.33: The x-ray brightness profiles were calcuated from the aluminum profiles of Fig. 4.32. Before the crash the x-ray profiles were hollow (top pair), because the aluminum was peaked near the plasma edge. After the crash, the profiles were slightly peaked or flat, as a large amount of aluminum was transported into the plasma.

the high density case, the low density, high q_a discharge of Fig. 4.36 had a very small sawtooth amplitude and there was only a small perturbation to the aluminum density profile. The total density dropped less than ~15%, both the H-like and He-like states remained unchanged, and the fully stripped density dropped by $\sim$ 70%. The effect of a sawtooth crash on the impurity density profile was thus dramatically different, depending on the shape of the profile prior to the onset of the instability.

A general conclusion from this collection of profiles is that the most peaked profile undergoes the greatest drop due to a sawtooth crash, and the most hollow profile undegoes the greatest increase. Consequently, discharges with long sawtooth periods, such as the high density discharge of Fig. 4.34, allow the aluminum density profiles to reach the most peaked state. This behavior was demonstrated numerically [63], and is in qualitative agreement with the observation of strong impurity accumulation coincident with sawtooth period lengthening or the complete cessation of sawteeth in several tokamaks [59,43,44,48,62,41,52,42]. This result is also reminiscent of strong impurity accumulation discovered in ELM-free H-mode plasmas [64]. This issue of impurity accumulation during periods with reduced MHD activity will be especially important for tokamak experiments operated in regimes of enhanced confinement, because those regimes also often exhibit detrimental improvement in impurity confinement. These observations serve to emphasize the need for proper inclusion of MHD instability-driven transport in transport modeling.

A more specific conclusion about the effect of sawteeth may be made by examining the profiles in the high density case of Fig. 4.34. In this case the profile was originally flat, then it was driven hollow by the sawtooth. This implies that the sawtooth indeed is behaving as a convective mechanism, not diffusive. If the process were purely diffusive, it would lead to perfectly flat profiles. Thus the rough agreement found with the convection-driven confinement scaling is not surprising. This result may be useful in determining the proper model to use for sawtooth-induced transport.

4.3.3 Charge State Distribution Profiles

The distribution of the three highest aluminum charge states was found from the density profiles shown in Figs. 4.21–4.29. Experimental profiles of the charge state fractions are shown in Figs. 4.37a–4.45a. For comparison the charge state fraction calculated under the assumption of coronal equilibrium using the atomic transition rates of Mewe [204] are given in Figs. 4.37b–4.45b. (Appendix E presents a comparison of Mewe's recom-

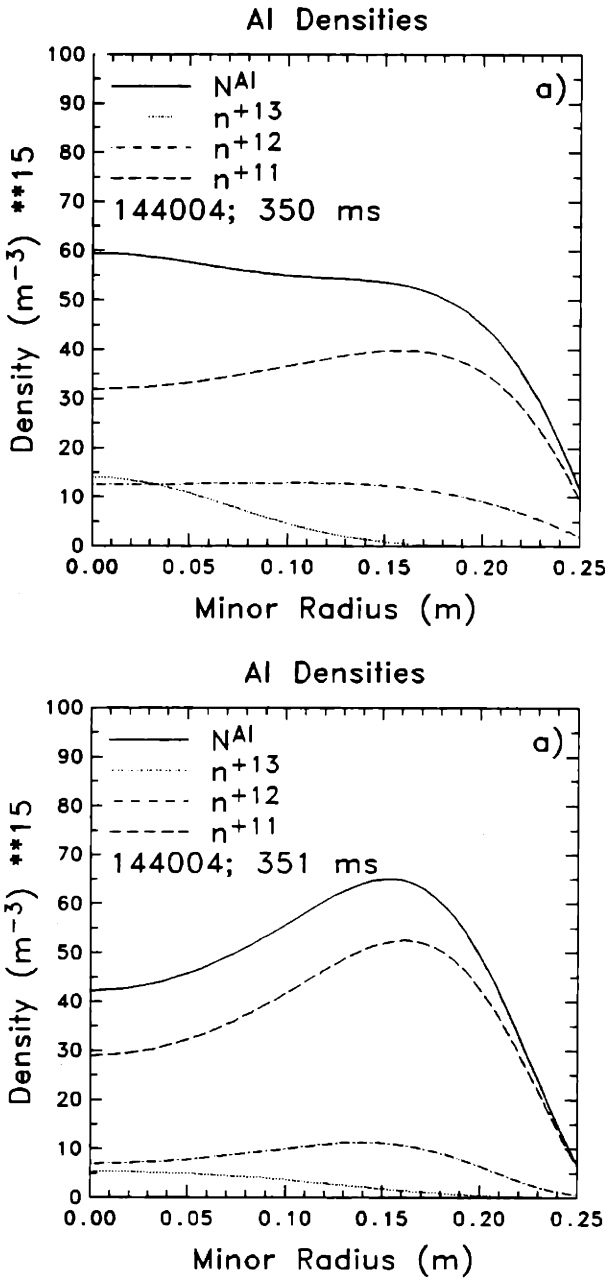

Figure 4.34: Aluminum density profiles are shown a) before and b) after a sawtooth crash in a high density, high current discharge (28/320/6.3).

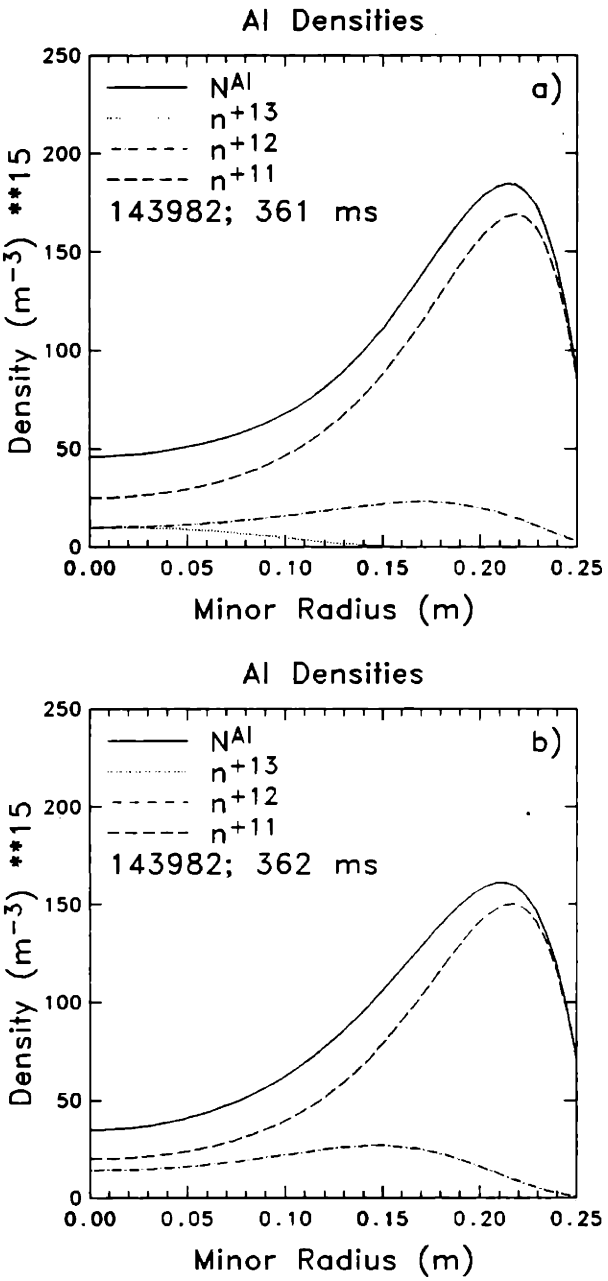

Figure 4.35: Aluminum density profiles are shown a) before and b) after a sawtooth crash in a low density, high current discharge (28/320/2.0).

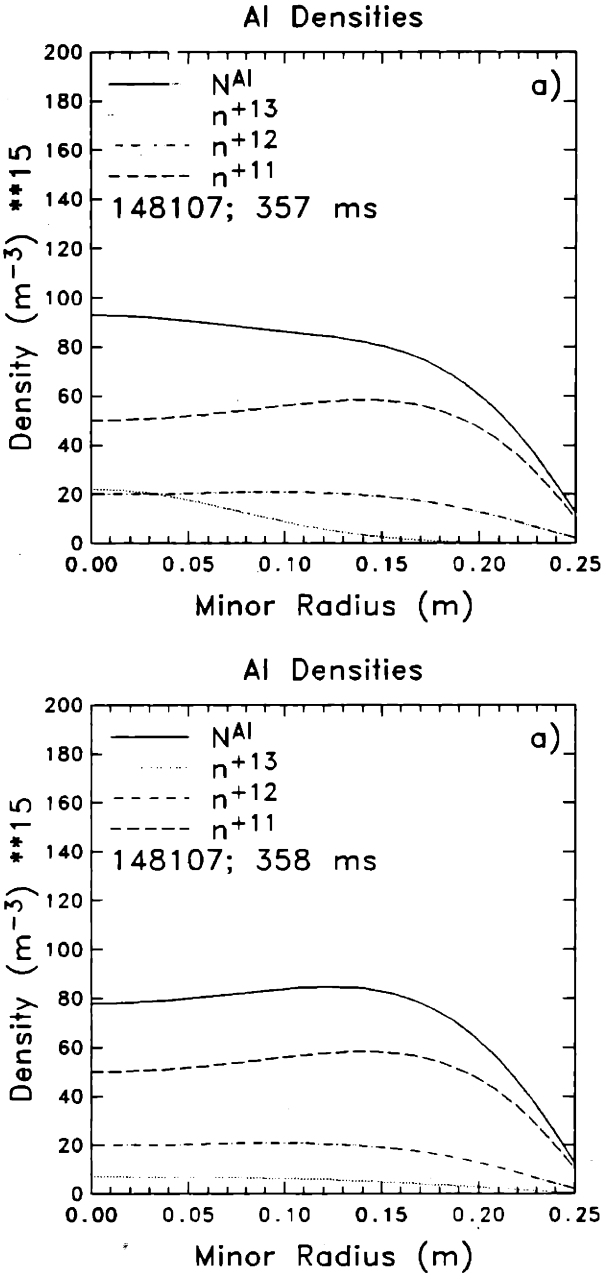

Figure 4.36: Aluminum density profiles are shown a) before and b) after a sawtooth crash in a low density, low current discharge (28/160/2.0).

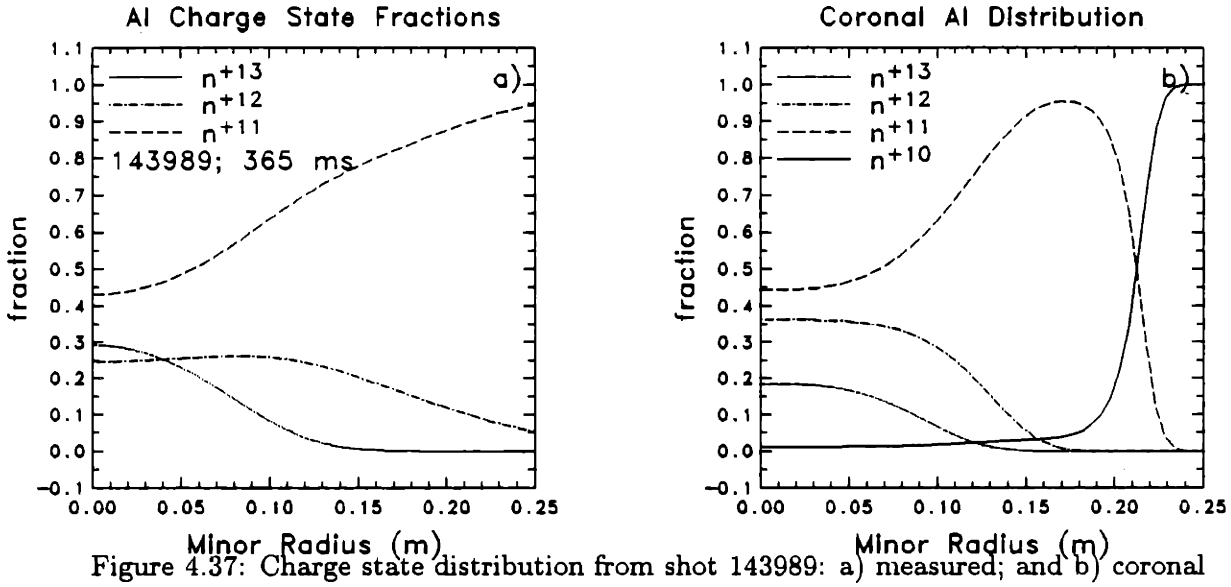

Figure 4.37: Charge state distribution from shot 143989: a) measured; and b) coronal equilibrium prediction.

bination rates with those of some other references that suggests the rates of Ref. [204] for recombination into He-like and Li-like states may be a factor of two too high.) In coronal equilibrium radiative and dielectronic recombination and collisional ionization are assumed to be the only important atomic processes. In a low density, optically thin plasma, this is usually a valid model, because collisional deexcitation and radiation-induced transitions are rare. The rate of change of a particular charge state density is then

$$\frac{\partial n_j}{\partial t} = I_{j-1} n_{j-1} - (R_j + I_j) n_j + R_{j+1} n_{j+1}, \tag{4.25}$$

where I_j and R_j are the collisional ionization and total (radiative plus dielectronic) recombination rates respectively.

In equilibrium the net rate of change is zero, so the charge state densities for all states of an atom of nuclear charge Z may be written in terms of one another as

$$\begin{aligned} -I_0 n_0 + R_1 n_1 &= 0 \\ I_0 n_0 - (I_1 + R_1) n_1 + R_2 n_2 &= 0 \\ &\vdots \\ I_{Z-2} n_{Z-2} - (I_{Z-1} + R_{Z-1}) n_{Z-1} + R_Z n_Z &= 0 \\ I_{Z-1} n_{Z-1} - R_Z n_Z &= 0 \end{aligned} \tag{4.26}$$

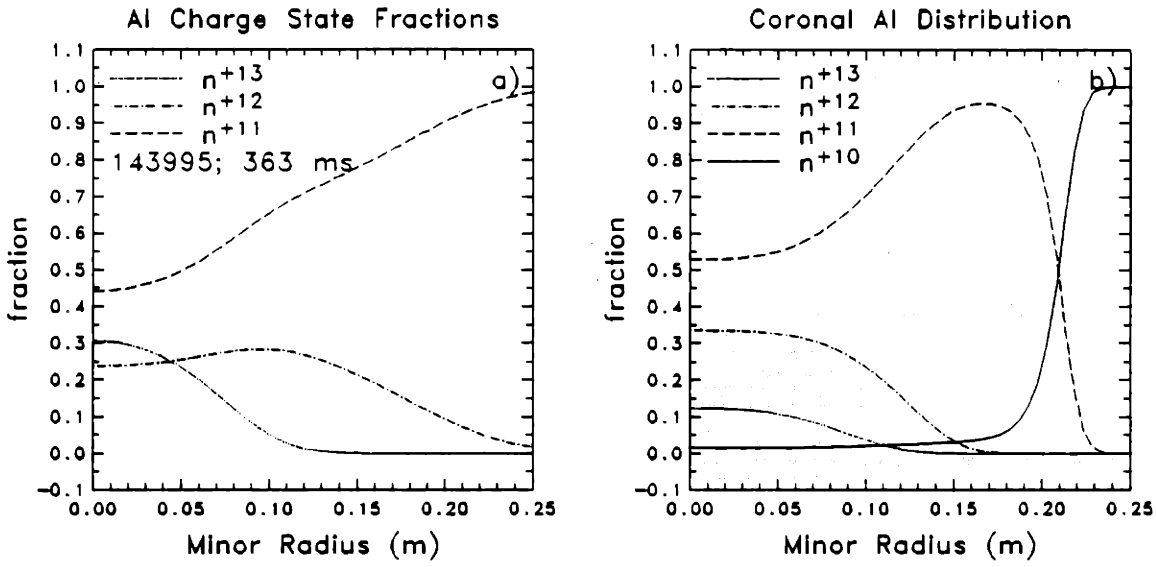

Figure 4.38: Charge state distribution from shot 143995: a) measured; and b) coronal equilibrium prediction.

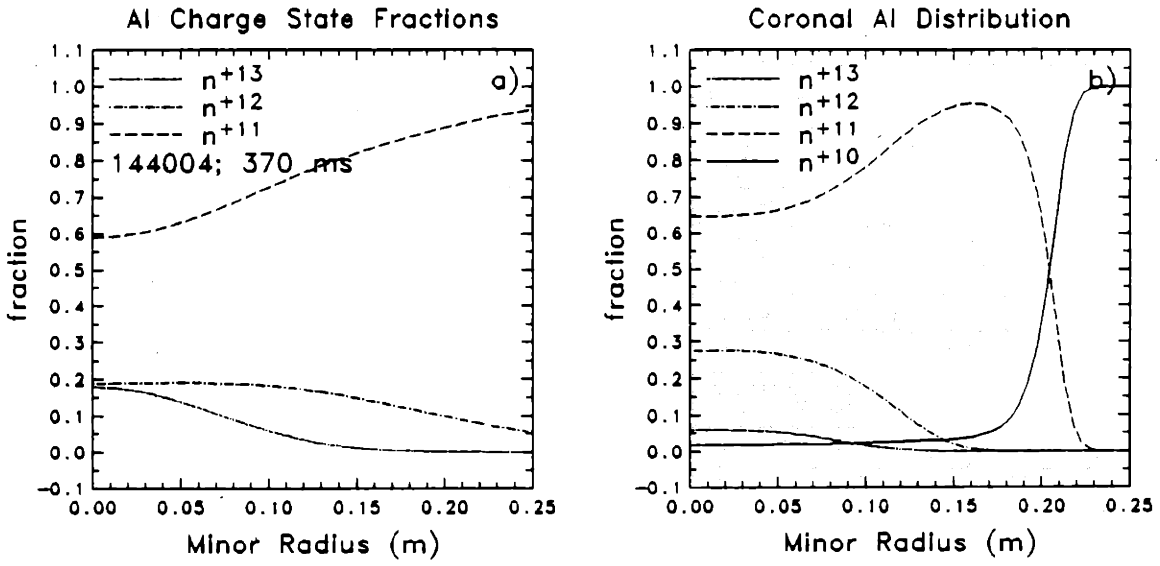

Figure 4.39: Charge state distribution from shot 144004: a) measured; and b) coronal equilibrium prediction.

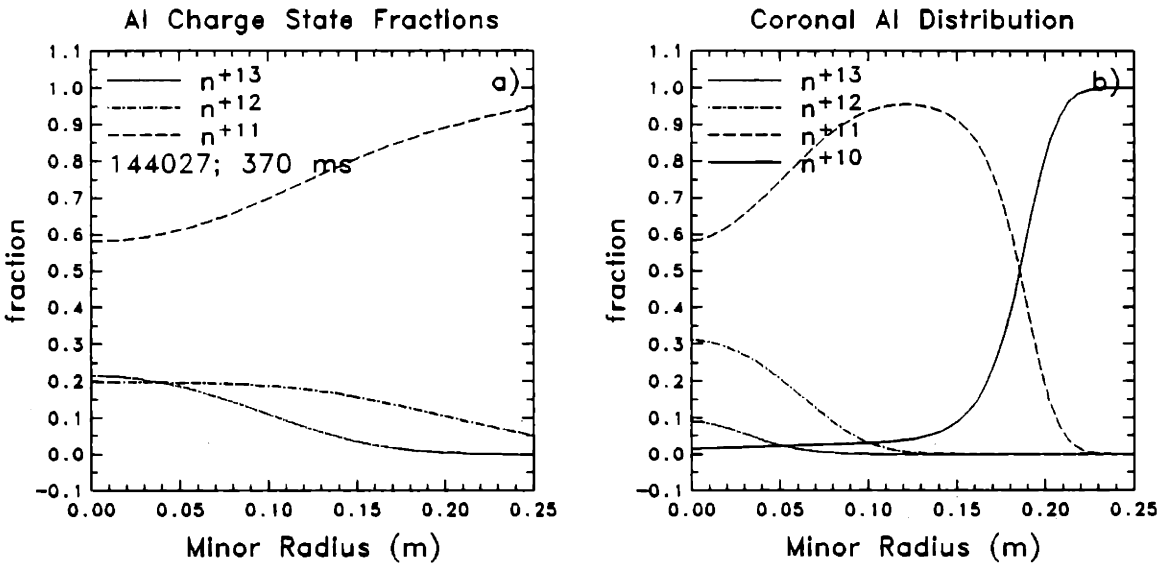

Figure 4.40: Charge state distribution from shot 144027: a) measured; and b) coronal equilibrium prediction.

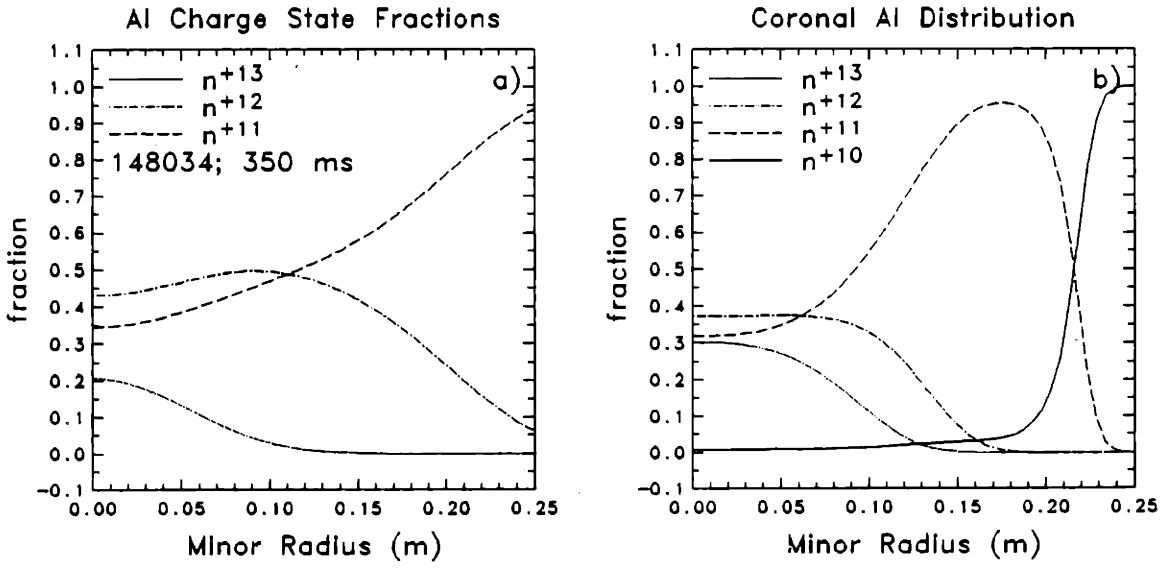

Figure 4.41: Charge state distribution from shot 148034: a) measured; and b) coronal equilibrium prediction.

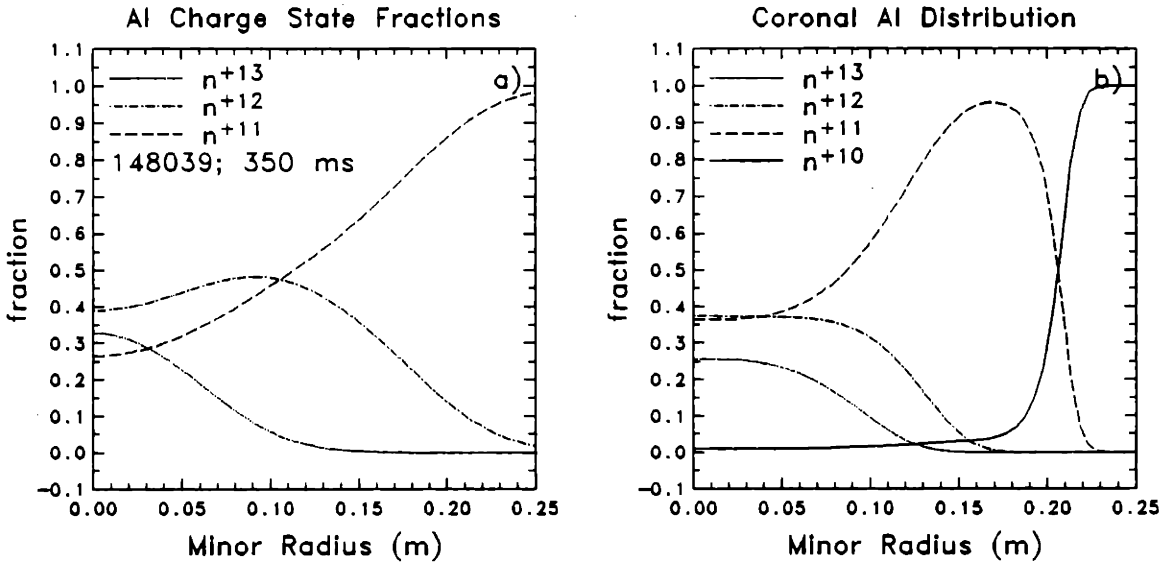

Figure 4.42: Charge state distribution from shot 148039: a) measured; and b) coronal equilibrium prediction.

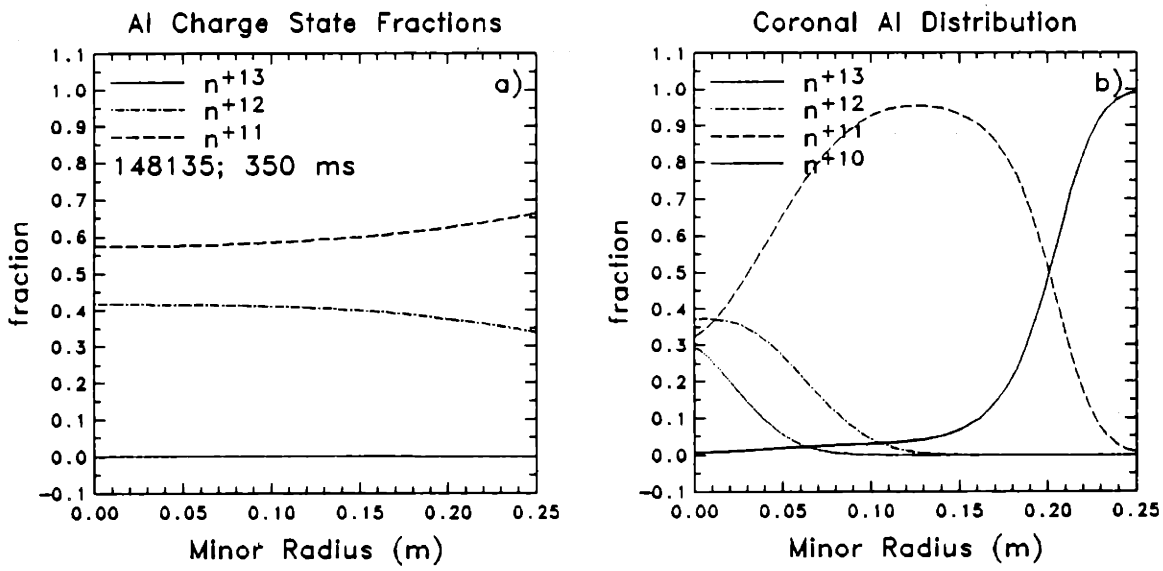

Figure 4.43: Charge state distribution from shot 148135: a) measured; and b) coronal equilibrium prediction.

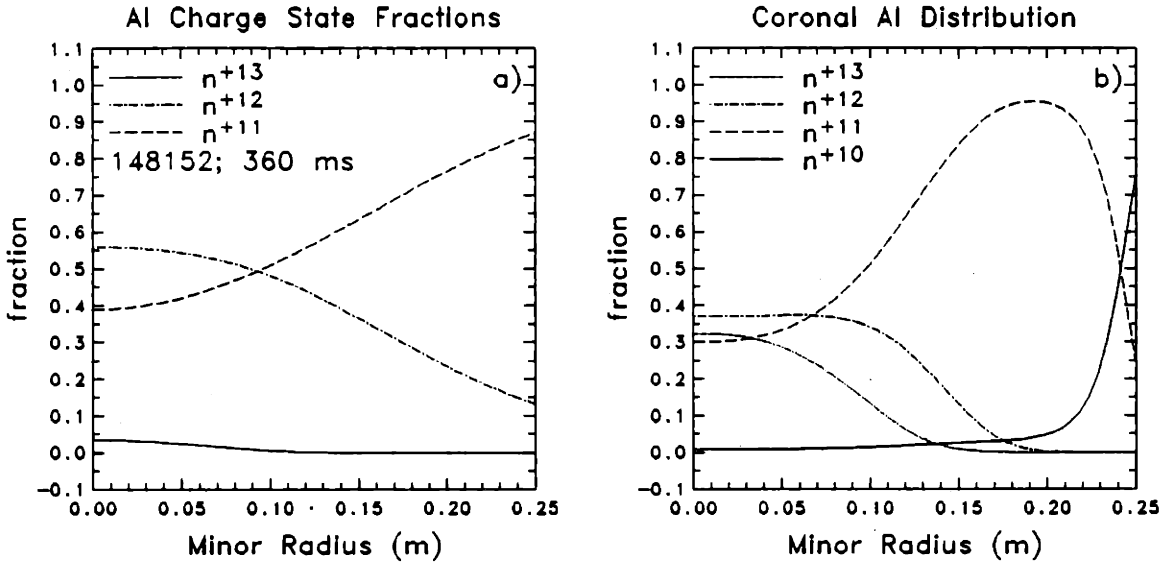

Figure 4.44: Charge state distribution from shot 148152: a) measured; and b) coronal equilibrium prediction.

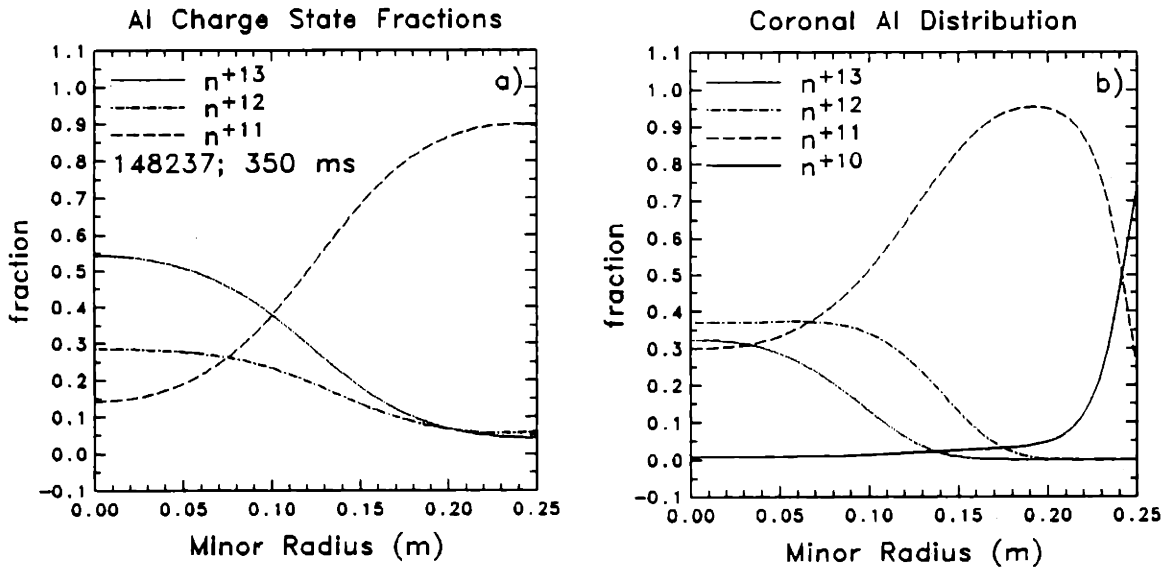

Figure 4.45: Charge state distribution from shot 148237: a) measured; and b) coronal equilibrium prediction.

Table 4 3:
Central Charge State Fractions

Shot	T_{e0} (keV)	τ_c (ms)	τ_s (ms)	τ_i (ms)	f_m^{+11}	f_m^{+12}	f_m^{+13}	f_c^{+11}	f_c^{+12}	f_c^{+13}
143989	0.86	20.5	4.0	20.9	39.5 ± 3.5	28.4 ± 3.3	30.6 ± 1.9	42.0	36.6	20.4
143995	0.75	29.2	6.1	24.1	44.7 ± 1.0	28.2 ± 4.5	26.0 ± 4.1	55.6	32.4	10.6
144004	0.68	28.0	5.7	28.0	51.6 ± 1.1	29.4 ± 7.5	18.3 ± 5.5	64.5	27.7	6.0
144027	0.73	23.7	2.6	40.0	52.6 ± 5.6	26.6 ± 6.6	20.8 ± 0.4	58.3	31.1	9.0
148034	0.96	30.5	3.6	14.7	32.8 ± 1.7	45.4 ± 2.4	20.7 ± 0.3	32.1	37.2	29.9
148039	0.92	40.6	4.5	13.4	26.8 ± 0.3	43.4 ± 4.4	28.9 ± 3.7	35.9	37.3	25.9
148135	0.97	33.2	0.8	28.6	58.0 ± 0.3	41.5 ± 0.5	0.4 ± 0.4	31.0	37.1	31.1
148152	0.98	32.0	2.9	13.4	34.8 ± 3.9	56.9 ± 0.6	7.6 ± 4.2	30.0	37.0	32.3
148237	1.16	96.0	3.1	11.0	13.8 ± 0.7	32.4 ± 4.4	52.3 ± 2.2	17.8	33.2	48.6

Thus, in this approximation, adjacent charge state densities are simply related through

$$\frac{n_{j+1}}{n_j} = \frac{I_j}{R_{j+1}}. \tag{4.27}$$

The results shown in Figs. 4.37–4.45 are summarized in Table 4.3 and Figs. 4.46a-c. The table repeats the central temperature, the measured confinement time, the sawtooth period and the ionization time from Table 4.2. Then the measured central charge state fractions are given, followed by the coronal prediction for the charge state densities in the last three columns. Fig. 4.46 shows graphically the quantities given in the last six columns of the table. Coronal calculations from two other references [190,205] are also shown in Fig. 4.46 as an indication of the uncertainties in theoretical atomic transition rates.

Most of the discharges examined were found to have charge state distributions close to the coronal predictions. This result was somewhat surprising since typical transport times for the aluminum were less than or of the same order of the longest ionization time (see Table 4.3). Furthermore the sawtooth period was always much less than the typical ionization time. Only two of the discharges in Table 4.3 had charge state balances far from coronal equilibrium. One of these (shot 148135) had an extremely high frequency sawteeth, ~ 1.25 kHz. The other had relatively slower sawteeth, ~ 350

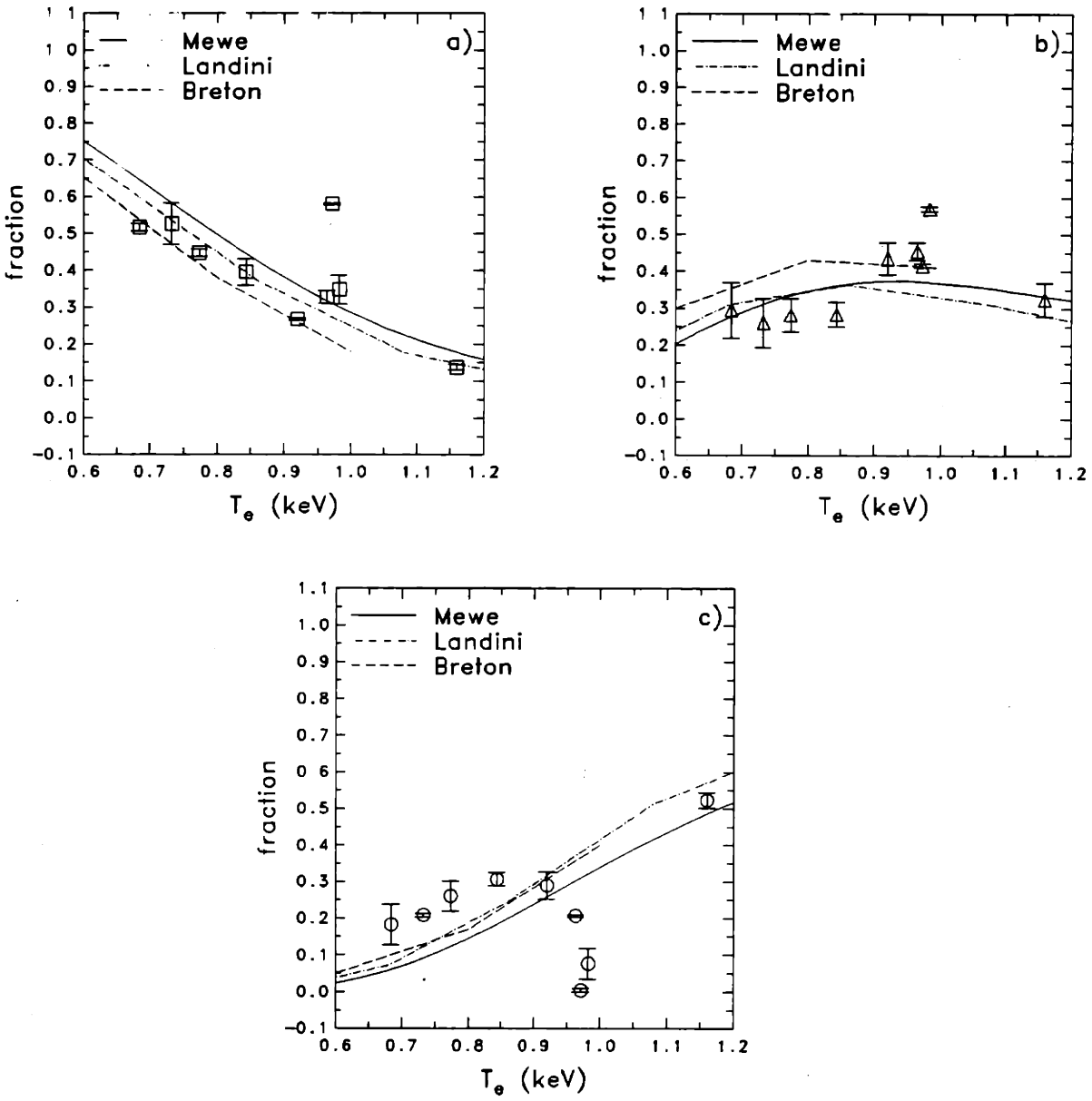

Figure 4.46: The measured central charge state fractions (points) from the 9 discharges in Tables 4.2 and 4.3 are compared to the charge state fractions predicted in coronal equilibrium (lines) for a) He-like aluminum, b) H-like aluminum and c) fully stripped aluminum. The solid lines represents a coronal calculation using the rates of Mewe [204], the dotted lines represent Landini's results [190], and the dashed lines represent the results of Breton [205]. The measured charge state distribution was quite close to coronal in most discharges, even though the atomic transition times were comparable to the transport times.

Hz, but q_a was extremely low, 2.3. Therefore the inversion radius was very large, and each sawtooth mixed a large plasma volume Thus sawteeth played an important role at high repetition frequency, but were less important in determining the charge state balance at lower repetition frequency.

That lower frequency sawteeth (with reasonable r_{inv}) are not so important in determining the overall charge state balance can be understood at least qualitatively by recalling the density profiles shown in Figs. 4.21–4.29. The profiles are generally relatively flat, so the sawteeth do not cause extremely large changes in the individual charge state densities (the biggest change in the fully stripped state was ~70%). Thus after each crash the aluminum does not start from a charge state balance completely out of coronal equilibrium, and the distribution can evolve back to coronal by the time of the next sawtooth crash.

4.3.4 Preliminary Observations of Up-Down Asymmetric Impurity Densities

Most impurity transport modelling in tokamaks is done in one-dimension; the toroidal and poloidal coordinates are often considered ignorable (*e.g.*, see chapter 5). In the hot central region of a tokamak plasma this is normally valid, because parallel transport times are very small compared to other characteristic times associated with mechanisms that can cause significant asymmetries along a flux surface. However, impurity density asymmetries have been found experimentally and predicted theoretically. Possible candidates for causing asymmetries are vertical ion drifts due to the magnetic field curvature [206], localized sources [207], asymmetries in ionization and recombination [208], MHD instabilities [207], and toroidal rotation induced by neutral beam injection [209].

Strong asymmetries in edge impurity density profiles have been observed in Alcator-A [206,29], PLT [207], PDX [208], and ASDEX [209]. Asymmetries in Alcator-A were attributed to the ability of an ion to drift upward a significant distance ($d_{\nabla B}$) during the time for a poloidal excursion of one radian. Asymmetries in PLT were attributed to operational details, specifically the gas feed and limiter conditions, or else to disruptive instabilities. Asymmetries in PDX were attributed to localized sources and poloidal asymmetries in particle recycling for species outside the limiter radius, and to vertical drifts for particles inside the limiter. A quasi-fluid neoclassical transport theory was shown to accurately reproduce the level of these asymmetries and the observed change

in direction during a single discharge [208,210]. Asymmetries in ASDEX were attributed to large toroidal rotation velocities induced by neutral beam injection, as predicted in neoclassical transport theory [211,212]. Because impurity density asymmetries have been observed elsewhere, and were predicted in collisional transport theory, evidence for such asymmetries was examined in TEXT.

The aluminum injected into TEXT constituted a trace, non-recycling impurity species (centrally $n_{Al} \simeq 5 \times 10^{16}\ \mathrm{m}^{-3}$, $Z_{Al} \simeq 11, n_e \simeq 5 \times 10^{19}\ \mathrm{m}^3$, so $\alpha_{Al} \equiv n_{Al} Z_{Al}^2 / n_e \simeq 0.1$). Observation of a non-recycling species is important in the context of poloidal asymmetries because, as noted above, such asymmetries can sometimes be attributed to asymmetries in recycling from the walls and limiter [208]. By examining a non-recycling impurity, this possible mechanism for density profile asymmetries is eliminated.

Only the horizontal array with a soft x-ray filter (25μm Be) was used to determine the up-down aluminum density asymmetry. No comparable in-out asymmetry was found in the data from the vertical-viewing array. Furthermore there was no change in the vertical plasma position measured by magnetic diagnostics. Thus the observed asymmetries could not be attributed to bulk up-down movement of the plasma column.

The level of asymmetry was quantified by defining the experimental asymmetry parameter

$$\Delta_x \equiv \frac{I(+p) - I(-p)}{I(+p) + I(-p)}, \tag{4.28}$$

where $I(\pm p)$ was the net signal from the x-ray detector viewing the chord with impact radius $\pm p$ (the net signal is the signal after subtracting the pre-injection background as described in section 4.2.3). An important feature of this parameter is that it was very closely related to the *local* asymmetry in the plasma; integration along a viewing chord did not cause Δ_x to vary much from the local up-down asymmetry in the x-ray emissivity, $\epsilon_s(r)$, defined through

$$\epsilon(r,\theta) = \epsilon(r)\left[1 + \epsilon_s(r)\sin\theta\right]. \tag{4.29}$$

The total x-ray emissivity was of course dependent on the electron density, the electron temperature, and all ionic species present. By subtracting the pre-injection background as described in section 4.2.3, only the aluminum radiation contributed to the net signal so the measured net emissivity could be expressed as

$$\begin{aligned}\epsilon(r,\theta) &= n_e(r,\theta)\left[n_{11}(r,\theta)P_{11}(T_e(r,\theta)) + n_{12}(r,\theta)P_{12}(T_e(r,\theta))\right. \\ &\quad \left. + n_{13}(r,\theta)P_{13}(T_e(r,\theta))\right].\end{aligned} \tag{4.30}$$

Asymmetries in the electron density and temperature are expected to be much smaller, by a factor of $\sqrt{m_e/m_i}$, than asymmetries in the impurity density. Therefore, impurity density asymmetries should by far dominate any asymmetries in the measured x-ray profiles, and Δ_x should constitute a direct measurement of the local impurity density up-down asymmetry, $n_s(r)$. As shown in section 4.3.2, He-like aluminum (n_{11}) and H-like aluminum (n_{12}) were the dominant charge states found in most of the TEXT discharges considered herein. Again, the power functions $P_j(T_e)$ for the four highest charge states are shown in Appendix C.

An example of the temporal evolution after an aluminum injection of Δ_x, at several different chord radii for a high density, low q_a hydrogen discharge is shown in Fig. 4.47. The signal was smoothed over a 10 ms period. Fig. 4.47a shows Δ_x obtained using the *total* $I(\pm p)$ (*i.e.*, $I(\pm p)$ with the preinjection background subtracted) in Eq. 4.28, and Fig. 4.47b shows Δ_x obtained using the net $I(\pm p)$. (Δ_x in Fig. 4.47b is very noisy before the injection because the quantity in the denominator $I(+p)+I(-p)$ is near zero.) The level of asymmetry prior to the injection can be seen in Fig. 4.47a; it is $\lesssim 5\%$, and is not monotonic with chord radius. The level of asymmetry after background subtraction is seen in Fig. 4.47b. Note the monotonic increase with radius from $\sim 2\%$ to $\sim 20\%$ as r goes from 2.7 to 17.7 cm. Profiles of Δ_x from six discharges are shown in Figs. 4.48 and 4.49. Figs. 4.48a–c show profiles of the asymmetry for low q_a, intermediate density discharges (2.8/320/4) with hydrogen, deuterium, and helium working ions respectively. Figs. 4.49a–c show Δ_x profiles for high q_a, low density discharges (2.8/150/2), again in hydrogen, deuterium and helium discharges. An asymmetry on the order of the inverse aspect ratio, ϵ, was found toward the plasma edge in all these discharges. Surprisingly Δ_x was not very sensitive to the global plasma parameters. The asymmetry increased with working gas mass and charge approximately as $\sqrt{m_i/Z_i}$, and decreased only slightly with decreasing current. The dependence on m_i and Z_i was the same as the dependence of the global impurity confinement time found in section 4.3.1. (The vertical error bars represent the standard deviation in the Δ_x parameter typically averaged over 10~20 ms, and the error bars in the x-direction represent the vertical extent of the x-ray viewing chords.)

As pointed out above, poloidal asymmetries are predicted in neoclassical transport theory [210,213,208,212]. Specifically, for a highly collisional impurity of charge Z in the Pfirsch-Schlüter regime, asymmetries in the flux surface of the order of the inverse

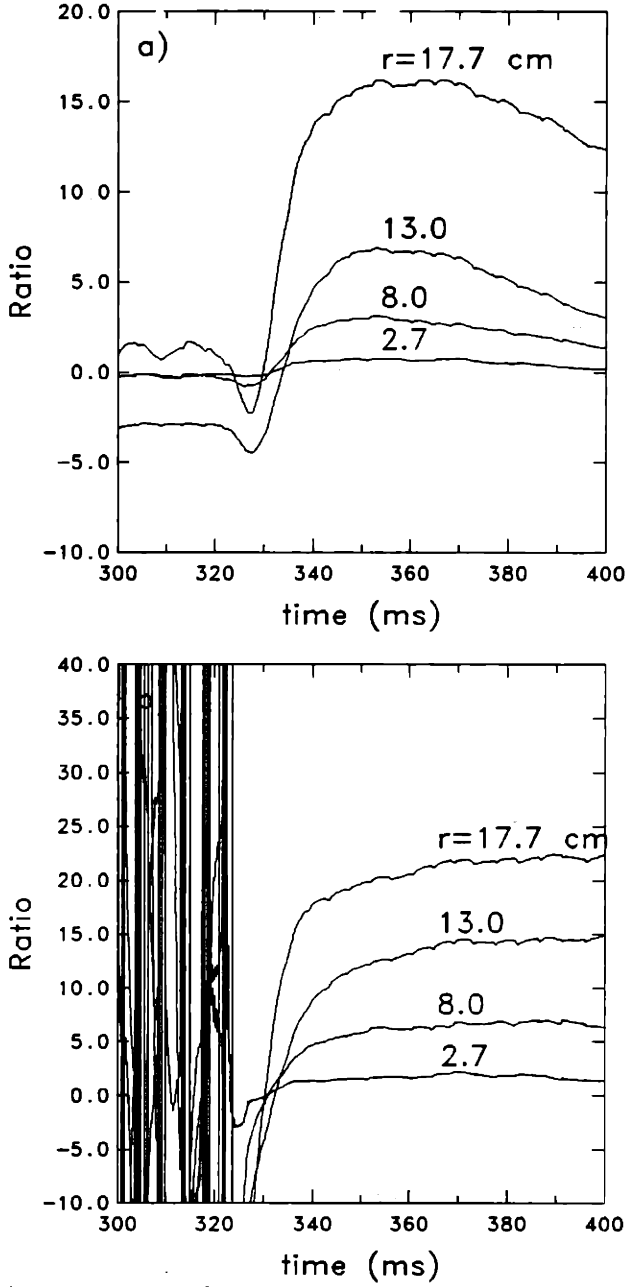

Figure 4.47: The experimental asymmetry parameter was measured at several chord radii. Aluminum was injected at 325 ms in this discharge ($B_T = 2.8\ T$, $I_p = 320$ kA, $\bar{n}_e = 6.3 \times 10^{13}$ cm^{-3}). a) The asymmetry parameter was calculated without performing the pre-injection background subtraction. Note the pre-injection asymmetries are $\lesssim 5\%$, and vary randomly with the radius. b) The asymmetry parameter after pre-injection background subtraction is of the same order as the inverse aspect ratio.

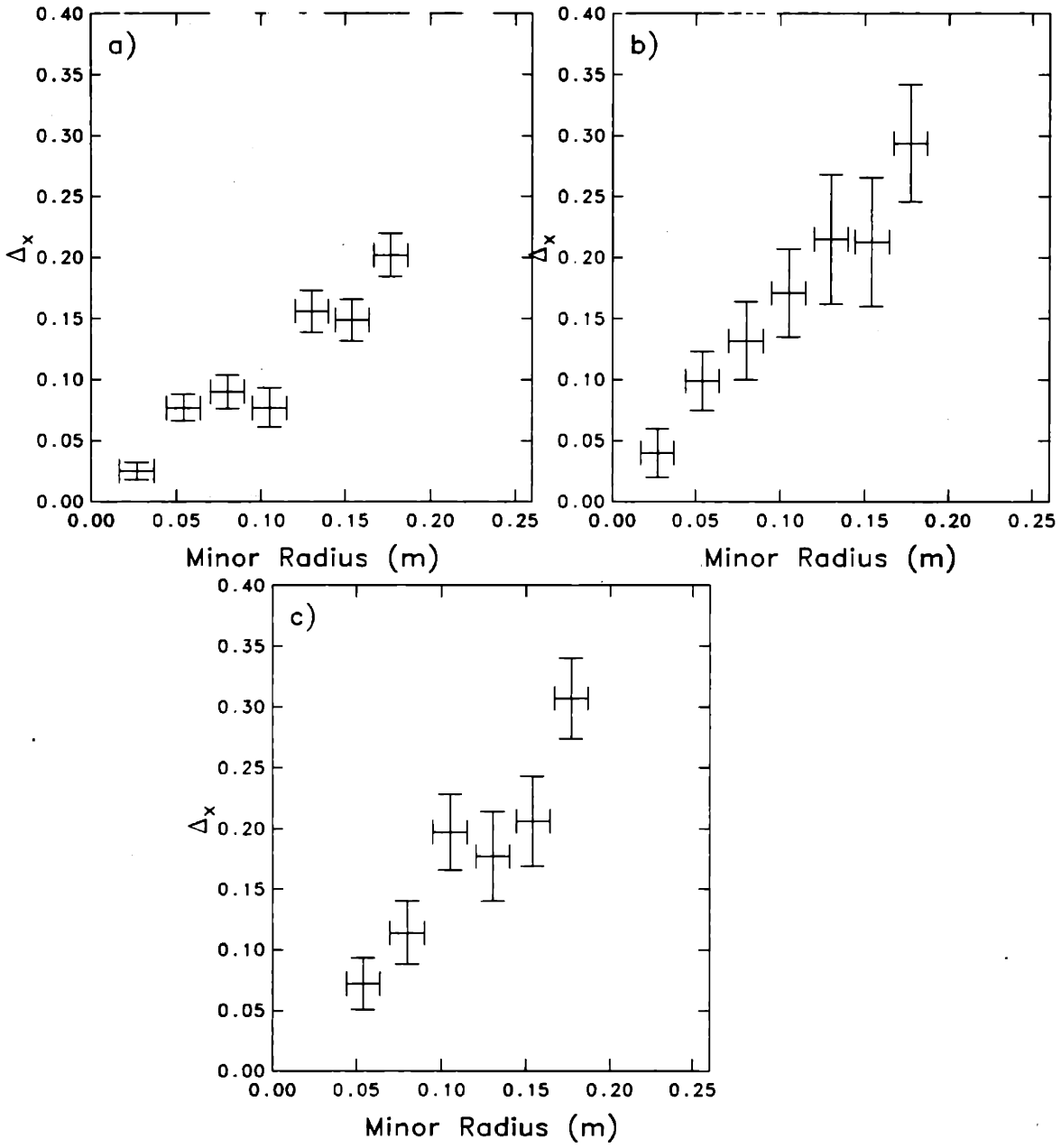

Figure 4.48: The measured asymmetry parameter is shown for three different discharges. The global plasma parameters were 2.8/320/4) in a) hydrogen, b) deuterium, and c) helium working gases.

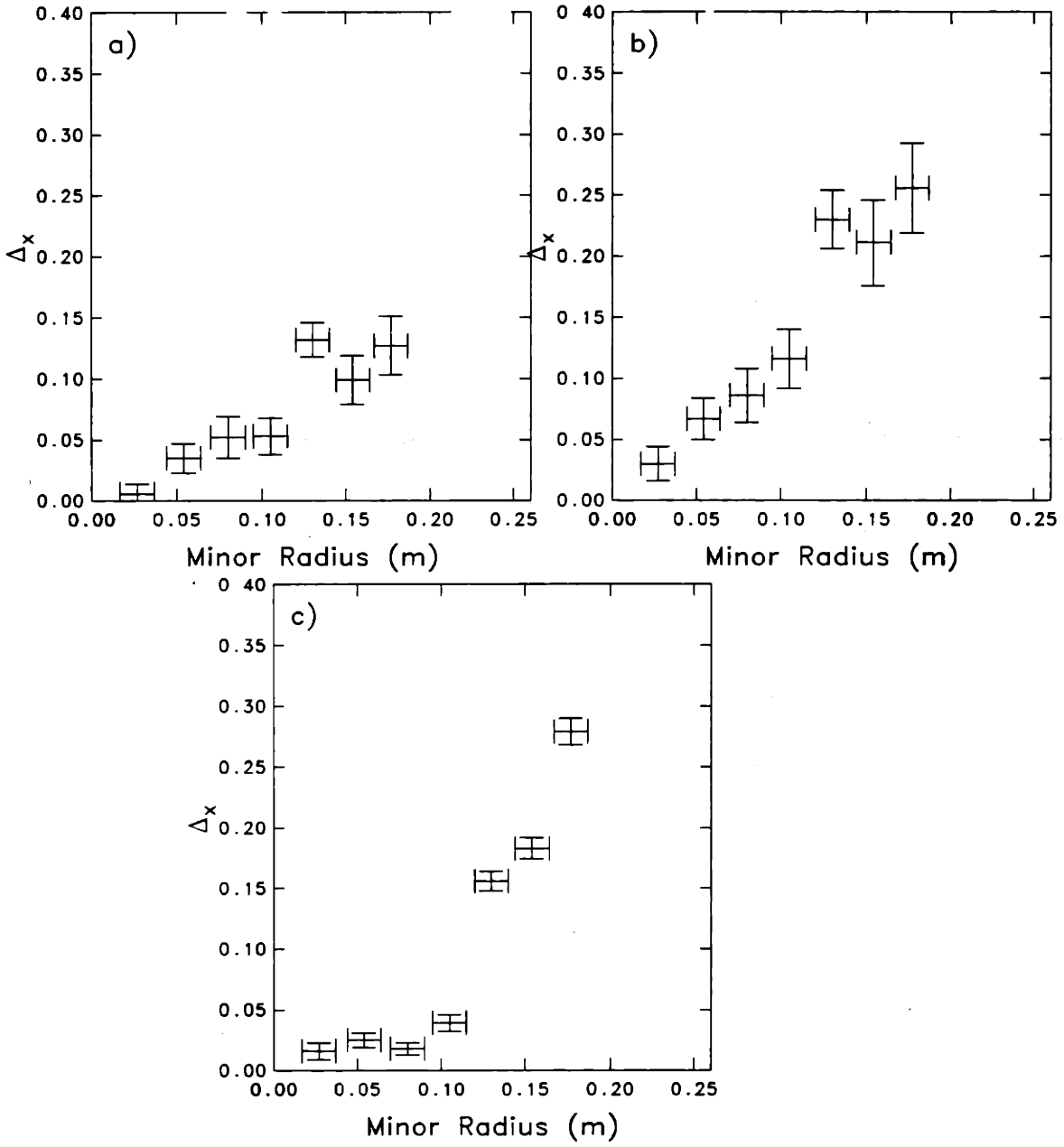

Figure 4.49: The measured asymmetry parameter is shown for three different discharges. The global plasma parameters were 2.8/150/2 in a) hydrogen, b) deuterium, and c) helium working gases.

aspect ratio $\epsilon = r/R$ are predicted when the parameter

$$\Delta = \sqrt{2}\frac{\delta_{pi} Z^2 \nu_i}{\omega_{ti}} \tag{4.31}$$

is of order 1. Here δ_{pi} is the ratio of the working ion gyroradius in the poloidal field to the radial density gradient scale length, ν_i is the total working ion collision frequency, and ω_{ti} is the working ion transit frequency, given by v_{thi}/Rq. Hsu and Sigmar have recently shown that in a toroidal plasma with a small toroidal rotation velocity, the up-down asymmetry is given by [212]

$$n_s(r) = \frac{\epsilon a_\Delta A_d (2 + b_\omega)}{1 + a_\Delta^2 A_d^2} \tag{4.32}$$

where

$$a_\Delta = \frac{2\Delta}{(1 - \frac{T_I}{ZT_i})\frac{T_e \alpha}{T_i + T_e} + \frac{T_I}{T_i}} \left[\frac{576 + 488\sqrt{2}\alpha + 128\alpha^2}{576 + 1208\sqrt{2}\alpha + 434\alpha^2} \right], \tag{4.33}$$

and

$$A_d = -\frac{1}{2}\left\{ r\frac{\partial}{\partial r}\ln\bar{n}_i - \frac{T_I}{ZT_i}\frac{\partial}{\partial r}\ln\bar{n}_I \right\}, \tag{4.34}$$

where a bar over a quantity here indicates its flux surface average. The impurity strength parameter is $\alpha_I = n_I Z_I^2 / n_i$. The normalized toroidal rotation is

$$b_\omega = \frac{2(\mu - 1 + \frac{T_i - T_I/Z}{T_i + T_e})\frac{\omega^2 R^2 Z}{v_{thi}^2}}{(1 - \frac{T_I}{ZT_i})\frac{T_e}{T_i + T_e}\alpha + \frac{T_I}{T_i}} \tag{4.35}$$

It is important to note from Eq. 4.32 that, in the case of zero toroidal rotation, the maximum asymmetry is $n_{s,max} = \epsilon$.

Sufficient experimental and theoretical information was not available to make detailed comparisons between experiment and theory. Specifically the density profile of the heavy intrinsic impurity in TEXT (titanium) was not well known and the toroidal rotation velocity has not yet been measured in TEXT. Also, the theory described above is for a single impurity species diffusing on the working ions. The experimental situation involves a trace impurity diffusing on working ions and at least two other impurity species (carbon and titanium). A full theoretical treatment of this more complicated situation is not yet available.

In summary, preliminary evidence of up-down asymmetric impurity density profiles was found. The experimental asymmetry parameter Δ_x increased with the mass and charge of the working ions approximately as $\sqrt{m_i/Z_i}$. It also decreased weakly with the total plasma current and the electron density. The asymmetry usually increased

nearly linearly with minor radius. It must be emphasized that this is a very preliminary observation Possible systematic causes for the observed asymmetries in the x-ray signals have not been completely ruled out. Some of these possible causes are enumerated below.

1. It is possible that the horizontal x-ray array was not properly aligned. This may be measured in the future. However, it should be noted that if the horizontal array were much out of alignment, strong asymmetries would be found in the x-ray signals before impurity injection and on the hard filter signal after injections. Neither of these was observed. (Fig. 4.47a shows that the level of asymmetry prior to an aluminum injection was $\simeq 5\%$ for all the x-ray chords.)

2. Calibration errors could have caused the observed asymmetries. This could be tested by mounting the detectors upside-down and performing the injection experiments again. However, calibration errors would also lead to asymmetries before the injection.

3. An uneven beryllium window, or pinholes in one side of the beryllium window would cause observed asymmetries. However, the data shown in Figs. 4.48 and 4.49 represents data taken with two different beryllium windows in the horizontal x-ray array. It is unlikely that two independent windows would have pinholes in the exact same place.

4. Changes in the plasma vertical position would cause the observed asymmetries. However, magnetic measurements showed no large change in vertical position. Furthermore the centroid of the x-ray brightness profiles from the horizontal array was found to agree well with magnetic measurements of the vertical plasma center in other experiments. This indicated that the magnetic diagnostics were reliably reporting the true vertical plasma center.

5. The x-ray imaging system was installed on the port directly adjacent to the limiter. There may be some plasma/limiter interaction causing the observed asymmetry. This could be tested by moving the x-ray array to a port away from the limiter.

6. Plasma parameters other than the impurity density may have asymmetries. As noted above, asymmetries in the electron density and the electron temperature are expected to be less than those in the impurity density by a factor of $\sqrt{m_e/m_i}$. Up-down asymmetries in the ion temperature have been observed in TEXT with an active charge exchange diagnostic [203].

Thus the observation of up-down asymetries in impurity density profiles requires verification It would also be useful to study other impurities to see if the Z^2 scaling predicted in Eqs. 4 31 and 4 32 holds.

4.4 Conclusions

Several facets of measured aluminum transport in TEXT were described in this chapter. First, an approximate scaling for the impurity confinement time was established by examining general trends in the data: $\tau_c \simeq 1286 Z_{eff} \bar{n}_e \sqrt{m_i/Z_i}/I_P$. A slightly more accurate scaling was found by performing a regression analysis on the data: $\tau_c \simeq 571 Z_{eff}^{1.16} \bar{n}_e^{1.25} (m_i/Z_i)^{0.57} I_P^{-0.93}$. These two different scalings agree well considering the small database of 105 discharges. Second, aluminum density profiles averaged over a sawtooth period were shown. The sawteeth were then shown to play an important role in the overall impurity transport. Sawteeth significantly enhanced the inward flow of impurities just after an injection, when the impurities were concentrated near the plasma edge. Sawteeth also acted to prevent central accumulation of impurities by periodically ejecting particles from the plasma center. The sawtooth behaved as a convective transport mechanism. Third, the measured charge state balance was compared to coronal equilibrium calculations. The aluminum ions were close to coronal except in those discharges with very short sawtooth period or large inversion radii. Finally, preliminary evidence for an up-down asymmetry in the aluminum density was shown.

The next chapter describes numerical transport simulations. A few of the discharges discussed in this chapter were chosen, and modelling was performed in order to try and find the operative diffusion and convection.

Chapter 5

Simulation of the Transport of Injected Impurities

5.1 Introduction

Two quantities of primary interest from a measurement of time-dependent profiles of an injected impurity are the transport parameters: the diffusion coefficient and convective velocity. These coefficients are very often difficult to unfold from the experimental data. The fundamental reason for this difficulty is the form of the particle transport equation for species j in cylindrical coordinates,

$$\frac{\partial n_j}{\partial t} = \frac{1}{r}\frac{\partial}{\partial r} r\left[D_j \frac{\partial n_j}{\partial r} + V_j n_j\right] + I_{j-1}n_{j-1} \quad (I_j + R_j)n_j + R_{j+1}n_{j+1} \qquad (5.1)$$

where the diffusion coefficient D_j and the convective velocity V_j may be arbitrary functions of radius. The atomic transition coefficients I_j and R_j give the rates for ionization and recombination respectively, and they are related to the more conventional transition rates [204] by implicit inclusion of the electron density: $I_j = n_e S_j$, and $R_j = n_e \alpha_j$. Values for S_j and α_j used herein were obtained from Ref [204]; there is some evidence that these recombination rates may be as much as a factor of two too high for recombination into the He-like and Li-like charge states (see Appendix E).

It is clear from the form of Eq. 5.1 that to obtain values for D and V from measurements of time-dependent particle density profiles one must accurately know both the time dependence and the *gradient* of the density. The latter consideration imposes the most difficulty. Gleaning gradients from experimental data is often uncertain because small fluctuations in data can lead to large errors in the inferred slope. Thus from measurements with limited spatial and temporal resolution, it is often impossible to accurately determine the actual values of D and V and their radial dependencies.

Analytic solutions have been found to Eq. 5.1 when it is couched in the form of an eigenvalue problem with the separable solution $n(r,t) = n(r)F(t)$ [63,214,215]. While this is not the most general form, solutions of this form are often useful in the interpretation of experimental impurity transport data when the radial dependence of D and V is restricted. Specifically, when D is assumed constant ($D = D_0$) and V is assumed linear with the radius ($V = V_0(r/a)$), Eq. 5.1 reduces to Kummer's Equation with confluent hypergeometric functions as the eigensolutions [216,35,65,217]. The eigensolution with the longest time constant represents the quasi-equilibrium density profile that decays with a constant exponential decay time equivalent to the particle confinement time, τ_c. The eigensolution with the second longest time constant represents the response of the density profile to perturbations. For example, it corresponds to the time scale for the post-injection initial profile to evolve to the quasi-equilibrium profile. By matching these two time constants to experimentally-determined values, D_0 and V_0 may be inferred from the data. Similar models with constant D and linear V have been used successfully to match impurity transport data in several experiments [63,35,65,52,218,47,31,55], as well as working ion transport [217]. However, in many instances this sort of model is insufficient to explain transport data [37,30,29]. In the present work with aluminum injected into TEXT, for example, such a simple model can easily predict the correct time behavior of the central soft x-ray brightness, but the profile shapes are then not predicted correctly. Furthermore, an *ad hoc* model with constant D and linear V is not very physical, and is not the result of any theory.

An alternate approach to finding D and V from experimental data is numerical simulation. In this method, a computer model is created and the values of D and V are varied in the model until they agree well with the data. This chapter describes two numerical methods used for computer simulation that have been compared to the experimental data from impurity injection experiments on TEXT. The different methods, explicit and implicit, differ in the treatment of the quantity n_j on the right side of Eq. 5.1. (A lucid comparison between explicit and implicit methods can be found in Ref. [219].) In the explicit method, Eq. 5.1 is written in the general form

$$\frac{\partial n}{\partial t} \equiv \frac{n' - n}{\Delta t} = f(n,t), \tag{5.2}$$

where n is the density at time t, and n' is the density at time $t + \Delta t$. In the implicit method, Eq. 5.1 is written in a slightly different form:

$$\frac{\partial n}{\partial t} \equiv \frac{n' - n}{\Delta t} = f(n,n',t), \tag{5.3}$$

so that the function on the right hand side depends not only on the density before the time step, but also on the density after it. In general the accuracy of explicit methods is proportional to the time step [219] and somewhat faster than implicit methods because the function $f(n,t)$ in Eq. 5.2 need only be simply evaluated at the total number of time steps. The accuracy of implicit methods is approximately proportional to the time step squared [220,219].

Both models have been implemented for modelling impurity transport in TEXT. The details of both models are presented in the two following sections.

5.2 Explicit Numerical Charge State Transport Code

In the explicit numerical simulation, the transport equation for species j,

$$\frac{\partial n_j}{\partial t} = \frac{1}{r}\frac{\partial}{\partial r} r \left[D_j \frac{\partial n_j}{\partial r} + V_j n_j \right] + I_{j-1} n_{j-1} - (I_j + R_j) n_j + R_{j+1} n_{j+1}, \tag{5.4}$$

is solved by writing the time derivative on the left hand side as $\Delta n_j / \Delta t \equiv \left(n_j' - n_j \right) / \Delta t$, and using the density profile *before* the time step explicitly on the right hand side of Eq. 5.4. Thus the calculated change in density profile depends completely on the density profile prior to the time step.

The radial gradients in such a code are calculated using the central difference scheme [220], so for a quantity q, for example,

$$\frac{\partial q}{\partial r} \equiv \frac{q^{i+1} - q^{i-1}}{2\Delta}, \tag{5.5}$$

and

$$\frac{\partial^2 q}{\partial r^2} \equiv \frac{q^{i+1} - 2q^i + q^{i-1}}{\Delta^2}, \tag{5.6}$$

where the superscripts denote the spatial mesh location and Δ is the spatial step size. Eq. 5.4 now takes the form

$$\begin{aligned} n_j'^i \;=\; & n_j^i + \Delta t \left\{ \frac{n_j^{i+1}}{4 r^i \Delta^2} \left[r^i \left(4D^i + D^{i+1} - D^{i-1} + 2\Delta V^i \right) + 2\Delta D^i \right] \right. \\ & + \frac{n_j^i}{2 r^i \Delta^2} \left[r^i \left(\Delta \left(V^{i+1} - V^{i-1} \right) - 4D^i \right) + 2\Delta^2 V^i \right] \\ & + \frac{n_j^{i-1}}{4 r^i \Delta^2} \left[r^i \left(4D^i - D^{i+1} + D^{i-1} - 2\Delta V^i \right) - 2\Delta D^i \right] \\ & \left. + I_{j-1}^i n_{j-1}^i - \left(I_j^i + R_j^i \right) n_j^i + R_{j+1}^i n_{j+1}^i \right\}, \end{aligned} \tag{5.7}$$

which can more conveniently be written in matrix form [220,221],

$$\vec{n}' = \overleftrightarrow{\xi} : \vec{n} \equiv \vec{w} \tag{5.8}$$

The density vectors $\vec{n}'$ and $\vec{n}$ have dimensions equal to the number of spatial zones N_s, and each vector element is itself a vector with dimension equal to $Z+1$, the total number of charge states. The matrix $\overleftrightarrow{\xi}$ is thus a tridiagonal matrix with dimension $N_s \times N_s$:

$$\overleftrightarrow{\xi} = \begin{bmatrix} \overleftrightarrow{b}^1 & \overleftrightarrow{c}^1 & & & & \\ \overleftrightarrow{a}^2 & \overleftrightarrow{b}^2 & \overleftrightarrow{c}^2 & & & \\ 0 & \overleftrightarrow{a}^3 & \overleftrightarrow{b}^3 & \overleftrightarrow{c}^3 & & \\ & & & \ddots & & \\ & & & & \overleftrightarrow{a}^{N_s-1} & \overleftrightarrow{b}^{N_s-1} & \overleftrightarrow{c}^{N_s-1} \\ & & & & 0 & \overleftrightarrow{a}^{N_s} & \overleftrightarrow{b}^{N_s} \end{bmatrix} \tag{5.9}$$

Furthermore, the elements of $\overleftrightarrow{\xi}$ are also matrices with dimensions $(Z+1) \times (Z+1)$. In the simulation of injected aluminum in TEXT, only the four highest charge states are considered, so $\overleftrightarrow{a}$, $\overleftrightarrow{b}$ and $\overleftrightarrow{c}$ are 4×4 square matrices, and have the form

$$\overleftrightarrow{a} = \begin{bmatrix} T_1^{i,-1} & & & \\ & T_2^{i,-1} & & \\ & & T_3^{i,-1} & \\ & & & T_4^{i,-1} \end{bmatrix}$$

$$\overleftrightarrow{b} = \begin{bmatrix} 1+T_1^{i,0}-(I_1) & R_1 & & \\ I_1 & 1+T_2^{i,0}-(I_2+R_2) & R_3 & \\ & I_2 & 1+T_3^{i,0}-(I_3+R_3) & R_4 \\ & & I_3 & 1+T_4^{i,0}-R_4 \end{bmatrix}$$

$$\overleftrightarrow{c} = \begin{bmatrix} T_1^{i,+1} & & & \\ & T_2^{i,+1} & & \\ & & T_3^{i,+1} & \\ & & & T_4^{i,+1} \end{bmatrix}. \tag{5.10}$$

The "transport operators" $T^{i,-1,0,+1}$ are taken directly from Eq. 5.7, and are

$$\begin{aligned} T^{i,-1} &\equiv \left(\Delta t/4r^i\Delta^2\right)\left[r^i\left(4D^i - D^{i+1} + D^{i-1} - 2\Delta V^i\right) - 2\Delta D^i\right] \\ T^{i,0} &\equiv \left(\Delta t/2r^i\Delta^2\right)\left[r^i\left(\Delta\left(V^{i+1} - V^{i-1}\right) - 4D^i\right) + 2\Delta^2 V^i\right] \\ T^{i,+1} &\equiv \left(\Delta t/4r^i\Delta^2\right)\left[r^i\left(4D^i + D^{i+1} - D^{i-1} + 2\Delta V^i\right) + 2\Delta D^i\right]. \end{aligned}$$

Therefore, once the diffusion coefficient and the convective velocity are specified, the problem is completely defined. A typical simulation is then undertaken by constructing

an initial density profile and stepping Eq 5.8 forward in time with some small time step (typically $\Delta t \sim 5\ \mu$s, and the code is run for ten or twenty thousand time steps to achieve a total simulation time of 50–100 ms).

5.3 Implicit Numerical Charge State Transport Code

The implicit code solves the same continuity equation as the explicit code,

$$\frac{\partial n_j}{\partial t} = \frac{1}{r}\frac{\partial}{\partial r} r\left[D_j \frac{\partial n_j}{\partial r} + V_j n_j\right] + I_{j-1} n_{j-1} - (I_j + R_j) n_j + R_{j+1} n_{j+1}. \tag{5.11}$$

The significant difference in the solution is that the density terms on the right hand side are taken to be an average of the density before and after the time step,

$$n_j^{RHS} = \frac{n_j' + n_j}{2}. \tag{5.12}$$

Then the matrix equation analogous to Eq. 5.8 in the implicit case is slightly more complicated [221],

$$\overleftrightarrow{\chi}\, \vec{n}' = \overleftrightarrow{\xi}\, \vec{n} \equiv \vec{w}. \tag{5.13}$$

In this expression $\overleftrightarrow{\chi}$ and $\overleftrightarrow{\xi}$ have nearly identical forms to $\overleftrightarrow{\xi}$ in Eq. 5.9, but the individual elements are all divided by two because of the average taken in Eq. 5.12.

The solution to Eq. 5.13 is more complicated than simply stepping Eq. 5.8 forward in time because a large matrix equation must be inverted at each time step. A straightforward method for this solution is to perform it recursively [220]. To understand this method, note the form of the $\overleftrightarrow{\chi}$ matrix

$$\overleftrightarrow{\chi} = \begin{bmatrix} \overleftrightarrow{\beta}^1 & \overleftrightarrow{\gamma}^1 & 0 & & & & \\ \overleftrightarrow{\alpha}^2 & \overleftrightarrow{\beta}^2 & \overleftrightarrow{\gamma}^2 & 0 & & & \\ 0 & \overleftrightarrow{\alpha}^3 & \overleftrightarrow{\beta}^3 & \overleftrightarrow{\gamma}^3 & & & \\ & & & \ddots & & & \\ & & & & \overleftrightarrow{\alpha}^{N_s-1} & \overleftrightarrow{\beta}^{N_s-1} & \overleftrightarrow{\gamma}^{N_s-1} \\ & & & & & \overleftrightarrow{\alpha}^{N_s} & \overleftrightarrow{\beta}^{N_s} \end{bmatrix} \tag{5.14}$$

Then Eq. 5.13 is seen to have the form, at spatial mesh point i,

$$\overleftrightarrow{\alpha}^i\, \vec{n}^{i-1} + \overleftrightarrow{\beta}^i\, \vec{n}^i + \overleftrightarrow{\gamma}^i\, \vec{n}^{i+1} = \vec{w}^i. \tag{5.15}$$

Motivated by this form, a recursive sort of relation is posited;

$$\vec{n}^{i+1} = \overleftrightarrow{x}^i\, \vec{n}^i + \vec{y}^i. \tag{5.16}$$

This is then substituted into Eq. 5.15 to yield

$$\left(\overleftrightarrow{\beta}^{i} + \overleftrightarrow{\gamma}^{i}\overleftrightarrow{x}^{i}\right)\vec{n}^{i} = \overleftrightarrow{\alpha}^{i}\vec{n}^{i-1} + \vec{w}^{i} - \overleftrightarrow{\gamma}^{i}\vec{y}^{i}. \tag{5.17}$$

By comparison with Eq. 5.16, the desired recursion relations for $\overleftrightarrow{x}$ and $\vec{y}$ are arrived at immediately:

$$\left(\overleftrightarrow{\beta}^{i} + \overleftrightarrow{\gamma}^{i}\overleftrightarrow{x}^{i}\right)\overleftrightarrow{x}^{i-1} = -\overleftrightarrow{\alpha}^{i} \tag{5.18}$$

and

$$\left(\overleftrightarrow{\beta}^{i} + \overleftrightarrow{\gamma}^{i}\overleftrightarrow{x}^{i}\right)\vec{y}^{i-1} = \vec{w}^{i} - \overleftrightarrow{\gamma}^{i}\vec{y}^{i}. \tag{5.19}$$

The boundary condition at $r = a$ ($i = N_s$) is applied to obtain $\overleftrightarrow{x}^{N_s-1}$ and $\vec{y}^{N_s-1}$. One typical boundary condition is to specify some constant density (most often zero) at the plasma edge. From Eq. 5.16, this boundary condition gives trivially

$$\vec{y}^{N_s-1} = \begin{bmatrix} n_1(r=a) \\ n_2(r=a) \\ n_3(r=a) \\ n_4(r=a) \end{bmatrix} \tag{5.20}$$

and

$$\overleftrightarrow{x}^{N_s-1} = 0. \tag{5.21}$$

Another possible boundary condition, motivated more by physical considerations, is to specify the particle flux at the plasma edge. To determine $\overleftrightarrow{x}^{N_s-1}$ and $\vec{y}^{N_s-1}$ from this boundary condition, the flux at the boundary, $\Gamma = -D\nabla n - Vn$ is written in the discrete form

$$\Gamma^{N_s} = -D^{N_s}\frac{n^{N_s} - n^{N_s-1}}{\Delta} - V^{N_s}n^{N_s}, \tag{5.22}$$

which easily becomes

$$n^{N_s} = \frac{D^{N_s}}{D^{N_s} + \Delta V^{N_s}}n^{N_s-1} - \frac{\Delta\Gamma^{N_s}}{D^{N_s} + \Delta V^{N_s}}. \tag{5.23}$$

Again, by comparison with Eq. 5.16, the $\overleftrightarrow{x}^{N_s-1}$ and $\vec{y}^{N_s-1}$ are found to be

$$\overleftrightarrow{x}^{N_s-1} = \begin{bmatrix} \frac{D_1^{N_s}}{(D_1^{N_s}+\Delta V_1^{N_s})} & & & \\ & \frac{D_2^{N_s}}{(D_2^{N_s}+\Delta V_2^{N_s})} & & \\ & & \frac{D_3^{N_s}}{(D_3^{N_s}+\Delta V_3^{N_s})} & \\ & & & \frac{D_4^{N_s}}{(D_4^{N_s}+\Delta V_4^{N_s})} \end{bmatrix} \tag{5.24}$$

and

$$\vec{y}^{N_s-1} = \begin{bmatrix} \Delta\Gamma_1^{N_s}/(D_1^{N_s} + \Delta V_1^{N_s}) \\ \Delta\Gamma_2^{N_s}/(D_2^{N_s} + \Delta V_2^{N_s}) \\ \Delta\Gamma_3^{N_s}/(D_3^{N_s} + \Delta V_3^{N_s}) \\ \Delta\Gamma_4^{N_s}/(D_4^{N_s} + \Delta V_4^{N_s}) \end{bmatrix} \tag{5.25}$$

However, simulations using the constant flux boundary conditions lead to density profiles that decay linearly with time. In contrast, the experimental behavior is always described well by an exponential decay of the impurity signal. Therefore for comparison with experiments the former boundary condition was used herein.

Once the edge values $\overleftrightarrow{x}^{N_s-1}$ and $\overleftrightarrow{y}^{N_s-1}$ are known, the solution proceeds by stepping down through the spatial mesh points from $i = N_s - 1$ to $i = 1$, calculating values of $\overleftrightarrow{x}^i$ and $\vec{y}^i$ from Eqs. 5.18 and 5.19. The flux is zero at the plasma center, so the transport operators $T^{1;-1,0,+1}$ must have a special form. This form is found by examining the divergence of the flux

$$\nabla \cdot \Gamma = \frac{1}{r}\frac{\partial}{\partial r} r \left[D\frac{\partial n}{\partial r} + Vn \right], \tag{5.26}$$

and noting that $\partial n/\partial r|_{r=0} = V(r=0) = 0$. Then

$$\nabla \cdot \Gamma = D\frac{\partial^2 n}{\partial r^2} + n\frac{\partial V}{\partial r}, \tag{5.27}$$

which becomes, in discrete form,

$$\nabla \cdot \Gamma(r=0) = D^{(1)}\left(\frac{n^{(2)} - 2n^{(1)} + n^{(0)}}{\Delta^2}\right) + n^{(1)}\left(\frac{V^{(2)} - V^{(0)}}{2\Delta}\right) \tag{5.28}$$

(superscripts "0" result from continuing the gradients through negative r, so that $i = 0$ corresponds to $r = -\Delta$; recall $i = 1$ corresponds to $r = 0$). Invoking cylindrical symmetry about the plasma center requires that $n^{(2)} = n^{(-1)}$, $V^{(2)} = V^{(-1)}$, so that

$$\nabla \cdot \vec{\Gamma}(r=0) = 2D^{(1)}\left(\frac{n^{(2)} - n^{(1)}}{\Delta^2}\right) + \frac{n^{(1)}V^{(2)}}{\Delta}, \tag{5.29}$$

and the proper transport terms for the plasma center are

$$\begin{aligned} T^{1,-1} &\equiv 0 \\ T^{1,0} &\equiv (\Delta t/2)\left[V^{(2)}/\Delta - 2D^{(1)}/\Delta^2\right] \\ T^{1,+1} &\equiv (\Delta t/2)\left[2D^{(1)}/\Delta^2\right]. \end{aligned} \tag{5.30}$$

The central density is then found from Eqs. 5.16 and 5.15 at r=0,

$$\begin{aligned} \overleftrightarrow{\beta}^1\ \vec{n}^{(1)} + \overleftrightarrow{\gamma}^1\ \vec{n}^{(2)} &= \vec{w}^1 \\ \vec{n}^{(2)} &= \overleftrightarrow{x}^1\ \vec{n}^{(1)} + \vec{y}^1 \end{aligned}$$

So that the solution to

$$\left(\overleftrightarrow{\beta}^1 + \overleftrightarrow{\gamma}^1 \overleftrightarrow{x}^1\right) \vec{n}^{(1)} = \vec{w}^1 - \overleftrightarrow{\gamma}^1 \vec{y}^1 \tag{5.31}$$

with the proper transport terms in 5.30, $\overleftrightarrow{\beta}$ and $\overleftrightarrow{\gamma}$ gives the correct central density $\vec{n}^1$. The density vector at all the other spatial points is subsequently found by applying the recursion Eq. 5.16. Thus the implicit solution of Eq. 5.8 requires solving five 4×4 matrix equations at each of the N_s spatial mesh points (Eqs. 5.18 and 5.19). These matrix equations are solved using the double precision IMSL routine DLSARG.

5.4 Benchmarking the Transport Codes

To ensure the accuracy of both simulation codes, their results were compared with the analytic results previously mentioned. These solutions were given by Seguin [214,63] or Fussmann [215] for the case of constant D_0 and linear $V = V_0(r/a)$. The ratio of V_0 to D_0 is parameterized as $S \equiv V_0 a/2D_0$, and the solutions for a few values of S, after some minor corrections in the time dependence, are:

$$S = 0 : n(r,t) = n_0 J_0(2.408 r/a) e^{-5.783 D_0 t/a^2} \tag{5.32}$$

$$S = -1 : n(r,t) = n_0 \left[1 - (r/a)^2\right] e^{-8 D_0 t/a^2} \tag{5.33}$$

$$S = +1 : n(r,t) = n_0 \left[1 - (r/a)^2\right] e^{-(r/a)^2} e^{-4 D_0 t/a^2} \tag{5.34}$$

$$S = -\sqrt{2} + 2 : n(r,t) = n_0 \left[1 + 25(r/a)^2 + \frac{1}{2} S^2 (r/a)^4\right] e^{12 D_0 t/a^2} \tag{5.35}$$

$$S = +\sqrt{2} - 2 : n(r,t) = n_0 \left[1 - 25(r/a)^2 + \frac{1}{2} S^2 (r/a)^4\right] e^{-S(r/a)^2} e^{8 S D_0 t/a^2} \tag{5.36}$$

Thus there are two comparisons to be made between the code predictions and the exact analytic results: first, the time behavior of the density n_j, and second, the specific profile shape. Both codes have been tested against all the above solutions and are in excellent agreement. Examples of simulation results for the case $S = +1$ are shown in Figs. 5.1 and 5.2 for the explicit and implicit codes respectively. The specific parameters for these simulations were: $D_0 = 1.0$ m$^2/s$, $V_0 = 7.982$ m$/s$, $a = 0.26$ m (the TEXT minor radius), and the initial density profile was a Gaussian centered near the plasma edge at $r = 0.23$ m with a width of $0.05\ a$, and an amplitude of 10^{19}m^{-3}.

Figs. 5.1a and 5.2a show the behavior of the four central charge state densities with time. The particles are transported inward such that the density peaks on axis after about 8 ms, and then the profile decays due to diffusion. The time constant of this final

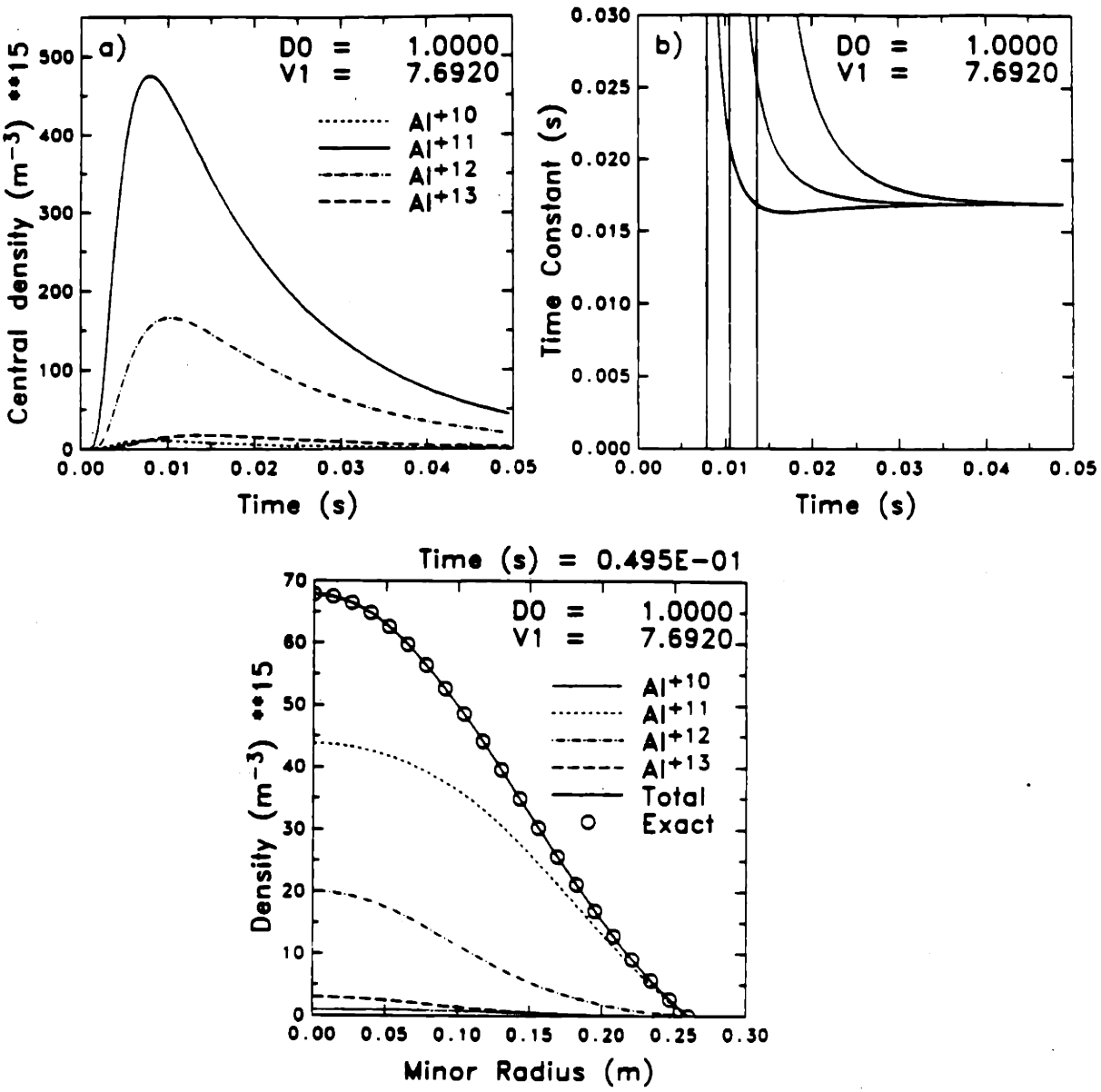

Figure 5.1: An example of the results from the explicit transport simulation code is shown for the case of aluminum injected into a typical TEXT plasma. Only the four highest ionization states are considered. a) The central density peaks in about 8 ms, then decays away diffusively with a time constant of 16.9 ms, exactly the value predicted by the analytic expression of Eq. 5.34. b) The time constant is calculated as $\tau = -\Delta t \ln(n'/n)$. c) After about 20 ms, higher frequency harmonic solutions to the diffusion equation have died away, and the aluminum density profile decays with this characteristic shape. The profile calculated by the code at about 50 ms is shown to agree with the "exact" solution of Eq. 5.34 given by the circles.

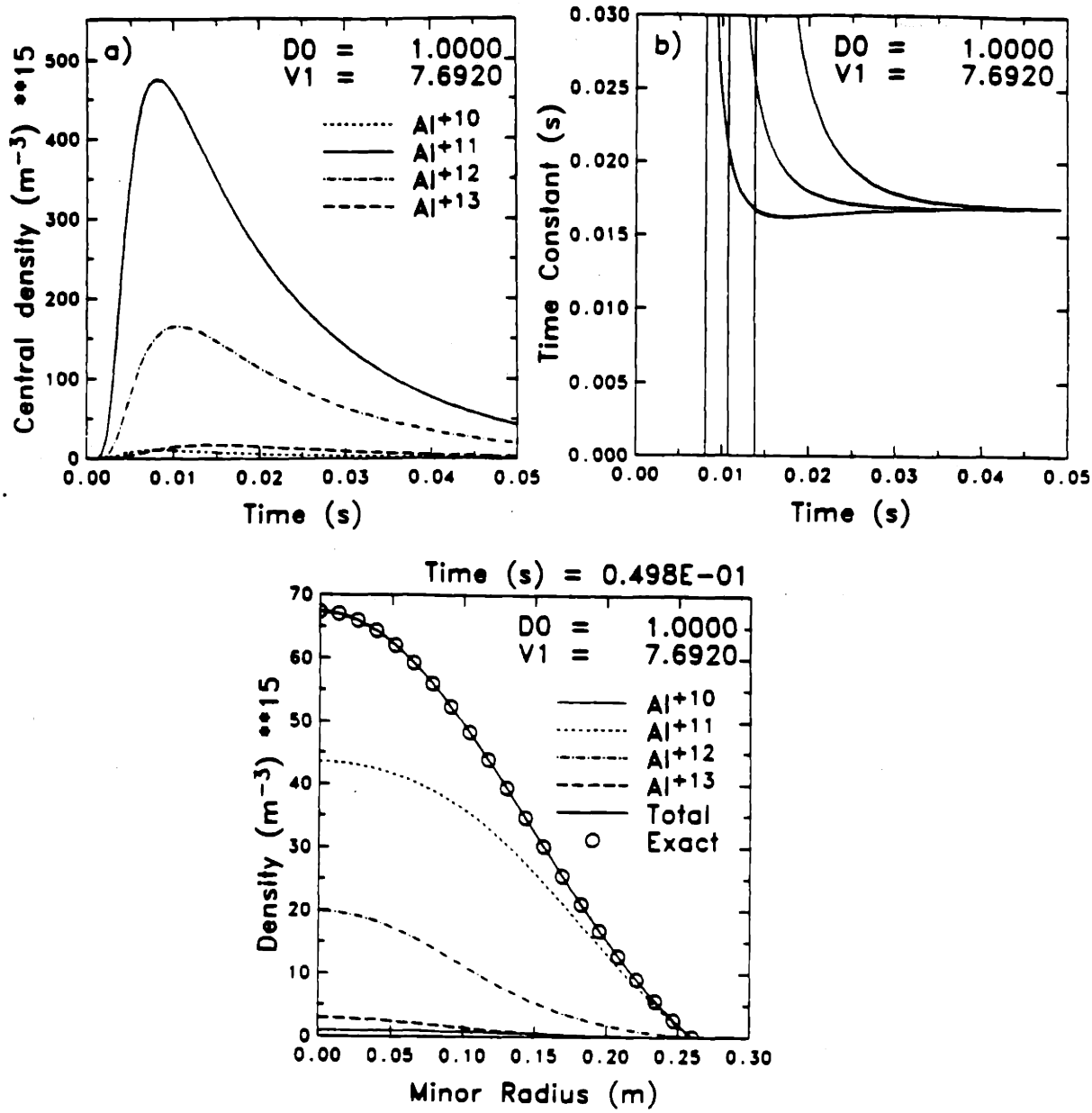

Figure 5.2: An example of the results from the implicit transport simulation code for the same case as in Fig. 5.1. Note that the implicit and the explicit codes have excellent agreement. Another important point is that the He-like state is dominant for these typical TEXT conditions, as has been shown from the experimental results of chapter 4.

decay is shown in Figs. 5.1b and 5 2b. This time constant is calculated at each time step as $\tau = -\Delta t/ln(n'/n)$ The time constant predicted from Eq. 5.34, $\tau = 4D/a^2$, is 16.9 ms and the results of both codes show the decay time asymptotes to 16.9 ms, exactly the same as the analytical result. The simulations also correctly predict the shape of the profile as shown in Figs. 5.1c and 5.2c

5.5 Sawtooth Model Incorporated in the Transport Codes

It was demonstrated experimentally (see chapter 4) that sawtooth oscillations can play a strong role in overall impurity transport. The sawtooth crashes are critical in enhancing the inward flow of impurity particles just after injection, when there is a positive density gradient, and they also appear to be important in preventing the accumulation of impurities in the plasma center. To properly simulate impurity transport, an accurate model for the sawtooth crash is therefore required.

A simple model for sawtooth induced changes in the density profiles of all the aluminum charge states was incorporated into the transport codes. In the model the profiles were flattened periodically from the plasma center out to the mixing radius r_{mix}. Both the inversion radius and the mixing radius were obtained from the x-ray emissivity profiles. The difference between the Abel inverted emissivity profiles before and after a sawtooth crash was used to find these radii. In the model, particles were conserved, so that

$$n(r)|_{post} = n_{post} = \frac{\int_0^{r_{mix}} n_{pre}(r) r\, dr}{r_{mix}^2}, \quad 0 \le r \le r_{mix} \tag{5.37}$$

$$n(r)_{post} = n(r)_{pre}, \; r_{mix} \le r \le a \tag{5.38}$$

where n_{post} is the constant density following the sawtooth crash and n_{pre} is the density profile before the crash.

A trigger mechanism for the sawtooth crash was not specified because the exact trigger of a crash is theoretically unclear [222]. Thus in the model sawteeth could be made to occur either at a constant frequency or at specified times to match the experiment.

It was also shown in chapter 4 that the sawtooth acts as a convective transport process by driving impurity profiles from a flat state to a hollow state. Thus a simple flattening model may not be sufficient to describe the sawtooth behavior accurately. However, the specific nature of the sawtooth convection is unknown, so it cannot yet

be modelled. As alluded to earlier, the TFR [60] and ASDEX [48] groups successfully modeled sawtooth behavior with an enhanced outward convection. This model is not sufficiently general, however, to describe the tremendous impurity inflow during a sawtooth crash in the early phase of an injection experiment. Therefore the simple flattening model was used in this work to approximate the sawtooth behavior.

5.6 Simulations of TEXT Discharges with Aluminum Injection

To simulate impurity injection experiments in TEXT, an initial aluminum density profile peaked near the plasma edge was input and allowed to evolve in time. Typically the initial profile was assumed to be a Gaussian centered at about $r_0 = 0.24$ m (recall $a = 0.26$ m) with an e^{-1} width of $\sigma/a \simeq 0.1$. The exact simulation results were insensitive to the details of the initial profile within $0.23 \lesssim r_0 \lesssim 0.25$ m and $0.05 \lesssim \sigma/a \lesssim 0.15$. The results were sensitive to the location of the initial profile with respect to the sawtooth mixing radius. The electron density profile was assumed to be stationary in time since the perturbation due to the injection was small and density fluctuations due to sawteeth were $\lesssim 3$ - 5% [58], much smaller than the temperature oscillations. Some simulations were run without the sawtooth model to simulate the "global" transport inclusive of coherent MHD effects. In those cases, the electron temperature profile was also assumed to be stationary and equal to the measured temperature profile averaged over a sawtooth period. In those simulations with sawteeth explicitly modelled, the electron temperature was assumed to evolve linearly in time from its post-crash profile to its pre-crash value; at the time of a crash, the temperature profile was reset to its measured post-crash value.

5.6.1 Transport Simulations with Anomalous Coefficients

To model the aluminum transport in TEXT only the simplest, anomalous model possible, namely one with only a constant diffusion coefficient D_0 and zero convection was used. This model was very convenient because the diffusion coefficient could be easily related to the observed confinement time using Eq. 5.32, which gives $D_0 = a^2/5.783\tau_c$. However, Eq. 5.32 also indicates that the quasi-equilibrium profiles obtained with constant D are zeroeth-order Bessel functions, which does not agree with the observed profiles shown in the last chapter. This discrepancy is further illustrated in Fig. 5.3, which shows the temporal behavior of the central aluminum densities and three soft

x-ray signals from each array at different chord radii (each array used a different filter); the x-ray chord radii were approximately 0, 10, and 15 cm and the filter responses are described in chapter 3 and Appendix C. The discharge was a low q_a, high density discharge. Using the constant D model with $D_0 = 0.5$ m^2/s, the time dependence of the central x-ray signals were matched easily, but the outer x-ray signals calculated in the simulation were much too low. Also note that the central hard filter x-ray signal from the simulation was too low by almost a factor of 2.

Sawteeth, which act as a source of impurity particles in the outer plasma by periodically expelling material from the center, cannot alleviate the discrepancies between the constant D model and the experimental observations. Fig. 5.4 shows results from a constant D simulation including sawteeth. The effect of the sawteeth was to reduce the value of D required to match the temporal behavior of the data by about 20%, but the sawteeth did not broaden the profiles enough to match the large x-ray signals in the outer part of the plasma. Furthermore, impurity profiles observed in discharges with only small sawteeth could not be explained with only a constant diffusion coefficient either. If the sawtooth were the principal cause of disagreement with a constant D model, one might expect D_0 to work well in a weakly sawtoothing discharge. For example Fig. 5.5 shows the results of a simulation for a low density, high q_a discharge with very small sawteeth using $D_0 = 0.4$ m^2/s. The simulated x-ray signals in the outer part of the plasma were again much smaller than the observed signals. (In this discharge the rapid rise and fall of the central hard-filtered x-ray signal (Fig. 5.5d) just after the injection was not due only to aluminum radiation, but mostly to a fast transient in the electron temperature due to the injection. This transient completely died away within 20 ms after the injection.)

In a sense, the atomic transition rate coefficients (I and R) constitute another pair of free parameters in the numerical modeling in addition to the transport coefficients. These transition rates can affect the x-ray signals calculated in the simulations, especially in the outer regions. This is because the balance between ionization and recombination strongly impacts the amount of highly ionized impurities that can be transported to the outer regions before recombining. Furthermore, the atomic transition rates determine the relative signal levels in the arrays with different filters. The ionization rates are known with relative accuracy, but there is some uncertainty in the recombination rates, especially in the dielectronic recombination component. Recombination coefficients from several different references are compared in Appendix E, where it is shown

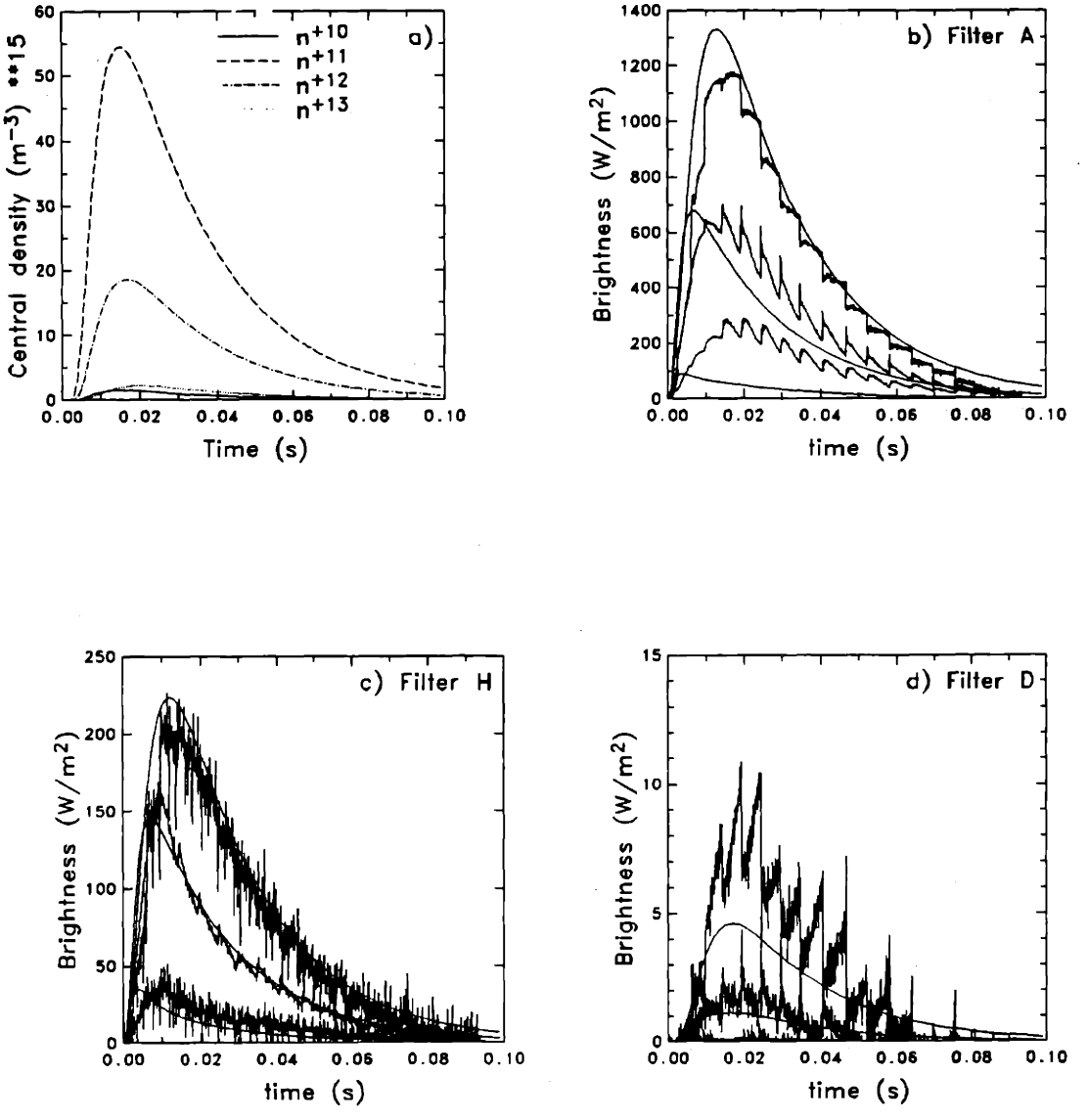

Figure 5.3: Simulation results using a constant D model are compared to data from a low q_a, high density discharge in TEXT. Sawteeth are not taken into account in this simulation. a) The central aluminum densities peak near 17 ms, then decay with a time constant of 23 ms. b) Only the temporal behavior of the central soft x-ray signals are matched well using $D = 0.5$ m^2/s; but the outer x-ray signals from the simulation are too low. (The different signals are from different chord radii: top trace, $r = 0$; middle trace $r \simeq 10$ cm; and bottom trace, $r \simeq 15$ cm.) c) The central krypton filter signal was also matched well, and d) the hard filter signal was too low by almost a factor of 2.

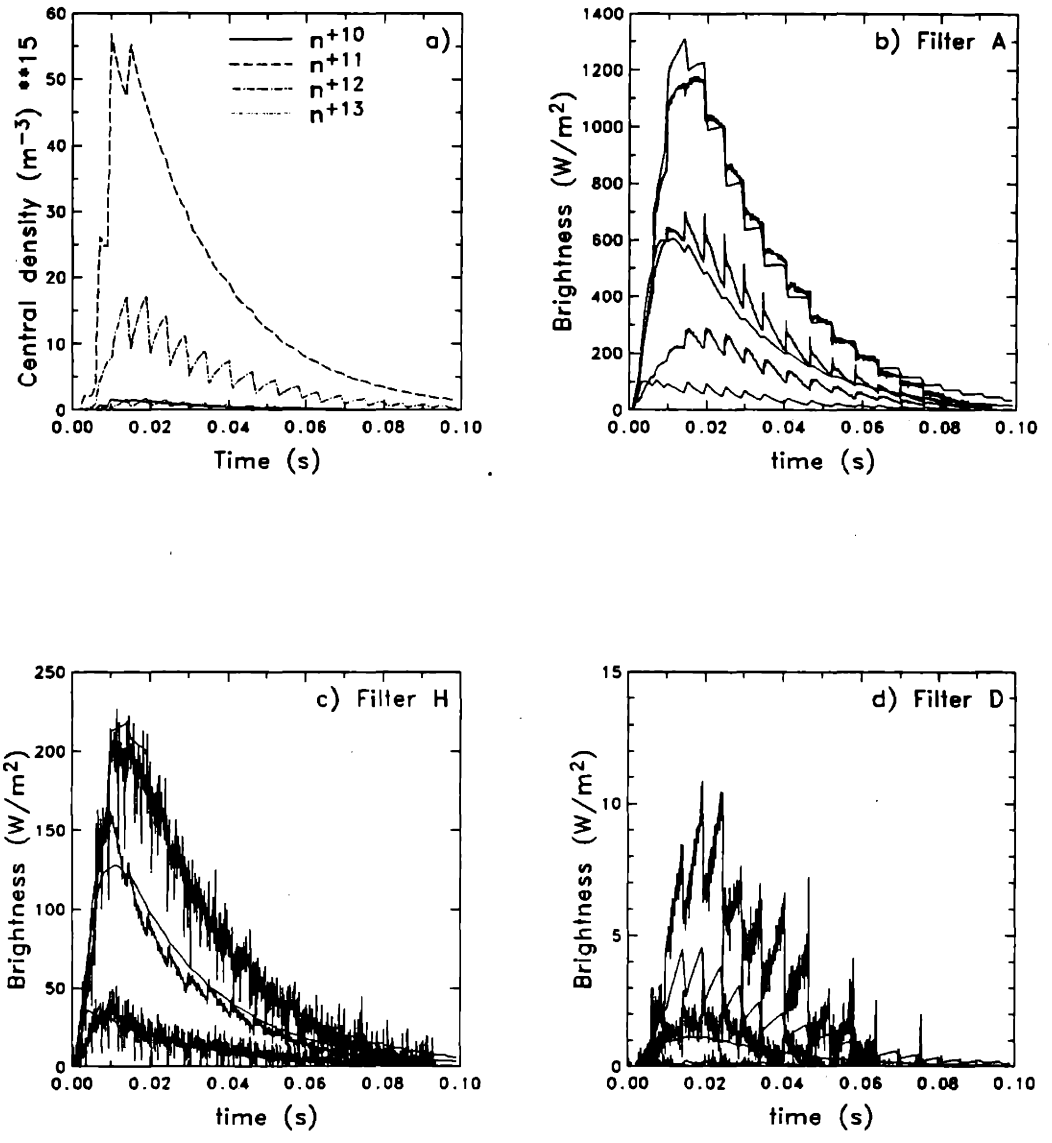

Figure 5.4: Simulation results using a constant D model, including the effect of sawteeth, for the same discharge as shown in Fig. 5.3. The temporal behavior of the central soft x-ray signals are again matched well using $D = 0.35$ m^2/s (30% smaller than without sawteeth), but again the outer x-ray signals from the simulation are too low.

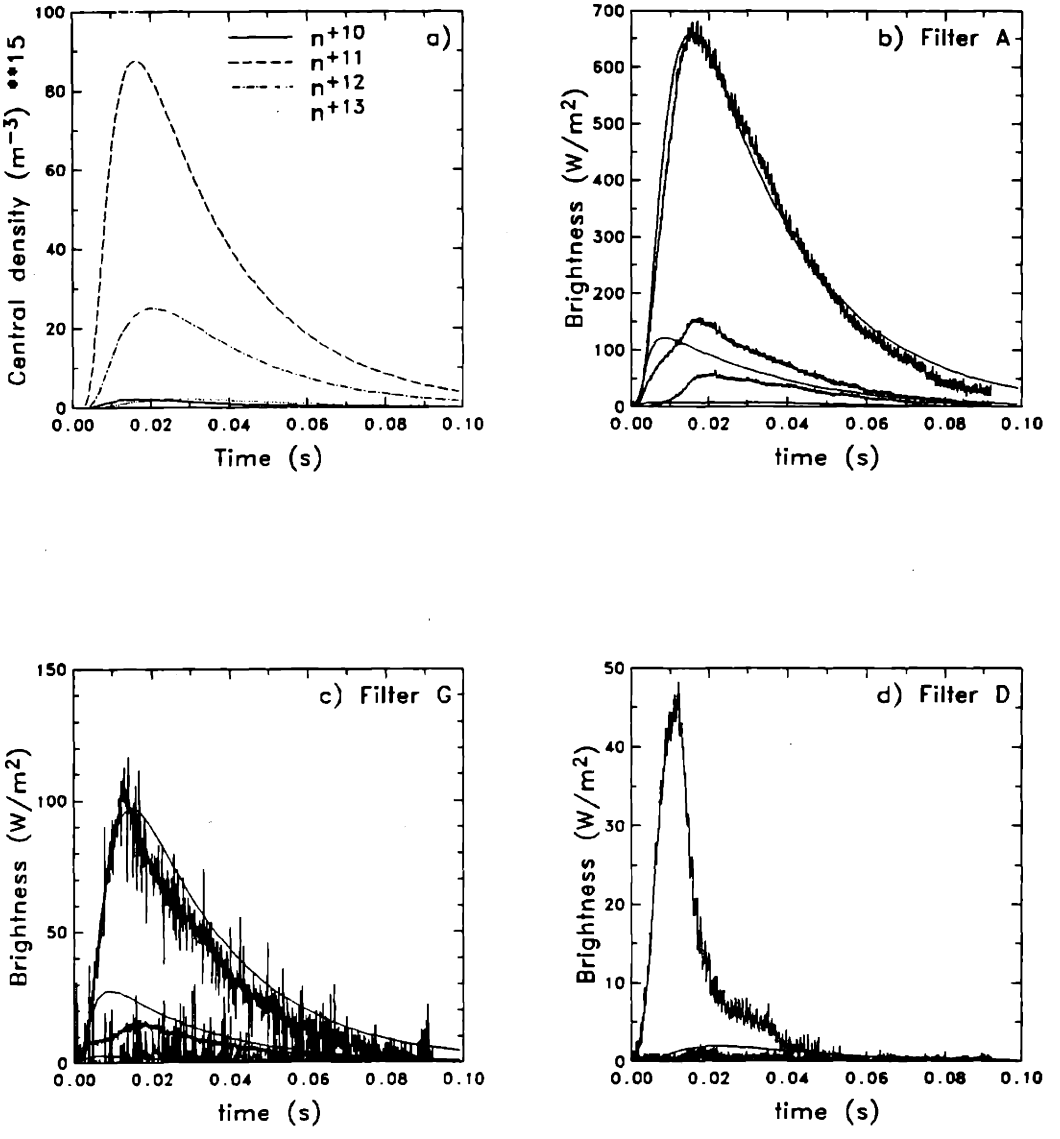

Figure 5.5: Simulation results using a constant D model are compared to data from a high q_a, low density discharge with very small sawteeth in TEXT. As in the low q_a case (Figs. 5.3 and 5.4), the central soft filter x-ray data is matched well, but the signals from the outer part of the plasma are too low in the simulation. a) The central aluminum densities, b) the soft filter x-ray data at chord radii of about 0, 10, and 15 cm, c) the krypton filter x-ray data, and d) the hard filter x-ray signals. Note $D = 0.4$ m^2/s here, smaller than in the low q_a simulation without sawteeth.

that the recombination rates from Ref. [204] may be as much as a factor of 2 too high for the H-like and He-like charge states (These rates were used in the simulations shown in Figs 5.3–5.5.)

Thus to determine the effect of varying the recombination rates, a simulation was performed for the same discharge as shown in Fig 5.3. The total recombination rates into the He-like and Li-like states were reduced by a factor of two, as suggested by the results from Ref. [223]. The result of this simulation is shown in Fig. 5.6. The main difference was that the H-like state density was increased by almost a factor of 2. In the x-ray signals the outer channels were increased somewhat because of the higher density of highly-ionized aluminum in the colder part of the plasma. However the increase in the outer signals was still not large enough to match the data; the simulated filter A signal at 0.15 m was still a factor of two too low. The central hard filter x-ray signal was increased by about 25%, and the outer hard filter signal was increased to the point where it did agree fairly well with the data. The conclusion from this exercise is that decreased total recombination into the He-like and Li-like states improved the simulation with respect to the data, but a factor of 2 decrease was not sufficient to bring the simulation into complete agreement with the data.

It is obvious from the simulations shown above and from the aluminum profiles in chapter 4 that some mechanism is required to transport the higher charge states rapidly toward the plasma edge. This has not yet been found. However, the constant diffusion coefficients used above match the central data well.

5.6.2 Transport Simulation with Neoclassical Coefficients

A simulation using neoclassical coefficients was performed for a single well-diagnosed TEXT discharge. The discharge conditions were 2.8/320/6. The ion temperature was measured in an identical discharge using an active charge exchange system [203]. The carbon density profile, averaged over a sawtooth period, was measured using charge exchange recombination spectroscopy in a similar sawtoothing discharge. The carbon density profile was found to be slightly broader than the electron density profile [62]. Thus for the simulation the carbon profile was assumed to be similar to the electron density profile, and the absolute density was chosen to yield a Z_{eff} that matched the total plasma current through Spitzer resistivity. Profiles of the other intrinsic impurities (oxygen, titanium, iron, and chromium) in TEXT are not well known. The effect of oxygen should be similar to that of carbon because of its similar mass and charge.

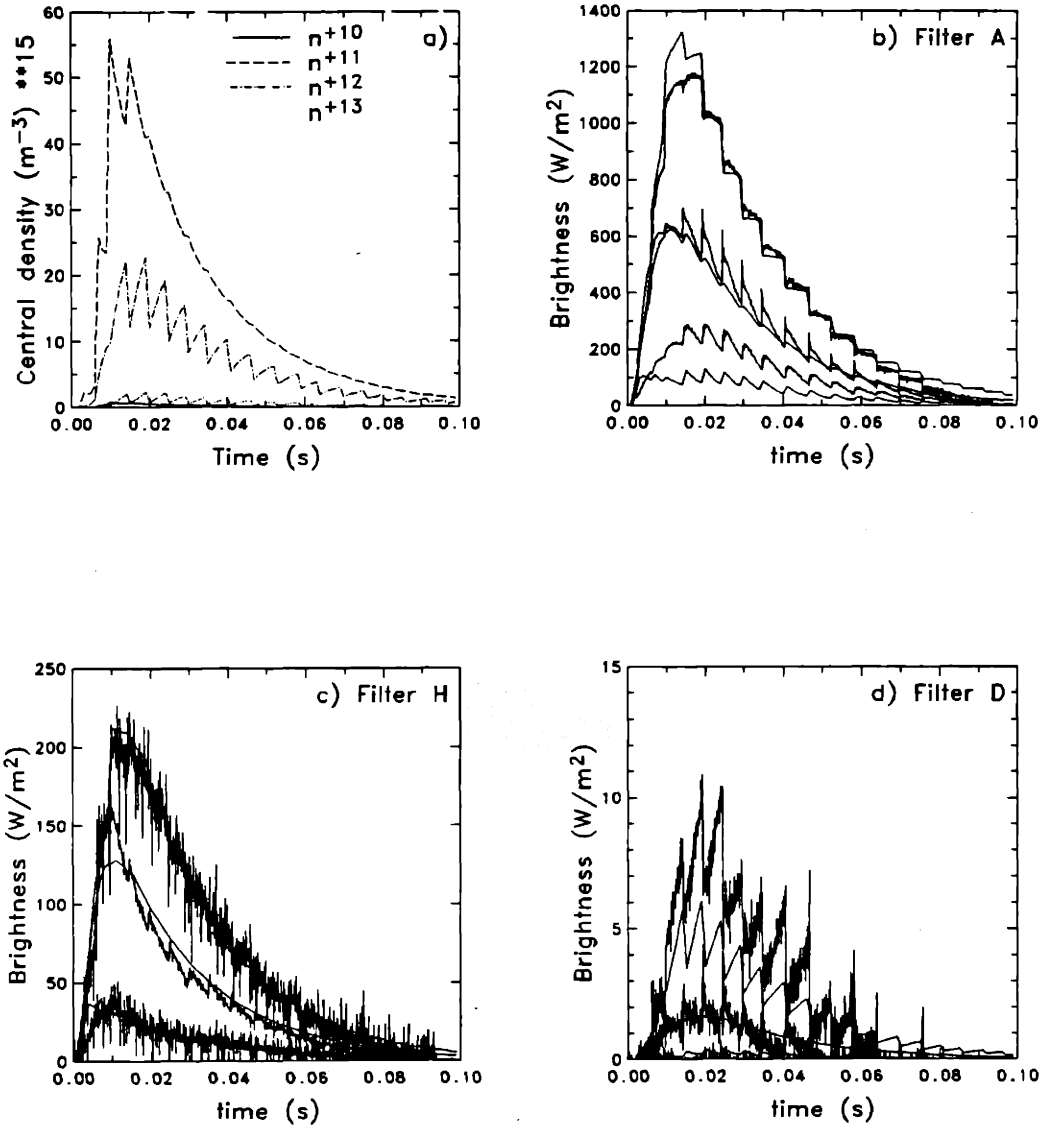

Figure 5.6: Simulation results using reduced recombination rates. In this case the H-like state density and the fully stripped state density were increased by almost a factor of 2 in the plasma center. In the x-ray signals the outer channels were slightly increased, but still not by enough to match the data.

Therefore, a model with only carbon should adequately cover the effects of light impurities. The heavy impurities were neglected; their densities were much lower than that of the light impurities, but heavy impurity effects could be important because of their higher collisionality.

The neoclassical transport coefficients were calculated from the ion temperature, electron density, and carbon density profiles using the formalism described in chapter 1. As mentioned in that chapter, no explicit theoretical formulae exists for a trace impurity frictioning on working ions and a main impurity, except in the Pfirsch-Schlüter collisionality regime. To calculate the classical particle flux, the Pfirsch-Schlüter result was therefore used, divided by $2q^2$. This is accurate because the classical and Pfirsch-Schlüter fluxes only differ by a factor of $2q^2$ (compare Eqs. 1.29 and 1.31), and the L coefficients depend only on collisionality and mass ratios. The classical coefficients are then written

$$D_{Al}^{Cl} = \frac{c^2 T}{e_{Al} B_0^2 n_{Al}} \frac{L_{11}^{TT}}{e_{Al}} \tag{5.39}$$

$$V_{Al}^{Cl} = \frac{c^2 T}{e_{Al} B_0^2 n_{Al}} \left[\frac{L_{11}^{Ti}}{e_i} \frac{\partial \ln n_i}{\partial r} + \left(\frac{L_1 + L_2}{e_I} \right) \frac{\partial \ln n_I}{\partial r} + \left(\frac{L_1 + L_2 + L_3}{e_I} + \frac{L_{11}^{Ti} + L_{12}^{Ti}}{e_i} \right) \frac{\partial \ln T}{\partial r} \right]. \tag{5.40}$$

To calculate the neoclassical coefficients in the banana-plateau regime, the condition of ambipolarity is considered:

$$Z_{Al} \Gamma_{Al}^{BP} = -Z_C \Gamma_C^{BP} - Z_H \Gamma_H^{BP}. \tag{5.41}$$

The individual carbon and hydrogen fluxes are then written in terms of the friction using the banana-plateau part of Eq. 1.15,

$$Z_{Al} \Gamma_{Al}^{BP} = \frac{I}{e} \frac{\langle F_{C1}^{\parallel} B \rangle}{\langle B^2 \rangle} + \frac{I}{e} \frac{\langle F_{H1}^{\parallel} B \rangle}{\langle B^2 \rangle}, \tag{5.42}$$

where $I = RB_\phi$. Then the friction terms F_{C1} and F_{H1} are divided into components. For example, the carbon friction is the sum of carbon-hydrogen friction and carbon-aluminum friction:

$$Z_{Al} \Gamma_{Al}^{BP} = \frac{I}{e} \frac{\langle (F_{CH1}^{\parallel} + F_{CAl1}^{\parallel}) B \rangle}{\langle B^2 \rangle} + \frac{I}{e} \frac{\langle (F_{HC1}^{\parallel} + F_{HAl1}^{\parallel}) B \rangle}{\langle B^2 \rangle}. \tag{5.43}$$

Note that $F_{CH1}^{\parallel} = -F_{HC1}^{\parallel}$, so these terms cancel and the result is

$$Z_{Al} \Gamma_{Al}^{BP} = \frac{I}{e} \frac{\langle F_{CAl1}^{\parallel} B \rangle}{\langle B^2 \rangle} + \frac{I}{e} \frac{\langle F_{HAl1}^{\parallel} B \rangle}{\langle B^2 \rangle}. \tag{5.44}$$

Thus the aluminum flux has two components: the flux driven by friction on carbon and the flux driven by friction on hydrogen. To obtain the total D and V for aluminum these individual components were obtained by applying Eq. 1.30 twice, once with i =H and I =Al, and again with i =C and I =Al. The banana-plateau coefficients are then

$$D_{Al}^{BP} = \sum_j \frac{3c^2T}{B_0^2 R_0^2 e_{Al}^2 n_{Al}} \left(\frac{1}{1/K_{11}^j + 1/K_{11}^{Al}} \right), \tag{5.45}$$

and

$$\begin{aligned} V_{Al}^{BP} &= \sum_j \frac{3c^2T}{B_0^2 R_0^2 e_{Al}^2 n_{Al}} \left(\frac{1}{1/K_{11}^j + 1/K_{11}^{Al}} \right) \\ &\times \left[-\frac{e_{Al}}{e_j} \frac{\partial \ln n_j}{\partial r} - \frac{\partial \ln T}{\partial r} \left(\frac{3}{2} \left(1 - \frac{Z_{Al}}{Z_j} \right) + \frac{Z_{Al} K_{12}^j}{Z_j K_{11}^j} - \frac{K_{12}^{Al}}{K_{11}^{Al}} \right) \right], \end{aligned} \tag{5.46}$$

where the sum over j represents the application of Eq. 1.30 twice, and the index j represents either H or C. Again, the viscosity coefficients K_{11}^j and K_{12}^j were obtained using Eq. 1.24. The Pfirsch-Schlüter coefficients are

$$D_{Al}^{PS} = \frac{2c^2Tq^2}{e_{Al} B_0^2 n_{Al}} \frac{L_{11}^{TT}}{e_{Al}}, \tag{5.47}$$

and

$$\begin{aligned} V_{Al}^{PS} = & \frac{2c^2Tq^2}{e_{Al} B_0^2 n_{Al}} \left[\frac{L_{11}^{Ti}}{e_i} \frac{\partial \ln n_i}{\partial r} + \left(\frac{L_1 + L_2}{e_I} \frac{\partial \ln n_I}{\partial r} \right) \right. \\ & \left. + \left(\frac{L_1 + L_2 + L_3}{e_I} + \frac{L_{11}^{Ti} + L_{12}^{Ti}}{e_i} \right) \frac{\partial \ln T}{\partial r} \right], \end{aligned} \tag{5.48}$$

where again the L coefficients are given in Appendix B. Examples of the neoclassical transport coefficients from this calculation are shown in Fig. 5.7. The diffusion coefficient and convective velocity are shown for He-like aluminum with a constant density of 5×10^{16} m^{-3}, which corresponds to the approximate aluminum density measured during the injection experiments. The banana-plateau diffusion is dominant in the plasma center, the Pfirsch-Schlüter diffusion is dominant nearer the edge, and the classical diffusion is small, but significant, across the entire plasma. In the convection term the Pfirsch-Schlüter contribution is by far the dominant term. The temperature and ion gradient terms combine in V^{PS} to create a large outward convection in qualitative agreement with the experimentally required convection. The ion collisionalities are shown in Fig. 5.8, which shows that the aluminum ions are indeed in the plateau regime inside of about 7 cm, and in the Pfirsch-Schlüter regime outside of 7 cm. (Recall

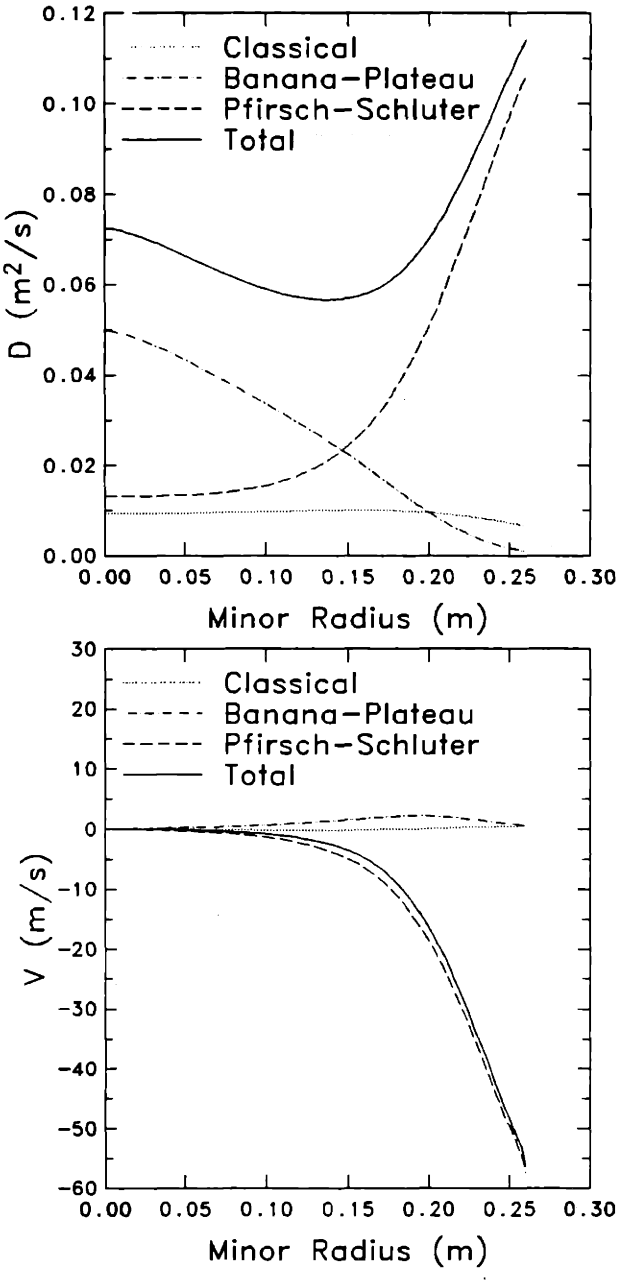

Figure 5.7: The neoclassical diffusion and convection for He-like aluminum are shown. In the diffusion coefficient the banana-plateau term is dominant in the center, and the Pfirsch-Schlüter term is dominant toward the plasma edge, because of the increasing collisionality. In the convection coefficient the Pfirsch-Schlüter term is dominant across the entire plasma, and it is directed outward because of the ion temperature gradients.

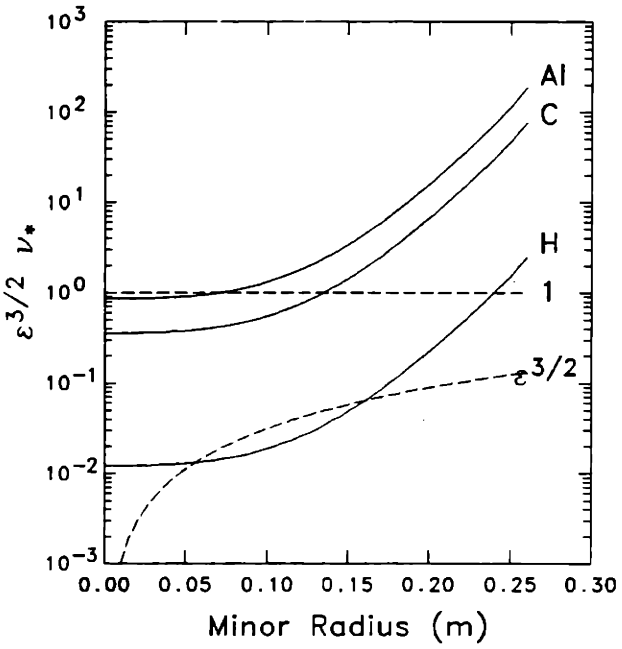

Figure 5.8: The collisionality parameter is shown for the working hydrogen (H) ions, the main carbon impurity (C) and the injected aluminum (Al). The aluminum was in the plateau regime ($\epsilon^{3/2}\nu_* < 1$) in the plasma center, and in the Pfirsch-Schlüter regime farther out. This explains why the banana-plateau diffusion coefficient was dominant near the plasma center (see Fig. 5.7).

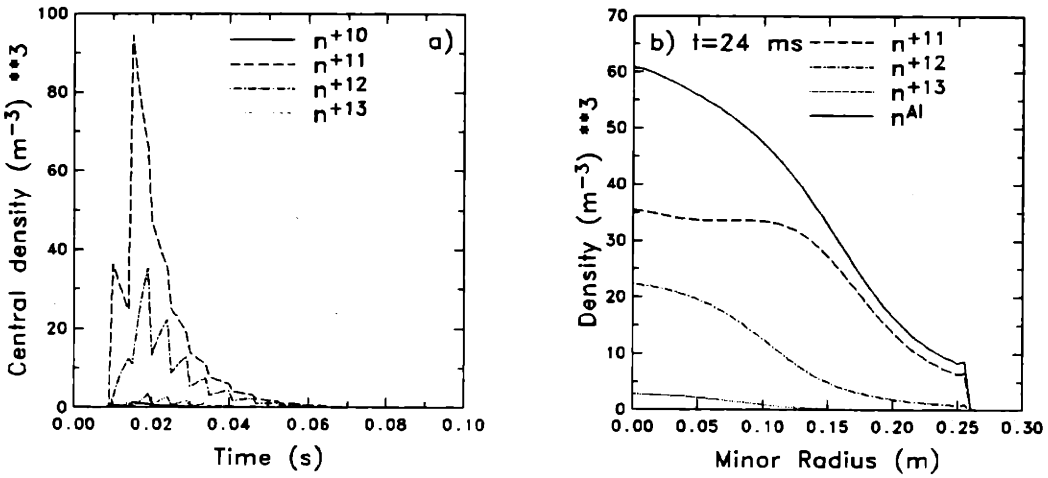

Figure 5.9: The result of a transport simulation using the neoclassical coefficients from Eqs. 5.39–5.48 is shown. a) The central densities obtained in the simulation were very small. b) The quasi-equilibrium profile was peaked because the edge density was eroded outward by convection faster than the central particles diffuse out.

the collision frequency boundary between the banana-plateau regime and the Pfirsch-Schlüter regime is $\epsilon^{3/2}\nu_* = 1$.)

The result of a numerical simulation using the neoclassical coefficient including sawteeth is shown in Fig. 5.9. The neoclassical results do not agree with the experimental data. The central densities achieved with the neoclassical coefficients were much too small by about 12 orders of magnitude. This was because of the strong outward convection, which prevented the aluminum from moving toward the plasma center (see Fig. 5.7). The aluminum density profile eventually peaked, but not because of an inward pinch. Rather, this peaking occurred because the material near the edge was transported outward faster than the material near the center. Thus the experiment implies transport different from neoclassical predictions; specifically the ratio of D to V must be greater than the neoclassical values to allow the aluminum ions to diffuse into the plasma before they are transported out by the convection.

This result is interesting, because it is in direct contrast to the common belief that

neoclassical transport universally results in peaked impurity profiles. In this case the aluminum starts in the edge region, where it is highly collisional, and thus in the Pfirsch-Schlüter regime. In this collisionality regime, temperature gradients *prevent* impurity peaking—so called "temperature screening." On the other hand, temperature gradient terms in the banana-plateau collisionality regime lead to "temperature peaking."

Chapter 6

Comparison of Measured Particle Transport Coefficients on TEXT from Different Techniques

It is informative to compare the results of this impurity transport study with previous results of particle transport experiments in TEXT. To this end Table 6 compares many measured particle transport coefficients from TEXT.

Many experimental techniques have been applied to the problem of determining particle transport coefficients. In TEXT these methods have included spectroscopy of impurity line radiation or charge exchange recombination radiation, electron density profile measurements coupled with H_α determination of the neutral hydrogen source distribution, sawtooth pulse propagation (SPP) from high resolution interferometry, pellet injection, gas puff (G.P.) and oscillating gas puff (OGP) experiments, and the x-ray imaging method described herein. All these methods yielded generally similar values for D (typically on the order of $0.5 \sim 2.0$ m^2/s) and V (typically on the order of $5 \sim 30$ m/s). A notable exception in the case of D is the result from Ref. [196], where D near the limiter radius, calculated from measurements of the turbulent electron density fluctuations and potential fluctuations, was found to vary rapidly with radius from ~ 12 m^2/s, 2 cm inside the limiter radius, to ~ 1 m^2/s, 1 cm outside the limiter radius. It is important to note that the methods used for this measurement are the only ones used to determine D near the edge [224]. All other methods, including x-ray imaging diagnostice, give a value for central D. The value of D found from the measurements of turbulent fluctuations, combined with the measured electron density gradient was

Table 6.1: This table summarizes the results from measurements of particle transport coefficients in TEXT using various experimental methods: S=spectroscopy, SPP=sawtooth pulse propagation (of electrons), CXRS=charge exchange recombination spectroscopy, GP=gas puff, OGP=oscillating gas puff, XRI=x-ray imaging. The columns labeled f_D and f_V describe the radial dependence of the diffusion coefficient and convection respectively.

Measured Particle Transport Coefficients on TEXT

Method	Species	Condition	$D_0(m^2/s)$	f_D	$V_0(m/s)$	f_V	r(m)	Ref.
S	Sc	2.8/200/4.2	0.9±0.2	const.	6.0±0.5	$V_0(r/a)$	-	[35]
FIR n_e+ H_α source	H	2.0/200/4	10–1	rapid	-	-	.25–.28‡	[196]
SPP	e	2.0/300/4	5.5	const.	-	-	0.14-0.26	[58]
SPP	e	2.0/200/4	2.1	const.	-	-	0.14-0.26	[58]
CXRS	C	2.8/250/3(6*)	0.15±0.02	const.	6.5±1.0	$V_0(r/a)$	-	[52]
S	Sc	2.8/300/3.5	1.0	const.	10	$V_0(r/a)$	-	[225]
G.P.	H	2.8/300/3.5	1.5±0.02	const.	29±9	$V_0(r/a)$	≤0.2	[225]
OGP	H	2.8/300/4.0	0.6	const.	5.0	$V_0(r/a)$	≤0.26	[217]
OGP	H	2.8/300/6.0	0.23	const.	1.7	$V_0(r/a)$	≤0.26	[217]
OGP	H	1.5/150/1.0	2.30	const.	21.0	$V_0(r/a)$	≤0.26	[217]
XRI	Al	2.8/320/6.0	0.35	const.	-	-	≤0.10	†
XRI	Al	2.8/160/2	0.4	const.	-	-	≤0.10	†

* Carbon transport was measured after a frozen hydrogen pellet was injected into a plasma with central line averaged density = 3×10^{19} m^{-3}, raising the density to 6×10^{19} m^{-3}.
† This work.

‡ Again, this is the only method applicable to the edge region [224].

shown to give a particle flux consistent with the flux inferred from the electron density profile and source measurements. Another deviation from the general results for D was found for carbon ($D \simeq 0.1$ m^2/s) transport following pellet injection [52]. In that case D was close to the neoclassical prediction.

The values of constant D_0 used in the previous chapter to match the central x-ray signals are included for comparison. They are in good agreement with the other values, especially the values of D found for the working ions during oscillating gas puff experiments.

Chapter 7

Summary and Conclusions; Suggestions for Future Work

7.1 Summary

This thesis has described a set of impurity transport experiments performed in TEXT using multiply filtered x-ray imaging arrays. Aluminum was injected into TEXT and temporally resolved radial profiles of the absolute density of the three highest charges states were measured with the x-ray imaging system.

The model for calculating the x-ray emissivity was outlined in chapter 2. It included continuum from bremsstrahlung and radiative recombination, and lines from collisional excitation, dielectronic recombination, and recombination into upper levels. All the numerical parameters for calculating this radiation are tabulated in Appendix C.

The x-ray imaging system was described in chapter 3. The entire system consisted of 92 x-ray detectors in three arrays viewing the plasma from the same toroidal location. The horizontal x-ray array was absolutely calibrated, and the vertical array was cross-calibrated relative to the vertical array. In the course of the absolute calibration measurements it was determined that the sensitive depth of silicon surface barrier detectors is determined by the physical thickness of the detector, not the thickness of the depletion layer. This result will be particularly important for x-ray imaging systems used to diagnose very high temperature plasmas. The x-ray imaging system was used to measure profiles of injected aluminum in TEXT. For the first time a set of three filters was used to measure the density of three different impurity species. One of the filters was a novel krypton edge absorption filter to discriminate between the He-like and H-like aluminum charge states. Another filter with a higher low energy cutoff, sensitive

primarily to radiative recombination, was used to separate the fully stripped aluminum density.

Experimental results were described in chapter 4. The aluminum ion confinement time was measured in many discharges, and a confinement time scaling was found by performing a regression analysis on the data. The resulting scaling was: $\tau_c \simeq 571\ Z_{eff}^{1.16} \bar{n}_e^{1.25} I_P^{-0.93} (m_i/Z_i)^{0.57}$. This is the first report of the density and isotope charge (Z_i) dependence of τ_c in TEXT. Sawtooth-averaged aluminum density profiles were measured in several different discharge conditions. The profiles were fairly flat relative to the electron density profile. Sawteeth apparently strongly determine the aluminum profile shape, since discharges with short sawtooth periods exhibited hollow profiles, and discharges with small sawteeth exhibited slightly peaked profiles.

The charge state distribution from these profiles was found to be close to coronal equilibrium except in those discharges with very fast sawteeth or else a very large sawtooth inversion radius. Density profile changes during sawtooth crashes were also measured. Immediately after an injection the soft x-ray signal is rising and the impurity density is peaked near the plasma edge. At that time, the sawteeth can strongly enhance the inward impurity transport, ostensibly by periodically destroying the flux surfaces. In the later decay phase of the soft x-ray signal, after the x-ray signals have peaked, sawteeth also modify the aluminum density profiles by periodically ejecting material from the plasma center. Those discharges with the longest sawtooth periods obtained the most peaked aluminum density profiles. Thus the sawteeth may play a role in preventing central impurity accumulation. Some preliminary evidence for up-down asymmetric density profiles was also presented in chapter 4. The observed experimental asymmetry parameter was of the same order as neoclassical predictions. This was not necessarily anticipated since the overall impurity transport could not be adequately modeled using only neoclassical transport coefficients.

Numerical transport simulations were described in chapter 5. Using anomalous transport coefficients the data could not be matched with either a constant D model or a constant D, linear V model. Neoclassical simulations were also unsuccessful at matching the experimental data. The neoclassical convective velocity, driven by ion temperature gradients and ion density gradients in the Pfirsch-Schlüter collisionality regime, is very large and directed outward. This prevented any significant amount of aluminum from ever reaching the plasma center.

7.2 Future Work

In principle, the method of x-ray imaging can be used to measure profiles of intrinsic impurities as well as injected impurities. The situation is complicated in TEXT because there are several different intrinsic impurities. Carbon is the primary light impurity, but there is also a significant amount of oxygen. Titanium from the limiter is the primary high Z impurity, but there is also iron, and to a lesser extent chromium and nickel, from stainless steel. Profiles of the fully-stripped carbon and oxygen were measured using active charge exchange recombination spectroscopy [62]. The charge state distribution of the heavy impurities is not well known. However, with improved spectroscopic information in the x-ray region, this issue could be addressed. If the charge state distribution of the heavy impurities were known, the x-ray imaging method could be used to obtain profiles of the carbon and titanium. This would be of great importance since it would yield $Z_{eff}(r)$ with good spatial and temporal resolution.

Further work on improving the observations of up-down asymmetries is also tenable. The first step would be to repeat some impurity injections and systematically rule out the possible causes other than impurity density profiles listed in chapter 4. The second step would be to check the Z^2 scaling predicted by Eq. 4.31. Again a spectroscopic measurement would also be valuable. For example, a rotating mirror system could be used to scan the plasma vertically. If the asymmetries were real and disagreed with neoclassical theory, an explanation for their existence should be sought.

To improve the neoclassical modeling discussed in chapter 5, more accurate profiles of the carbon and titanium are required. As mentioned above, the x-ray imaging system may be able to provide profiles of the intrinsic impurities. If the heavy impurities are important in determining test impurity transport, further development of neoclassical transport theory is also required. A four-species, possibly mixed regime, theory would be necessary to treat the aluminum, hydrogen, carbon and titanium transport all self-consistently.

Injected impurity transport was examined in only some of the normal TEXT operating regimes. It will be interesting to repeat some of the same experiments in other regimes. For example aluminum could be injected into ECH-heated plasmas or into plasmas after impurity pellet-injection. These experiments might help provide a more fundamental understanding of the impurity transport by exposing changes in the transport due to various perturbations.

Finally, the capability of the x-ray imaging system could be improved to be more useful for the forthcoming TEXT upgrade. In particular the arrays could be modified to allow better imaging of the edge region. Understanding edge plasma phenomena is crucial for understanding improved confinement under H-mode conditions, one of the primary goals of the TEXT upgrade. Several specific improvements would be required to adequately perform edge imaging with the existing arrays. First the beryllium windows must be replaced with filters that have much lower energy response, or a filter wheel with several different filters could be added to the arrays (a five-position filter wheel already exists in the vertical array). Second the preamplifiers must be improved, perhaps by incorporating a switchable gain, to increase the dynamic range of the system to allow simultaneous edge and central imaging. With these two changes edge plasma behavior such as ELMs may be studied with the imaging system. Detailed quantitative impurity studies in the edge may not be possible with the x-ray imaging system alone because of the complicated spectrum in the UV and VUV wavelength region. However, the mode structure of ELMs, and their impact on global plasma behavior could easily be studied.

Appendix A

Neoclassical Calculations of K_{ij}^{a} in the Pfirsch-Schlüter Regime

From Ref. [24], the viscocity matrix in the Pfirsch-Schlüter collisionality regime is written

$$K_{ij}^{a} = p_a \tau_{aa} \iota_{ij}^{a}, \tag{A.1}$$

where

$$\iota_{11}^{a} = \frac{q_a^{11}}{Q_a}, \tag{A.2}$$

$$\iota_{12}^{a} = \frac{(7/2)(q_a^{11} + q_a^{01})}{Q_a} = \iota_{21}^{a}, \tag{A.3}$$

$$\iota_{22}^{a} \frac{(49/4)(q_a^{11} + q_a^{00} + 2q_a^{01})}{Q_a}, \tag{A.4}$$

and

$$Q_a = (2/5)(q_a^{00} q_a^{11} - q_a^{01} q_a^{01}) \tag{A.5}$$

$$q_a^{ij} = \sum_b \left(\frac{n_b e_b^2}{n_a e_a^2} \right) (q_{ab}^{ij} - \delta_{ab} r_{ab}^{ij}). \tag{A.6}$$

The q_{ab}^{ij} matrix elements are given explicitly for Coulomb collisions (with $x_{ab} \equiv v_{Tb}/v_{Ta}$), as

$$q_{ab}^{00} = (3 + 5x_{ab}^2)(1 + x_{ab}^2)^{-3/2} \tag{A.7}$$

$$q_{ab}^{01} = \frac{3}{2}(3 + 7x_{ab}^2)(1 + x_{ab}^2)^{-5/2} \tag{A.8}$$

$$q_{ab}^{11} = \frac{35x_{ab}^6 + \frac{77}{2}x_{ab}^4 + \frac{185}{4}x_{ab}^2 + \frac{51}{4}}{(1 + x_{ab}^2)^{7/2}}, \tag{A.9}$$

and the r_{ab}^{ij} matrix elements are

$$r_{aa}^{00} = \frac{1}{\sqrt{2}} \tag{A.10}$$

$$r_{aa}^{01} \quad \frac{3}{2\sqrt{2}} \tag{A.11}$$

$$r_{aa}^{11} \quad \frac{15}{4\sqrt{2}}. \tag{A.12}$$

Appendix B

Neoclassical Calculation of the Trace Impurity Flux in the Pfirsch-Schlüter Regime

Coefficients for Eq. 1.28 are summarized, from Ref. [24]. They are

$$L_1 = -\frac{m_I n_I}{\tau_{IT}}(d_0 + 0.236 d_3) - \frac{m_i n_i}{\tau_{DT}}[1 - C_1(\bar{Z}_{iI}, 0)], \tag{B.1}$$

$$L_2 = \frac{m_I n_I}{\tau_{IT}}(0.236 d_3), \tag{B.2}$$

$$L_3 \frac{m_I n_I}{\tau_{IT}} d_3, \tag{B.3}$$

$$L_{11}^{TT} = \frac{m_I n_I}{\tau_{IT}} d_0 + \frac{m_i n_i}{\tau_{iT}}, \tag{B.4}$$

$$L_{11}^{Ti} = \frac{m_i n_i}{\tau_{iT}} C_1(\bar{Z}_{iI}, 0), \tag{B.5}$$

$$L_{12}^{Ti} = \frac{m_i n_i}{\tau_{iT}} C_2(\bar{Z}_{DI}, 0), \tag{B.6}$$

where the collision times τ_{ab} are defined below. The variables labeled d are

$$d_0 = -\left(\frac{m_T}{m_I}\right)^{1/2}\left[\hat{M}^{00} - \frac{\hat{M}^{01}\hat{M}^{10}}{\hat{M}^{11}}\right], \tag{B.7}$$

$$d_1 = 0.88\left(\frac{m_T}{m_I}\right)^{1/2}\left[\hat{N}^{01} - \frac{\hat{M}^{01}\hat{N}^{11}}{\hat{M}^{11}} - \frac{4}{15}\left(\hat{N}^{02} - \frac{\hat{M}^{01}\hat{N}^{12}}{\hat{M}^{11}}\right)\right], \tag{B.8}$$

$$d_2 = \frac{\hat{M}^{01}}{\hat{M}^{11}}, \tag{B.9}$$

$$d_3 = \frac{1}{0.885}\left[\left(\frac{Z_I^2}{Z_T^2}\right) d_2 - d_1\right], \tag{B.10}$$

Here, the coefficients C_1, C_2 as functions of two arbitrary variables α and β are

$$C_1(\alpha,\beta) \quad 1 \quad \frac{0.52\alpha}{0.59 + \alpha + 1.34\beta^2}, \tag{B.11}$$

$$C_2(\alpha,\beta) = 1.5 - \frac{0.29 + 1.20\alpha}{0.59 + \alpha + 1.34\beta^2}. \tag{B.12}$$

We also have defined

$$\tilde{Z}_{iI} = \frac{n_I Z_I^2}{n_i}, \tag{B.13}$$

$$\beta = \omega_{Ti}\tau_{Ti}, \tag{B.14}$$

where ω_{Ti} is the transit frequency of the working ions, and

$$\hat{M}^{ij} = M_{TI}^{ij} - \frac{M_{TI}^{i2}M_{TI}^{2j}}{M_{TI}^{22}}, \tag{B.15}$$

$$\hat{N}^{ij} = N_{TI}^{ij} - \frac{M_{TI}^{i2}N_{TI}^{2j}}{M_{TI}^{22}}. \tag{B.16}$$

For arbitrary species indices a and b one has

$$M_{ab}^{00} = -\left(1 + \frac{m_a}{m_b}\right)(1 + x_{ab}^2)^{-3/2} = -N_{ab}^{00}, \tag{B.17}$$

$$M_{ab}^{01} = M_{ab}^{10} = -\frac{3}{2}\left(1 + \frac{m_a}{m_b}\right)(1 + x_{ab}^2)^{-5/2} = -N_{ab}^{10}, \tag{B.18}$$

$$M_{ab}^{11} = -\left(\frac{13}{4} + 4x_{ab}^2 + \frac{15}{2}x_{ab}^4\right)(1 + x_{ab}^2)^{-5/2}, \tag{B.19}$$

$$N_{ab}^{11} = \frac{27}{4}\frac{T_a}{T_b}x_{ab}^2(1 + x_{ab}^2)^{-5/2}, \tag{B.20}$$

$$M_{ab}^{02} = -\frac{15}{8}\left(1 + \frac{m_a}{m_b}\right)(1 + x_{ab}^2)^{-7/2} = -x_{ba}N_{ba}^{02}, \tag{B.21}$$

$$M_{ab}^{12} = -\left(\frac{69}{16} + 6x_{ab}^2 + \frac{63}{4}x_{ab}^4\right)(1 + x_{ab}^2)^{-7/2}, \tag{B.22}$$

$$N_{ab}^{12} = \frac{225}{16}\frac{T_a}{T_b}x_{ab}^4(1 + x_{ab}^2)^{-7/2}, \tag{B.23}$$

$$M_{ab}^{22} = -\frac{(443/64) + 17x_{ab}^2 + (459/8)x_{ab}^4 + 28x_{ab}^6 + (175/8)x_{ab}^8}{(1 + x_{ab}^2)^{9/2}}, \tag{B.24}$$

$$N_{ab}^{22} = \frac{2625}{64}\frac{T_a}{T_b}\frac{x_{ab}^4}{(1 + x_{ab}^2)^{(9/2)}}, \tag{B.25}$$

$$x_{ab} = \frac{v_{Tb}}{v_{Ta}}, \tag{B.26}$$

where $v_{Ta} = \sqrt{2T/m_a}$. It is important to note that

$$M_{ab}^{j0} + N_{ab}^{j0} = 0, \tag{B.27}$$

$$M_{ab}^{ij} = M_{ab}^{ji}, \tag{B.28}$$

$$\frac{N_{ab}^{ij}}{T_a v_{Ta}} = \frac{N_{ba}^{ji}}{T_b v_{Tb}}, \tag{B.29}$$

and the collision time is taken from Braginskii [69] to be

$$\tau_{ab} = \left(\frac{3\sqrt{\pi}}{4}\right) \frac{m_a^2 v_{Ta}^3}{4\pi n_b e_a^2 e_b^2 \ln \Lambda} \qquad m_a < m_b \ . \tag{B.30}$$

Appendix C

Atomic Parameters for X-Ray Emissivity Calculations

This appendix contains the atomic physics parameters and references for the calculation of line radiation from several impurities: aluminum, silicon, titanium and iron. The parameters for aluminum and silicon were tabulated because these are the elements injected into TEXT for impurity transport studies. The parameters for titanium and iron were tabulated because these are the dominant high Z intrinsic impurities in TEXT. Plots of most of the power functions calculated for impurities and filters relevant to this work are shown at the end of the Appendix. The parameters listed for each collisionally excited transition are the wavelength $\lambda(\text{Å})$, the energy E(keV) and the oscillator strength f_{ij}. The line intensity is always calculated with the Gaunt factor $< g_{ij} >$ assumed to be equal to 0.2 [78] for use in Eq. C.1

$$P_{ij} = 5.06 \times 10^{-10} \frac{f_{ij} < g_{ij} > e^{-h\nu/T_e}}{\sqrt{T_e}} \ \text{keVcm}^3\text{s}^{-1}, \tag{C.1}$$

with $h\nu$ and T_e both in keV. Some authors prefer to set the oscillator strength at some constant value and adjust the Gaunt factor to achieve the proper line intensity [98]. I have taken the approach of maintaining $< g_{ij} >$ constant and varying f_{ij} to maintain the correct *product* $f_{ij} < g_{ij} >$. It is important to realize that the two methods obtain the same overall line intensities.

Parameters for calculating the total line intensity from dielectronic satellite lines are also given in this appendix for H-like and He-like ions. The parameters listed are for use in Eq. C.2

$$P_d = 5.23 \times 10^{-27} \frac{\bar{E}_s Q_d}{g_1 (T_e)^{3/2}} e^{-E_s/T_e} \ \text{keVcm}^3\text{s}^{-1}. \tag{C.2}$$

The particular parameters listed include the *average* satellite energy $\bar{E}_s$ (keV) and the total dielectronic rate coefficient $Q_d = \sum_{\substack{\text{all} \\ \text{satellites}}} g_s A_r A_a/(A_a + \sum A_r)$ for both H-like and He-like ions. The parameters for aluminum are listed in Table C.1, those for silicon are in Table C.2, those for titanium are in Table C.3, and those for iron are in Table C.4.

Using the method described in chapter 2, and the parameters shown in this appendix, the total x-ray power functions for several combinations of impurity species and x-ray absorption filters were calculated. Table C.5 lists the characteristics of all the x-ray filters used in the imaging arrays on TEXT. Figures C.1, C.2, C.3, and C.4 show the x-ray power functions for the main intrinsic impurities in TEXT: carbon, oxygen, titanium, and iron. Since the charge state distribution is not known for these elements, coronal equilibrium was assumed for the calculations. This should be a good approximation for carbon and oxygen, because the binding energy of the last electron is low compared to typical TEXT temperatures near the plasma center. Thus these ions should be fully stripped over the portion of the plasma where the x-ray signal is strong. However, the accuracy of the assumption of coronal equilibrium for titanium is unknown.

The power functions for injected aluminum are shown in the next four figures. Figures C.5, C.6, C.7, and C.8 show the x-ray power functions for the four highest charge states of aluminum for filters A, D, F and G respectively. The latter two filters are both krypton filters with different krypton pressure used in the Array A vacuum box.

Table C.1:
Atomic Physics Parameters for Aluminum (Z=13)

Line Parameters

Transition	λ(Å)	E(keV)	f_{ij}	A_{REC}	η	Ref.
H-like ions:						
$1s\ ^2S_{1/2} - 2p\ ^2P_{3/2}$	7.170	1.729	0.26	3.99	0.70	[98]
$1s\ ^2S_{1/2} - 2p\ ^2P_{1/2}$	7.170	1.729	0.26	-	-	[98]
$1s\ ^2S_{1/2} - 3p\ ^2P_{1/2}$	6.050	2.049	0.081	0.86	0.70	[98]
He-like ions:						
$1s^2\ ^1S_0 - 1s2p\ ^1P_1$	7.700	1.610	0.69	9.97	0.87	[98]
$1s^2\ ^1S_0 - 1s2p\ ^3P_2$	7.810	1.588	0.09	25.64	0.81	[98]
$1s^2\ ^1S_0 - 1s2p\ ^3P_1$	7.810	1.588	0.09	-	-	[98]
$1s^2\ ^1S_0 - 1s2s\ ^3S_1$	7.870	1.575	0.036	0.79	0.54	[98]
$1s^2\ ^1S_0 - 1s3p\ ^1P_1$	6.650	1.864	0.135	0.37	0.70	[98]

Dielectronic Satellite Parameters

Ion	$\bar{E}_s$ (keV)	Q_d	Ref.
H-like	1.709	3.037×10^{14}	[89]
He-like	1.571	1.874×10^{14}	[89]

Table C.2:
Atomic Physics Parameters for Silicon (Z=14)

Line Parameters

Transition	λ(Å)	E(keV)	f_{ij}	A_{REC}	η	Ref.
H-like ions:						
$1s\ ^2S_{1/2} - 2p\ ^2P_{3/2}$	6.180	2.006	0.503	3.99	0.70	[98]
$1s\ ^2S_{1/2} - 2p\ ^2P_{1/2}$	6.180	2.006	0.503	-	-	[98]
$1s\ ^2S_{1/2} - 3p\ ^2P_{1/2,3/2}$	5.220	2.375	0.080	0.86	0.70	[98]
$1s\ ^2S_{1/2} - 4p\ ^2P_{1/2,3/2}$	4.950	2.505	0.022	0.30	0.70	[98]
$1s\ ^2S_{1/2} - 5p\ ^2P_{1/2,3/2}$	4.830	2.567	0.0096	0.15	0.70	[98]
$1s\ ^2S_{1/2} - 6p\ ^2P_{1/2,3/2}$	4.770	2.599	0.0047	0.08	0.70	[98]
He-like ions						
$1s^2\ ^1S_0 - 1s2p\ ^1P_1$	6.650	1.864	0.655	9.97	0.87	[98]
$1s^2\ ^1S_0 - 1s2p\ ^3P_2$	6.690	1.853	0.125	25.64	0.81	[98]
$1s^2\ ^1S_0 - 1s2p\ ^3P_1$	6.690	1.853	0.125	-	-	[98]
$1s^2\ ^1S_0 - 1s2s\ ^3S_1$	6.740	1.840	0.100	0.79	0.54	[98]
$1s^2\ ^1S_0 - 1s3p\ ^1P_1$	5.680	2.183	0.128	0.37	0.70	[98]
$1s^2\ ^1S_0 - 1s4p\ ^1P_1$	5.410	2.292	0.050	0.18	0.70	[98]
$1s^2\ ^1S_0 - 1s5p\ ^1P_1$	5.290	2.344	0.024	0.10	0.70	[98]

Dielectronic Satellite Parameters

Ion	$\bar{E}_s$ (keV)	Q_d	Ref.
H-like	1.984	2.072×10^{14}	[89]
He-like	1.836	2.451×10^{14}	[89]

Table C.3:
Atomic Physics Parameters for Titanium (Z=22)

Line Parameters

Transition	λ(Å)	E(keV)	f_{ij}	Ref.
H-like ions:				
$1s\ ^2S_{1/2} - 2p\ ^2P_{3/2}$	2.490	4.979	0.405	[91,92]
$1s\ ^2S_{1/2} - 2p\ ^2P_{1/2}$	2.496	4.968	0.382	[91,92]
He-like ions:				
$1s^2\ ^1S_0 - 1s2p\ ^1P_1$	2.610	4.751	0.464	[93,94]
$1s^2\ ^1S_0 - 1s2p\ ^3P_2$	2.618	4.735	0.122	[93,94]
$1s^2\ ^1S_0 - 1s2p\ ^3P_1$	2.622	4.728	0.116	[93,94]
$1s^2\ ^1S_0 - 1s2s\ ^3S_1$	2.636	4.703	0.287	[93,94]
Li-like ions:				
$1s^22p\ ^2P_{3/2} - 1s^24d\ ^2D_{5/2}$	11.958	1.037	0.110	[226]
$1s^22p\ ^2P_{3/2} - 1s^24d\ ^2D_{3/2}$	11.958	1.037	0.012	[226]
$1s^22p\ ^2P_{1/2} - 1s^24d\ ^2D_{3/2}$	11.872	1.044	0.120	[226]
$1s^22s\ ^2S_{1/2} - 1s^24p\ ^2P_{1/2,3/2}$	11.452	1.083	0.099	[226]
$1s^22p\ ^2P_{3/2} - 1s^25d\ ^2D_{5/2}$	10.690	1.160	0.040	[226]
$1s^22p\ ^2P_{3/2} - 1s^25d\ ^2D_{3/2}$	10.690	1.160	0.0045	[226]
$1s^22p\ ^2P_{1/2} - 1s^25d\ ^2P_{5/2}$	10.620	1.168	0.045	[226]
$1s^22s\ ^2S_{1/2} - 1s^25p\ ^2P_{1/2,3/2}$	10.278	1.206	0.040	[226]
$1s^22p\ ^2P_{3/2} - 1s^26d\ ^2D_{5/2}$	10.109	1.227	0.0198	[226]
$1s^22p\ ^2P_{3/2} - 1s^26d\ ^2D_{3/2}$	10.109	1.227	0.0022	[226]
$1s^22p\ ^2P_{1/2} - 1s^26d\ ^2D_{3/2}$	10.046	1.234	0.0221	[226]
$1s^22s\ ^2S_{1/2} - 1s^26p\ ^2P_{1/2,3/2}$	9.733	1.274	0.0211	[226]
$1s^22s\ ^2S_{1/2} - 1s^27p\ ^2P_{1/2,3/2}$	9.434	1.314	0.0124	[226]
$1s^22s\ ^2S_{1/2} - 1s^28p\ ^2P_{1/2,3/2}$	9.246	1.341	0.0077	[226]
$1s^22p\ ^2P_{3/2} - 1s^27d\ ^2D_{5/2}$	9.788	1.267	0.0113	[226]
$1s^22p\ ^2P_{3/2} - 1s^27d\ ^2D_{3/2}$	9.788	1.267	0.012	[226]
$1s^22p\ ^2P_{1/2} - 1s^27d\ ^2D_{3/2}$	9.733	1.274	0.0126	[226]
$1s^22p\ ^2P_{3/2} - 1s^28d\ ^2D_{3/2}$	9.591	1.293	0.00079	[226]
$1s^22p\ ^2P_{3/2} - 1s^28d\ ^2D_{5/2}$	9.591	1.293	0.0071	[226]
$1s^22p\ ^2P_{1/2} - 1s^28d\ ^2D_{3/2}$	9.534	1.300	0.0083	[226]
$1s^22p\ ^2P_{3/2} - 1s2p^2\ ^2D_{5/2}$	2.635	4.704	0.190	[226]
$1s^22p\ ^2P_{1/2} - 1s2p^2\ ^2D_{3/2}$	2.632	4.711	0.310	[226]
$1s^22p\ ^2P_{1/2} - 1s2p^2\ ^2P_{1/2}$	2.630	4.714	0.280	[226]
$1s^22p\ ^2P_{3/2} - 1s2p^2\ ^2P_{3/2}$	2.630	4.735	0.330	[226]

Dielectronic Satellite Parameters

Ion	$\bar{E}_s$ (keV)	Q_d	Ref.
H-like	4.964	1.326×10^{15}	[91,92]
He-like	4.699	1.933×10^{15}	[92]

Table C.4:
Atomic Physics Parameters for Iron (Z=26)
Line Parameters

Transition	λ(Å)	E(keV)	f_{ij}	Ref.
H-like ions:				
$1s\ ^2S_{1/2}$ - $2p\ ^2P_{1/2}$	1.782	6.960	0.426	[98]
$1s\ ^2S_{1/2}$ $2p\ ^2P_{3/2}$	1.777	6.977	0.426	[98]
$1s\ ^2S_{1/2}$ - $3p\ ^2P_{1/2}$	1.510	8.211	0.069	[98]
$1s\ ^2S_{1/2}$ - $4p\ ^2P_{1/2,3/2}$	1.430	8.670	0.019	[98]
$1s\ ^2S_{1/2}$ - $5p\ ^2P_{1/2,3/2}$	1.400	8.856	0.0083	[98]
$1s\ ^2S_{1/2}$ - $6p\ ^2P_{1/2,3/2}$	1.390	8.920	0.0041	[98]
He-like ions:				
$1s^2\ ^1S_0 - 1s2p\ ^1P_1$	1.850	6.702	0.571	[98]
$1s^2\ ^1S_0 - 1s2p\ ^3P_2$	1.855	6.683	0.289	[98]
$1s^2\ ^1S_0 - 1s2p\ ^3P_1$	1.859	6.669	0.289	[98]
$1s^2\ ^1S_0$ - $1s2s\ ^3S_1$	1.868	6.637	0.049	[98]
$1s^2\ ^1S_0 - 1s3p\ ^1P_1$	1.592	7.788	0.160	[227]
$1s^2\ ^1S_0 - 1s4p\ ^1P_1$	1.518	8.168	0.057	[227]
$1s^2\ ^1S_0 - 1s5p\ ^1P_1$	1.460	8.492	0.028	[227]
Li-like ions:				
$1s^22s\ ^2S_{1/2} - 1s^23p\ ^2P_{1/2}$	10.650	1.164	0.380	[227]
$1s^22s\ ^2S_{1/2} - 1s^23p\ ^2P_{3/2}$	10.610	1.169	0.380	[227]
$1s^22s\ ^2S_{1/2} - 1s^24p\ ^2P_{1/2}$	7.989	1.552	0.096	[227]
$1s^22s\ ^2S_{1/2} - 1s^24p\ ^2P_{3/2}$	7.979	1.554	0.096	[227]
$1s^22s\ ^2S_{1/2} - 1s^25p\ ^2P_{3/2}$	7.233	1.714	0.042	[227]
$1s^22s\ ^2S_{1/2} - 1s2s2p\ ^2P_{1/2}$	1.863	6.655	0.400	[227]
$1s^22s\ ^2S_{1/2}$ $1s2s2p\ ^2P_{3/2}$	1.861	6.662	0.400	[227]
Be-like ions:				
$1s^22s^2\ ^1S_0$ $1s2s^22p\ ^1P_1$	1.872	6.623	0.780	[227]
B-like ions:				
$1s^22s^22p\ ^2P_{3/2} - 1s^22s^23s\ ^2S_{1/2}$	12.380	1.002	0.019	[227]
$1s^22s^22p\ ^2P_{1/2} - 1s^22s^23s\ ^2S_{1/2}$	12.220	1.015	0.019	[227]
$1s^22s^22p\ ^2P_{1/2} - 1s^22s^23d\ ^2D_{3/2}$	11.727	1.057	0.660	[227]
$1s^22s^22p\ ^2P_{3/2} - 1s^22s^24d\ ^2D_{5/2}$	9.05	1.370	0.120	[227]
$1s^22s^22p\ ^2P_{1/2} - 1s^22s^22p\ ^2D_{3/2}$	8.97	1.382	0.120	[227]
$1s^22s^22p\ ^2P_0 - 1s2s^22p^2\ ^2P_0$	1.886	6.574	0.590	[227]
C-like ions:				
$1s^22s^22p^2\ ^3P_2 - 1s^22s^22p3s\ ^3P_2$	13.052	0.950	0.050	[227]
$1s^22s^22p^2\ ^3P_1 - 1s^22s^22p3d\ ^1D_2$	12.500	0.992	0.620	[227]
$1s^22s^22p^2\ ^3P_2 - 1s^22s^22p3d\ ^3F_3$	12.469	0.994	0.230	[227]
$1s^22s^22p^2\ ^3P_2 - 1s^22s^22p3d\ ^3D_3$	12.401	1.000	0.588	[227]
$1s^22s^22p^2\ ^3P_1 - 1s^22s^22p3d\ ^3D_2$	12.397	1.000	0.480	[227]
$1s^22s^22p^2\ ^3P_0 - 1s^22s^22p3d\ ^3D_1$	12.262	1.011	1.280	[227]
$1s^22s^22p^2\ ^3P_2 - 1s^22s^22p3d\ ^3P_2$	12.273	1.010	0.216	[227]
$1s^22s^22p^2\ ^3P_0 - 1s^22s2p^23p\ ^3P_0$	11.865	1.045	0.060	[227]

Line Parameters for Fe (Z=26) cont'd

Transition	λ(Å)	E(keV)	f_{ij}	Ref.
$1s^22s^22p^2\ ^3P_0$ - $1s^22s2p^23p\ ^3P_0$	11.698	1.060	0.060	[227]
$1s^22s^22p^2\ ^3P_0$ - $1s^22s2p^23p\ ^3D_0$	11.742	1 056	0.239	[227]
N-like ions:				
$1s^22s^22p^3\ ^4S_{3/2}$ - $1s^22s^22p^23s\ ^4P_{5/2}$	13.720	0.904	0.042	[227]
$1s^22s^22p^3\ ^4S_0$ - $1s^22s^22p^24d\ ^4P_0$	9.700	1.278	0.160	[227]
O-like ions				
$1s^22s^22p^4\ ^3P_2$ - $1s^22s^22p^33s\ ^3D_3$	14.720	0.842	0.038	[227]
$1s^22s^22p^4\ ^3P_0$ - $1s^22s^22p^33s\ ^3P_1$	14.549	0.852	0.023	[227]
$1s^22s^22p^4\ ^3P_1$ - $1s^22s^22p^33d\ ^3D_2$	13.993	0.886	0.460	[227]
$1s^22s^22p^4\ ^3P_2$ - $1s^22s^22p^33d\ ^3D_3$	13.763	0.901	0.240	[227]
$1s^22s^22p^4\ ^3P_1$ - $1s^22s^22p^33d\ ^3D_2$	13.705	0.905	0.460	[227]
$1s^22s^22p^4\ ^3P_2$ - $1s^22s^22p^33d\ ^3D_3$	13.518	0.918	0.740	[227]
$1s^22s^22p^4\ ^3P_1$ - $1s^22s^22p^33d\ ^3P_1$	13.428	0.923	0.370	[227]
$1s^22s^22p^4\ ^3P_1$ - $1s^22s^22p^33d\ ^3P_2$	13.547	0.915	0.410	[227]
$1s^22s^22p^4\ ^3P_2$ - $1s^22s^22p^33d\ ^3P_2$	13.503	0.918	0.250	[227]
$1s^22s^22p^4\ ^3P_0$ - $1s^22s^22p^33d\ ^3D_1$	13.442	0.922	1.390	[227]
F-like ions:				
$1s^22s^22p^5\ ^2P_{3/2}$ - $1s^22s^22p^4\ ^4D_{3/2}$	14.783	0.839	0.050	[227]
$1s^22s^22p^5\ ^2P_{1/2}$ - $1s^22s^22p^43d\ ^4P_{3/2}$	14.772	0.839	0.260	[227]
$1s^22s^22p^5\ ^2P_{1/2}$ - $1s^22s^22p^43d\ ^4P_{1/2}$	14.630	0.847	0.740	[227]
$1s^22s^22p^5\ ^2P_{3/2}$ - $1s^22s^22p^43d\ ^4P_{1/2}$	14.581	0.850	0.240	[227]
$1s^22s^22p^5\ ^2P_{3/2}$ - $1s^22s^22p^43d\ ^4P_{3/2}$	14.551	0.852	0.140	[227]
$1s^22s^22p^5\ ^2P_{1/2}$ - $1s^22s^22p^43d\ ^2S_{1/2}$	14.467	0.857	0.006	[227]
$1s^22s^22p^5\ ^2P_{1/2}$ - $1s^22s^22p^43d\ ^2P_{3/2}$	14.419	0.860	0.210	[227]
$1s^22s^22p^5\ ^2P_{3/2}$ - $1s^22s^22p^43d\ ^2P_{1/2}$	14.293	0.867	0.031	[227]
$1s^22s^22p^5\ ^2P_{3/2}$ - $1s^22s^22p^43d\ ^2P_{3/2}$	14.214	0.872	0.014	[227]
Ne-like ions:				
$1s^22s^22p^6\ ^1S_0$ - $1s^22s2p^63p\ ^1P_1$	13.824	0.897	0.210	[227]
$1s^22s^22p^6\ ^1S_0$ - $1s^22s^22p^54s\ ^3P_1$	12.681	0.978	0.024	[227]
$1s^22s^22p^6\ ^1S_0$ - $1s^22s^22p^54s\ ^1P_1$	12.509	0.991	0.040	[227]
$1s^22s^22p^6\ ^1S_0$ - $1s^22s^22p^54d\ ^3P_1$	12.320	1.006	0.090	[227]
$1s^22s^22p^6\ ^1S_0$ - $1s^22s^22p^54d\ ^3D_1$	12.263	1.011	0.310	[227]
$1s^22s^22p^6\ ^1S_0$ - $1s^22s^22p^54d\ ^1P_1$	12.121	1.023	0.410	[227]
$1s^22s^22p^6\ ^1S_0$ - $1s^22s^22p^55d\ ^3D_1$	11.251	1.102	0.140	[227]
$1s^22s^22p^6\ ^1S_0$ - $1s^22s^22p^55d\ ^1P_1$	11.130	1.114	0.130	[227]
$1s^22s^22p^6\ ^1S_0$ - $1s^22s^22p^56d\ ^1P_1$	10.660	1.163	0.060	[227]

Dielectronic Satellite Parameters

Ion	$\bar{E}_s$ (keV)	Q_d	Ref.
H-like	6.926	1.911×10^{15}	[89]
He-like	6.639	1.487×10^{15}	[89]

Table C.5: This table lists the thicknesses of the materials used in the x-ray absorption filters in the imaging system on TEXT. The filters all consisted of combinations of beryllium, aluminum, gold, carbon, and krypton. The thicknesses are listed in the form ρt in mg/cm^2.

Filter	Be	Al	Au	C	Kr
A	4.69	0.0	0.048	0.0	0.0
B	4.69	0.195	0.048	1.47	0.0
C	4.69	4.86	0.0	0.0	0.0
D	4.69	0.67	0.0	30.5	0.0
E	4.69	0.67	0.0	0.0	0.0
F	4.69	0.67	0.0	0.0	0.357
G	4.69	0.67	0.0	0.0	1.73
H	4.69	0.67	0.0	0.0	1.48

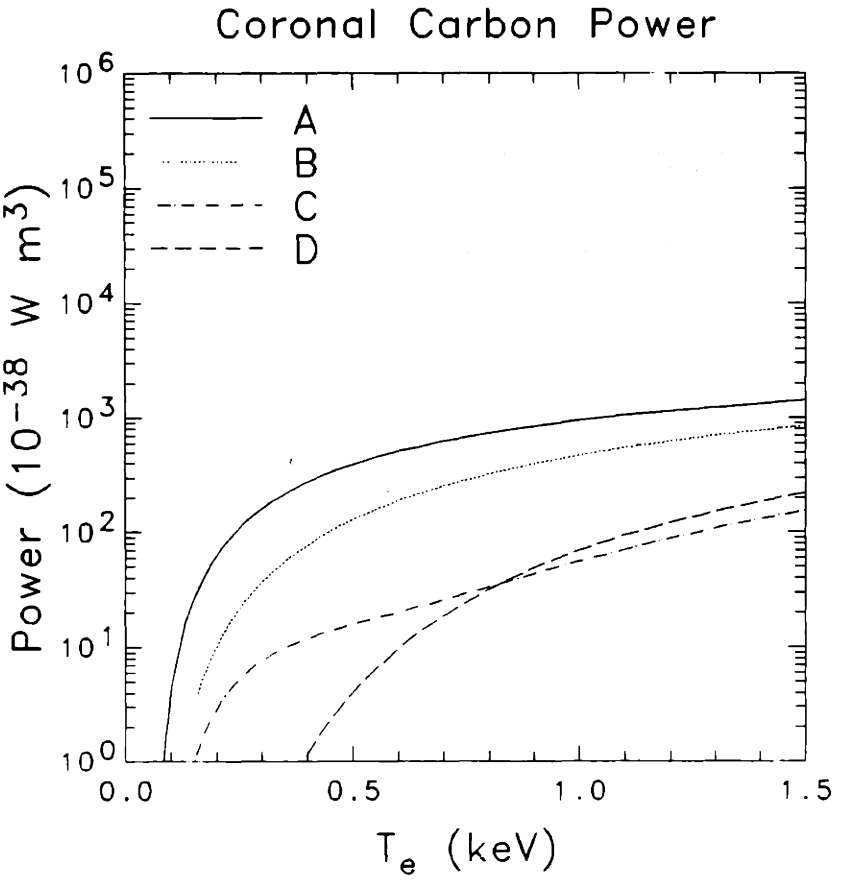

Figure C.1: The x-ray power functions for carbon in coronal equilibrium for filters A, B, C, and D.

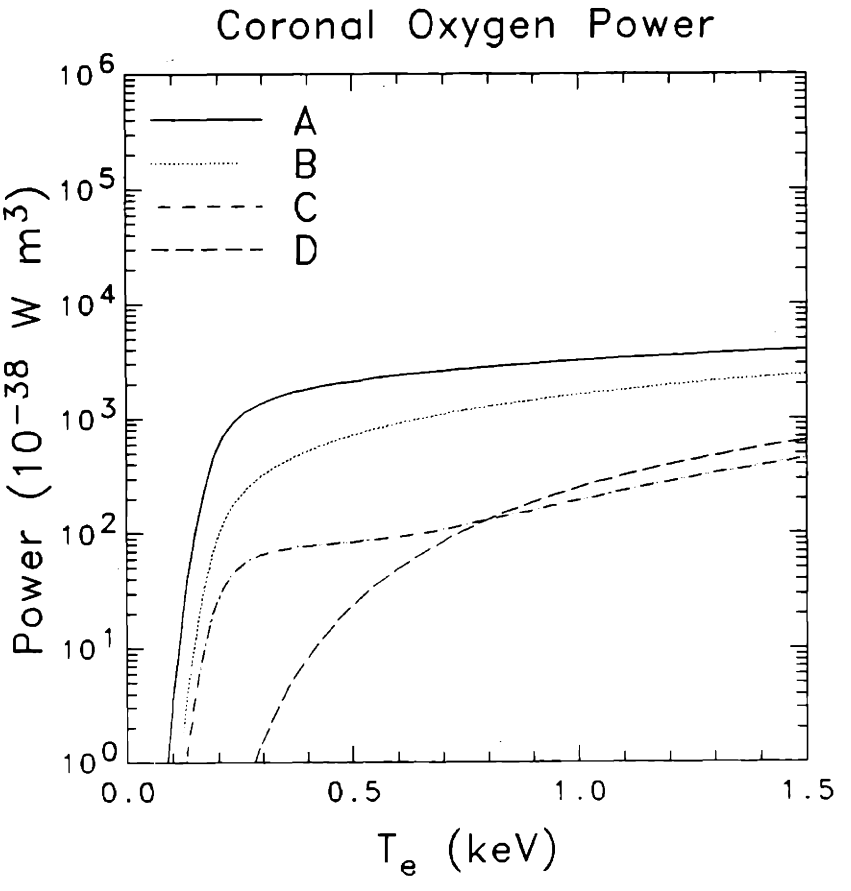

Figure C.2: The x-ray power functions for oxygen in coronal equilibrium for filters A, B, C, and D.

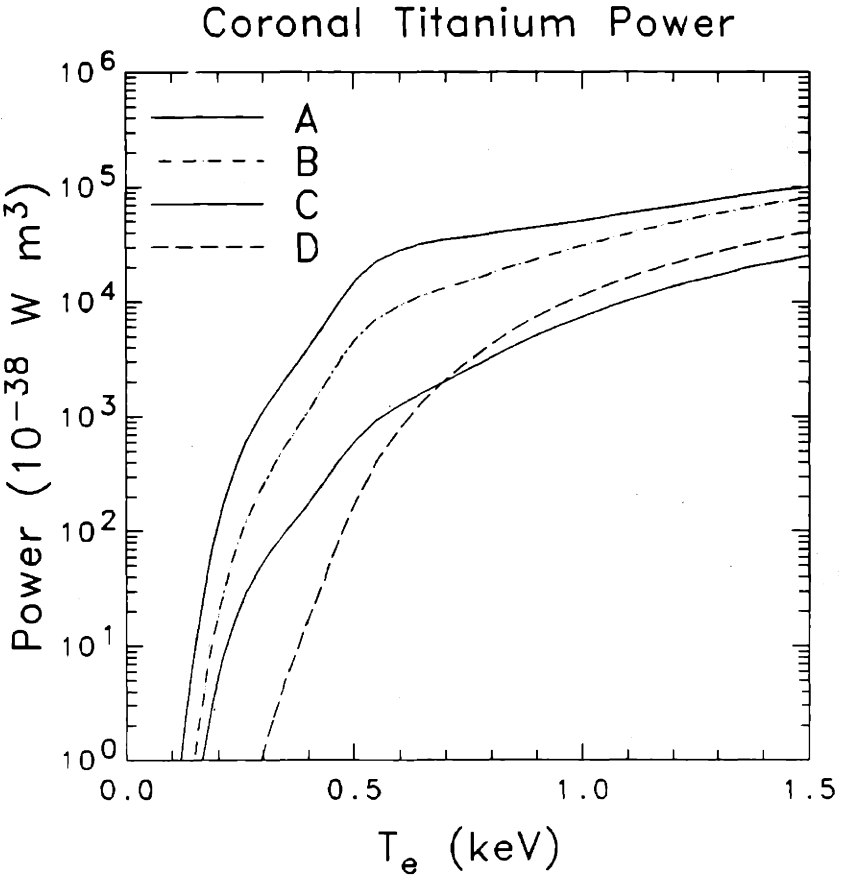

Figure C.3: The x-ray power functions for titanium in coronal equilibrium for filters A, B, C, and D.

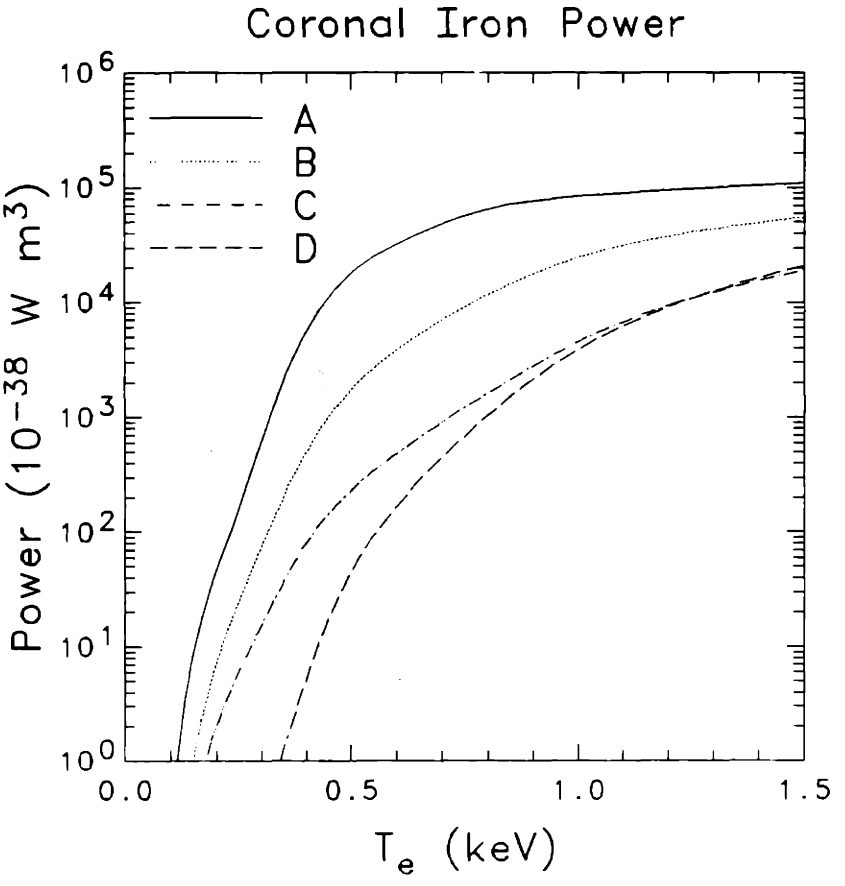

Figure C.4: The x-ray power functions for iron in coronal equilibrium for filters A, B, C, and D.

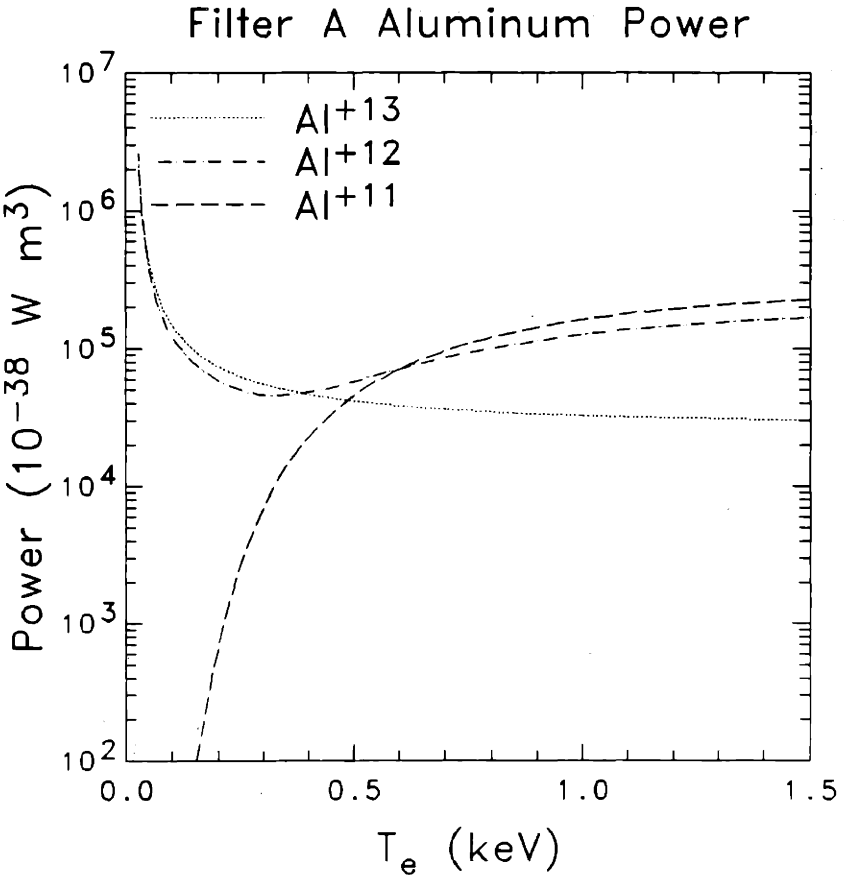

Figure C.5: The x-ray power functions for He-like through fully stripped aluminum for filter A.

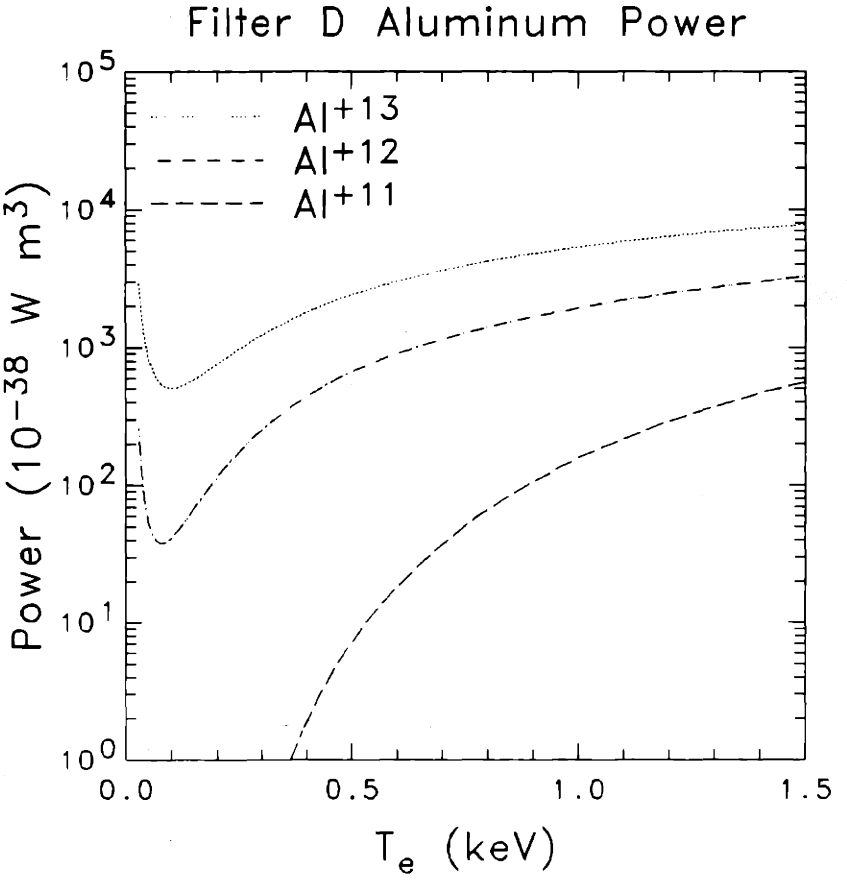

Figure C.6: The x-ray power functions for He-like through fully stripped aluminum for filter D.

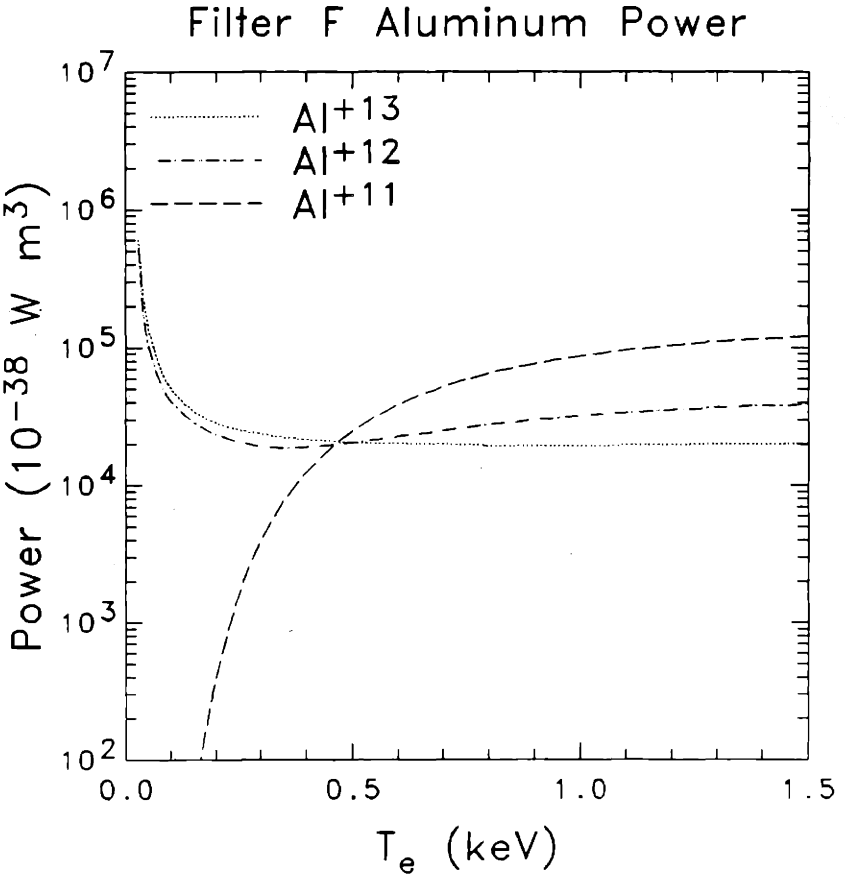

Figure C.7: The x-ray power functions for He-like through fully stripped aluminum for filter F.

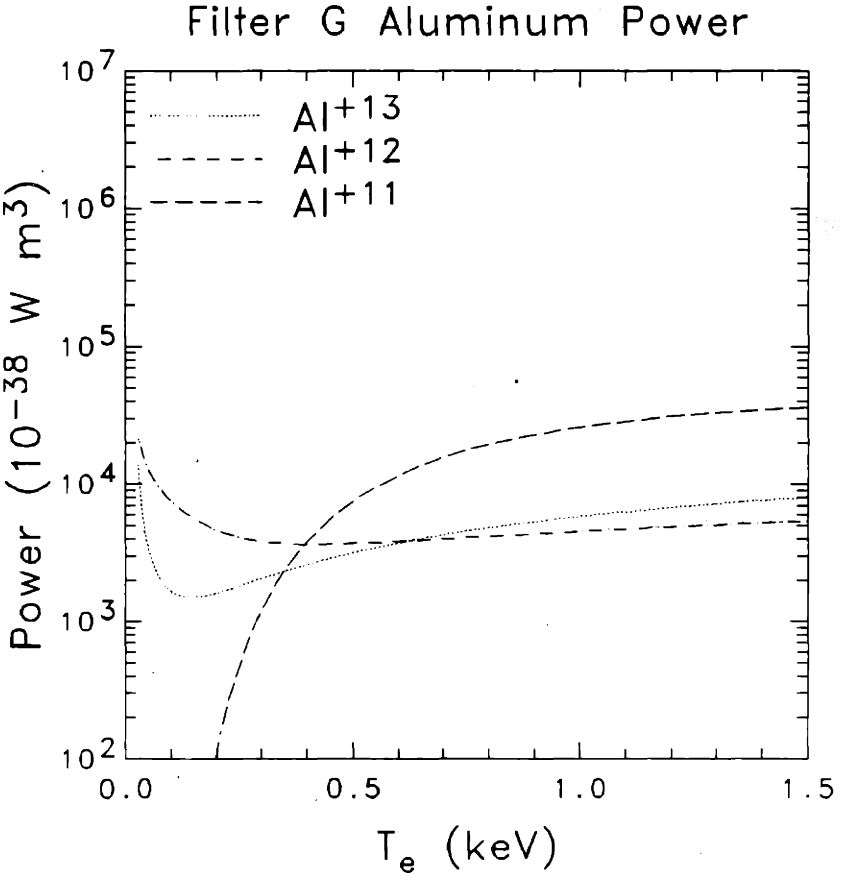

Figure C.8: The x-ray power functions for He-like through fully stripped aluminum for filter G.

Appendix D

Some Comments on Abel Inversion

D.1 Introduction

Plasma diagnostics often require inferring local plasma parameters from measurements of chord integrals [228,229]. For example soft x-ray detectors, density interferometers, bolometers, and monochromators measure line-integrated quantities of the form

$$g(p) = \int_{-\sqrt{a^2-p^2}}^{\sqrt{a^2-p^2}} f(z)dz, \tag{D.1}$$

where p is the chord impact parameter, z is the chord length through the plasma, a is the (circular) plasma minor radius and f is the local plasma parameter of interest. The solution to Eq. D.1 has been known for some time [230], and has applications in many fields other than plasma diagnostics [231] such as radiology [232,233,234] and astronomy [235]. The solution is written [229]

$$f(r) = -\frac{1}{\pi}\int_r^a \frac{\partial g}{\partial p}\frac{dp}{(p^2 - r^2)^{1/2}}. \tag{D.2}$$

This solution requires knowledge of profile gradients.

The normal procedure for Abel inversion is to fit the measured profile ($g(p)$; the brightness profile x-ray imaging) to some smooth function, calculate the gradient, and integrate numerically to obtain the local quantity ($f(r)$; the emissivity for x-rays). The function chosen for fitting the brightness profile must be chosen with care, depending on the particular shape of the profile. For example in TEXT, the most common function used to fit the x-ray brightness profile was of the form

$$g_{fit}(p) = G_0 e^{-(p/\sigma a)^\beta}, \tag{D.3}$$

where G_0, σ, and β are the fit parameters. Two limiting cases, very broad and very peaked brightness profiles, are discussed in this appendix.

D.2 Broad X-Ray Brightness Profiles

In TEXT discharges with high plasma current (low q_a), the electron density and temperature profiles are quite broad. Consequently the x-ray brightness profile is also very broad. Very broad brightness profiles can imply hollow emissivity profiles. In fact is the emissivity profile were radially constant, the resultant brightness profile would be parabolic. This implies that any brightness profile flatter than a parabola is the signature of a hollow emissivity profile.

An example of a broad brightness profile and the resultant emissivity profile obtained after Abel inversion is shown in Fig. D.1. (The solid line in the brightness plot was obtained by numerically integrating the Abel inverted emissivity.) Note the hollowness of the emissivity. The same brightness profile was also inverted by forcing it to not be hollow by fitting the emissivity, not the brightness, to an exponential function of the form of Eq. D.3. The result is shown in Fig. D.2. The hollow emissivity profile gives a brightness profile that is more in agreement with the data.

D.3 Peaked X-Ray Brightness Profiles

In contrast to the broad profiles found in low q_a discharges, very peaked brightness profiles are found in high q_a discharges. These peaked profiles must also be inverted with some care. When Eq. D.3 is used to fit peaked profiles, the power in the exponential term, β, can be less than 2. This means that the gradient of the brightness varies more slowly than r^1 near the plasma center. When this occurs the inverted emissivity profile can become extremely peaked because of the integration of the gradient divided by $\sqrt{p^2 - r^2}$ in Eq D.2. The result of naively applying the fit of Eq. D.3 is illustrated in Fig. D.3. Note that the emissivity profile obtained is extremely peaked. In fact it has a discontinuous slope at the origin. One method to avoid this effect is to force the gradient to be linear near the origin, effectively cancelling the $1/\sqrt{p^2 - r^2}$ in the integral. The result of this treatment is shown in Fig. D.4. In this case the emissivity is not as peaked as in Fig. D.3, and its slope is continuous at the origin. The resultant brightness profile also fits the data a little better.

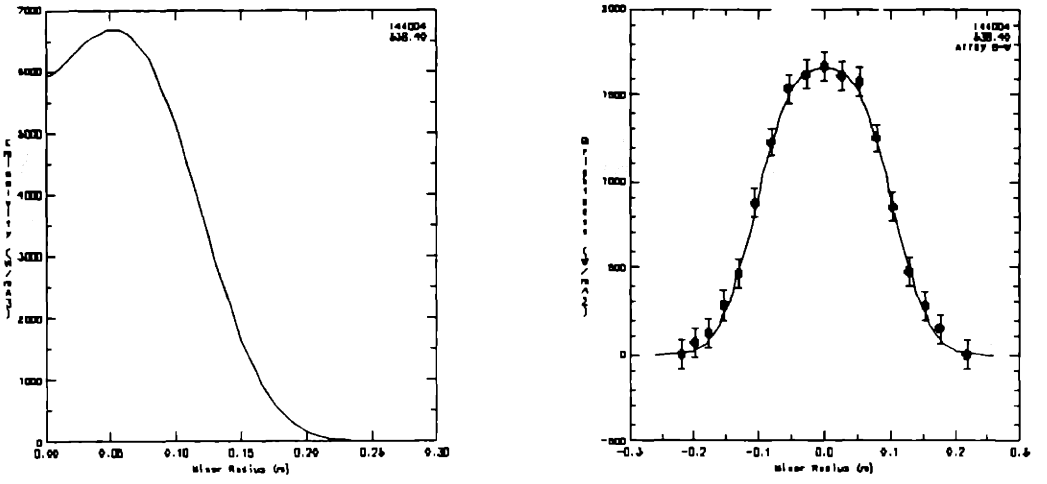

Figure D.1: The measured brightness profile and the resultant emissivity profile are shown in the case of a low q_a TEXT discharge. This sort of discharge typically has very broad electron density and temperature profiles and also broad x-ray brightness profiles. This implies hollow x-ray emissivity profiles as shown by the inversion.

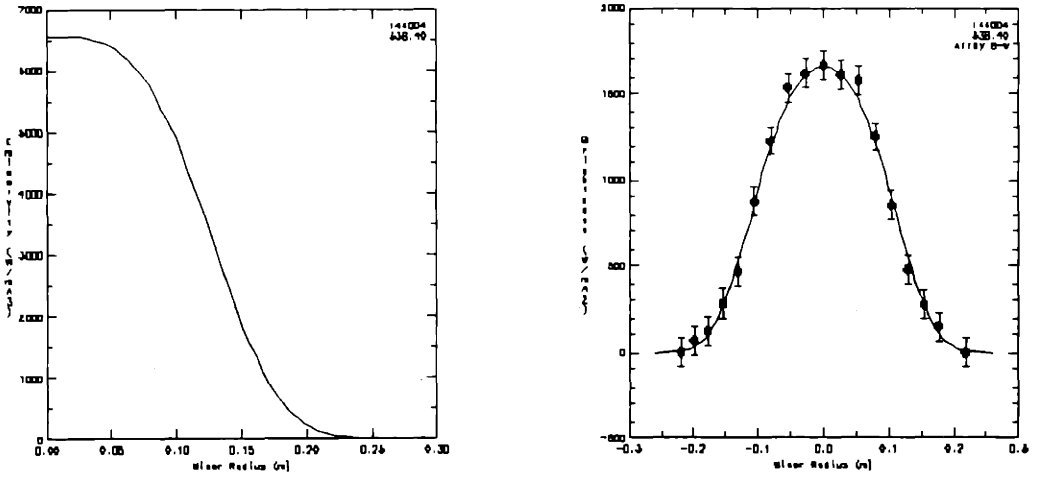

Figure D.2: The same brightness profile as shown in Fig D.1 was inverted by forcing it to not be hollow. The brightness profile calculated from the inverted profile in this case does not agree with the data as well as the brightness calculated from the hollow profile.

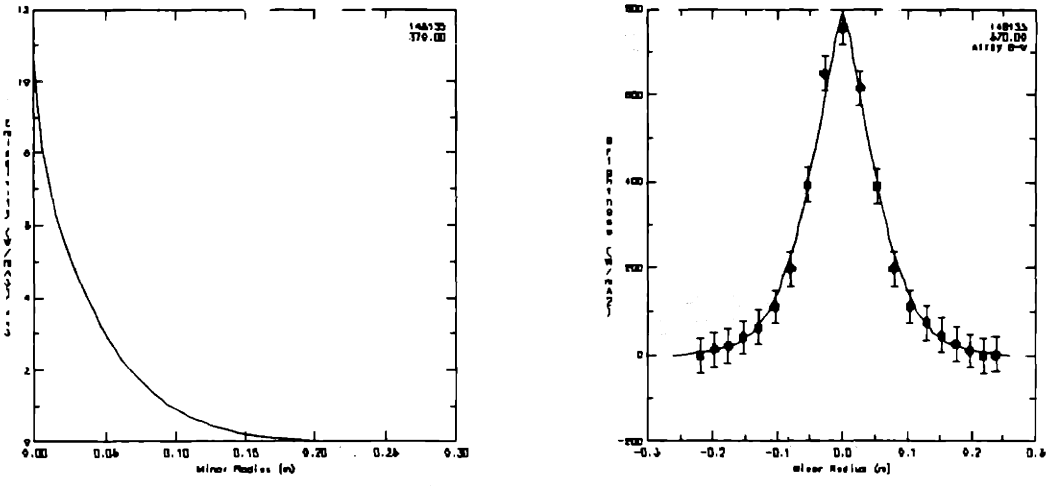

Figure D.3: The emissivity obtained by inverting a peaked brightness profile is extremely peaked. In fact it is discontinuous at the plasma center.

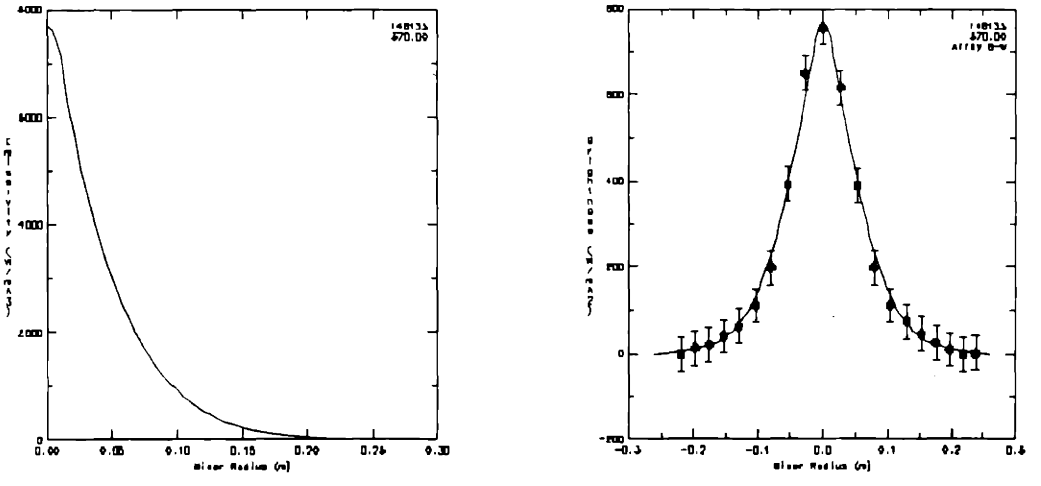

Figure D.4: The emissivity profile obtained by inverting a peaked brightness profile, but also forcing the derivative of the brightness to be linear inside of about 1.5 cm, is not as peaked as that in Fig. D.3. The resultant brightness profile also fits the data a little better.

Appendix E

Comparison of Recombination Rates for Aluminum

There are uncertainties in the atomic transition rates used in the transport codes of chapter 5. While the ionization rates are relatively well known, there can be large uncertainties in the recombination rate coefficients. The dielectronic component of the recombination is especially uncertain. In order to estimate the uncertainties in the recombination rates for aluminum, values obtained using the formalism of several different authors were compared. The recombination rates were calculated for an electron temperature of 1 keV using the rates of Mewe [204], Shull and van Steenberg [236], and Arnaud and Rothenflug [223]. The total radiative recombination was also calculated for comparison by integrating Eq.2.6 over the photon energy (the lowest six quantum shells were summed over in this calculation).

The results are displayed in the table. There is good agreement between all the radiative recombination rates into the H-like state (within $\sim$ 15%). The agreement is not so good for recombination rates into the He-like or Li-like states. The largest discrepancy is between the results from Mewe [204] and from Arnaud and Rothenflug [223]. Comparison between these results indicate that Mewe's total rates for recombination into the He-like and Li-like states may be as much as a factor of 2 too high.

Table E.1: The recombination rates for the three highest charge states of aluminum obtained from three different references are compared. The recombination rate coefficients are listed in 10^{-18} m^3s^{-1}.

Comparison of Recombination Rates for Aluminum

	full–H	H–He			He–Li		
Ref.	α_r	α_r	α_α	α_{tot}	α_r	α_α	α_{tot}
[204]	1.44	1.19	1.87	3.06	0.35	2.83	3.18
[236]	1.36	0.78	1.14	1.92	0.32	2.12	2.44
[223]	1.23	0.84	0.68	1.52	0.41	1.28	1.69
$\int$ Eq. 2.6	1.33	0.87	-	-	0.24	-	-

Appendix F

Uncertainties in Aluminum Density Profiles

It was pointed out in chapter 4 that the contrast between the krypton filter and the soft x-ray filter is degraded at low electron temperatures. When $T_e \lesssim 450$ eV, these filters cannot accurately discriminate between the He-like and H-like resonance line radiation. This appendix discusses some of the inherent uncertaintites in aluminum densities obtained using x-ray imaging with multiple filters.

At low temperatures, there is no significant amount of fully stripped aluminum, so Eqs. 4.1–4.3 are reduced to two equations for the soft filter and krypton filter emissivities:

$$\epsilon_A = n_e \left[n_{11} P_{11}^A(T_e) + n_{12} P_{12}^A(T_e) \right] \tag{F.1}$$

$$\epsilon_G = n_e \left[n_{11} P_{11}^G(T_e) + n_{12} P_{12}^G(T_e) \right] \tag{F.2}$$

(Even if the fully stripped state were present, its contribution to the filter A and G signals is negligible; see Figs. C.5 and C.8.) These two equations easily give the solutions

$$n_{11} = \frac{1}{n_e} \frac{\epsilon_A P_{12}^G - \epsilon_G P_{12}^A}{P_{11}^A P_{12}^G - P_{12}^A P_{11}^G}, \tag{F.3}$$

$$n_{12} = \frac{1}{n_e} \frac{\epsilon_A P_{11}^G - \epsilon_G P_{11}^A}{P_{11}^A P_{12}^G - P_{11}^A P_{12}^G}. \tag{F.4}$$

Using these relations, the change (or error) in n_{11} or n_{12} can be easily related to a change (or error) in n_e, ϵ, or P. The result is for n_{11} (n_{12} has similar behavior)

$$\frac{\delta n_{11}}{n_{11}} = \frac{\delta n_e}{n_e} \tag{F.5}$$

$$\frac{\delta n_{11}}{n_{11}} = \frac{\delta \epsilon_A}{\epsilon_A} \left(\frac{1}{1 - \epsilon_G P_{12}^A / \epsilon_A P_{12}^G} \right) \tag{F.6}$$

$$\frac{\delta n_{11}}{n_{11}} = \frac{\delta P_{12}^G}{P_{12}^G} \left[\frac{1}{1 - \epsilon_G P_{12}^A / \epsilon_A P_{12}^G} + \frac{1}{1 - P_{12}^A P_{11}^G / P_{12}^G P_{11}^A} \right]. \tag{F.7}$$

In these expressions, $\delta n_{11}/n_{11}$ on the left-hand side is the relative error in the He-like aluminum density. It is related to the relative error of other quantities on the right-hand side. The uncertainty in n_{11} is directly proportional to the uncertainty in the electron density. So are the other charge states, so uncertainties in n_e do not affect the charge state balance, but only the absolute densities. The relation between the uncertainty in n_{11} and that in the emissivity depends on the factor $\epsilon_G P_{12}^A/\epsilon_A P_{12}^G$. When this approaches unity, uncertainties in n_{11} due to small errors in emissivity grow large. The factor $\epsilon_G P_{12}^A/\epsilon^A P_{12}^G$ depends on the particular discharge. It is shown for a high q_a TEXT discharge in Fig. F.1. In this case it approaches 1.5 near $r = 0.16$ m, so the uncertainty in n_{11} due to uncertainty in the emissivity was maximum at that radius and equal to twice the relative uncertainty in the emissivity. Finally, the uncertainty in n_{11} is related to the uncertainty in the x-ray power function by the same factor as the emissivity, and by the factor $1/(1 - P_{12}^A P_{11}^G/P_{12}^G P_{11}^A)$. Therefore when $P_{12}^A P_{11}^G/P_{12}^G P_{11}^A$ approaches one, small errors in the x-ray power functions (for example, through errors in T_e) will lead to large errors in the aluminum density. This quantity is plotted in Fig. F.2. The figure shows that the factor approaches 2 below $T_e \simeq 400$ eV, so at that temperature the relative n_{11} uncertainty is directly proportional to the uncertainty in the x-ray power function. Between $T_e \sim 175$ eV and $T_e \sim 100$ eV the factor $P_{12}^A P_{11}^G/P_{12}^G P_{11}^A$ drops quickly from 2 to one, so when $T_e \sim 100$ eV, the relative uncertainty in n_{11} due to uncertainties in the x-ray power functions becomes extremely large. Furthermore, for low temperatures the uncertainty in the P values due to uncertainties in the electron temperature can be large because they vary rapidly with temperature (again, see Figs. C.5–C.8).

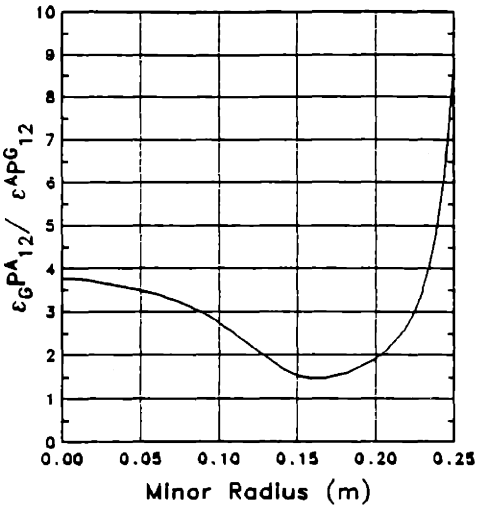

Figure F.1: This figure shows the parameter $\epsilon_G P^A_{12}/\epsilon^A P^G_{12}$ for a high q_a TEXT discharge (the same as shown in Fig. 4.12). This parameter determines the relationship between uncertainties in the emissivity and resultant uncertainties in the He-like aluminum density. For this discharge the parameter was ≥ 1.5, so the relative n_{11} uncertainty was at most twice $\delta\epsilon/\epsilon$.

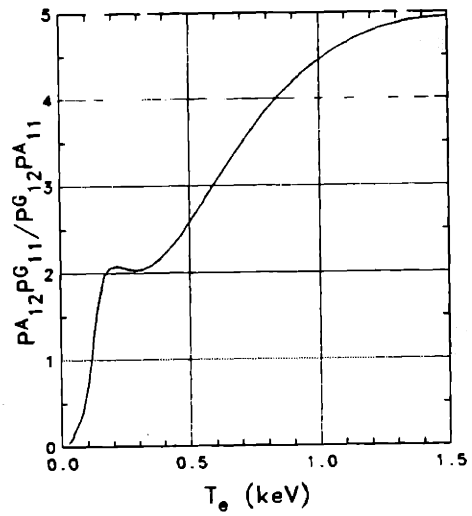

Figure F.2: This figure shows the quantity $P^A_{12}P^G_{11}/P^G_{12}P^A_{11}$ as a function of electron temperature. The relative error in aluminum density due to uncertainties in the x-ray emissivity is largest for $T_e \lesssim 400$ eV, where this factor has values between 1 and 2.

Bibliography

[1] S. Glasstone and R. H. Lovberg. *Controlled Thermonuclear Reactions.* Robert E. Krieger Publishing, Malabar, FL, 1960.

[2] H. A. Bethe and C. L. Critchfield. The formation of deuterons by proton combination. *Physical Review*, 54:248, 1938.

[3] H. A. Bethe. Energy production in stars. *Physical Review*, 55:434, 1939.

[4] Irving Langmuir. The interaction of electron and positive ion space charges in cathode sheaths. *Physical Review*, 33:954, 1929.

[5] E. J. Hellund. *The Plasma State.* Reinhold, London, 1961. The description of plasma as the fourth state is attributed to Sir William Crookes, 1879.

[6] Irwin Goodwin. Numbers game: Bush's 1990 R&D budget uses Reagan's figures in making deals. *Physics Today*, 42:43–49, May 1989.

[7] S. E. Jones. Muon-catalysed fusion revisited. *Nature*, 321:127, May 1986.

[8] S. E. Jones, E. P. Palmer, J. B. Czirr, D. L. Decker, G. L. Jensen, J. M. Thorne, S. F. Taylor, and J. Rafelski. Observation of cold nuclear fusion in condensed matter. *Nature*, 338:737, April 1989.

[9] M. Fleischmann, S. Pons, and M. Hawkins. Electrochemically induced nuclear fusion of deuterium. *Journal of Electroanalytical Chemistry*, 261:301, 1989. And erratum **262** 187 (1989).

[10] D. Albagli, R. Ballinger, V. Cammarata, X. Chen, R. M. Crooks, C. Fiore, M. J. P. Guadreau, I. Hwang, C. K. Li, P. Linsay, S. C. Luckhardt, R. R. Parker, R. D. Petrasso, M. O. Schloh, K. W. Wenzel, and M. Wrighton. Measurement and analysis of neutron and gamma ray emission rates, other fusion products, and

power in electrochemical cells having Pd cathodes. Submitted to *Journal of Fusion Energy*, 1989.

[11] R. D. Petrasso, X. Chen, K. W. Wenzel, R. R. Parker, C. K. Li, and C. Fiore. Problems with the γ ray spectrum in the Fleischmann *et. al.* experiments. *Nature*, 339:183, May 1989.

[12] R. D. Petrasso, X. Chen, K. W. Wenzel, R. R. Parker, C. K. Li, and C. Fiore. Absence of neutrons and γ rays from the Fleischmann and Pons cold fusion experiments. *Nature*, 339:667, May 1989.

[13] M. Fleischmann, S. Pons, M. Hawkins, and R. J. Hoffman. Measurements of γ rays from cold fusion. *Nature*, 339:667, 1989.

[14] M. H. Salamon, M. E. Wrenn, H. E. Bergeson, K. C. Crawford, W. H. Delaney, C. L. Henderson, Y. Q. Li, J. A. Rushko, G. M. Sandquist, and S. M. Seltzer. Limits on the emissions of neutrons, gammas, electrons and protons from cold fusion cells. Submitted to *Nature*, 1989.

[15] L. A. Artsimovich and K. B. Kartashev. Effect of a transverse magnetic field on toroidal discharge. *Soviet Physics—Doklady*, 7(10):919, April 1962.

[16] G. G. Dolgov-Savel'ev, V. S. Mukhovatov, V. S. Streklav, M. N. Shepelev, and N. A Yavlinskii. Toroidal discharge in a strong magnetic field. *Soviet Physics JETP*, 11(2):287, August 1960.

[17] P. Rebut, November 1989. Joint European Torus Press Release.

[18] J. D. Lawson. Some criteria for a power producing thermonuclear reactor. In *Proceedings of the London Physical Society*, volume B70, page 6, 1957.

[19] T. F. Stratton. X-ray spectroscopy. In Huddlestone and Leonard, editors, *Plasma Diagnostic Techniques*, chapter 8, page 259. Academic Press, 1965.

[20] M. Murakami, J. D. Callen, and L. A. Berry. Some observations on maximum densities in tokamak experiments. *Nuclear Fusion*, 16:347, 1976.

[21] M. Greenwald, J. L. Terry, S. M. Wolfe, S. Ejima, M. G. Bell, S. M. Kaye, and G. H. Neilson. A new look at density limits in tokamaks. *Nuclear Fusion*, 28:2199, 1988.

[22] L. Spitzer. *The Physics of Fully Ionized Gases.* Wiley, NY, second edition, 1962.

[23] T. S Hahm, P. H. Diamond, P. W. Terry, L. Garcia, and B. A. Carreras. Role of impurity dynamics in resistivity-gradient-driven turbulence and tokamak edge plasma phenomena. *Physics of Fluids*, 30(5):1452, May 1987.

[24] S. P. Hirshmann and D. J. Sigmar. Neoclassical transport of impurities in tokamak plasmas. *Nuclear Fusion*, 21:1079, 1981.

[25] Kim Molvig, David E. Baldwin, James E. Leiss, R. Bruce Miller, Tihiro Ohkawa, Ronald R. Parker, Francis W. Perkins, Fred L. Ribe, and Marshall N. Rosenbluth. Report on confinement and machine physics. Technical report, Magnetic Fusion Advisory Committee, June 1989.

[26] F. L. Hinton and R. D. Hazeltine. Theory of plasma transport in toroidal confinement systems. *Review of Modern Physics*, 48(2):239, April 1976.

[27] J. Hugill. Transport in tokamaks—a review of experiment. *Nuclear Fusion*, 23(3), 1983.

[28] R. C. Isler. Impurities in tokamaks. *Nuclear Fusion*, 24(12):1599, 1984.

[29] K. I. Chen, J. L. Terry, H. W. Moos, and E. S. Marmar. Spatial profiles of light impurity ions in the Alcator A tokamak plasma. *Nuclear Fusion*, 20:189, 1980.

[30] TFR Group. Light impurity transport in the TFR tokamak: Comparison of oxygen and carbon line emission with numerical simulation. *Nuclear Fusion*, 22(9):1173, 1982.

[31] TFR Group. Heavy-impurity transport in the TFR tokamak—comparison of line emission with numerical simulations. *Nuclear Fusion*, 23:559, 1983.

[32] H. Kubo, T. Sugie, A. Sakasai, Y. Koide, N. Nishimo, T. Hirayama, T. Nishitani, K. Nagashima, N. Akaoka, H. Takeuchi, and the JT60 Team. Spectroscopic study of impurities in neutral beam heated and ohmically heated JT-60 discharges. *Nuclear Fusion*, 29(4):571, 1989.

[33] Y. Koide, T. Hirayama, T. Sugie, A. Sakasai, H. Kubo, N. Akaoka, T. Nishitani, K. Nagashima, H. Shirai, H. Takeuchi, and the JT60 Team. Study of impurity transport in ohmically and neutral beam heated divertor discharges in JT-60. *Nuclear Fusion*, 28(10):1835, 1988.

[34] E. S. Marmar, J. E. Rice, J. L. Terry, and F. H. Seguin. Impurity injection experiments on the Alcator C tokamak. *Nuclear Fusion*, 22(12):1567, 1982.

[35] W. K. Leung, W. L. Rowan, J. C. Wiley, R. V. Bravenec, K. W. Gentle, W. L. Hodge, D. M. Patterson, P. E. Phillips, T. R. Price, and B. Richards. Interpretation of impurity confinement time measurements in tokamaks. *Plasma Physics and Controlled Fusion*, 28(12A):1753, 1986.

[36] B. C. Stratton, A. T. Ramsey, F. P. Boody, C. E. Bush, R. J. Fonck, R. J. Groebner, R. A. Hulse, R. K. Richards, and J. Schivell. Spectroscopic study of impurity behaviour in neutral beam heated and ohmically heated TFTR discharges. *Nuclear Fusion*, 27:1147, 1987.

[37] S. A. Cohen, J. L. Cecchi, and E. S. Marmar. Impurity transport in a quiescent tokamak plasma. *Physical Review Letters*, 35(22):1507, 1975.

[38] B. Zurro, C. Pardo, and F. Mompeán. Observation of neoclassical particle confinement behaviour in the low field tokamak TJ-1. *Plasma Physics and Controlled Fusion*, 30(12):1767, 1988.

[39] V. A. Rozhanskii. Impurity transport in tokamaks. *Soviet Journal of Plasma Physics*, 6(4):465, July 1980.

[40] W. Engelhardt, O. Klüber, D. Meisel, H. Murmann, S. Sesnic, G. Fussmann, E. Glock, N. Gottardi, F. Karger, G. Lisitano, H. M. Mayer, and F. Wagner. Accumulation of impurities and stability behaviour in the high-density regime of pulsator. In *Plasma Physics and Controlled Nuclear Fusion Research, Proceedings of the 7th International Conference, Innsbruck, 1978*, page 123, Vienna, 1979. IAEA.

[41] R. D. Petrasso, D. J. Sigmar, K. W. Wenzel, J. E. Hopf, M. Greenwald, J. L. Terry, and J. Parker. Observations of centrally peaked impurity profiles following pellet injection in the Alcator-C tokamak. *Physical Review Letters*, 57(6):707, August 1986. And references therein.

[42] K. W. Wenzel and D. J. Sigmar. Neoclassical analysis of impurity transport following transition to improved particle confinement. Submitted to *Nuclear Fusion*, 1989.

[43] R. D. Petrasso, J. Hopf, K. W Wenzel, D. J. Sigmar, J. L. Terry, and M. Greenwald. Evidence for a sign change in the convective velocity. *Bulletin of the American Physical Society*, 31:1588, 1986.

[44] M. Kaufmann, K. Büchl, G. Fussmann, O. Gehre, K. Grassie, O. Gruber, G. Haas, G. Janeschitz, M. Kornherr, K. Lackner, R. S. Lang, K. F. Mast, K. McCormick, V. Mertens, J. Neuhauser, H. Niedermeyer, W. Sandmann, W. Schneider, D. Zashe, and H.-P. Zehrfeld. Pellet injection with improved confinement in ASDEX. *Nuclear Fusion*, 28(5):827, 1988.

[45] K. H. Steuer, H. Röhr, G. Fussmann, G. Janeschitz, A. Kallenback, H. D. Murmann, and the ASDEX team. Impurity accumulation and Z_{eff} profiles in ASDEX high confinement regimes. In *16th European Conference on Controlled Fusion and Plasma Physics*, volume 13B, page 191, Venice, 1989.

[46] K. Ida, R. J. Fonck, S. Sesnic, R. A. Hulse, and B. LeBlanc. Observation of Z-dependent impurity accumulation in the PBX tokamak. *Physical Review Letters*, 58(2):116, 1987.

[47] K. Ida, R. J. Fonck, S. Sesnic, R. A. Hulse, B. LeBlanc, and S. F. Paul. Impurity behaviour in PBX L- and H-mode plasmas. *Nuclear Fusion*, 29(2):231, 1989.

[48] G. Fussmann, G. Janeschitz, and the ASDEX Team. Study of impurity accumulation in the ASDEX tokamak. In Prof. S. Methfessel and G. Thomas, editors, *Controlled Fusion and Plasma Physics*, Madrid, Spain, June 1987. European Physical Society.

[49] J. Castracane, Y. Demers, L. Könen, and A. Pospieszczyk. Impurity injection experiment on the TEXTOR tokamak: Effect of detached plasmas on confinement time. *Nuclear Fusion*, 27:1921, 1987.

[50] Y. Demers and J. Castracane. Impurity transport in detached plasmas. *Plasma Physics and Controlled Fusion*, 31:955, 1989.

[51] M. E. Perry, D. Content, H. W. Moos, N. Brooks, and M. A. Mahdavi. Impurity transport correlations with electron density profiles. *Bulletin of the American Physical Society*, 33:1964, 1988.

[52] E. J. Synakowski, R. D. Bengtson, A. Ouroua, A. J. Wootton, and S. K. Kim. Spectroscopic measurements of light impurity peaking after pellet injection on TEXT. *Nuclear Fusion*, 29(2):311, 1989

[53] TFR Group. Are heavy impurities in TFR tokamak plasmas at ionization equilibrium. *Plasma Physics*, 22:851, 1980.

[54] R. D. Petrasso, F. H. Seguin, N. G. Loter, E. Marmar, and J. Rice. Fully ionized and total silicon abundances in the Alcator-C tokamak. *Physical Review Letters*, 49(25):1826, December 1982.

[55] C. Breton, A. Compant la Fontaine, C. De Michelis, W. Hecq, J. Lasalle, P. Lecoustey, M. Mattioli, G. Mazzitelli, P. Platz, and J. Ramette. Relevance of heavy-impurity transport simulations of TFR tokamak plasmas to ionisation equilibrium evaluations. *Journal of Physics B*, 16:2627, 1983.

[56] S. von Goeler, W. Stodiek, and N. Sauthoff. Studies of internal disruptions and $m = 1$ oscillations in tokamak discharges with soft-x-ray techniques. *Physical Review Letters*, 33(20):1201, November 1974.

[57] B. B. Kadomtsev. Disruptive instability in tokamaks. *Soviet Journal of Plasma Physics*, 1(6):389, September 1975.

[58] S. K. Kim, D. L. Brower, W. A. Peebles, and N. C. Luhmann. Experimental measurement of electron particle diffusion from sawtooth-induced density-pulse propagation in the Texas experimental tokamak. *Physical Review Letters*, 60(7):577, 1988.

[59] G. L. Jahns, S. Ejima, R. J. Groebner, N. H. Brooks, R. K. Fisher, C. L. Hsieh, T. S. Taylor, J. C. Wesley, N. Fujisawa, and T. Sugawara. Dynamic behaviour of intrinsic impurities in Doublet III discharges. *Nuclear Fusion*, 22(8):1049, 1982.

[60] TFR Group et al. Dielectronic satellite spectrum of heliumlike argon: A contribution to the physics of highly charged ions and plasma impurity transport. *Physical Review A*, 32(4):2374, October 1985.

[61] K. Ida, R. J. Fonck, R. A. Hulse, and B. LeBlanc. Some effects of MHD activity on impurity transport in the PBX tokamak. Technical Report 2264, Princeton Plasma Physics Laboratory, 1985.

[62] E. J. Synakowski. *Light Impurity Studies on TEXT Using Charge-Exchange Recombination Spectroscopy.* PhD thesis, University of Texas, Physics Department, October 1988.

[63] F. H. Seguin, R D. Petrasso, and E. Marmar. Effects of internal disruptions on impurity transport in tokamaks. *Physical Review Letters*, 51(6):455, 1983.

[64] M. Keilhacker, G. Fussmann, G. von Gierke, G. Janeschitz, M. Kornherr, K. Lackner, E. R. Müller, P. Smeulders, F. Wagner, G. Becker, K. Bernhardi, U. Ditte, A. Eberhagen, O. Gehre, J. Gernhardt, E. Glock, T. Grave, O. Gruber, G. Haas, M. Hesse, F. Karger, S. Kissel, O. Klübber, G. Lisitano, H. M. Mayer, K. McCormick, D. Meisel, V. Mertens, H. Murmann, H. Niedermeyer, W. Poschenrieder, H. Rapp, F. Ryter, F. Schneider, G. Siller, F. Söldner, E. Speth, A. Stäbler, K.-H. Steuer, and O. Vollmer. Confinement and beta-limit studies in ASDEX H-mode discharges. In *Plasma Physics and Controlled Nuclear Fusion Research (10th International Conference Proceedings, London 1984)*, page 71, Vienna, 1985. IAEA.

[65] W. K. Leung. *Investigation of Impurity Transport in Texas Experimental Tokamak.* PhD thesis, University of Texas, Physics Department, December 1984.

[66] A. J. Wootton, R. D. Bengtson, J. A. Boedo, R. V. Bravenec, K. L. Empson, K. W. Gentle, W. L. Hodge, C. C. Klepper, J. Porter. A. MacMahon, S. C. McCool, W H. Miner, D. M. Patterson, P. E. Phillips, B. Richards, C. P. Ritz, T. L Rhodes, D. W. Ross, W. L. Rowan, J. Wiley, D. L. Brower, S. K. Kim, N. C. Luhmann, W. A. Peebles, J. S. DeGrassie, T. E. Evans, G. L. Jackson, N. Ohyabu, P. H. Diamond, T. S. Hahm, P. W. Terry, S. Fan, Y. He, J. C. Forster, R. L. Hickock, P. M. Schoch, G. Haas, F. Karger, X. Yu, S. Zheng, and R. Isler. Particle and thermal transport and resonant field experiments in TEXT. In *Plasma Physics and Controlled Nuclear Fusion Research*, volume 1, page 187. IAEA, 1987.

[67] A. J. Wootton, B. Carreras, H. Matsumoto, K. McGuire, R. McKnight, W. A. Peebles, Ch. Ritz, P. W. Terry, and S. Zweben. Fluctuations and anomalous transport in tokamaks. Technical Report 340, University of Texas Fusion Research Center, Austin, TX, July 1989. and references therein.

[68] G. Fussmann, J. Hofmann, G. Janeschitz, K. Krieger, E. R. Müller, R. Nolte, L. B. Ran, D. E. Roberts, H. Röhr, K. H. Steuer, H. R. Yang, and the ASDEX

Team . Impurity accumulation in plasma regimes with high energy confinement. *Journal of Nuclear Materials*, 162:14, 1989.

[69] S. I. Braginskii. Transport processes in a plasma. In M. A. Leontovich, editor, *Reviews of Plasma Physics*, page 205. Consultants Bureau, NY, 1965.

[70] D. J. Sigmar, 1989. Private communication.

[71] R. D. Petrasso, M. Gerrasimenko, F. H. Seguin, R. Krogstad, and E. Marmar. X-ray imaging studies of Alcator-A radiation and internal disruptions. *Nuclear Fusion*, 21(7):881, 1981. And references therein.

[72] University of Texas Fusion Research Center. *TEXT User Handbook*, seventh edition, June 1985.

[73] K. W. Gentle. The Texas experimental tokamak (TEXT) facility. *Nuclear Technology/Fusion*, 1:479, October 1981.

[74] W. L. Karzas and R. Latter. Electron radiative transitions in a coulomb field. *Astrophysical Journal Supplement Series*, 6:167, 1961.

[75] V. I. Kogan and V. S. Lisitsa. Fusion research and electromagnetic emission from plasmas. *Soviet Journal of Plasma Physics*, 9(1):43, 1983.

[76] S. von Goeler, W. Stodiek, E. Eubank, et al. Thermal x-ray spectra and impurities in the ST tokamak. *Nuclear Fusion*, 15:301, 1975.

[77] W. L. Rowan, 1988. Private communication.

[78] H. Van Regemorter. Rate of collisional excitation in stellar atmospheres. *Astrophysical Journal*, 136:906, 1962.

[79] A. C. Kolb and R. W. P. McWhirter. Ionization rates and power loss from θ-pinches by impurity radiation. *Physics of Fluids*, 7(4):519, 1964.

[80] A. Burgess. Dielectronic recombination and the temperature of the solar corona. *Astrophysical Journal*, 139(2):776, 1964.

[81] A. Burgess. A general formula for the estimation of dielectronic recombination coefficients in low-density plasmas. *Astrophysical Journal*, 141(4):1588, 1965.

[82] B. W. Shore. Dielectronic recombination. *Astrophysical Journal*, 158:1205, 1969.

[83] A. H. Gabriel. Dielectronic satellite spectra for highly-charged helium-like ion lines. *Monthly Notices of the Royal Astronomical Society*, 160:99, 1972.

[84] A. H. Gabriel and T. H. Paget. Measurement and interpretation of dielectronic recombination satellite line intensities. *Journal of Physics B*, 5:673, March 1972.

[85] C. P. Bhalla, A. H. Gabriel, and L. P. Presnyakov. Dielectronic satellite spectra for highly-charged helium-like ions—II. *Monthly Notices of the Royal Astronomical Society*, 172:359, 1975.

[86] F. Bely-Dubau, J. Dubau, P. Faucher, and A. H. Gabriel. Dielectronic satellite spectra for highly charged helium-like ions—VI. Iron spectra with improved inner-shell and helium-like excitation rates. *Monthly Notices of the Royal Astronomical Society*, 198:239, 1982.

[87] J. Dubau, M. Loulergue, and L. Steenman-Clark. Calculations of the atomic parameters for the dielectronic satellite lines of the Mg X II resonance line. *Monthly Notices of the Royal Astronomical Society*, 190:125, 1980.

[88] F. Bely-Dubau et al. Dielectronic satellite spectra for highly-charged helium-like ions—VII. Calcium spectra—theory and comparison with smm observations. *Monthly Notices of the Royal Astronomical Society*, 201:1155, 1982.

[89] L. A. Vainshtein and U. I. Safranova. Wavelengths and transition probabilities of satellites to resonance lines of H- and He-like ions. *Atomic Data and Nuclear Data Tables*, 21(1):49, January 1978.

[90] M. Bitter, K. W. Hill, N. R. Sauthoff, P. C. Efthimion, E. Meservey, W. Roney, S. von Goeler, R. Horton, M. Goldman, and W. Stodiek. Dielectronic satellite spectrum of heliumlike iron (Fe XXV). *Physical Review Letters*, 43(2):129, July 1979.

[91] M. Bitter et al. Dielectronic satellite spectra of hydrogenlike titanium (Ti XXII). *Physical Review A*, 29(2):661, February 1984.

[92] M. Bitter et al. Satellite spectra for heliumlike titanium. II. *Physical Review A*, 32(5):3011, November 1985.

[93] F. Bely-Dubau et al. Satellite spectra for heliumlike titanium. *Physical Review A*, 26(6):3459, December 1982.

[94] F. Bely Dubau, M. Bitter, J. Dubau, et al. Measurement of the Fe-XXV dielectronic recombination rate coefficient in the PLT tokamak plasma. *Physics Letters*, 93A(4):189, January 1983.

[95] E. Källne, J. Källne, and J E Rice. Observation of H- and He-like x-ray line emission in high-density tokamak plasmas. *Physical Review Letters*, 49(5):330, August 1982.

[96] J. E. Rice, E. S. Marmar, E. Källne, and J. Källne. Radial profiles of ground-state transitions of heliumlike argon from the Alcator-C tokamak. *Physical Review A*, 35(7):3033, April 1987.

[97] R. Bartiromo, F. Bombarda, and R. Giannella. Spectroscopic study of nonthermal plasmas. *Physical Review A*, 32(1):531, July 1985.

[98] R. Mewe, E. H. B. M. Gronenschild, and G. H. J. van den Oord. Calculated x-radiation from optically thin plasmas V. *Astronomy and Astrophysics Supplement Series*, 62:197, November 1985.

[99] K. W. Wenzel and R. D. Petrasso. X-ray imaging arrays for impurity transport studies on TEXT. To be published in *Review of Scientific Instruments.*, February 1989.

[100] B. L. Cohen. *Concepts of Nuclear Physics.* McGraw-Hill, NY, 1971.

[101] G. Knoll. *Radiation Detection and Measurement.* Wiley, 1979.

[102] G. Bertolini and A. Coche, editors. *Semiconductor Detectors.* Elsevier-North Holland, Amsterdam, 1968.

[103] F. S. Goulding. Semiconductor detectors for nuclear spectrometry. Technical Report UCRL-16231, University of California, Lawrence Radiation Laboratory, Berkeley, California, July 1965.

[104] R. A. Langley. Study of the response of silicon-barrier detectors to protons and α-particles. *Nuclear Instruments and Methods*, 113:109, 1973.

[105] EG&G Ortec. *The Whys and Wherefores of Charged Particle Detector Spectrometry*, May 1985.

[106] EG&G Ortec. *Nuclear Instruments and Systems Catalog*, 1987.

[107] W. W. Heidbrink and J D Strachan. Tokamak ion temperature and poloidal field diagnostics using 3-MeV protons *Review of Scientific Instruments*, 56(4):501, April 1985

[108] T. Saito, I. Katanuma, Y Kiwamoto, T. Kariya, and S. Miyoshi. Enhanced velocity diffusion along electron-cyclotron-resonance heating characteristics observed in hot-electron energy spectra in the plasma loss cone. *Physical Review Letters*, 59(24):2748, 1987

[109] S. J. Sanders, D. G. Kovar, B. B. Back, C. Beck, B. K. Dichter, D. Henderson, R. V F. Janssens, J. G. Keller, S. Kaufmann, T.-F. Wang, B. Wilkins, and F. Videbaek. Asymmetric fission of ^{56}Ni. *Physical Review Letters*, 59(25):2856, 1987.

[110] Y. Ohara, Y. Miura, H. Kimura, C. Konagai, and H. Takeuchi. Measurement of neutral beam species ratio by solid-state detector. *Review of Scientific Instruments*, 56(4):525, 1985.

[111] Y. Miura, H. Takeuchi, Y. Ohara, C. Konagai, and H. Kimura. Application of silicon surface barrier detector for fast neutral particles. *Review of Scientific Instruments*, 56(5):1111, May 1985.

[112] H. Duong and W. W. Heidebrink. *Bulletin of the American Physical Society*, 34(9), 1989.

[113] M. Malacarne and I. H. Hutchinson. Soft x-ray imaging diagnostic on the HBTX IA reversed field pinch. Technical Report CLM-R 227, Culham Laboratory, Abingdon, Oxon, UK, September 1982.

[114] G. A. Wurden. Soft x-ray array results on the ZT-40M reversed-field pinch. *Physics of Fluids*, 27(3):551, March 1984.

[115] A. Weller. Measurements of the radiation energy distribution in the soft x-ray region in the Wendelstein VII-A stellarator. Technical Report IPP 2/277, Max Planck Institute fur Plasmaphysik, Garching bei München, FRG, October 1985.

[116] X. Chen. *Hot Electron Plasma Equilibrium and Stability in the Constance B Mirror Experiment.* PhD thesis, MIT, Physics Department, 1988. And personal communication.

[117] N. R. Sauthoff, S. von Goeler, and W. Stodiek. A study of disruptive instabilities in the PLT tokamak using x-ray techniques. *Nuclear Fusion*, 18(10):1445, 1978.

[118] K. McGuire and D. C. Robinson. Sawtooth oscillations in a small tokamak. *Nuclear Fusion*, 19(4):505, 1979.

[119] R. D. Petrasso, M. Gerassimenko, F. H. Seguin, J. Ting, R. Krogstad, P. Gauthier, W. Hamilton, A. T. Ramsey, and P. Burnstein. Soft x-ray imaging instrument for the Alcator A tokamak. *Review of Scientific Instruments*, 51(5), May 1980.

[120] T. P. Kochanski. *Characteristics of Low Frequency MHD Fluctuations in the PRETEXT Tokamak.* PhD thesis, University of Texas, Physics Department, March 1981.

[121] K. W. Wenzel, R. D. Durst, M. S. Foster, R. D. Petrasso, and W. L. Rowan. X-ray imaging on the Texas experimental tokamak. *Bulletin of the American Physical Society*, 32(9):1842, 1987.

[122] S. B. Kim. Double sawtooth oscillations in the TEXT tokamak. *Nuclear Fusion*, 26(9):1251, 1986.

[123] M. A. Dubois, A. L. Pecquet, and C. Reverdin. Internal disruptions in the TFR tokamak: A phenomenological analysis. *Nuclear Fusion*, 23(2):147, 1983.

[124] J. D. Bell. Master's thesis, University of Tennessee, ORNL-TM/8851, 1984.

[125] J. D. Bell, J. L. Dunlap, V. K. Paré, J. D. Callen, H. C. Howe, E. A. Lazarus, M. Murakami, and C. E. Thomas. Measurement of χ_e in ISX-B beam-heated discharges by heat pulse propagation. *Nuclear Fusion*, 24(8):997, 1984.

[126] J. L. Dunlap, B. A. Carreras, V. K. Paré, J. A. Holmes, S. C. Bates, J. D. Bell, H. R. Hicks, V. E. Lynch, and A. P. Navarro. Magnetohydrodynamic instability with neutral-beam heating in the ISX-B tokamak. *Physical Review Letters*, 48(8):538, February 1982.

[127] Q. Zhao, J. Chen, J. Zie, L. Li, G. Zhang, M. Wang, and Y. Huo. Suppression of tearing modes in tokamaks by a helical magnetic field. In *Plasma Physics and Controlled Nuclear Fusion Research, Proceedings of the 10th International Conference, London*, page 345, Vienna, 1984. IAEA.

[128] J Kiraly, M Bitter S von Goeler, K W Hill, L. C. Johnson, K. McGuire, S Sesnic, N R Sauthoff, F. Tenney, and K. M. Young. Fast multichannel electron temperature diagnostic for TFTR using x-ray imaging. *Review of Scientific Instruments*, 56(5)·827, May 1985.

[129] K. Hill, S. von Goeler, M. Bitter, W. Davis, L. Dudek, E. Fredd, L. C. Johnson, J. Kiraly, K. McGuire, J. Montagne, E. Moshey, N. R. Sauthoff, and K. M. Young. Tokamak fusion test reactor x-ray imaging diagnostic. *Review of Scientific Instruments*, 56(5):830, May 1985.

[130] TFTR Group. In *Plasma Physics and Controlled Nuclear Fusion Research, Proceedings of the 11th International Conference, Kyoto*, page 51, Vienna, 1986. IAEA.

[131] J. Kiraly, M. Bitter, P. Efthimion, S. von Goeler, B. Grek, K. W. Hill, D. Johnson, K. McGuire, N. Sauthoff, S. Sesnic, F. Stauffer, G. Tait, and G. Taylor. Multichord time resolved electron temperature measurements by the x-ray absorber foil method on TFTR. *Nuclear Fusion*, 27(3):397, 1987.

[132] R. Décoste. Efficient reconstruction techniques for x-ray tomography on toroidal plasmas with arbitrary cross-sections. *Bulletin of the American Physical Society*, 30(9):1416, 1985.

[133] R. Décoste and P. Noël. Image reconstruction techniques for computed tomography from sparse data: X-ray imaging on the Varennes tokamak and other applications. *Opt. Test and Metrology, SPIE*, 661:50, 1986.

[134] E. D. Fredrickson, K. McGuire, B. Grek, K.-I. Hattori, D. Johnson, and A. W. Morris. Determination of the structure of magnetic islands on TFTR. *Review of Scientific Instruments*, 59:1797, 1988.

[135] R. B. Spielman, W. W. Hsing, and D. L. Hanson. Photoconducting x-ray detectors for z-pinch experiments. *Review of Scientific Instruments*, 59:1804, 1988.

[136] R. T. Snider, R. Evanko, and J. Haskovev. Toroidal and poloidal soft x-ray imaging system on the DIII-D tokamak. *Review of Scientific Instruments*, 59:1807, 1988.

[137] A. Holland, R J. Fonck, E J Powell and S Sesnic Tomographic imaging of MHD activity in tokamaks by combining diode arrays and a tangentially viewing pinhole camera. *Review of Scientific Instruments*, 59:1819, 1988.

[138] J. P. Anthes X-ray response of AlGaAs/GaAs radiation-hardened double-heterostructure photodiode compared to Si: *p-i-n* photodiodes. *Review of Scientific Instruments*, 59:1846, 1988.

[139] E. L. Dereniak and D. C. Crowe. *Optical Radiation Detectors*. Wiley, 1984.

[140] W VII-A Team and NI-Group. Impurity transport in the wendelstein vii-a stellarator. *Nuclear Fusion*, 25(11):1593, November 1985.

[141] L. C. Johnson, M. Bitter, R. Chouinard, et al. TFTR vertical x-ray imaging system. *Review of Scientific Instruments*, 57(8):2133, August 1986.

[142] David J. Johnson. An x-ray spectral measurement system for nanosecond plasmas. *Review of Scientific Instruments*, 45(2):191, February 1974.

[143] Gary L. Jahns. Observation of tokamak plasmas with an array of pin diode detectors. In *X-Ray Imaging*, page 36. Society of Photo-Optical Instrumentation Engineers, 1977.

[144] G. L. Jahns, M. Soler, B. V. Waddell, J. D. Callen, and N. R. Hicks. Internal disruptions in tokamaks. *Nuclear Fusion*, 18(5), 1978.

[145] J. Shiloh, A. Fisher, and N. Rostoker. Z pinch of a gas jet. *Physical Review Letters*, 40(8):515, February 1978.

[146] R. S. Granetz and J. F. Camacho. Soft-x-ray tomography on Alcator C. *Nuclear Fusion*, 25(6):727, 1985.

[147] J. F. Camacho. Soft x-ray tomography on the Alcator C tokamak. Master's thesis, MIT, Department of Electrical Engineering, May 1985.

[148] A. W. Edwards, D. J. Campbell, W. W. Englehardt, H.-U. Fahrbach, R. D. Gill, R. S. Granetz, S. Tsuji, B. L. D. Tubbing, A. Weller, J. Wesson, and D. Zasche. Rapid collapse of a plasma sawtooth oscillation in the jet tokamak. *Physical Review Letters*, 57(2):210, July 1986.

[149] A. Weller, A. D Cheetham, A W Edwards R. D. Gill, A Gondhalekar, R. S. Granetz, J. Snipes, and J A Wesson. Persistent density perturbations at rational-q surfaces following pellet injection in the joint European torus. *Physical Review Letters*, 59(20):2303, November 1987.

[150] A. W. Edwards, H -U. Fahrbach, R. D. Gill, R. Granetz, E. Oord, G. Schramm, S. Tsuji, A. Weller, and D. Zasche. Jet soft x-ray diode array diagnostic. *Review of Scientific Instruments*, 57(8).2142, August 1986.

[151] JT-60 Team. Impurity and MHD behaviour in JT-60 divertor discharges. In *Plasma Physics and Controlled Nuclear Fusion Research, Proceedings of the 11th International Conference, Kyoto*, page 217, Vienna, 1986. IAEA.

[152] JT-60 Group. The jt-60 diagnostic system. *Fusion Engineering and Design*, 5:117, 1987.

[153] F. Venneri, K. Boulais, and G. Gerdin. Construction and operation of a fast time-resolved soft x-ray spectrometer. *Bulletin of the American Physical Society*, 31(9):1461, 1986.

[154] J. L. Gaines and R. D. Ernst. In J. L. Duggan and L. L. Morgan, editors, *Proceedings of the 4th Conference on Scientific and Industrial Applications of Small Accelerators*, page 229, 1977.

[155] K. W. Wenzel and R. D. Petrasso. X-ray response of silicon surface-barrier diodes at 8 and 17.5 keV: Evidence that the x-ray sensitive depth is not generally the depletion depth. *Review of Scientific Instruments*, 59(8):1380, August 1988.

[156] M. Martini. Semiconductor radiation probes for nuclear medicine and radiobiology, the state of the art. *IEEE Transactions Nuclear Science*, 20(1):294, 1973.

[157] M. Martini and A. Hyder, 1987. EG&G Ortec, private communication.

[158] *Tennelec Silicon Charged Particle Detector Catalog #DO-986-3.0K*, 1986. And Dr. John Sanders, Tennelec Inc., private communication, 1987.

[159] M. Mansouri, July 1987. United Detector Technology senior project applications engineer, private communication.

[160] W H McMaster, N Kerr Del Grande, J. H Mallett, and J. H Hubbell. Compilation of x-ray cross sections Technical Report UCRL 50174-SEC 2-R1, Lawrence Livermore Radiation Laboratory, May 1969.

[161] B L. Henke, P Lee, T J. Tanaka, R. L. Shimabukuro, and B. K. Fujikawa. Low-energy x-ray interaction coefficients: Photoabsorption, scattering, and reflection. *Atomic Data and Nuclear Data Tables*, 27(1):1, 1982.

[162] The energy to create an electron-hole pair in silicon (3.62 eV) is about three times the band gap energy (1.1 eV). This is due to the distribution of the kinetic energy of the ionization products [237].

[163] K. G. McKay. Electron-hole production in germanium by alpha-particles. *Physical Review*, 84(4):829, November 1951.

[164] K. G. McKay and K. B. McAfee. Electron multiplication in silicon and germanium. *Physical Review*, 91(5):1079, September 1953.

[165] V. S. Vavilov. On photo-ionization by fast electrons in germanium and silicon. *Journal of Phys. Chem. Solids*, 8:223, 1959.

[166] R. H. Pehl, F. S Goulding, D. A. Landis, and M. Lenzlinger. Accurate determination of the ionization energy in semiconductor detectors. *Nuclear Instrumentation and Methodology*, 59:45, 1968.

[167] R. D. Ryan. Precision measurements of the ionization energy and its temperature variation in high purity silicon radiation detectors. *IEEE Transactions and Nuclear Science*, NS 20(1):473, 1973.

[168] F. S. Goulding, 1988. Lawrence Berkeley Laboratory, private communication.

[169] P. J. Ebert, J. L. Gaines, and G. R. Leipelt. *Nuclear Instrumentation and Methodology*, 99:29, 1972.

[170] K. W. Wenzel, M. E. Austin, R. D. Petrasso, B. Richards, and W. L. Rowan. Measurements of impurity profiles using soft x-ray arrays on TEXT. *Bulletin of the American Physical Society*, 33:2026, 1988.

[171] E. S. Marmar, J. L. Cecchi, and S. A. Cohen. System for rapid injection of metal atoms into plasmas. *Review of Scientific Instruments*, 46:1149, September 1975.

[172] E. S. Marmar. Measurement of current density profiles in the Alcator C tokamak: Zeeman polarimetry with lithium pellets. *Bulletin of the American Physical Society*, 32:1847, 1987.

[173] J. L. Terry, E. S. Marmar, B. Lipschultz, and M. J. Greenwald. The ablation and fueling physics of lithium pellets injected into Alcator C plasmas. *Bulletin of the American Physical Society*, 32:1840, 1987.

[174] M. E. Austin, R. Gandy, K. W. Gentle, and P. Phillips. Electron temperature profile measurements on TEXT using a 10-channel grating polychromator. *Bulletin of the American Physical Society*, 31:1574, 1986.

[175] J. L. Porter, P. E. Phillips, S. C. McCool, S. B. Kim, D. W. Ross, W. H. Miner, and J. C. Wiley. Current diffusion in TEXT. *Nuclear Fusion*, 27:205, 1987.

[176] M. R. Bizak, B. Richards, W. L. Rowan, J. C. Wiley, and H. S. Seung. Soft x-ray spectroscopy on TEXT. *Bulletin of the American Physical Society*, 28:1034, 1983.

[177] Y. He and R. V. Bravenec. Status of TEXT bolometry. Report 305, University of Texas Fusion Research Center, May 1988.

[178] J. Chen, M. S. Foster, S. C. McCool, A. J. Wootton, and X. Y. Yu. The MHD effects of an ergodic magnetic limiter in alternating current mode. *Bulletin of the American Physical Society*, 33:2023, 1988.

[179] P. M. Schoch, K. A. Connor, T. P. Crowley, J. W. Heard, R. L. Hickock, S. C. McCool, V. Simcic, B. A. Smith, A. J. Wootton, and Y. Z. Yang. 16th European conference on controlled fusion and plasma physics. To be published, 1989.

[180] J. F. Camacho and R. S. Granetz. Soft x-ray tomography diagnostic for the Alcator C tokamak. *Review of Scientific Instruments*, 57:417, 1986.

[181] B. A. Smith, R. S. Granetz, K. W. Wenzel, S. C. McCool, and M. S. Foster. Soft x-ray tomography on TEXT. *Bulletin of the American Physical Society*, 33:2025, 1988.

[182] R. S. Granetz and P. Smeulders. X-ray tomography on JET. *Nuclear Fusion*, 28:457, 1988.

[183] C. Janicki, R Décoste, and C. Simm. High resolution soft-x-ray tomography of sawtooth oscillations on the tokamak de varennes *Physical Review Letters*, 62(26), 1989.

[184] J. L. Snipes. *The Dynamics of Sawtooth Phenomena in TEXT.* PhD thesis, University of Texas at Austin, Physics Dept , August 1985. FRC Report # 275, (August 1985).

[185] K. W. Wenzel, R. D. Petrasso, J. E. Hopf, S. C. McCool, and M. S. Foster. Soft x-ray diagnostics on the Texas experimental tokamak. *Bulletin of the American Physical Society*, 31:1574, 1986.

[186] H. K. Tseng, C. D. Eshelman, T. J. Dolan, E. Leal-Quiros, R. Hane, J. Javedani, and H. Prelas. Initial x-ray imaging results on the Missouri mirror. *Bulletin of the American Physical Society*, 33:2054, 1988.

[187] EG&G Ortec nuclear instruments and systems catalog. Oak Ridge, TN, 1987.

[188] S. C. McCool, R. V. Bravenec, D. L. Brower, M. S. Foster, K. W. Gentle, S. B. Kim, S. K. Kim, N. C. Luhmann, Jr., D. M. Patterson, W. A. Peebles, P. E. Phillips, B. Richards, W. L. Rowan, B. A. Smith, K. W. Wenzel, and A. J. Wootton. Scaling of soft x-ray profiles and sawteeth in TEXT. *Bulletin of the American Physical Society*, 32:1842, 1987.

[189] DSP Technology Inc. Freemont, CA, 1987.

[190] M. Landini and B. C. Monsignori Fossi. Ionization balance for ions of Na, Al, P, Cl, A, K, Ca, Cr, Mn, Fe and Ni. *Astronomy and Astrophysics Supplement Series*, 7:291, 1972.

[191] D. R. Terry, W. L. Rowan, W. J. Connally, and W. K. Leung. Texas experimental tokamak impurity injection system. In *Symposium on Fusion Energy*, volume 2, page 1959, 1983.

[192] V. S. Mukhovatov and V. D. Shafronov. Plasma equilibrium in a tokamak. *Nuclear Fusion*, 11:605, 1971.

[193] S. C. McCool, F. C. Anderson, M. L. Walker, R. V. Bravenec, D. L. Brower, R. K. Fisher, K. W. Gentle, J. S. Leffler, N. C. Luhmann, Jr., W. A. Peebles,

P. E. Phillips B Richards, W L. Rowan, P. M. Schoch, B A. Smith, K. W. Wenzel, and A J Wootton Impurity pellet injection experiments on TEXT. *Bulletin of the American Physical Society*, 33:2024, 1988.

[194] M. L. Walker, F C Anderson, S. C McCool, K. R. Carter, T. K. Herman, and E. Marmar. A versatile impurity pellet injection system for TEXT. *Bulletin of the American Physical Society*, 33:2024, 1988.

[195] P.M. Valanju, 1988. Private communication.

[196] W. L. Rowan, C. C. Klepper, Ch. P. Ritz, R. D. Bengtson, K. W. Gentle, P. E. Phillips, T. L. Rhodes, B. Richards, and A. J. Wootton. Global particle confinement in the Texas experimental tokamak. *Nuclear Fusion*, 29:1077, 1988.

[197] R. K. Janev, D. S. Belíc, and B. H. Bransden. Total and partial cross sections for electron caputre in collisions of hydrogen atoms with fully stripped ions. *Physical Review A*, 28(3), 1983.

[198] A. G. Meigs and W. L. Rowan, June 1989. Private communication.

[199] R. V. Bravenec, K. W. Gentle, P. E. Phillips, T. R. Price, W. L. Rowan, K. Empson, W. L. Hodge, C. Klepper, T. P. Kochanski, D. M. Patterson, J. Porter, and B. Richards. Confinement time scaling in TEXT. *Plasma Physics and Controlled Fusion*, 27:1335, 1985.

[200] M. Greenwald, D. Gwinn, S. Milora, J. Parker, S. Wolfe, M. Besen, F. Camacho, S. Fairfax, C. Fiore, M. Foord, R. Gandy, R. Granetz, B. LaBombard, B. Lipschultz, B. Lloyd, E. Marmar, S. McCool, D. Pappas, R. Petrasso, P. Pribyl, J. Rice, D. Schuresko, Y. Takase, J. Terry, and R. Watterson. Energy confinement of high-density pellet-fueled plasmas in the Alcator C tokamak. *Physical Review Letters*, 53(4):352, 1984.

[201] B. LaBombard. *Poloidal Asymmetries in the Limiter Shadow of the Alcator-C Tokamak*. PhD thesis, MIT, Nuclear Engineering Department, May 1986. And private communication, August 1989.

[202] L. A. Artsimovich. Tokamak devices. *Nuclear Fusion*, 12:215, 1972.

[203] A. Ouroua. *Ion Thermal Diffusion in the Texas Experimental Tokamak*. PhD thesis, University of Texas, Physics Department, July 1989.

[204] R. Mewe and J Schrijver. Heliumlike ion line intensities *Astronomy and Astrophysics*, 65:99, 1978

[205] C. Breton, C. DeMichelis, M. Finkenthal, and M. Mattioli. Ionization equilibrium of selected elements from neon to tungsten of interest in tokamak plasma research. EUR-CEA-PC-949, March 1978.

[206] J. L. Terry, E. S. Marmar, K. I. Chen, and H. W. Moos. Observation of poloidal asymmetry in impurity-ion emission due to ∇b drifts. *Physical Review Letters*, 39(25):1615, December 1977.

[207] S. Suckewer, E. Hinnov, and J. Schivell. Rapid scanning of spatial distribution of spectral line intensities in PLT tokamak. Technical Report PPPL-1430, Princeton Plasma Physics Laboratory, NJ, March 1978.

[208] K. Brau, S. Suckewer, and S. K. Wong. Vertical poloidal asymmetries of low-Z element radiation in the PDX tokamak. *Nuclear Fusion*, 23(12):1657, December 1983.

[209] J. P. Smeulders. Tomography of quasi-static deformations of constant-emission surfaces of high-beta plasmas in ASDEX. *Nuclear Fusion*, 26:267, 1986.

[210] K. H. Burrell and S. K. Wong. Theoretical explanation of the poloidal asymmetry of impurity spectral line emission in collisional tokamak plasmas. *Nuclear Fusion*, 19(12):1571, 1979.

[211] D. J. Sigmar, R. Zanino, and C. T. Hsu. Evolution of poloidal variation of impurity density and ambipolar potential in rotating tokamak plasma, part I. Technical Report PFC/RR-87-8, MIT Plasma Fusion Center Report, September 1987.

[212] C. T. Hsu and D. J. Sigmar. Transport induced by ion-impurity friction in strongly rotating, collisional tokamak plasmas. Submitted to *Plasma Physics and Controlled Nuclear Fusion*, 1989.

[213] C. S. Chang and R. D. Hazeltine. Impurity transport in the collisional regime for large poloidal variations. *Nuclear Fusion*, 20:11, 1980.

[214] F. H. Seguin, E. S. Marmar, and R. D. Petrasso. Eigenfunction analysis of radial particle transport in tokamaks. *Bulletin of the American Physical Society*, 28:1120, 1983.

[215] G Fussmann. Analytical modelling of impurity transport in toroidal devices. *Nuclear Fusion*, 26(8):983, 1986.

[216] M. Abromowitz and I. A. Stegun. *Handbook of Mathematical Functions*. Dover Publications, NY, 1972.

[217] K. W. Gentle, B. Richards, and F. Waelbroeck. A measurement of hydrogen ion transport parameters in tokamak discharges. *Plasma Physics Controlled Fusion*, 29(9):1077, 1987.

[218] R. J. Hawryluk, S. Suckewer, and S. P. Hirshman. Low-z impurity transport in tokamaks. *Nuclear Fusion*, 19(5):607, 1979.

[219] A. C. Hindmarsh and L. R. Petzold. Numerical methods for solving ordinary differential equations and differential/algebraic equations. Energy technology review, Lawrence Livermore National Laboratory, September 1988.

[220] D. Potter. *Computational Physics*. J. Wiley and Sons, NY, 1973.

[221] R. A. Hulse. Numerical studies of impurities in fusion plasmas. *Nuclear Technology/Fusion*, 3:259, March 1983.

[222] J. Wesson *Tokamaks*. Oxford Science Publications, 1987.

[223] M. Arnaud and R. Rothenflug. An updated evaluation of recombination and ionization rates. *Astronomy and Astrophysics Supplement Series*, 60(6):425, 1985.

[224] Alan J. Wootton, August 1989. Private communication.

[225] K. W. Gentle, R. D. Bengtson, R. V. Bravenec, D. L. Brower, W. L. Hodge, T. P. Kochanski, N. C. Luhmann, Jr., D. M. Patterson, W. A. Peebles, P. E. Phillips, E. J. Powers, T. P. Price, B. Richards, C. P. Ritz, D. W. Ross, W. L. Rowan, R. Savage, J. C. Wiley, and Y. S. Wan. Transport studies in the TEXT tokamak. Technical report, 1984.

[226] K. Mori, W. L. Wiese, T. Shirai, Y. Nokai, K. Ozawa, and T. Kato. Spectral data and grotrian diagrams for highly ionized titanium, Ti V-Ti XXII. *Atomic Data and Nuclear Data Tables*, 34(1):79, January 1986.

[227] K. Mori, M. Otsuka, and T. Kato. Grotrian diagrams for highly ionized iron FeVIII-FeXXVI. *Atomic Data and Nuclear Data Tables*, 23(3):195, March 1979.

[228] R. H Huddlestone and S. L. Leonard. *Plasma Diagnostic Techniques.* Academic Press, 1965.

[229] I. H. Hutchinson. *Principles of Plasma Diagnostics.* Cambridge University Press, Cambridge, 1987.

[230] N. H. Abel. *J. Reine Angew. Math.*, 1:153, 1826.

[231] K. Bockasten. Transformation of observed radiances into radial distribution of the emission of a plasma. *Journal of the Optical Society of America*, 51(9):943, September 1961.

[232] W. L. Barr. Method for computing the radial distribution of emitters in a cylindrical source. *Journal of the Optical Society of America*, 52(8):885, August 1962.

[233] A. M. Cormack. Representation of a function by its line integrals, with some radiological applications. *Journal of Applied Physics*, 34(9):2722, 1963.

[234] A. M. Cormack. Representation of a function by its line integrals, with some radiological applications II. *Journal of Applied Physics*, 35(10):2908, 1964.

[235] R. N. Bracewell and A. C. Riddle. Inversion of fan-beam scans in radio astronomy. *Astrophysical Journal*, 150:427, 1967.

[236] J. M. Shull and M. van Steenberg. The ionization equilibrium of astrophysically abundant elements. *The Astrophysical Journal Supplement Series*, 48(1):95, 1982.

[237] W. E. Drummond and J. L. Moll. Hot carriers in Si and Ge radiation detectors. *Journal of Applied Physics*, 42(13):5556, December 1971.